



**HAL**  
open science

# Heavy fermions and Hund's metals in iron-based superconductors

Pablo Villar Arribi

► **To cite this version:**

Pablo Villar Arribi. Heavy fermions and Hund's metals in iron-based superconductors. Materials Science [cond-mat.mtrl-sci]. Université Grenoble Alpes, 2018. English. NNT : 2018GREAY070 . tel-02151075

**HAL Id: tel-02151075**

**<https://theses.hal.science/tel-02151075>**

Submitted on 7 Jun 2019

**HAL** is a multi-disciplinary open access archive for the deposit and dissemination of scientific research documents, whether they are published or not. The documents may come from teaching and research institutions in France or abroad, or from public or private research centers.

L'archive ouverte pluridisciplinaire **HAL**, est destinée au dépôt et à la diffusion de documents scientifiques de niveau recherche, publiés ou non, émanant des établissements d'enseignement et de recherche français ou étrangers, des laboratoires publics ou privés.

## THÈSE

Pour obtenir le grade de

### **DOCTEUR DE LA COMMUNAUTÉ UNIVERSITÉ GRENOBLE ALPES**

Spécialité : Physique de la Matière Condensée et du Rayonnement

Arrêté ministériel : 25 mai 2016

Présentée par

**Pablo VILLAR ARRIBI**

Thèse dirigée par **Luca DE' MEDICI**, ESPCI

préparée au sein du **Laboratoire European Synchrotron  
Radiation Facility**  
dans l'**École Doctorale Physique**

### **Fermions lourds et métaux de Hund dans les supraconducteurs à base de fer**

### **Heavy fermions and Hund's metals in iron- based superconductors**

Thèse soutenue publiquement le **3 décembre 2018**,  
devant le jury composé de :

**Madame ROSER VALENTI**

PROFESSEUR, UNIV. GOETHE DE FRANCFORT - ALLEMAGNE,  
Rapporteur

**Monsieur MASSIMO CAPONE**

PROFESSEUR, SISSA TRIESTE - ITALIE, Rapporteur

**Monsieur SIMONE FRATINI**

DIRECTEUR DE RECHERCHE, CNRS DELEGATION ALPES, Président

**Monsieur PATRICK BRUNO**

DIRECTEUR DE RECHERCHE, ESRF GRENOBLE, Examineur

**Monsieur FREDERIC HARDY**

CHERCHEUR, INSTITUT DE TECH. KARLSRUHE - ALLEMAGNE,  
Examineur





---

# Heavy fermions and Hund's metals in iron-based superconductors

Pablo Villar Arribi



# Acknowledgements

It is always nice to look back and take some time to think about all the good moments one has experienced along these last years. Here I would like to thank to all my family, friends, co-workers, colleagues and people that have been present in one way or another during my PhD.

First of all, I must deeply thank my advisor Dr. Luca de' Medici for his expert guidance and his trust in me. I would not have completed this project without your infinite patience, your continuous encouragement and your invaluable suggestions. Your cheerful and positive personality has been a source of inspiration for me both in and outside science. I will be always grateful to you for having taught me that much and for giving me the opportunity to share these three years next to you. It has been a real honor and a pleasure.

I am also very thankful to all the other people with who I have expended 1/3 of my time in the last years at the lab, in particular to all the members of the theory groups of ESRF and ILL in Grenoble. Andrey, Jordan and Begüm, sharing the PhD journey together has been really good fun and I wish you all the best for the future. Also thanks to William, Alessandro, Chloe, Nicolás, Hender, Bruno, Elisa, Filippo, Sarah, Samuel and all the other young colleagues that I met at the theory group and with whom I have shared lots of good moments and lots of coffees. I am also very grateful to Prof. Patrick Bruno, Dr. Keith Gilmore and Dr. Tim Ziman for their permanent advice whenever it was needed and for sharing their time in very useful and fruitful discussions. Also to Dr. Marie-Bernadette Lepetit, Dr. Dominique Bicut, Prof. Jacques Villain and to all the other senior members of the group for making life at the lab so stimulating. Last but not least, I should also thank my new officemates at the LPEM-ESPCI in Paris, Lorenzo, Mary and Tommaso, for the great atmosphere they have provided during the last weeks of the redaction of this manuscript.

I want to acknowledge also all the help that I have had from all those people that have been key in carrying out successfully this project. I would like to specially

---

thank Dr. Adriano Amaricci for his patience and help with the DMFT codes, Dr. Sara Lafuerza and Dr. Frederic Hardy for providing an invaluable insight about the experimental measurements and also for their collaboration, and finally Dr. Andrés Cano and Prof. Fabio Bernardini for helpful discussions and their collaboration.

I am also grateful to Prof. Roser Valentí, Prof. Massimo Capone, Prof. Patrick Bruno, Dr. Simone Fratini and Dr. Frederic Hardy for having accepted being part of the thesis committee.

I must express also my gratitude to Prof. Víctor Pardo, Prof. Jesús Mosqueira and Prof. Javier Castro for sharing with me their passion about physics and helping me to awaken mine. I certainly would not be here today if it was not for their guidance in the early stages of my career. In addition to them I also want to thank Adolfo, Cris, Juan, Ivan and Pablo among others for having shared those times together. You have also contributed to that process without any doubt.

I cannot forget about all my friends and colleagues from Grenoble: you have also made an important contribution to support me in this journey. Thanks to all my spanish pals, who made me feel like home from the first day, and specially to Alberto for these three really memorable years in Caserne de Bonne. I want to thank here also those with whom I have shared hours and kilometers of suffering on the bike discovering and exploring the amazing alpine roads. Me and my painful legs salute you. Also those who have enjoyed with me the skiing slopes and the awesome powder days so many times, I hope to be back soon and have the opportunity to repeat those experiences. Also I am glad to have met so many nice people at the ESRF to have shared so many good moments with all of you. A particular mention should go to the SSD-2017 organization committee for such an amazing experience.

I want to remember also all the good friends and colleagues from my university years in Spain, in particular those from Santiago with whom I still enjoy very good moments every time I go back home, and specially all my friends from Cedeira for their continuous support and for making me feel happy when we meet. Vémonos na Xira!

To conclude, I want to thank all my family (in Cedeira, Madrid and in Brussels), but in particular my parents María and Manuel, my sister Cora and my grandmother Ricardina for their infinite love and care throughout my entire life. Gracias por haberme apoyado siempre, por vuestro esfuerzo y dedicación permanentes y por haber creído siempre en mí.

# Summary

Materials where the electrons responsible for the low-energy properties experience strong correlations are today very investigated in search of emerging new phases with surprising and/or useful properties. Iron-based superconductors (IBSC - introduced in Chapter 1) are now considered in this class of compounds. Using the many-body techniques (pedagogically introduced in Chapter 2) necessary for the theoretical treatment of these correlations (slave-spin mean field theory - SSMFT - and dynamical mean field theory - DMFT - in conjunction with density functional theory, DFT), in this thesis I address several properties of IBSC.

First (Chapter 4) I analyze the very hole-doped compounds in the IBSC family, that show experimentally some behaviors typical of the so-called “heavy fermions”, compounds typically of rare earth or actinides, where extremely correlated electrons coexist with others less correlated. In particular I focus on the specific heat and the thermoelectric power and show how these properties can be understood in the recently developed paradigm of “Hund’s metals” (presented in Chapter 3). Indeed the intra-atomic exchange (the “Hund’s coupling”) is responsible for these materials of transition metal elements showing heavy-fermionic physics. I show also that typical heavy-fermionic features of the excitation spectrum, known as Van Hove singularities are well captured by our modelization within DFT+SSMFT. I then use DMFT in a model in order to study the direct impact of the Van Hove singularities on the strength of correlations.

In a second part (Chapter 5) I show how FeSe, the presently most studied IBSC, is also in a Hund’s metal phase, but it is brought to the frontier of this phase by pressure. This frontier is connected to an enhancement of the electronic compressibility which correlates positively then with the enhancement of superconductivity found in experiments. I perform an analogous study on the record holder for the highest critical superconducting temperature, the monolayer FeSe where I also find an enhanced compressibility. This supports the recent proposal that the frontier of a Hund’s metal favors high-temperature superconductivity.

---

Finally (Chapter 6) I study the nature of magnetism in another family of IBSC, the iron-germanides. I explore different possible magnetic orders with DFT simulations and study their competition (which can in principle favor superconductivity) in several compounds where different chemical substitutions are applied to the parent compound  $\text{YFe}_2\text{Ge}_2$ . I also study the effect of chemical pressure on this compound.

# Résumé

Les matériaux dans lesquels les électrons responsables des propriétés de basse énergie sont soumis à fortes corrélations sont aujourd’hui très étudiés à la recherche de nouvelles phases émergentes aux propriétés surprenantes et/ou utiles. Les supraconducteurs à base de fer (IBSC - introduits dans le Chapitre 1) sont maintenant considérés dans cette classe de composés. En utilisant des techniques multi-corps (introduits pédagogiquement dans le Chapitre 2) nécessaires pour le traitement théorique de ces corrélations (théorie du champ moyen de spin esclave - SSMFT - et théorie du champ moyen dynamique - DMFT - en conjonction avec la théorie du fonctionnelle de la densité, DFT), dans cette thèse, j’étudie plusieurs propriétés d’IBSC.

D’abord (Chapitre 4), j’analyse les composés très dopés de la famille de IBSC, qui montrent expérimentalement certains comportements typiques des “fermions lourds”, des composés typiquement des terres rares ou des actinides, où des électrons extrêmement corrélés coexistent avec des électrons moins corrélés. En particulier je me concentre sur la chaleur spécifique et le pouvoir thermoélectrique et je montre comment ces propriétés peuvent être comprises dans le paradigme récemment développé “métaux de Hund” (présentés dans le Chapitre 3). En effet, l’échange intra-atomique (le “couplage de Hund”) est responsable de ces matériaux à éléments métal de transition en montrant la physique des fermions lourds. Je montre aussi que les caractéristiques typiquement fermions-lourds du spectre d’excitation, connues car les singularités de Van Hove sont bien capturées par notre modélisation au sein de DFT+SSMFT. J’utilise ensuite DMFT dans un modèle afin d’étudier l’impact direct des singularités de Van Hove sur la force des corrélations.

Dans une seconde partie (Chapitre 5), je montre comment FeSe, le IBSC actuellement le plus étudié, se trouve également dans une phase métal de Hund, mais il est amené à la frontière de cette phase par la pression. Cette frontière est liée à une augmentation de la compressibilité électronique qui est positivement corrélée à l’augmentation de la supraconductivité trouvée dans les expériences. Je réalise une étude analogue sur le détenteur du record pour la température supraconductrice cri-

---

tique la plus élevée, la monocouche FeSe où je trouve également une compressibilité augmentée. Cela appuie la récente proposition selon laquelle la frontière du métal de Hund favorise la supraconductivité à haute température.

Enfin (Chapitre 6), j'étudie la nature du magnétisme dans une autre famille de IBSC, les germanides de fer. J'explore différents ordres magnétiques possibles avec des simulations DFT et leur concurrence (ce qui peut en principe favoriser la supraconductivité) dans plusieurs composés où différentes substitutions sont appliquées au composé parent  $\text{YFe}_2\text{Ge}_2$ . J'étudie également l'effet de la pression chimique sur ce composé.

# Contents

<b>Acknowledgements</b>	<b>3</b>
<b>Summary</b>	<b>5</b>
<b>Résumé</b>	<b>7</b>
<b>1 Introduction</b>	<b>13</b>
1.1 Strongly-correlated materials . . . . .	14
1.1.1 Fermi liquid theory . . . . .	14
1.1.2 Heavy fermions . . . . .	15
1.1.3 Unconventional superconductors . . . . .	17
1.2 Iron-based superconductors . . . . .	18
1.2.1 122 family of IBSC . . . . .	20
1.2.2 Collapsed 122 family of IBSC . . . . .	21
1.2.3 11 family of IBSC . . . . .	22
<b>2 Models and methods for strongly-correlated electron systems</b>	<b>25</b>
2.1 Density functional theory . . . . .	27
2.1.1 The Hohenberg-Kohn theorems . . . . .	27
2.1.2 The Kohn-Sham equations . . . . .	29
2.2 The Hubbard model and extensions . . . . .	34
2.3 Slave-Spin Mean-Field Theory . . . . .	37
2.3.1 Mean-field decoupling and approximations . . . . .	40
2.3.2 Set of self-consistent equations . . . . .	42
2.3.3 Generalization to several orbitals . . . . .	42
2.4 Dynamical Mean-Field Theory . . . . .	43
2.4.1 Mapping into an impurity model . . . . .	45
2.4.2 The DMFT equations . . . . .	46

2.4.3	The DMFT self-consistent cycle . . . . .	48
2.5	Realistic simulations with Slave-Spin Mean-Field Theory . . . . .	50
<b>3</b>	<b>Hund's metals</b>	<b>53</b>
3.1	Introduction . . . . .	54
3.2	Evidences in IBSC . . . . .	54
3.2.1	Mass enhancement . . . . .	54
3.2.2	Large fluctuating magnetic moments . . . . .	56
3.2.3	Orbital selectivity . . . . .	57
3.3	General phenomenology of Hund's metals from model studies . . . . .	59
3.4	Electronic compressibility . . . . .	66
<b>4</b>	<b>d-electron heavy fermions in iron-based superconductors</b>	<b>71</b>
4.1	Signatures of heavy-fermionic behavior in the 122 family of IBSC . . . . .	72
4.2	Realistic simulations of 122 stoichiometric IBSC . . . . .	73
4.3	Electronic structure of the 122 family of IBSC . . . . .	75
4.3.1	Study of Van Hove singularities in $\text{KFe}_2\text{As}_2$ . . . . .	77
4.4	DMFT study of the influence of Van Hove singularities on correlations . . . . .	79
4.5	d-electron heavy-fermions in IBSC . . . . .	83
4.6	Summary and conclusions . . . . .	90
4.7	Résumé et conclusions . . . . .	91
<b>5</b>	<b>Electronic compressibility in FeSe</b>	<b>93</b>
5.1	The special case of FeSe . . . . .	94
5.2	Calculations of electronic compressibility . . . . .	95
5.3	FeSe under pressure . . . . .	97
5.4	Results in FeSe/STO . . . . .	101
5.5	Summary and conclusions . . . . .	103
5.6	Résumé et conclusions . . . . .	103
<b>6</b>	<b>Study of magnetism in <math>\text{YFe}_2\text{Ge}_2</math> and related compounds</b>	<b>105</b>
6.1	The $\text{YFe}_2\text{Ge}_2$ system and related compounds . . . . .	106
6.2	DFT calculations . . . . .	107
6.3	Results . . . . .	108
6.3.1	$\text{YFe}_2\text{Ge}_2$ under pressure . . . . .	111
6.4	Summary and conclusions . . . . .	112
6.5	Résumé et conclusions . . . . .	112
<b>A</b>	<b>DFT</b>	<b>115</b>
A.1	Exchange-Correlation functionals . . . . .	115
A.2	The APW+lo method . . . . .	116

<b>B</b>	<b>Hubbard model in the particle-hole symmetric form</b>	<b>119</b>
B.1	1 band Hubbard model . . . . .	119
B.2	Multi-orbital Hubbard model . . . . .	120
<b>C</b>	<b>Derivation of transport equations</b>	<b>123</b>
C.1	Boltzmann Transport formalism . . . . .	123
C.1.1	Relaxation time approximation . . . . .	127
C.2	Sommerfeld expansion for the transport coefficients . . . . .	130
C.3	Sommerfeld coefficient . . . . .	132
<b>D</b>	<b>Green's functions formalism</b>	<b>135</b>
D.1	Quick reminder about statistical mechanics . . . . .	135
D.2	Green's function . . . . .	135
D.3	Finite temperature formalism . . . . .	137
<b>E</b>	<b>DMFT</b>	<b>139</b>
E.1	Different limits for DMFT . . . . .	139
E.1.1	The non-interacting limit . . . . .	139
E.1.2	The atomic limit . . . . .	139
E.1.3	Infinite coordination limit . . . . .	139
E.2	Some remarks about the calculations . . . . .	140
<b>F</b>	<b>Heavy-fermionic behavior of the 122 family of IBSC</b>	<b>141</b>
F.1	Van Hove singularities in the 122 family of IBSC . . . . .	141
F.2	Van Hove singularities in a 1-band model . . . . .	145



# 1

## Introduction

In this chapter we present the concepts that will be needed for the discussions during the rest of the manuscript. We introduce the electronic correlations and their main implications, in particular the emergence of new unexpected behavior and phases in materials. The ideas of quasiparticles and mass renormalization are introduced as they arise in Fermi liquid theory and then discussed in the context of materials, in particular heavy fermions. We also present unconventional superconductors, and more in detail iron-based materials. We explain the general features of these compounds to then briefly review the 122 and the 11 families which are the main subject of study throughout the text. We present their phase diagrams, some spectroscopic features and discuss briefly the magnetism and superconductivity in these cases.

---

Dans ce chapitre, nous présentons les concepts qui seront nécessaires aux discussions du reste du manuscrit. Nous introduisons les corrélations électroniques et leur principales implications, en particulier l'apparition de nouveaux comportements et phases inattendus dans les matériaux. Les idées de quasiparticules et de renormalisation de la masse sont brièvement abordés dans le contexte de la théorie des liquides de Fermi et des fermions lourds, qui sont également présentés. Du point de vue des matériaux, après une brève introduction aux supraconducteurs non conventionnels, les matériaux à base de fer sont présentés. Nous expliquons les caractéristiques générales de ces composés pour ensuite décrire plus en détail les familles 122 et 11 qui constituent l'objectif principal d'étude dans l'ensemble du texte. Nous présentons leurs diagrammes de phase, certaines caractéristiques spectroscopiques et discutons brièvement du magnétisme et de la supraconductivité dans ces cas.

## 1.1 Strongly-correlated materials

In a material, most of the electronic properties are governed by the electrons that are closer to the Fermi level. In many cases, when the kinetic energy of the electrons is very high, they will be delocalized along the solid and behave essentially independently from one another. Usual band theory based on a wave-like picture of the electronic states is sufficient to describe many properties of the system. However, in some materials these active electrons come from  $3d$  or  $4f$  atomic shells, which have a reduced spatial extension reduced compared to other orbitals<sup>1</sup> whose sizes are typically on the order of the inter-atomic distances. When this happens, the energy cost of having two electrons nearby is comparable to the kinetic energy gain of delocalizing them along the solid that the electrons start to avoid each other<sup>2</sup>, thus mutually influencing their motion. We say that their motion becomes correlated. Materials in which this happens are known as strongly-correlated materials.

A direct consequence of this type of description is the existence of a new type of insulating phase fully driven by correlations. This is the Mott insulator, named after N. F. Mott [1]. This happens when the conduction bands host a density of carriers corresponding to an integer number  $n$  of electrons per lattice site on average and for a sufficiently high electronic interaction strength. At these perfect fillings, the lowest energy state may be that with exactly  $n$  electrons on each lattice site, without any spacial charge fluctuation. This implies a complete breakdown of the usual band theory, since this configuration would correspond to a metallic state in that framework. It is in the vicinity of this new type of insulator where many of the characteristic signatures of the strongly-correlated electron systems are displayed [2], in particular huge changes in the resistivity, emerging magnetic phases, unconventional superconductivity or colossal magnetoresistance. Some of the most studied materials in this context are  $V_2O_3$  [3, 4], fullerenes [5, 6], Mn oxides [7] and Cu oxides [8, 9, 10].

### 1.1.1 Fermi liquid theory

This phenomenological theory developed by L. D. Landau [11], allows to describe the normal-metal behavior that many of these strongly-correlated materials display in a part of their phase diagrams. Despite the presence of strong interactions, many times these fermionic systems retain the properties of a non-interacting Fermi gas.

---

<sup>1</sup>The quantum number  $l$  governs the radial part of the wave function, and the  $3d$  and  $4f$  are the first set of orbitals with quantum number  $l = 2, 3$  respectively, which implies that they do not have to be orthogonal to any other  $d$  or  $f$  shells, so their charge cloud doesn't need to have nodes in the radial coordinate. This makes the  $3d$  and  $4f$  orbitals really compact in space.

<sup>2</sup>Pauli's exclusion principle prevents to have two electrons (fermions) in the same quantum state, but one can always end up with two electrons with anti-parallel spins in the same orbital. However, sometimes due to Coulomb repulsion, the energy cost of having these doubly-occupied orbitals can be such that it is energetically more favorable avoiding them at all cost.

Landau realized that it was possible to adiabatically connect the states of a non-interacting gas of fermions (an idealized system) with those of a system of strongly interacting fermions (a Fermi liquid) as long as no phase transition occurred in the system. This allows to describe the original strongly-interacting fermionic system with an equivalent system of non-interacting particles, the so-called Landau quasiparticles, in which the effect of the original interactions among the electrons is enclosed into their enhanced effective mass  $m^*$  and in the so-called Landau parameters, which contain information about the residual interaction among quasiparticles.

One of the key ideas by Landau is that an electron with a momentum state asymptotically close to the Fermi surface has very little phase space available for scattering with other electrons (because all the other electronic states are already occupied). A direct consequence of this is that the inelastic scattering rate has this very particular dependency

$$\tau_{FL}^{-1} \propto (\epsilon - \epsilon_F)^2 + \pi^2 T^2. \quad (1.1)$$

The description of a system as a Fermi liquid is valid as long as the quasiparticles have a sufficiently long enough lifetime<sup>3</sup>, this is, generally at very low temperatures and for excitations close to the Fermi level. When this condition is fulfilled, one can still use the Sommerfeld's model of a non-interacting Fermi gas to describe many of the properties of these systems. In particular we have that Pauli's susceptibility will be defined like

$$\chi = \mu_B^2 \frac{D^*(\epsilon_F)}{1 + F_0^A}. \quad (1.2)$$

or the low-temperature specific heat like

$$C = \frac{\pi^2}{3} D^*(\epsilon_F) k_B^2 T = \gamma T, \quad (1.3)$$

where we can see that these two quantities are proportional to the density of states of quasiparticles at the Fermi level  $D^*(\epsilon_F)$ . Another important quantity is the resistivity, which will have a dependence of the type

$$\rho = \rho_0 + AT^2, \quad (1.4)$$

which can be shown to follow directly from eq. (1.1).

### 1.1.2 Heavy fermions

A particularly interesting family of compounds where the effect of strong correlations becomes quite evident are those involving  $f$ -electrons coming from rare-earth

---

<sup>3</sup>From eq. (1.1) one can easily see that at  $T = 0K$ , quasiparticles at the Fermi level have an infinite lifetime.

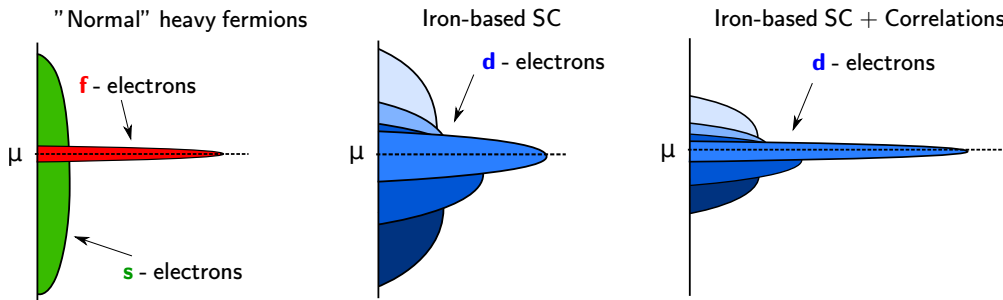


**Figure 1.1:** Schematic representation of the densities of states of conventional heavy-fermionic materials (left-figure) and its hypothetical analogy in *d*-electron iron based superconductors (second and third panels).

ions together with other atoms like Al, Cu or Pt. One of the signatures of these compounds is the formation of quasiparticles with very large effective masses that can reach sometimes up to a thousand times the bare electron mass. This feature gives its name to this family of compounds, they are known as “heavy fermions” or “heavy-fermionic materials”. These extremely heavy quasiparticles arise due to the hybridization of the localized *f*-orbitals with the broad conduction bands of the other metallic atoms, giving rise to very narrow bands in the quasiparticle spectrum (left scheme in Fig. 1.1).

A peculiar behavior of these compounds is that at high temperature the *f*-electrons become localized and thus the compound is a bad metal with the magnetic susceptibility following a Curie law due to these localized magnetic moments. However, at low temperature, these local magnetic moments of the *f*-electrons are screened by the conduction electrons with which they hybridize and thus form this very heavy quasiparticles close to the Fermi level, with their physics well described by Fermi-liquid theory. These narrow bands correspond to a very large value of the quasiparticle density of states close to the Fermi level, thus these compounds typically display also very large values of the Sommerfeld coefficient  $\gamma = C/T|_{T \rightarrow 0}$  (linear coefficient of the specific heat at low temperature) and their magnetic susceptibility will be now of Pauli type (constant and proportional of the quasiparticle density of states).

The screening of the magnetic moments at low temperatures is known as the Kondo effect due to J. Kondo who first studied this phenomenon in 1964 [12] treating them like diluted magnetic impurities in a metal [13]. This process has a characteristic energy scale that is determined by the Kondo temperature  $T_K$  above which the heavy quasiparticles become incoherent and die. For more complete reviews about this topic see Refs. [14, 15, 16, 17].

In the context of *d*-electron materials, the most notable compound displaying this type of behavior is  $\text{LiV}_2\text{O}_4$ , with a value of the Sommerfeld coefficient of  $\gamma = 420 \text{ mJ}\cdot\text{mol}^{-1}\cdot\text{K}^{-2}$  [18]. Another hypothetical family of compounds in which the

same phenomena can happen are the iron-based superconductors (IBSC) that will be described in the following section. In particular  $\text{KFe}_2\text{As}_2$  displays a low temperature magnetic susceptibility of Pauli type [19] with a crossover temperature of  $\sim 50$  K and large values of the Sommerfeld coefficient of  $\sim 100 \text{ mJ}\cdot\text{mol}^{-1}\cdot\text{K}^{-2}$  [20] of an order comparable to that of other heavy fermions.

### 1.1.3 Unconventional superconductors

Some materials become superconductors below some critical temperature  $T_c$ , and many of these are successfully described by the theory of Bardeen, Cooper and Schrieffer, the BCS theory [21, 22] or its more general equivalent, the Migdal-Eliashberg theory [23, 24, 25]. In these theories, the superconducting pairing mechanism is mediated by lattice vibrations. The compounds whose superconductivity is explained by those theories are named conventional superconductors. Up to now, the conventional superconductor at ambient pressure which has the highest  $T_c$  is  $\text{MgB}_2$ , which becomes superconducting at 39 K [26]. Superconductivity in this compound has been discussed theoretically [27, 28], and for a while it was thought that this was the upper bound for any conventional superconductor. However, theoretical predictions by Neil Ashcroft in 1968 [29] already suggested that one could find conventional superconductivity in metallic hydrogen and indeed this was realized experimentally in a relatively similar compound: metallic  $\text{H}_2\text{S}$  under very high pressures [30]. More recent claims [31] show evidences for conventional superconductivity at 260 K.

All the other materials in which the superconducting properties cannot be explained by these theories receive the name of unconventional superconductors<sup>4</sup>. This nomenclature encloses several families of materials, many of which share a very similar phase diagram, typical of correlated materials, that is dominated by a magnetic phase at integer fillings which typically dies in favor of other phases, among them a superconducting one to finally behave like a Fermi liquid far from the half-filled case. Among all of them, there is one family that deserves a special mention: Cu-based superconducting oxides, broadly known as cuprates. They were discovered in 1986 by Bednorz and Müller [32]. They all have a common layer in all the different families, in this case made of Cu and O, where superconductivity occurs but its origin is still not clear. For more information about these compounds see Refs. [8, 9, 10].

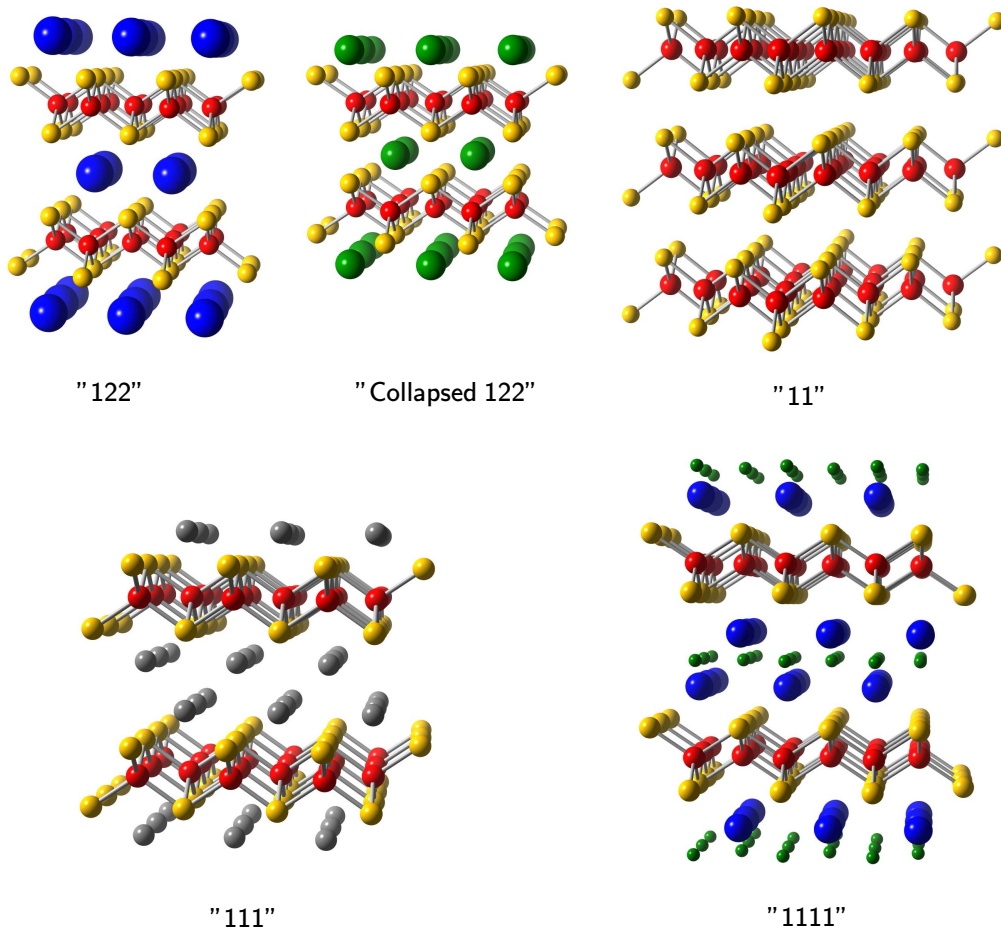


**Figure 1.2:** Crystal structures of some of the most representative families of IBSC, in particular the 122 family, the collapsed phase of the 122 family, the 11 family, the 111 family and the 1111 family. The common layers in all of them are made of Fe (red atoms) and tetrahedrally coordinated ligands (in yellow). The interlayer spacers appear in different colors.

## 1.2 Iron-based superconductors

High- $T_c$  superconductivity in these materials was discovered in 2008 by H. Hosono and co-workers [33]. This denomination refers to a broad class of layered superconducting materials containing Fe atoms. Although they have been already present for more than 10 years still they pose very interesting challenges [34]. This family of materials are all formed by a stack of planes made of Fe with tetrahedrally coordinated ligands, mainly pnictogens or chalcogens where superconductivity occurs.

<sup>4</sup>Many of these unconventional superconductors also received the name of high-temperature superconductors (HTSC) This is due to the high superconducting critical temperature that some of them display, making them susceptible to be cooled down with liquid nitrogen and not with liquid helium, which is much more expensive. These two nomenclatures get very commonly mixed nowadays, and sometimes they are even used as synonyms.

These planes are in most cases separated by another spacer layer of different atoms.

One can classify the IBSC depending on the stoichiometry of the different compounds. In Fig. 1.2 we display the crystal structures of the most common families of IBSC and their common nomenclature. LaFeAsO (which is the parent compound of the so-called “1111”-family) was the first reported IBSC, but other different families were rapidly discovered, being the “11”, “111” and the “122” families the most studied ones. The only family that does not have an interlayer spacer is the “11”. Over the years, many new families with other stoichiometries have been discovered<sup>5</sup>, but the common block of Fe-ligand buckled planes is always present in all of them.

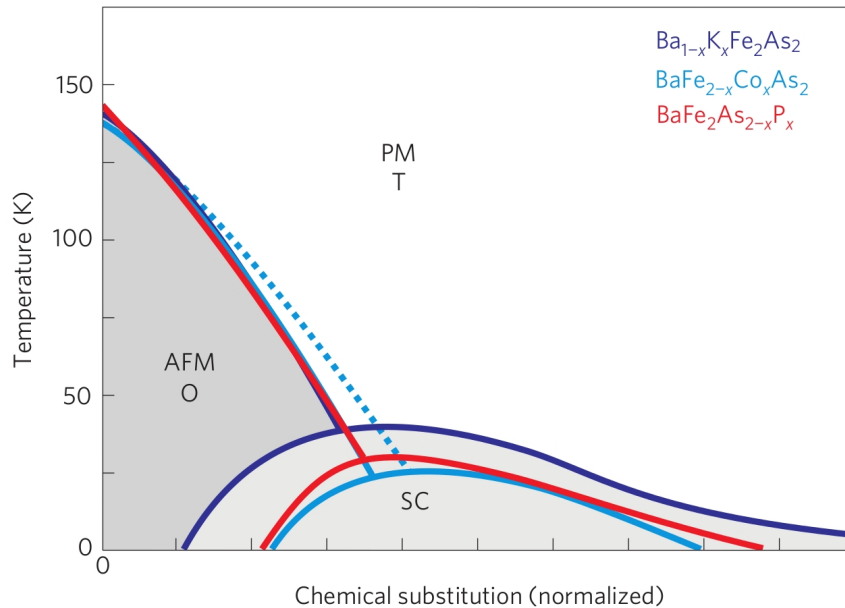


**Figure 1.3:** Schematic phase diagram of IBSC. Figure from Ref. [35].

IBSC have some similarities with other unconventional superconductors. In particular, the topology of the phase diagrams presents some common trends among most of the families (see Fig. 1.3). There is a stoichiometric parent compound that at high-temperature has a paramagnetic phase with tetragonal symmetry. Upon cooling, there is an structural transition into an orthorhombic magnetic phase, also called nematic phase<sup>6</sup>, sometimes accompanied by the formation of long-range magnetic order (typically antiferromagnetic). When this parent compound is doped (both with holes or with electrons) or put under pressure (as represented in the horizontal axis in Fig. 1.3 which is also valid for pressure), the paramagnetic tetragonal

<sup>5</sup>See Ref. [35] for a general and brief review, Ref. [34] for a more updated review of the different families. More interesting and complete introduction to these compounds can be also found in Refs. [36, 37, 38, 39].

<sup>6</sup>In a nematic transition, the fourfold rotational symmetry is broken and accompanied by a tetragonal-to-orthorhombic structural transition. The origin of this term comes from the field of liquid crystals.

phase is recovered and when temperature is lowered more a superconducting dome is found. The particular phase depends on the exact chemical composition. For more details about the phase diagrams of these compounds see Ref. [37]

In terms of the electronic band structure of these compounds, density functional theory (DFT) calculations show a manifold of several bands of mainly Fe-3*d* character (although some content of ligand *p*-orbitals is always present) crossing the Fermi level, with a total bandwidth of around  $W \sim 4$  eV, which in the paramagnetic metallic phase shows a Fermi surface of a compensated semi-metal, this is, with both electron and hole pockets. The nesting of these pockets is, in the main theories based on itinerant electrons, responsible for the low-temperature instabilities like magnetism and superconductivity. There are however some exceptions that question the general validity of these theories, for instance, the systematic disagreement between the measured and calculated electronic band structures and magnetic moments, and also the difficulty in predicting material trends in the superconducting properties in this broad group of compounds. Also it is now accepted that standard DFT does not provide a quantitatively accurate Fermi surface for IBSC. The basic compensated semi-metal character with both hole- and electron- pockets is indeed correctly predicted but the size of the pockets is in all cases too large compared to Angle-Resolved Photoemission Spectroscopy (ARPES)<sup>7</sup> measurements, which also show a much less dispersive electronic band structure. All this and other particular evidences signal a missing ingredient that is not taken into account, or at least not in an explicit way, in these theories and that can be crucial to understand many of the properties of these materials: many-body electronic correlations.

### 1.2.1 122 family of IBSC

We briefly describe here the so-called 122 family of IBSC. As it can be seen in Fig. 1.2, the layers of Fe-ligands, which in this family is typically As or P are separated by a single layer of atoms, mainly alkali metals or alkaline earths (Ba, K, Rb or Cs). The parent compound of this family, BaFe<sub>2</sub>As<sub>2</sub>, is tetragonal at room-temperature, and it becomes magnetic and changes into an orthorhombic structure below 140 K [40]. It allows various different types of substitutions (both in the Fe-ligand plane and in the interlayer spacers and both iso- and alio-valent) and in a very wide range of electronic densities. This stoichiometric compound has a nominal filling in its Fe-3*d* shell of 6 electrons in 5 orbitals. When doped with holes in the interlayer spacer, one can end up reaching another stoichiometric compound, KFe<sub>2</sub>As<sub>2</sub>, which has 5.5 electrons per Fe-3*d* shell. Then it can be further modi-

<sup>7</sup>This is one of the state-of-the-art experimental techniques to measure the spectrum of electronic excitations of a material. Hard X-ray photons with a certain energy are shined into the sample. Due to the photoelectric effect, the sample emits photons at a certain angle and energy that are then captured by an angular detector, which allows to reconstruct the dispersion relation of these electrons in the sample.

fied by isovalent substitution of  $K \leftrightarrow (\text{Rb}, \text{Cs})$ , which increases the Fe-Fe distance. On the other hand, Fe can be substituted by Co, Cr or Mn, which allows to play with the doping directly in the Fe-plane. These substitutions can induce superconductivity, different magnetic phases or structural changes, thus providing a very useful tool to explore in detail the phase diagram of these materials under a wide range of parameters. In particular when these substitutions introduce electron- or hole-doping, superconductivity arises in the system. The optimal electron-doping (at which the critical superconducting temperature  $T_c$  is maximal) occurs for the compound  $\text{Ba}(\text{Fe}_{0.93}\text{Co}_{0.07})_2\text{As}_2$ , which has a  $T_c$  is  $\sim 23$  K. In the hole-doped region, the optimal  $T_c$  occurs at  $\sim 38$  K for  $\text{Ba}_{0.6}\text{K}_{0.4}\text{Fe}_2\text{As}_2$ <sup>8</sup>. The hole-doped end member of the family,  $\text{KFe}_2\text{As}_2$ , has a  $T_c \sim 3$  K. Also, high-quality samples with clean surfaces are available, thus facilitating measurements like those performed in ARPES experiments, which can probe the electronic structure of these compounds.

### 1.2.2 Collapsed 122 family of IBSC

This family shares the same crystal structure than the usual 122 family, a body-centered tetragonal structure with Fe-ligand planes separated by a spacer cation, but with the peculiarity that the  $c$  crystallographic axis is shorter compared to the typical compounds of the 122 family. The stability of this phase has been argued to be due to the formation of new bonds among the Fe-ligands of different planes [41].

There are several IBSC that exhibit superconductivity in this collapsed phase, like  $\text{CaFe}_2\text{As}_2$  under pressure [42, 43] or  $\text{KFe}_2\text{As}_2$ , but among the several compounds that share this crystal structure,  $\text{YFe}_2\text{Ge}_2$  is one of the most studied ones, since it is the parent compound of a new class of IBSC, the so-called iron germanides. It was synthesized for the first time more than 20 years ago [44] in the quest of new heavy-fermion compounds. Further characterizations have been carried out along the years [45] but it was not until the discovery of high- $T_c$  superconductivity in the iron-based compounds that this system became attractive once more. In this compound, superconductivity was reported for the first time in 2014 [46], and although its nature has been intensively debated [47], it has been finally confirmed that it displays unconventional superconductivity [48]. This compound is paramagnetic at room temperature, but it becomes magnetic when doped with Lu [45, 49], showing that there is also a proximity between superconductivity and magnetism in iron-germanides.

From the point of view of strong correlations, we can point out a few evidences. An unusually high Sommerfeld coefficient  $\gamma \sim 100$  mJ/(mol·K<sup>2</sup>) has been measured [45, 46, 48]. In addition, large fluctuating magnetic moments have also been found in X-Ray Photoemission Spectroscopy [50] and by spin susceptibility measurements [49].

<sup>8</sup>See Ref. [40] for a complete phase diagram of superconductivity in this family.

### 1.2.3 11 family of IBSC

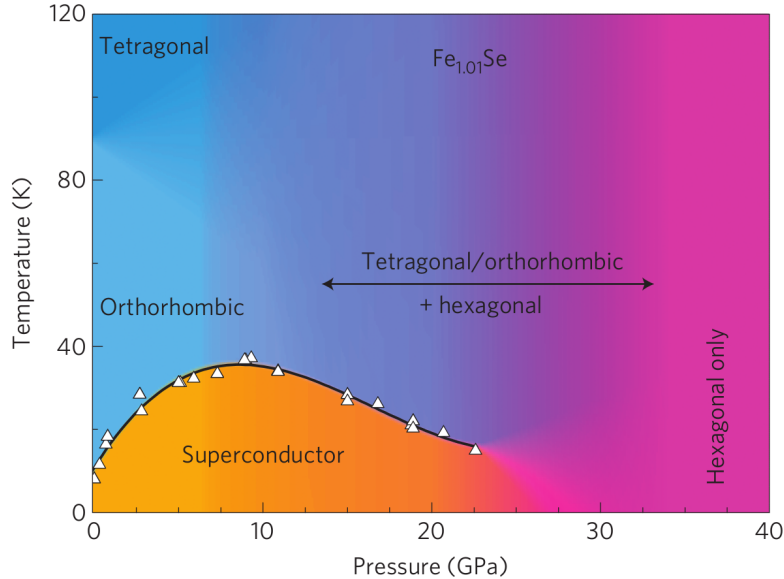


**Figure 1.4:** Schematic phase diagram of FeSe, one of the members of the 11 family of IBSC. Figure from Ref. [51].

This family is mainly composed of two compounds: FeSe and FeTe. Both compounds consist in a stack of planes of Fe atoms with Se/Te atoms alternatively above and below forming a tetrahedral environment around each of these Fe atoms (see Fig. 5.1a). Although FeTe is also interesting, this compound is not superconducting in bulk and, due to the typically lesser quality of the crystals, is much less studied than FeSe, which we will mainly describe in this section.

The phase diagram of FeSe is shown in Fig. 1.4: at ambient pressure this compound is a non-magnetic metal. Below a temperature of around 90 K, it undergoes a tetragonal-to-orthorhombic transition (nematic transition) [52] but no long-range magnetic order emerges with it. Below  $\sim 9$  K, FeSe becomes superconducting, which makes it one of the few stoichiometric superconducting IBSC. The origin of superconductivity in this case is probably unrelated to magnetism, since there is no presence of it. Superconductivity is however very effectively enhanced when applying hydrostatic pressure, unlike in many other IBSC. The maximum  $T_c \sim 37$  K is reached in the range between 7 and 9 GPa in this orthorhombic phase [51, 53], beyond which a decrease of  $T_c$  is seen in experiments. This is due to the coexistence of different crystallographic phases (tetragonal, hexagonal, orthorhombic,...) [51, 54]. Another surprising behavior of this material is found when a single layer is deposited on a SrTiO<sub>3</sub> substrate. This system shows the highest  $T_c$  ( $>65$  K, and perhaps even over 100 K) [55] reported thus far in IBSC.

Regarding the electronic structure of this compound, there are also some basic

details that must still be understood. The band structure of FeSe calculated with DFT clearly differs from the one observed experimentally. First of all, the total dispersion of the Fe-3*d* bands seen by ARPES is  $\sim 3$  times smaller and many features around the Fermi level do not coincide. One common trend is the presence of both hole-like pockets around the  $\Gamma$  point and electron-like pockets around the M point due to the compensated nature of these compounds. However, there is a discrepancy about how many pockets are around each of these points, specially around the  $\Gamma$  point [56]. A common feature that is seen in FeSe (and to some extent in all IBSC) is the so-called “red/blue shift”, which consists in energy shifts of the energy-momentum dispersions close to the center and the corners of the Brillouin Zone which have opposite direction, resulting in a shrinking of the size of the electron and hole pockets. These have been clearly observed in ARPES and in Quantum Oscillation measurements, which also show, together with specific heat measurements, a strongly orbital-dependent renormalization mass. Spectroscopic measurements also show some other interesting phenomena in this compound, among them the presence of Hubbard bands detected by ARPES measurements [57, 58], or a strong dependence of the electronic structure with temperature [59, 60, 61]. Another very interesting feature recently observed by quasiparticle interference on STM measurements is the heavily orbitally-differentiated nature of the quasiparticles close to the superconducting gap [62, 63]. A very complete review of all these spectroscopic measurements of the electronic structure of FeSe showing all these features and many others can be found in Ref. [56].



# 2

## Models and methods for strongly-correlated electron systems

In this chapter we present the basic tools that we have used along this project to perform the calculations both in materials and in models. We discuss two of the main approaches to the calculation of the electronic structure and the excitation spectrum of materials: the one-body approach where dynamical correlations are neglected and the many-body approach in which correlations are treated explicitly. We introduce 3 of the state-of-the-art methods that are used nowadays in this context, namely Density Functional Theory (DFT) in the case of the one-body approach, and Slave-Spins Mean-Field Theory (SSMFT) and Dynamical Mean-Field Theory (DMFT) in the context of the many-body problem. We present the basic concepts and main derivations. We also show the derivation of the Hubbard model in detail from a more general many-body Hamiltonian in its one-band form, and we generalize it to the multi-orbital case. Finally we briefly explain the DFT+SSMFT scheme that will be used to perform calculations in Chapters 4 and 5.

---

Dans ce chapitre, nous présentons les outils que nous avons utilisés tout au long de ce projet pour effectuer les calculs pour des matériaux et dans les modèles. Nous discutons deux des approches principales pour le calcul de la structure électronique et du spectre des excitations des matériaux: l'approche à un corps où les corrélations dynamiques sont négligées et l'approche à plusieurs corps, dans lequel les corrélations sont traitées explicitement. Nous présentons 3 méthodes utilisées dans ce contexte, à savoir la théorie du fonctionnelle de la densité (DFT) dans le cas de l'approche à un corps, et la théorie de champ moyen de spins esclaves (SSMFT) et la théorie du champ moyen dynamique (DMFT) dans le contexte du problème à plusieurs corps. Nous présentons les concepts élémentaires et les dérivations principales. Nous aussi montrons la dérivation du modèle de Hubbard en détail à partir d'un Hamiltonien à plusieurs corps plus générale, sous sa forme à une bande, et généralisé au cas multi-orbital. Enfin, nous expliquons brièvement le schéma DFT + SSMFT qui sera utilisé pour effectuer les calculs dans les Chapitres 4 et 5.

The theoretical study and characterization of the electronic properties of a material from a theoretical point of view requires a good description of its spectrum of electronic excitations. However, its computation is far from being a straightforward task. The many-body nature of the problem due to the huge number of electrons makes the size of the Hilbert space such that it is impossible to deal with it. Solving the problem in an exact manner becomes impossible and the use of approximations is thus obliged.

One has then to analyze the motion of electrons in a material in presence of dynamical correlations, that sometimes can play a very important role and pose challenging problems. These correlations appear when, under certain conditions (in particular strong electronic interactions and proximity to commensurate fillings) the energy cost of having two electrons nearby is so high compared to the kinetic energy gain of delocalizing them along the solid that the electrons start to avoid each other<sup>1</sup>, thus mutually influencing their motion. In this context an important distinction can be made among the different techniques to calculate this spectrum of electronic excitations. According to the specific treatment of these dynamical electronic correlations we would like to classify these techniques in two categories: one in which they are treated explicitly and another one in which they are neglected or treated on average as an effective potential.

The techniques in the first category aim to solve models in which the electronic interactions are treated explicitly. This adds an extra level of complexity to the problem due to the aforementioned huge size of the Hilbert space. The approximations performed here are typically related with a proper selection of a subset in this massive Hilbert space, or with the inclusion of some extra degrees of freedom that, if treated properly, allow to decouple variables of the original problem and solve it in an easier way. Among these techniques we can find slave-particle methods, dynamical mean-field theory, perturbative expansions in the Green's function formalisms,...

The second group of techniques relies on a very crude approximation. This is to assume that electrons behave independently from one another. Like that we get rid of part of the complexity of the problem, that now can be transformed into an effective one-body problem in which the effect of these electronic correlations is treated on average in an effective potential. Among the techniques that use this approach we find density functional theory, Hartree-Fock or tight-binding approximations, to name a few.

We now introduce the main techniques that are used along this work<sup>2</sup>, and also how they can be combined among themselves. These are density functional theory

---

<sup>1</sup>Pauli's exclusion principle prevents to have two electrons (fermions) in the same quantum state, but one can always end up with two electrons with anti-parallel spins in the same orbital. However, sometimes due to Coulomb repulsion, the energy cost of having these doubly-occupied configurations can be such that it is energetically more favorable avoiding them at all cost.

<sup>2</sup>We describe DFT following the descriptions provided in Refs. [64, 65]. For SSMFT we use as main source Ref. [66], and for DMFT we have followed Refs. [67, 68].

(DFT), slave-spins mean-field theory (SSMFT) and dynamical mean-field theory (DMFT). In between, we will also present the Hubbard model which is needed to introduce properly SSMFT and DMFT.

## 2.1 Density functional theory

One of the most successful and used techniques nowadays is density functional theory (DFT)[69]. It is a very useful tool to calculate the electronic structure of systems in which dynamical electronic correlations are negligible. The main difference between DFT and other methods for computing the ground state for an  $N$ -electron system is that the computed quantity here is the ground-state electron density  $n(\mathbf{r})$ , which is a 3-dimensional quantity (and maybe the spin variables) instead of a  $3N$ -dimensional wave function. We will see how this electronic density turns out to be sufficient to completely characterize the electronic system. In particular, it can be proved that the ground-state energy of a many-particle system is a functional of this electronic density. By minimizing this functional one can determine the ground-state density and thus all the properties of the ground state. The formulation of this theory is completely rigorous, however the main caveat here is the impossibility to compute exactly the functional to be minimized since this theory does not provide an analytical expression for it, and thus approximations are needed. It is in this functional in which the effect of correlations is included.

In the context of strongly correlated materials, DFT can be used as a first approximation to describe the non-interacting part of a more complex model that includes dynamical electronic correlations. It also provides a platform with which one can study in first approximation the electronic structure of the system, specially when a big predictive power is not needed.

### 2.1.1 The Hohenberg-Kohn theorems

Let's assume we have an  $N$ -electron system (a material) which can be described through a many-body Hamiltonian of the form:

$$\hat{\mathcal{H}}_e = \hat{T} + \hat{V}_{ee} + \hat{V}_{en} = \sum_i \frac{\hat{\mathbf{p}}_i^2}{2m} + \frac{1}{2} \sum_{i \neq j} \frac{e^2}{|\mathbf{r}_i - \mathbf{r}_j|} - \sum_i \sum_l \frac{z_l e^2}{|\mathbf{r}_i - \mathbf{R}_l|}, \quad (2.1)$$

which includes the kinetic energy of the electrons, the Coulomb interaction between them and the electron-nuclei interaction for each of the electrons. The index  $i$  runs over all the electrons while the index  $l$  runs over the different atomic nuclei of the system. One very important approximation we have made here is that the nuclei positions are fixed since their mass is much larger compared to that of the electrons. This is known as the Born-Oppenheimer approximation [70]. This is key since it allows us to consider the atomic nuclei as a background positive charge.

If one wishes to compute the effect of the motion of the nuclei (lattice vibrations for instance), then eq. (2.1) should be modified, and the remaining problem will be more complicated to solve.

For the sake of convenience we define:

$$\hat{V}_{en} = \sum_i \sum_l \frac{z_l e^2}{|\mathbf{r}_i - \mathbf{R}_l|} = \sum_i v_{ext}(\mathbf{r}_i) \quad \text{with} \quad v_{ext} = \sum_l \frac{z_l e^2}{|\mathbf{r}_i - \mathbf{R}_l|}. \quad (2.2)$$

Considering as the only variable of the problem the potential  $v_{ext}(\mathbf{r})$  (that we will call external potential<sup>3</sup>), while everything else (electron mass, electron charge, internal interactions, ...) is kept fixed, we can now introduce the first Hohenberg-Kohn theorem [71]. It says that there is a one-to-one correspondence between the ground-state electron density  $n(\mathbf{r})$  of an  $N$ -electron system and the external potential  $v_{ext}(\mathbf{r})$  which acts on it. Suppose we know the form of this external potential  $v_{ext}(\mathbf{r})$  and hence the total Hamiltonian of the system  $\hat{\mathcal{H}}_e$ . Both eigenvalues and eigenfunctions of the electronic system can be obtained diagonalizing that Hamiltonian. In particular, one can always obtain the ground state of the system  $|\Psi_0\rangle = |\Psi_0(\mathbf{r}_1, \mathbf{r}_2, \dots, \mathbf{r}_N)\rangle$  which will be also a function of this external potential  $\Psi_0[v_{ext}(\mathbf{r})]$ , and also the electron density of the ground state can be directly computed as

$$n(\mathbf{r}) = \langle \Psi_0(\mathbf{r}_1, \dots, \mathbf{r}_N) | \sum_i \delta(\mathbf{r} - \mathbf{r}_i) | \Psi_0(\mathbf{r}_1, \dots, \mathbf{r}_N) \rangle. \quad (2.3)$$

This indicates that the ground-state electron density is also a function only of the external potential acting on the electrons of the system. Thus, there exists a functional that relates  $n(\mathbf{r})$  with  $v_{ext}(\mathbf{r})$ .

$$n(\mathbf{r}) = n[v_{ext}(\mathbf{r})]. \quad (2.4)$$

It can be also proved that given two external potentials which only differ in one constant, their respective electron densities will be the same  $n(\mathbf{r})$  (both potentials can be re-scaled by means of an additive constant). This relation is also invertible, thus the external potential  $v_{ext}(\mathbf{r})$  can be determined up to a constant if one knows the ground-state electron density  $n(\mathbf{r})$ , leading to

$$v_{ext}(\mathbf{r}) = v_{ext}[n(\mathbf{r})], \quad (2.5)$$

which means that if we know the electron density of a system, we can determine univocally the external potential, and with it the total Hamiltonian, which gives us access to all the properties of the system.

$v_{ext} \longrightarrow |\Psi_0\rangle \longrightarrow \text{Observables} \quad (\langle \Psi_0 | \Psi_0 \rangle)$

---

<sup>3</sup>The name external comes from the fact that it includes “external” variables to the  $N$ -electron system, like the atomic positions  $\mathbf{R}_l$  and the atomic charges  $z_l$ .

Not only the external potential but also both the kinetic energy and the electron-electron interaction are functionals of the electron density. That way one can write the following functional for the total energy of that  $N$ -electron system, which receives the name of Hohenberg-Kohn functional:

$$\begin{aligned} E[n(\mathbf{r})] &= T[n(\mathbf{r})] + V_{ee}[n(\mathbf{r})] + \int v_{ext}(\mathbf{r})n(\mathbf{r})d\mathbf{r} \\ &= F[n(\mathbf{r})] + \int v_{ext}(\mathbf{r})n(\mathbf{r})d\mathbf{r}. \end{aligned} \tag{2.6}$$

Its properties are reflected in the second Hohenberg-Kohn theorem, which states that the total energy of an  $N$ -electron system, defined as a functional of the electron density, takes its minimum value when that density is the ground-state electron density of the system. In other words, given an external potential  $v_{ext}$ , the ground-state energy is obtained minimizing the energy functional  $E[n(\mathbf{r})]$  with respect to the electron density  $n(\mathbf{r})$  for a fixed number of electrons

$$N = \int n(\mathbf{r})d\mathbf{r}. \tag{2.7}$$

Taking into account this condition with a Lagrange multiplier  $\mu$ , one has to find the minimum of the functional

$$E[n(\mathbf{r})] - \mu \left[ \int n(\mathbf{r})d\mathbf{r} - N \right].$$

The electron density of the ground state will then have to fulfill the following condition

$$\frac{\delta E[n(\mathbf{r})]}{\delta n(\mathbf{r})} \equiv \frac{\delta F[n(\mathbf{r})]}{\delta n(\mathbf{r})} + v_{ext}(\mathbf{r}) = \mu. \tag{2.8}$$

That minimum value is the ground-state energy. It can be proved that this Lagrange multiplier is the chemical potential, which of course at zero temperature coincides with the Fermi energy. This second theorem is a consequence of the variational principle of Quantum Mechanics (also called Rayleigh-Ritz variational principle), which states that the expected value of the Hamiltonian is minimum if it is calculated with the true ground-state wave function.

### 2.1.2 The Kohn-Sham equations

The  $N$ -electron problem gets thus reduced to finding  $F[n(\mathbf{r})]$  and solve the variational problem. However, Hohenberg-Kohn theorems do not say anything about the form of this functional or how to obtain a close approximation. W. Kohn and L. J. Sham [72] solved this issue and made tractable this initial  $N$ -electron problem by mapping it into an effective one-body problem. They developed a method involving

a set of equations (the Kohn-Sham equations) that allow to obtain the ground-state density and the ground-state energy of the system. All this is described in this section.

In summary, to obtain these Kohn-Sham equations, the functional in eq. (2.6) has to be minimized with respect to  $n(\mathbf{r})$ . However this is done in a very clever way. This method includes an intermediate key step which consists in considering an auxiliary non-interacting electron system (the aforementioned effective one-body system) which has the same ground-state electronic density as that of the real system, and that fulfills the following ordinary time-independent Schrödinger equation with an effective potential

$$\left[ -\frac{\hbar^2 \nabla^2}{2m} + V_{eff} \right] \phi_i(\mathbf{r}) = \varepsilon_i \phi_i(\mathbf{r}). \quad (2.9)$$

The electron density for these  $N$  electrons in the auxiliary system can be decomposed as the sum of  $N$  different contributions of the spatial orthonormal orbitals  $\{\phi_i(\mathbf{r})\}$  in the form

$$n(\mathbf{r}) = \sum_i \phi_i^*(\mathbf{r}) \phi_i(\mathbf{r}), \quad (2.10)$$

where the sum is computed only for the occupied states. This ground state is constructed from a Slater product of the eigenfunctions of the different electronic states. The kinetic energy of this non-interacting electron system is defined as

$$T_{eff}[n(\mathbf{r})] = \sum_i \langle \phi_i(\mathbf{r}) | -\frac{\hbar^2 \nabla^2}{2m} | \phi_i(\mathbf{r}) \rangle, \quad (2.11)$$

which will be different from the kinetic energy of the real system, since now the functional basis set with which it is calculated is not the same. The total energy of the non-interacting electron system will then be

$$E[n(\mathbf{r})] = T_{eff}[n(\mathbf{r})] + \int V_{eff}(\mathbf{r}) n(\mathbf{r}) d\mathbf{r}. \quad (2.12)$$

The still-unknown effective potential  $V_{eff}$  must be calculated in a self-consistent manner starting from the premise that the energy functional of this “fictitious” system has to be as similar as possible to the real system functional and that its minimum will give a good approximation for the energy of the ground state and its electron density.

Now, for the real  $N$ -electron interacting system, we can rewrite the Hohenberg-Kohn functional from eq. (2.6) in a slightly different manner as

$$E[n(\mathbf{r})] = T_{eff}[n(\mathbf{r})] + \int v_{ext}(\mathbf{r}) n(\mathbf{r}) d\mathbf{r} + V_H[n(\mathbf{r})] + E_{xc}[n(\mathbf{r})], \quad (2.13)$$

in which we have introduced the so-called exchange-correlation functional  $E_{xc}[n(\mathbf{r})]$ . It is defined as

$$E_{xc}[n(\mathbf{r})] = T[n(\mathbf{r})] - T_{eff}[n(\mathbf{r})] + V_{ee}[n(\mathbf{r})] - V_H[n(\mathbf{r})], \quad (2.14)$$

where  $V_H$  is the Hartree potential which has the form

$$V_H[n(\mathbf{r})] = \frac{e^2}{2} \int \frac{n(\mathbf{r}')n(\mathbf{r})}{|\mathbf{r} - \mathbf{r}'|} d\mathbf{r}d\mathbf{r}'. \quad (2.15)$$

This allows us to rewrite the Hohenberg-Kohn functional in eq. (2.13) like:

$$E[n(\mathbf{r})] = T_{eff}[n(\mathbf{r})] + \int v_{ext}(\mathbf{r})n(\mathbf{r})d\mathbf{r} + \frac{e^2}{2} \int \frac{n(\mathbf{r}')n(\mathbf{r})}{|\mathbf{r} - \mathbf{r}'|} d\mathbf{r}d\mathbf{r}' + E_{xc}[n(\mathbf{r})]. \quad (2.16)$$

Replacing now this last expression into the minimum condition for the ground-state energy in eq. (2.8), we obtain

$$\frac{\delta T_{eff}[n(\mathbf{r})]}{\delta n(\mathbf{r})} + v_{ext}(\mathbf{r}) + e^2 \int \frac{n(\mathbf{r}')}{|\mathbf{r} - \mathbf{r}'|} d\mathbf{r}' + V_{xc}[n(\mathbf{r})] = \mu, \quad (2.17)$$

where we have that

$$V_{xc}[n(\mathbf{r})] = \frac{\delta E_{xc}[n(\mathbf{r})]}{\delta n(\mathbf{r})} \quad (2.18)$$

is the exchange-correlation potential. On the other hand, if we now apply this same condition in eq. (2.8) to the energy functional of the non-interacting electron system from expression (2.12) we obtain an equivalent condition for that system

$$\frac{\delta T_{eff}[n(\mathbf{r})]}{\delta n(\mathbf{r})} + V_{eff}(\mathbf{r}) = \mu. \quad (2.19)$$

Just by comparison between (2.17) and (2.19) we get that

$$V_{eff}(\mathbf{r}) = v_{ext}(\mathbf{r}) + e^2 \int \frac{n(\mathbf{r}')}{|\mathbf{r} - \mathbf{r}'|} d\mathbf{r}' + V_{xc}[n(\mathbf{r})]. \quad (2.20)$$

This effective one-particle potential is called the Kohn-Sham potential. Now, we can rewrite eq. (2.9) taking into account the previous results from expression (2.20) and we will finally obtain the Kohn-Sham equations:

$$\boxed{\left[ -\frac{\hbar^2 \nabla^2}{2m} + v_{ext}(\mathbf{r}) + e^2 \int \frac{n(\mathbf{r}')}{|\mathbf{r} - \mathbf{r}'|} d\mathbf{r}' + V_{xc}[n(\mathbf{r})] \right] \phi_i(\mathbf{r}) = \varepsilon_i \phi_i(\mathbf{r})}. \quad (2.21)$$

From these equations and taking into account all the considerations made above about the equivalence of the ground-state electron density for the real and non-interacting systems, we obtain that the ground-state energy of the system can be

calculated as

$$E[n(\mathbf{r})] = T_{eff}[n(\mathbf{r})] + \int v_{ext}(\mathbf{r})n(\mathbf{r})d\mathbf{r} + \frac{e^2}{2} \int \frac{n(\mathbf{r}')n(\mathbf{r})}{|\mathbf{r} - \mathbf{r}'|} d\mathbf{r}d\mathbf{r}' + E_{xc}[n(\mathbf{r})]. \quad (2.22)$$

At this point one should notice that the densities of these two systems have to coincide, owing to Hohenberg-Kohn theorems. That way one can use the functional basis set  $\{\phi_i\}$ , the so-called Kohn-Sham orbitals, of this equivalent non-interacting system to perform all the required integrals. These are essentially the Bloch wave functions corresponding to the Kohn-Sham effective potential. With them, we can build for instance the electronic density like:

$$n(\mathbf{r}) = \sum_i \phi_i^*(\mathbf{r})\phi_i(\mathbf{r}). \quad (2.23)$$

Finally, in order to be able to do calculations we have to obtain an expression for  $T_{eff}$ , but from eq. (2.9) one can see that it is possible to write

$$T_{eff}[n(\mathbf{r})] = \sum_i \langle \phi_i(\mathbf{r}) | \varepsilon_i - V_{eff}[n(\mathbf{r})] | \phi_i(\mathbf{r}) \rangle, \quad (2.24)$$

so if we insert the expression (2.20) for  $V_{eff}$  into eq. (2.24) and then replace all these terms in eq. (2.22) we arrive to a final expression for the energy of the system:

$$\begin{aligned} E[n(\mathbf{r})] &= \sum_i \varepsilon_i - \int V_{eff}(\mathbf{r})n(\mathbf{r})d\mathbf{r} + \int v_{ext}(\mathbf{r})n(\mathbf{r})d\mathbf{r} \\ &+ \frac{e^2}{2} \int \frac{n(\mathbf{r}')n(\mathbf{r})}{|\mathbf{r} - \mathbf{r}'|} d\mathbf{r}d\mathbf{r}' + E_{xc}[n(\mathbf{r})] \\ &= \sum_i \varepsilon_i - \frac{e^2}{2} \int \frac{n(\mathbf{r}')n(\mathbf{r})}{|\mathbf{r} - \mathbf{r}'|} d\mathbf{r}d\mathbf{r}' + E_{xc}[n(\mathbf{r})] - \int V_{xc}[n(\mathbf{r})]n(\mathbf{r})d\mathbf{r}. \end{aligned} \quad (2.25)$$

That way, if the external potential  $v_{ext}(\mathbf{r})$  and the exchange-correlation functional  $E_{xc}[n(\mathbf{r})]$  (or the exchange-correlation potential  $V_{xc}[n(\mathbf{r})]$ ) are known, the ground-state electron density can be computed in a self-consistent manner, and from it, all the properties of the system.

A scheme of a self-consistent calculation is sketched in Fig. (2.1). A set of initial parameters must be specified for each system that we want to study. These are the atomic coordinates  $\mathbf{R}_l$  and their charge  $z_l$  (thus the total number of electrons  $N$ ). Then, given an initial guess for the electron density  $n_0(\mathbf{r})$  (and provided we have selected an exchange-correlation functional) the potential  $V_{eff}$  can be calculated thanks to eq. (2.20). Once this potential is obtained, by solving the Kohn-Sham equations (2.21), one gets the eigenvalues and eigenfunctions (Kohn-Sham orbitals) of the system, and also the energy of the system  $E_0$ , which can be calculated through eq. (2.25). A new density  $n_1(\mathbf{r})$  is then built using these calculated Kohn-Sham or-

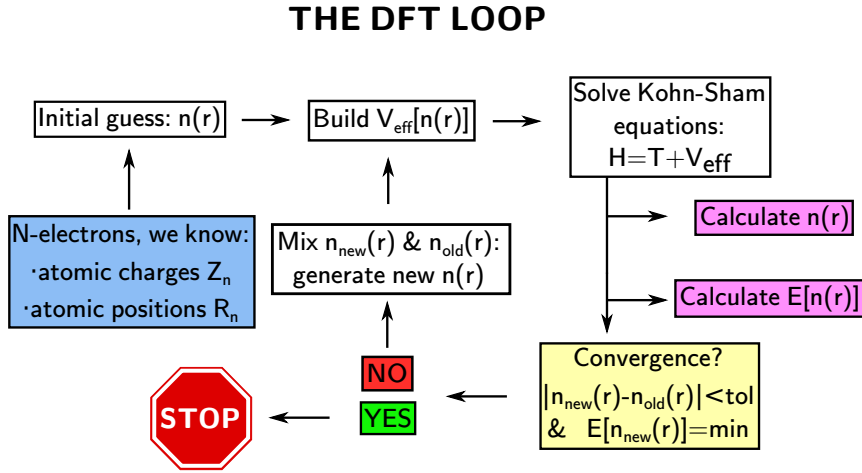


**Figure 2.1:** Scheme of the DFT loop to calculate self-consistently the ground-state density of an N-electron system.

bitals and this is used to compute a new  $V_{eff}$  and repeat the whole process iteratively. The final ground-state electron density is obtained once the convergence criteria for the density of the system are satisfied and the energy finds its absolute minimum value.

### Spin-polarized systems

In the previous treatment, we only mentioned one unique electron density, making no distinction between spin *up* and spin *down* electrons. However, almost in every system, it results much more interesting computing the energy taking into account that a net magnetization may exist, either spontaneous or due to an external magnetic field. In any case we can solve the problem dealing with two different electronic densities, one for the spin *up* electrons  $n_{\uparrow}(\mathbf{r})$  and another one for the spin *down* electrons  $n_{\downarrow}(\mathbf{r})$ . A similar minimization treatment for a Hohenberg-Kohn functional (which in this case depends on both electron densities  $n_{\uparrow}(\mathbf{r})$  and  $n_{\downarrow}(\mathbf{r})$ ), leads to the generalized Kohn-Sham equations for the spin-polarized case. Details about their derivation can be found in Ref. [64], but the important fact is that we similarly obtain an expression for the total energy functional which only depends on the two electron densities of spin *up* and *down*.

## 2.2 The Hubbard model and extensions

One of the most celebrated and successful models to treat dynamical electronic correlations explicitly is the Hubbard model<sup>4</sup>. Although it has been applied to different problems over the years, it has been mainly used in the description of different electronic phases in correlated materials.

Let's start writing the Hamiltonian in the following fashion:

$$\hat{\mathcal{H}}_e = \hat{\mathcal{H}}_0 + \hat{\mathcal{H}}_{int}. \quad (2.26)$$

We have separated it in two terms: the so-called “non-interacting” term or “bare Hamiltonian”  $\hat{\mathcal{H}}_0$  and the “interacting” term  $\hat{\mathcal{H}}_{int}$ . Now we can explicitly write these two components of the Hamiltonian in the most general form possible. The non-interacting part will read:

$$\hat{\mathcal{H}}_0 = \sum_{\sigma} \int d\mathbf{r} \Psi_{\sigma}^{\dagger}(\mathbf{r}) \left[ -\frac{\hbar^2 \nabla^2}{2m_e} + V(\mathbf{r}) \right] \Psi_{\sigma}(\mathbf{r}). \quad (2.27)$$

$V(\mathbf{r})$  in this context is the electrostatic potential created by the ions. However, if one is working within the DFT framework, this potential is the Kohn-Sham effective potential  $V_{eff}(\mathbf{r})$ . The interacting part will be:

$$\hat{\mathcal{H}}_{int} = \sum_{\sigma, \sigma'} \int d\mathbf{r} d\mathbf{r}' \Psi_{\sigma}^{\dagger}(\mathbf{r}) \Psi_{\sigma'}^{\dagger}(\mathbf{r}') \left[ \frac{1}{2} \frac{e^2}{|\mathbf{r} - \mathbf{r}'|} \right] \Psi_{\sigma'}(\mathbf{r}') \Psi_{\sigma}(\mathbf{r}), \quad (2.28)$$

where we have introduced the field operator  $\Psi_{\sigma}^{\dagger}(\mathbf{r})$  which creates an electron with spin  $\sigma$  in the point  $\mathbf{r}$ . We are now working in the formalism of second quantization.

The non-interacting part of the Hamiltonian  $\hat{\mathcal{H}}_0$  in eq. (2.27) can be diagonalized using Bloch wave functions  $\phi_{\mathbf{k},n}(\mathbf{r})$  (in the case of DFT we will obtain the Kohn-Sham orbitals), which are extended along all the solid. However, in this formulation and in what will follow in this chapter it is much more convenient to express everything in a local basis. Among the plethora of local basis that one can choose, one that arises quite naturally in this context is the basis of Wannier functions [76] (also-known as Wannier orbitals due to their resemblance with atomic orbitals). A Wannier orbital is generally defined as the Fourier transform of a Bloch wave function like

$$w_n(\mathbf{r} - \mathbf{R}) = \frac{1}{\sqrt{N}} \sum_{\mathbf{k} \in BZ} e^{-i\mathbf{k} \cdot \mathbf{R}} \phi_{\mathbf{k},n}(\mathbf{r}). \quad (2.29)$$

This Wannier orbital in a multi-orbital case can also be optimized in order to be maximally-localized [77]. It can be associated with the position of the ion centered

---

<sup>4</sup>It was introduced simultaneously by M. C. Gutzwiller [73], J. Kanamori [74] and J. Hubbard [75] in 1963 in the quest of an explanation for itinerant magnetism in transition metals.

at  $\mathbf{R}$ , and thus the field operator that was introduced before can now be expressed like

$$\Psi_\sigma^\dagger(\mathbf{r}) = \sum_i w_n^*(\mathbf{r} - \mathbf{R}_i) d_{in\sigma}^\dagger, \quad (2.30)$$

where  $d_{in\sigma}^\dagger$  creates an electron with spin  $\sigma$  in the  $n$ -th Wannier orbital centered around the lattice site  $i$ . Using this basis, the full Hamiltonian (2.26) can be rewritten like:

$$\hat{\mathcal{H}}_e = \sum_{ijmm'\sigma} t_{ij}^{mm'} d_{im\sigma}^\dagger d_{jm'\sigma} + \frac{1}{2} \sum_{ijkl} \sum_{mm'nn'} \sum_{\sigma\sigma'} V_{ijkl}^{mm'nn'} d_{im\sigma}^\dagger d_{jm'\sigma'}^\dagger d_{kn'\sigma'} d_{ln\sigma}, \quad (2.31)$$

where we have defined the hopping integrals  $t_{ij}^{mm'}$  like

$$t_{ij}^{mm'} = \int d\mathbf{r} w_m^*(\mathbf{r} - \mathbf{R}_i) \left[ -\frac{\hbar^2 \nabla^2}{2m_e} + V(\mathbf{r}) \right] w_{m'}(\mathbf{r} - \mathbf{R}_j), \quad (2.32)$$

which completely characterize the band structure obtained, for instance, by means of a DFT calculation, but in a local basis of Wannier orbitals. In other words, given a band structure written in a basis of delocalized Bloch wave functions (or Kohn-Sham orbitals), one can always rewrite it in a local basis of Wannier orbitals as a set of hopping integrals  $t_{ij}^{mm'}$  [77, 78]. The electron-electron interaction parameters will now read like

$$V_{ijkl}^{mm'nn'} = \int d\mathbf{r} d\mathbf{r}' w_m^*(\mathbf{r} - \mathbf{R}_i) w_{m'}^*(\mathbf{r} - \mathbf{R}_j) \frac{e^2}{|\mathbf{r} - \mathbf{r}'|} w_n(\mathbf{r} - \mathbf{R}_k) w_{n'}(\mathbf{r} - \mathbf{R}_l). \quad (2.33)$$

The main difference between the Hamiltonian of the Hubbard model in eq. (2.31) and the one used in DFT in eq. (2.9) is that part of the electron-electron interactions that are taken into account in the effective potential in eq. (2.9) and introduced in eq. (2.1), are now included in these hopping integrals  $t_{ij}^{mm'}$  in eq. (2.31). This effective potential introduced in Section 2.1 includes several terms, among them the so-called exchange-correlation potential, that includes some of the effects of correlations at an approximate level but that has not the power to do it in a dynamical manner. This description is improved in the Hubbard model by adding the second term to eq. (2.31), which takes into account the dynamical character of these electronic correlations. This new term however, may lead to a double-counting problem if  $\hat{\mathcal{H}}_0$  is calculated with DFT, since part of the contribution of correlations that is already included in the effective potential<sup>5</sup>.

So far, we have just rewritten the Hamiltonian in terms of a local basis and in the formalism of second quantization, but the problem ahead remains intractable because of the large amount of degrees of freedom present. One has to do some ap-

---

<sup>5</sup>Double-counting corrections have to be treated carefully. However, we will see that depending on the system, they can be controlled.

proximations, like for instance, integrate out the degrees of freedom of the electrons that are not close to the Fermi level and treat only explicitly the valence electrons. To do this one has to analyze first the energy scales of the system under study. The properties that we describe here in this text involve only electronic states which are very close to the Fermi level, and we do not expect contributions, for instance, from the core electrons. Our attempt is only to describe the electronic structure accurately in an energy window of a few eV around the Fermi level. However, the effect of these core electrons is not neglected, but is included in the form of a screened Coulomb interaction. This screened interaction describes the influence of all the electrons in the system but does not include the effect of the electrons from the orbitals close to the Fermi level, whose effect will be treated explicitly. The screening effects can be typically included into an effective Yukawa potential of the form

$$W(|\mathbf{r} - \mathbf{r}'|) = \frac{e^2}{|\mathbf{r} - \mathbf{r}'|} e^{-\lambda|\mathbf{r} - \mathbf{r}'|} \quad (2.34)$$

that includes an exponential decay of the interaction as one moves away from the ionic position. This allows to perform one of the most important simplifications for the interaction parameters since the integrals that involve only Wannier orbitals that are all in the same lattice site are going to be much larger than those involving Wannier orbitals from different sites, which can be neglected. We can thus only consider the on-site interactions<sup>6</sup> by imposing

$$V_{ijkl}^{mm'nn'} = U^{mm'nn'} \delta_{ij} \delta_{ik} \delta_{il} \quad (2.35)$$

If we now only consider the problem of one active orbital with only on-site interactions and we introduce the number operator like  $n_{i\sigma} \equiv d_{i\sigma}^\dagger d_{i\sigma}$  we obtain the one-band Hubbard model, whose Hamiltonian has the form:

$$\hat{\mathcal{H}}_e = \sum_{ij\sigma} t_{ij} d_{i\sigma}^\dagger d_{j\sigma} + U \sum_i n_{i\uparrow} n_{i\downarrow} \quad (2.36)$$

This is a useful model for materials in which the relevant physics happens only in one orbital. In the case of having several active orbitals, we can extend it to a multi-orbital case. Plugging expression (2.35) into eq. (2.31) we end up having a Hamiltonian of the form

$$\hat{\mathcal{H}}_e = \sum_{ijmm'\sigma} t_{ij}^{mm'} d_{im\sigma}^\dagger d_{jm'\sigma} + \frac{1}{2} \sum_i \sum_{mm'nn'} \sum_{\sigma\sigma'} U^{mm'nn'} d_{im\sigma}^\dagger d_{im'\sigma'}^\dagger d_{in'\sigma'} d_{in\sigma} \quad (2.37)$$

This is the more general form of a multi-orbital Hubbard Hamiltonian with only local interactions. It can be adapted depending on the symmetries of the problem

---

<sup>6</sup>The non-local terms which are neglected from now on can have important consequences in some contexts. In the literature they receive the name of long-range Coulomb interactions.

we are dealing with. For instance, in the case of  $d$  orbitals (which will be the case of study for real materials in this work), the following integrals can be defined [79]:

$$\begin{aligned}
 V_{iii}^{mmmm} &\equiv U = \int d\mathbf{r}d\mathbf{r}' |w_m(\mathbf{r})|^2 W(\mathbf{r}, \mathbf{r}') |w_m(\mathbf{r}')|^2 \\
 V_{iii}^{mm'm'm} &\equiv U' = \int d\mathbf{r}d\mathbf{r}' |w_m(\mathbf{r})|^2 W(\mathbf{r}, \mathbf{r}') |w_{m'}(\mathbf{r}')|^2 \\
 V_{iii}^{mm'mm'} &\equiv J = \int d\mathbf{r}d\mathbf{r}' w_m^*(\mathbf{r}) w_{m'}^*(\mathbf{r}') W(\mathbf{r}, \mathbf{r}') w_m(\mathbf{r}') w_{m'}(\mathbf{r}).
 \end{aligned} \tag{2.38}$$

In the case of cubic symmetry, for  $t_{2g}$  and  $e_g$  orbitals separately<sup>7</sup>, we can also write:

$$U' = U - 2J. \tag{2.39}$$

That way, the multi-orbital Hamiltonian has the form:

$$\begin{aligned}
 \hat{\mathcal{H}}_e &= \sum_{ijmm'\sigma} t_{ij}^{mm'} d_{im\sigma}^\dagger d_{jm'\sigma} \\
 &+ U \sum_{i,m} n_{im\uparrow} n_{im\downarrow} + U' \sum_{i,m \neq m'} n_{im\uparrow} n_{im'\downarrow} + (U' - J) \sum_{i,m < m'} n_{im\sigma} n_{im'\sigma} \\
 &- J \sum_{i,m \neq m'} d_{im\uparrow}^\dagger d_{im\downarrow} d_{im'\downarrow}^\dagger d_{im'\uparrow} + J \sum_{i,m \neq m'} d_{im\uparrow}^\dagger d_{im\downarrow}^\dagger d_{i,m'\downarrow} d_{i,m'\uparrow}.
 \end{aligned} \tag{2.40}$$

The term in the first row describes the usual hopping of electrons between different sites and different orbitals. The last two lines include the on-site interacting part of the Hamiltonian which contains the following terms: in the second line, respectively, the on-site intra-orbital Coulomb repulsion, on-site anti-parallel-spin inter-orbital Coulomb repulsion, on-site parallel-spin inter-orbital Coulomb repulsion; and on the third line the so-called spin-flip and pair hopping terms, that arise due to the (spin and orbital) rotational invariance of the problem.

In order to solve this multi-orbital Hamiltonian we can use different techniques. Among the variety of them, we will focus in slave-spins mean-field theory and dynamical mean-field theory, that we introduce in the following sections.

## 2.3 Slave-Spin Mean-Field Theory

There are several approaches that have been very successful in describing a broad variety of strongly-correlated materials, among them we can highlight a collection of methods that are based in the introduction of slave variables. These have been successfully used in different problems, and among them we can point out Slave Bosons [80], Slave Spins [81, 82] or Slave Rotors [83, 84]. The idea in all of them is to

---

<sup>7</sup>Along the text, we will assume that this is also valid for the 5-orbital case we will be dealing with.

add extra degrees of freedom through these slave variables that are then decoupled with a mean-field approximation. One can then treat the problem with a non-interacting effective Hamiltonian in which the effect of the electronic correlations is contained in the renormalization parameters that are obtained in the mean-field treatment of these slave particles.

The technique that we describe in this section is Slave-Spin Mean-Field Theory (SSMFT). It will be presented following the conventions used in Ref. [66] as it was introduced in Refs. [81, 82]. Many other interesting references of this method can be also found in the literature [85, 86, 87, 88, 89].

In order to present this technique, we are going to stick to the one-band Hubbard model from eq. (2.36), which will help to introduce it in a pedagogical manner. The main idea is to introduce a new composite variable for each electronic degree of freedom: a spin-like variable (a slave spin) together with a pseudo-fermionic variable (which mirrors the original electronic variable). This spin variable is not a physical spin, but a variable that has the same algebra that a spin-1/2 and that can be seen as a switch that is ON or OFF depending on whether or not there is a fermion with a given flavor (in the 1-band case this includes spin and site indices, whereas in the multi-orbital case it refers to spin, orbital and site indices) present in the state<sup>8</sup>. With this information we can build a new enlarged Hilbert space that includes the new physical states

$$\begin{aligned} |n_{i\sigma}^d = 1\rangle &\longrightarrow |n_{i\sigma}^f = 1; S_{i\sigma}^z = +1/2\rangle \\ |n_{i\sigma}^d = 0\rangle &\longrightarrow |n_{i\sigma}^f = 0; S_{i\sigma}^z = -1/2\rangle, \end{aligned} \quad (2.41)$$

but also the unphysical ones

$$\begin{aligned} |n_{i\sigma}^d = 1\rangle &\longrightarrow |n_{i\sigma}^f = 1; S_{i\sigma}^z = -1/2\rangle \\ |n_{i\sigma}^d = 0\rangle &\longrightarrow |n_{i\sigma}^f = 0; S_{i\sigma}^z = +1/2\rangle. \end{aligned} \quad (2.42)$$

In order to consider only the physical states a constraint must be introduced. In this case, one can require that the states must fulfill

$$f_{i\sigma}^\dagger f_{i\sigma} = S_{i\sigma}^z + \frac{1}{2}, \quad (2.43)$$

and in that way the unphysical states are eliminated. This expression is also very useful to rewrite our Hamiltonian in terms of these new variables. For instance, in the one-band Hubbard model from eq. (2.36), the interaction part can be written in

---

<sup>8</sup>Notice that there is a slave-spin for each fermion flavor  $\sigma$ . For instance, if there is a state with a spin-down electron, then the corresponding slave-spin variable to this spin-down electron will be  $+1/2$ , since this spin-species is present in the state.

a particle-hole symmetric way (see derivation in Appendix B.1) like

$$\hat{\mathcal{H}}_{int}[d^\dagger, d] = \frac{U}{2} \sum_i \left( \sum_\sigma (n_{i\sigma}^d - \frac{1}{2}) \right)^2. \quad (2.44)$$

Using eq. (2.43) we can write this interacting term in the particle-hole symmetric form in terms of these slave variables. We end up having that

$$\hat{\mathcal{H}}_{int}[S^z] = \frac{U}{2} \sum_i \left( \sum_\sigma S_{i\sigma}^z \right)^2. \quad (2.45)$$

Now, these new variables have to be taken into account through some new operators that have to be mapped into the old ones. The most natural choice for these new spin variables is of course the usual spin operators. One obvious choice could be for instance [90]

$$d_{i\sigma}^\dagger \longrightarrow f_{i\sigma}^\dagger S_{i\sigma}^+. \quad (2.46)$$

However, the choice of these new operators is not univocally defined. One can easily realize about that by looking that the action of  $f_{i\sigma}^\dagger S_{i\sigma}^+$  and  $f_{i\sigma}^\dagger 2S_{i\sigma}^x$  is the same in the physical Hilbert space. The most general expression we can write for these new operators is:

$$d_{i\sigma}^\dagger \longrightarrow f_{i\sigma}^\dagger O_{i\sigma}^\dagger \quad d_{i\sigma} \longrightarrow f_{i\sigma} O_{i\sigma}, \quad (2.47)$$

where  $O_{i\sigma}$  is a  $2 \times 2$  complex matrix which can be expressed like:

$$O_{i\sigma} = \begin{pmatrix} 0 & c_{i\sigma} \\ 1 & 0 \end{pmatrix} = S_{i\sigma}^- + c_{i\sigma} S_{i\sigma}^+. \quad (2.48)$$

In this matrix  $c_{i\sigma}$  is an arbitrary complex number that acts as a gauge freedom in the slave-variable approach. Basically, it can be tuned to reproduce some known limit<sup>9</sup> and then used everywhere else, like for instance the non-interacting limit, in which  $U = 0$ . Finally, we can rewrite eq. (2.36) with the new variables introduced in eq. (2.47) and the interaction term in the particle-hole symmetric form written above in eq. (2.45). We end up having a Hamiltonian in the enlarged Hilbert space of the form

$$\hat{\mathcal{H}} - \mu \hat{N} = \sum_{ij\sigma} t_{ij} O_{i\sigma}^\dagger O_{j\sigma} f_{i\sigma}^\dagger f_{j\sigma} + \frac{U}{2} \sum_i \left( \sum_\sigma S_{i\sigma}^z \right)^2 - \mu \sum_{i\sigma} n_{i\sigma}^f, \quad (2.49)$$

which is equivalent to eq. 2.36 in the subspace fulfilling the constraint in eq. (2.43).

---

<sup>9</sup>The detailed calculation of  $c_{i\sigma}$  can be found in Ref. [66].

### 2.3.1 Mean-field decoupling and approximations

So far we have just rewritten the original Hamiltonian into an enlarged Hilbert space submitted to a constraint. At this point we start performing some approximations that will make the problem much more easy to deal with. They are:

1. Do a mean-field decoupling of the auxiliary slave-spin variables from the fermionic degrees of freedom.
2. Treat the constraint on average. This will introduce Lagrange multipliers into our formulation.
3. Do a further mean-field approximation in the slave-spin variables.

#### Mean-field decoupling of the original Hamiltonian

The first approximation consists in doing a mean-field decoupling to the hopping part of the Hamiltonian in eq. (2.49) like

$$\sum_{ij\sigma} t_{ij} O_{i\sigma}^\dagger O_{j\sigma} f_{i\sigma}^\dagger f_{j\sigma} \approx \sum_{ij\sigma} t_{ij} \langle O_{i\sigma}^\dagger O_{j\sigma} \rangle f_{i\sigma}^\dagger f_{j\sigma} + \sum_{ij\sigma} t_{ij} O_{i\sigma}^\dagger O_{j\sigma} \langle f_{i\sigma}^\dagger f_{j\sigma} \rangle. \quad (2.50)$$

We can also define

$$\begin{aligned} Q_{ij} &= \langle O_{i\sigma}^\dagger O_{j\sigma} \rangle_s \\ J_{ij} &= t_{ij} \langle f_{i\sigma}^\dagger f_{j\sigma} \rangle_f. \end{aligned} \quad (2.51)$$

After this mean-field decoupling we now have 2 different decoupled Hamiltonians, one for the fermionic degrees of freedom and another for the slave-spin variables:  $\hat{\mathcal{H}} = \hat{\mathcal{H}}_f[f, f^\dagger] + \hat{\mathcal{H}}_s[O, O^\dagger]$  (remember that the interaction term had already been written in terms of the spin variables). These are:

$$\begin{aligned} \hat{\mathcal{H}}_f &= \sum_{ij\sigma} t_{ij} Q_{ij} f_{i\sigma}^\dagger f_{j\sigma} - (\mu + \lambda) \sum_{i\sigma} n_{i\sigma}^f \\ \hat{\mathcal{H}}_s &= \sum_{ij\sigma} J_{ij} O_{i\sigma}^\dagger O_{j\sigma} + \lambda \sum_{i\sigma} (S_{i\sigma}^z + \frac{1}{2}) + \frac{U}{2} \sum_i \left( \sum_\sigma S_{i\sigma}^z \right)^2, \end{aligned} \quad (2.52)$$

In this fashion, the parameters that enter in the fermionic Hamiltonian are average values of the slave-spin variables calculated in the other Hamiltonian and vice-versa.

#### Treating the constraint on average

We have to introduce now the partition function in order to calculate these average values of the operators in each of the Hamiltonians. In the enlarged Fock space that

includes both fermionic and slave-spin variables, this reads:

$$\mathcal{Z} = \text{Tr} \left[ e^{-\beta(\hat{\mathcal{H}} - \mu\hat{N})} \times \delta(S_{i\sigma}^z + \frac{1}{2} - n_{i\sigma}^f) \right]. \quad (2.53)$$

The Dirac delta function projects out the unphysical states discussed in eq. (2.42). However the partition function cannot be separable into fermionic and slave-spin variables. This can be achieved if we relax this constraint substituting the delta function for an exponential in the following way:

$$\delta(S_{i\sigma}^z + \frac{1}{2} - n_{i\sigma}^f) \approx e^{-\beta\lambda(S_{i\sigma}^z + \frac{1}{2} - n_{i\sigma}^f)}, \quad (2.54)$$

where we have introduced a Lagrange multiplier  $\lambda$  which is spin-independent, since we are only studying non-magnetic phases with this approach<sup>10</sup>. Defining the grand-canonical potential like  $\Omega = -\frac{1}{\beta} \log \mathcal{Z}$ , we adjust  $\lambda$  so it fulfills the condition  $\frac{\partial \Omega}{\partial \lambda} = 0$ . This implies that the constraint will be satisfied not exactly but on average. This can be seen expanding

$$\begin{aligned} \frac{\partial \Omega}{\partial \lambda} &= -\frac{1}{\beta} \frac{\partial(\log \mathcal{Z})}{\partial \lambda} = -\frac{1}{\beta \mathcal{Z}} \frac{\partial \mathcal{Z}}{\partial \lambda} = -\frac{1}{\beta \mathcal{Z}} \frac{\partial}{\partial \lambda} \left\{ \text{Tr} \left[ e^{-\beta(\hat{\mathcal{H}} - \mu\hat{N} + \lambda(S_{i\sigma}^z + \frac{1}{2} - n_{i\sigma}^f))} \right] \right\} \\ &= \frac{1}{\mathcal{Z}} \text{Tr} \left\{ e^{-\beta[\hat{\mathcal{H}} - \mu\hat{N} + \lambda(S_{i\sigma}^z + \frac{1}{2} - n_{i\sigma}^f)]} (S_{i\sigma}^z + \frac{1}{2} - n_{i\sigma}^f) \right\} = \langle S_{i\sigma}^z \rangle + \frac{1}{2} - \langle n_{i\sigma}^f \rangle, \end{aligned} \quad (2.55)$$

and as we said, the constraint is fulfilled on average.

### Mean-field approximation in the slave variables

One last step that needs to be performed in the case of the spin Hamiltonian  $\hat{\mathcal{H}}_s$  is a Weiss mean-field approximation. Mathematically, the following approximation is performed:

$$O_{i\sigma}^\dagger O_{j\sigma} \approx \langle O_{i\sigma}^\dagger \rangle O_{j\sigma} + O_{i\sigma}^\dagger \langle O_{j\sigma} \rangle. \quad (2.56)$$

Since  $\langle O_{j\sigma} \rangle = \langle O_{i\sigma} \rangle$  by translational invariance, this leads us to the following spin Hamiltonian :

$$\hat{\mathcal{H}}_s = \sum_i \hat{\mathcal{H}}_s^i = \sum_{i\sigma} (h_{i\sigma} O_{i\sigma}^\dagger + h_{i\sigma}^* O_{i\sigma}) + \lambda \sum_{i\sigma} (S_{i\sigma}^z + \frac{1}{2}) + \frac{U}{2} \sum_i \left( \sum_{\sigma} S_{i\sigma}^z \right)^2, \quad (2.57)$$

which is now a single-site Hamiltonian since we only have a summation in one lattice index. Using the second definition in eqs. (2.51) we have that

$$h_{i\sigma} = h_{\sigma} = \sum_j J_{ij} \langle O_{j\sigma} \rangle_s = \langle O_{j\sigma} \rangle_s \sum_j t_{ij} \left\langle f_{i\sigma}^\dagger f_{j\sigma} \right\rangle_f. \quad (2.58)$$

---

<sup>10</sup>Recently [88] a spin-dependent formulation has been proposed.

The last summation is nothing more than the average kinetic energy per spin of the pseudo-fermions.

### 2.3.2 Set of self-consistent equations

We have the 2 decoupled Hamiltonians for the slave-spins and the fermionic variables:

$$\begin{aligned}\hat{\mathcal{H}}_f &= \sum_{ij\sigma} t_{ij} Q_{ij} f_{i\sigma}^\dagger f_{j\sigma} - (\mu + \lambda) \sum_{i\sigma} n_{i\sigma}^f \\ \hat{\mathcal{H}}_s &= \sum_i \hat{\mathcal{H}}_s^i = \sum_{i\sigma} (h_{i\sigma} O_{i\sigma}^\dagger + h_{i\sigma}^* O_{i\sigma}) + \lambda \sum_{i\sigma} (S_{i\sigma}^z + \frac{1}{2}) + \frac{U}{2} \sum_i \left( \sum_{\sigma} S_{i\sigma}^z \right)^2,\end{aligned}\tag{2.59}$$

where we have defined the following parameters:

$$\begin{aligned}Q_{ij} &= \langle O_{i\sigma}^\dagger O_{j\sigma} \rangle_s = \left| \langle O_{i\sigma}^\dagger \rangle_s \right|^2 = Z_\sigma^2 \\ J_{ij} &= t_{ij} \langle f_{i\sigma}^\dagger f_{j\sigma} \rangle_f \\ h_{i\sigma} &= h_\sigma = \sum_j J_{ij} \langle O_{j\sigma} \rangle_s = \langle O_{j\sigma} \rangle_s \sum_j t_{ij} \langle f_{i\sigma}^\dagger f_{j\sigma} \rangle_f,\end{aligned}\tag{2.60}$$

and we have to consider also the constraint

$$\langle n_{i\sigma}^f \rangle_f = \frac{1}{2} + \langle S_{i\sigma}^z \rangle_s.\tag{2.61}$$

We have defined the inverse mass enhancement  $Z_\sigma$  (which in this formalism - as in any dynamical mean-field yielding a local self-energy- coincides with the quasiparticle weight [66]) in the first expression in (2.60) which is site-independent. Here it becomes clear how the parameters accompanying each of the Hamiltonians are averages calculated in the other Hamiltonian. These can be calculated self-consistently, in a similar fashion as in DFT.

### 2.3.3 Generalization to several orbitals

In the case having several orbitals in the problem, we have to generalize the formalism. The first difference is that all the variables now have also an orbital index  $m$  and each of the of the spin-orbitals species will have to fulfill its individual constraint

$$\langle n_{im\sigma}^f \rangle_f = \frac{1}{2} + \langle S_{im\sigma}^z \rangle_s.\tag{2.62}$$

The interaction part of the multi-orbital Hamiltonian from eq. (2.40) without the spin-flip and pair hopping terms (keeping only the density-density terms) can now be written in terms of the spin variables like:

$$\hat{\mathcal{H}}_{int}[S] = U \sum_m S_{m\uparrow}^z S_{m\downarrow}^z + U' \sum_{m \neq m'} S_{m\uparrow}^z S_{m'\downarrow}^z + (U' - J) \sum_{m < m', \sigma} S_{m\sigma}^z S_{m'\sigma}^z. \quad (2.63)$$

Following a similar strategy to decouple the fermionic variables from the slave-spins we end up having these 2 Hamiltonians:

$$\hat{\mathcal{H}}_f = \sum_{i \neq j, mm'\sigma} t_{ij}^{mm'} \sqrt{Z_m Z_{m'}} f_{im\sigma}^\dagger f_{jm'\sigma} + \sum_{im\sigma} (\epsilon_m - \mu + \lambda_m) n_{im\sigma}^f, \quad (2.64)$$

and

$$\hat{\mathcal{H}}_s = + \sum_{m\sigma} \left[ (h_{m\sigma} O_{m\sigma}^\dagger + h_{m\sigma}^* O_{m\sigma}) + \lambda_m (S_{m\sigma}^z + \frac{1}{2}) \right] + \hat{\mathcal{H}}_{int}[S]. \quad (2.65)$$

Where we define,

$$h_{m\sigma} = \sum_{m'} \langle O_{m'\sigma} \rangle_s \sum_j t_{ij}^{mm'} \langle f_{im\sigma}^\dagger f_{jm'\sigma} \rangle_f \quad (2.66)$$

and also the now orbitally-resolved quasiparticle weight:

$$Z_m = |\langle O_{m\sigma} \rangle_s|^2. \quad (2.67)$$

## 2.4 Dynamical Mean-Field Theory

Dynamical Mean-Field Theory (DMFT) is one of the most successful methods used nowadays to compute the spectrum of electronic excitations in strongly-correlated electron systems. The key idea here is to replace a lattice model which possesses a large number of degrees of freedom and thus it turns out to be impossible to solve, by an impurity embedded into a bath that is calculated self-consistently and represents the rest of the solid. The advantage of such an approach is that, first of all, an impurity model allows us to understand the local physics of the quantum many-body system that we try to model with the lattice model; but also that there are many techniques available to solve this impurity problem in a quite accurate manner, unlike the case of the lattice models, where typically much more drastic approximations are required and thus precision diminishes also enormously. The spirit of this approximation can be well illustrated with the familiar Weiss mean-field applied to the case of the magnetization in a system of spins described with an

Ising model. The Hamiltonian of such a system can be written like

$$\hat{\mathcal{H}} = - \sum_{\langle ij \rangle} J_{ij} S_i S_j + h \sum_i S_i. \quad (2.68)$$

Each spin  $S_i$  couples to its nearest neighbors  $S_j$  and also to an external magnetic field  $h$ . One quantity that may characterize the system is the local magnetization per site, which is  $m_i = \langle S_i \rangle$ . The trick here is to propose an effective model for a single site of a single spin coupled to an effective local magnetic field  $h_i^{eff}$ , which we can express like

$$\hat{\mathcal{H}}_{eff} = - \sum_i h_i^{eff} S_i. \quad (2.69)$$

This effective local magnetic field is the sum of the external magnetic field that was applied in the original problem, plus the magnetic field created on the site  $i$  by all the other neighboring spins  $S_j$  that generate a magnetization  $m_j$ . It can be calculated like:

$$h_i^{eff} \approx h + \sum_{\langle ij \rangle} J_{ij} m_j = h + z J m, \quad (2.70)$$

where  $z$  which is the number of nearest neighbors of site  $i$  and we have assumed translational invariance of the problem  $J_{ij} = J$ . Now we can calculate the thermal average magnetization of the system (that we call  $m$ ) from a self consistent equation

$$m = \tanh[\beta(h + z J m)]. \quad (2.71)$$

The idea behind DMFT is very similar to this Weiss mean-field approximation. We solve an equivalent effective local problem that captures the relevant local physics of the original lattice model. In this effective model, the single site will be coupled to the environment or bath, which is characterized by some quantity that is connected to the original lattice model (in the case of the Ising model, the effective magnetic field  $h^{eff}$  that is calculated with information from the original model), in this case through the bare Green's function of the effective local model. Then, a self-consistent equation will help us to make the final connection between the two models. The main difference with the classical mean-field is that in not all fluctuations are frozen. Spatial fluctuations are, but not local quantum fluctuations, that are fully taken into account.

The key idea from which DMFT was born is that lattice model of fermions can always be mapped into an quantum impurity model with a self-consistent condition [91] (this is exact in the limit of infinite connectivity or coordination [92]). This means that DMFT applied to materials is actually an approximation. This mapping is telling us that in this limit of infinite coordination, the local Green's function of this lattice model coincides with the impurity full-interacting Green's function. Everything that is not this case is an approximation. For instance, since we are only

dealing with a local quantity, the DMFT approximation is telling us thus that the self-energy of the lattice problem will be fully local (as it happens in the impurity problem).

### 2.4.1 Mapping into an impurity model

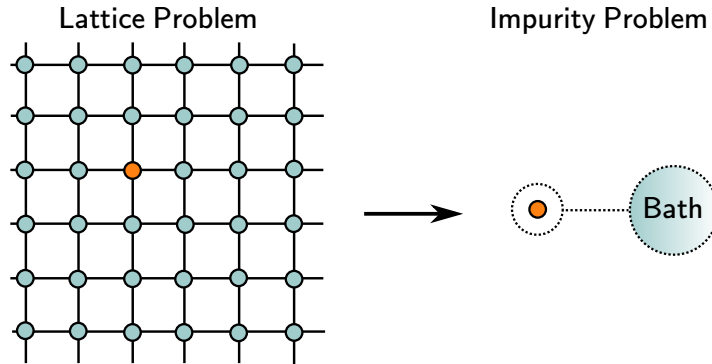


**Figure 2.2:** Scheme of the analogy between a lattice problem and a single atom embedded in an effective bath.

In DMFT an equivalence is established between the lattice problem, which is substituted by a single site embedded into a bath (Fig. 2.2) thus reducing enormously the number of degrees of freedom and making the problem solvable. Electrons can hop from the site to the bath back and forth. The interaction between this isolated site (impurity) and the bath is controlled by a hybridization function that allows the single site (impurity) to fluctuate among different states thus giving the dynamical character to the problem. Such a system can be described by the Hamiltonian of an Anderson impurity model

$$\begin{aligned} \hat{\mathcal{H}}_{AIM} &= \hat{\mathcal{H}}_{impurity} + \hat{\mathcal{H}}_{coupling} + \hat{\mathcal{H}}_{bath} \\ &= U n_{\uparrow} n_{\downarrow} + (\epsilon_0 - \mu)(n_{\uparrow} + n_{\downarrow}) + \sum_{l,\sigma} V_l (a_{l\sigma}^{\dagger} d_{\sigma} + d_{\sigma}^{\dagger} a_{l\sigma}) + \sum_{l,\sigma} \tilde{\epsilon}_l a_{l\sigma}^{\dagger} a_{l\sigma}. \end{aligned} \quad (2.72)$$

This Hamiltonian can be separated in 3 parts: *i*) the first two terms that describe the local physics of the impurity (there are no non-local contributions), *ii*) another term that includes hybridization or coupling of this impurity with the effective bath, whose degrees of freedom are accounted with a set of non-interacting fermions which are described by the operators  $(a_l, a_l^{\dagger})$ ; and *iii*) a term including the physics of this effective bath.

## 2.4.2 The DMFT equations

The main aim of DMFT is to calculate the local Green's function of the original lattice problem. This will provide all the information about the local physics of the problem. This local Green's function (at site  $i$ ) in the imaginary time formalism (introduced in Appendix D) is defined like:

$$G_{ii}^\sigma(\tau - \tau') \equiv - \left\langle \mathcal{T} d_{i\sigma}(\tau) d_{i\sigma}^\dagger(\tau') \right\rangle, \quad (2.73)$$

or in its spectral representation (derived also in Appendix D):

$$G_{ii}^\sigma(i\omega_n) = \sum_{a,b} (p_a + p_b) \frac{\langle a | d_{i\sigma} | b \rangle \langle b | d_{i\sigma}^\dagger | a \rangle}{i\omega_n - \omega_{ab}}, \quad (2.74)$$

where we have that  $\omega_{ab} = E_a - E_b$  and we have introduced the thermal probabilities like

$$p_a = \frac{e^{-\beta E_a}}{\mathcal{Z}}. \quad (2.75)$$

Now, for the Hamiltonian of the Anderson impurity model, we can define the bare Green's function  $\mathcal{G}_0$  like

$$\mathcal{G}_0^{-1}(i\omega_n) = i\omega_n + \mu - \varepsilon_0 - \Delta(i\omega_n), \quad (2.76)$$

where we define the hybridization function  $\Delta(i\omega_n)$  as:

$$\Delta(i\omega_n) = \sum_l \frac{|V_l|^2}{i\omega_n - \tilde{\varepsilon}_l}. \quad (2.77)$$

It includes the interaction parameters  $\tilde{\varepsilon}_l$  and  $V_l$  of the effective impurity Hamiltonian in eq. (2.72).

$\mathcal{G}_0$ , which should not be confused with the non-interacting ( $U = 0$ ) local Green's function of the original lattice model  $G_0$ , is the quantum equivalent of the Weiss mean-field, since it contains contains the information about all the other lattice sites through these set of parameters of the impurity bath. These parameters have to be chosen self-consistently in such a way that the impurity Green's function of the impurity  $G_{imp}$  coincides with the local Green's function of the lattice model  $G_{ii}$  (the Hubbard model).

We now need to find the self-consistent condition that allows us to solve the problem. One can observe that in the effective impurity model, a self-energy can be defined from the interacting Green's function and the Weiss dynamical mean-field

in eq. (2.76) using Dyson's equation

$$\begin{aligned}\Sigma_{imp}(i\omega_n) &= \mathcal{G}_0^{-1}(i\omega_n) - G_{imp}^{-1}(i\omega_n) \\ &= i\omega_n + \mu - \epsilon_0 - \Delta(i\omega_n) - G_{imp}^{-1}(i\omega_n).\end{aligned}\tag{2.78}$$

This self-energy is fully local<sup>11</sup>, since the effective impurity problem does not have any momentum dependence. We can also consider the self-energy of the original lattice model, which can be defined through the full Green's function like

$$G(\mathbf{k}, i\omega_n) = \frac{1}{i\omega_n + \mu - \epsilon_0 - \epsilon_{\mathbf{k}} - \Sigma(\mathbf{k}, i\omega_n)}.\tag{2.79}$$

where  $\epsilon_{\mathbf{k}}$  is the dispersion relation of the non-interacting part of the lattice model (Hubbard Hamiltonian from eq. (2.36)). We note here that this self-energy is written in its more general form, and that it possesses  $\mathbf{k}$ -momentum dependence. The key approximation in DMFT [91] is to assume that the lattice self-energy coincides<sup>12</sup> with the impurity self-energy (which is purely local). In real space this implies neglecting all the non-local components of the self-energy, so one will have that:

$$\Sigma_{ii} \approx \Sigma_{imp} \ ; \ \Sigma_{i \neq j} \approx 0.\tag{2.80}$$

In order to achieve the self-consistent equation, we have to sum over  $\mathbf{k}$  in (2.79), which allows us to obtain the local component  $G_{ii}(i\omega_n)$  of the full lattice Green's function:

$$G_{ii}(i\omega_n) = \sum_{\mathbf{k}} \frac{1}{i\omega_n + \mu - \epsilon_0 - \epsilon_{\mathbf{k}} - \Sigma_{imp}(i\omega_n)}.\tag{2.81}$$

Now using the definition of the impurity self-energy in eq. (2.78) we obtain:

$$\begin{aligned}G_{ii}(i\omega_n) &= \sum_{\mathbf{k}} \frac{1}{i\omega_n + \mu - \epsilon_0 - \epsilon_{\mathbf{k}} - [i\omega_n + \mu - \epsilon_0 - \Delta(i\omega_n) - G_{imp}^{-1}(i\omega_n)]} \\ &= \sum_{\mathbf{k}} \frac{1}{\Delta(i\omega_n) + G_{imp}(i\omega_n)^{-1} - \epsilon_{\mathbf{k}}}.\end{aligned}\tag{2.82}$$

Now we use again the mapping of the lattice problem into an impurity problem, more specifically the fact that the local physics of the lattice problem are completely contained in the physics of the single-impurity problem (provided that one has assumed a purely local self-energy). That way, this is a consistent approximation since it provides a unique determination of the local Green's function of the lattice (also called on-site Green's function) which will now coincide by construction

---

<sup>11</sup>This is not a novel concept. Local self-energies had already been used before, in particular in the context of heavy fermions.

<sup>12</sup>This approximation turns to be exact in the limit of infinite connectivity, often referred as the limit of infinite dimensions.

with the Green's function of the impurity model. That way we can finally write the self-consistent condition

$$G(i\omega_n) = \sum_{\mathbf{k}} \frac{1}{\Delta(i\omega_n) + G(i\omega_n)^{-1} - \epsilon_{\mathbf{k}}}, \quad (2.83)$$

where we have eliminated the subscripts of the two Green's functions since now they are equivalent. If one takes into account the definition of a density of states  $D(\epsilon) \equiv \sum_{\mathbf{k}} \delta(\epsilon - \epsilon_{\mathbf{k}})$ , the previous expression can also be written in the continuum like

$$G(i\omega_n) = \int d\epsilon \frac{D(\epsilon)}{\Delta(i\omega_n) + G(i\omega_n)^{-1} - \epsilon} \quad (2.84)$$

This self-consistent condition relates the local Green's function  $G(i\omega_n)$  with the dynamical mean-field  $\mathcal{G}_0(i\omega_n)$  (or equivalently  $\Delta(i\omega_n)$ ). We have thus obtained a closed set of equations that fully determine the two functions  $\mathcal{G}_0, G$  (or  $\Delta, G$ ).

One can also switch from a Hamiltonian formulation to the use of an effective action functional integral formalism, which allows to integrate out these degrees of freedom and obtain an effective action for the impurity orbital of the form

$$\mathcal{S}_{eff} = - \int_0^\beta d\tau d\tau' \sum_{\sigma} d_{\sigma}^{\dagger}(\tau) \mathcal{G}_0^{-1}(\tau - \tau') d_{\sigma}(\tau') + U \int_0^\beta d\tau n_{\uparrow}(\tau) n_{\downarrow}(\tau), \quad (2.85)$$

This effective action represents the dynamics of the local impurity. It describes the fluctuations between the 4 atomic states ( $|0\rangle, |\uparrow\rangle, |\downarrow\rangle, |\uparrow\downarrow\rangle$ ) which is allowed by having coupled this single site to the effective bath. In this case, the full Green's function of the effective impurity problem can be calculated directly like

$$G_{imp}(\tau - \tau') = \int \mathcal{D}d d^{\dagger} e^{-\mathcal{S}_{eff}} = \int \mathcal{D}d d^{\dagger} e^{\int d^{\dagger} \mathcal{G}_0 d - U \int n_{\uparrow} n_{\downarrow}}. \quad (2.86)$$

### 2.4.3 The DMFT self-consistent cycle

We have seen that the DMFT method establishes a one-to-one correspondence between the local Green's function of a lattice model (typically a Hubbard model) and the full Green's function of an effective impurity problem (that is represented with an Anderson impurity model). In order to achieve that, an approximation has to be made, this is that the self-energy of the lattice  $\Sigma_{ii}(i\omega_n)$  coincides with the self-energy of the impurity model  $\Sigma_{imp}(i\omega_n)$ . We have also seen how to derive a self-consistency condition in order to calculate the Green's function iteratively. In this section we explain this iterative process that is also summarized in Fig. (2.3).

1. The first step<sup>13</sup> is to propose some initial guess for the Anderson impurity

---

<sup>13</sup>Steps 1 and 2 in which one constructs a Hamiltonian form of the impurity problem are specific of exact diagonalization impurity solver. Other non-Hamiltonian solvers (like CTQMC) just need

## THE DMFT LOOP

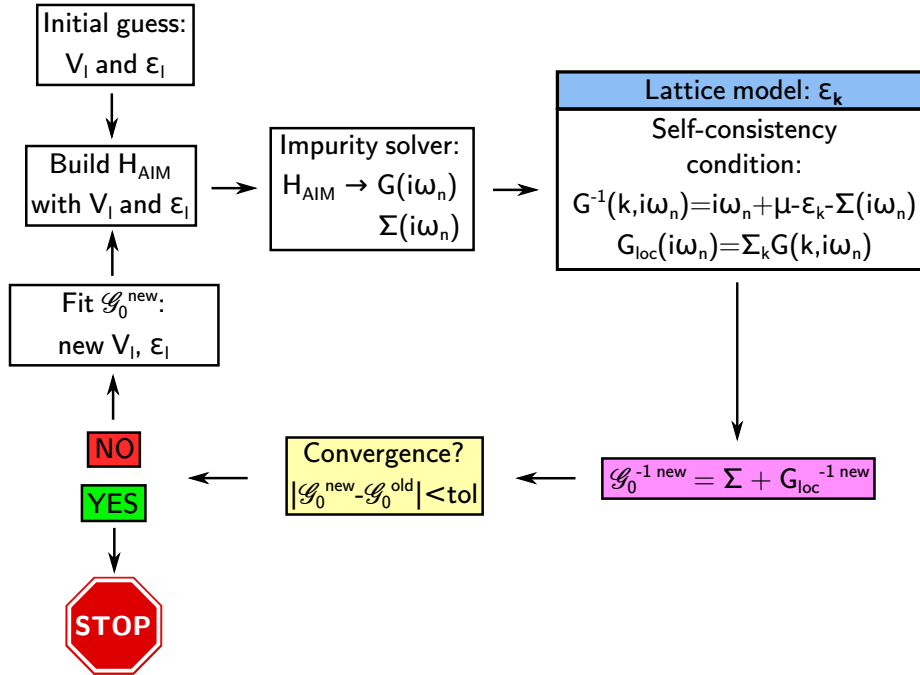


Figure 2.3: Scheme of the DMFT self-consistent cycle.

model, this is a set of values for  $V_l$  and  $\tilde{\epsilon}_l$ . The number of these parameters will determine the size of the Hilbert space we have to work with.

2. Once  $V_l$  and  $\tilde{\epsilon}_l$  have been set, one can build the Hamiltonian and also dynamical Weiss mean-field  $\mathcal{G}_0$  according to eq. (2.76).
3. The next step is obtaining the full Green's function of the effective impurity problem. For that one has to choose the impurity solver. There is a great variety of choice in that respect. One can find the early Montecarlo methods (used to study of the Hubbard model in infinite dimensions [93, 94, 95]), its improved version, Continuous-Time Quantum Montecarlo (CTQMC) (see Ref. [96]), iterative perturbation theory (IPT) [67, 91, 94] and its multi-orbital extension [97], numerical renormalization group [98, 99], density matrix renormalization group (DMRG) [100, 101] or the more usual exact diagonalization [102, 103, 104]. If one uses a method like Montecarlo sampling, then one has to solve the integral in eq. (2.85). Otherwise, one has to diagonalize the Hamiltonian in eq. (2.72) and then build the Green's function following the prescription in eq. (2.74).
4. Having obtained  $G_{imp}(i\omega_n)$ , one can also obtain the self-energy  $\Sigma(i\omega_n)$  of the

---

the Weiss mean-field  $\mathcal{G}_0$ .

effective impurity problem using Dyson's equation and the  $\mathcal{G}_0(i\omega_n)$  that has been built in step 2. Once all these quantities have been computed, one uses the self-consistency condition from eq. (2.83) or eq. (2.84) and calculates a new Green's function. It is only at this point when the information about the original lattice problem enters the cycle, typically through the dispersion relation  $\epsilon_{\mathbf{k}}$ .

5. From this new Green's function, using again the same self-energy  $\Sigma$  and Dyson's equation, we obtain a new dynamical Weiss field  $\mathcal{G}_0$  that can be fitted to eq. (2.76), thus obtaining a new set of  $V_l$  and  $\tilde{\epsilon}_l$  with which we can construct a new Hamiltonian for the effective impurity problem.
6. Convergence is achieved once the full Green's function  $G_{imp}$ , the dynamical Weiss field  $\mathcal{G}_0$  or the set of parameters  $V_l$  and  $\tilde{\epsilon}_l$  from two consecutive iterations do not differ more than a chosen tolerance factor.

## 2.5 Realistic simulations with Slave-Spin Mean-Field Theory

SSMFT can be a powerful tool to study the effect of correlations in materials. For that one can perform realistic simulations including correlations with the DFT+SSMFT scheme that we describe in this section. The first step is to identify which are the "active" electrons in the system that we want to study. In the case of IBSC, the common block in all of them are the layers of buckled planes made of Fe atoms with the ligands (pnictogens or chalcogens) located above and below alternatively. Mostly all IBSC are composed by a stacking of these planes that are separated by different spacers (or not, in the case of the 11 family). In most of these materials, there are 5 bands of mainly Fe-3d character crossing the Fermi level, with a total bandwidth  $\sim 4$  eV. We thus model the conduction electrons in IBSC with a 5-orbital Hubbard-Kanamori Hamiltonian

$$\hat{\mathcal{H}} - \mu\hat{N} = \hat{\mathcal{H}}_0 + \hat{\mathcal{H}}_{int} - \mu\hat{N}, \quad (2.87)$$

where  $\mu$  is the chemical potential and  $\hat{N}$  the total number of particles. The Hamiltonian includes two different terms. The first one is the non-interacting part that has already been introduced in eq. (2.40). It can be written like

$$\hat{\mathcal{H}}_0 = \sum_{i \neq j, m, m', \sigma} t_{ij}^{mm'} d_{im\sigma}^\dagger d_{jm'\sigma} + \sum_{i, m, \sigma} \epsilon_m \hat{n}_{im\sigma}, \quad (2.88)$$

where  $d_{im\sigma}^\dagger$  creates an electron with spin  $\sigma$  in orbital  $m = 1, \dots, 5$  on the site  $i$  of the lattice, and  $\hat{n}_{im\sigma} = d_{im\sigma}^\dagger d_{im\sigma}$  is the number operator. Notice that now we

have made explicit the difference between the hopping integrals  $t_{ij}^{mm'}$  and the on-site orbital energies  $\varepsilon_m = t_{ii}^{mm}$ . However, both are obtained by means of a tight-binding parametrization of the bare electronic band structure, which is calculated within a DFT framework. The DFT calculations have been mainly performed using the software package WIEN2K [105], although some checks have been also done using QUANTUM ESPRESSO [106]. This parametrization of the DFT band structure has to be written in a local basis (Wannier functions for instance [76]). In this project we have chosen always a set of maximally-localized Wannier functions [77] including only the conduction bands of mainly Fe-3d character, computed using the WANNIER90 code [78].

The second part of the model Hamiltonian includes the many-body interaction term, which in this context reads:

$$\hat{\mathcal{H}}_{int} = U \sum_m \hat{n}_{m\uparrow} \hat{n}_{m\downarrow} + U' \sum_{m \neq m'} \hat{n}_{m\uparrow} \hat{n}_{m'\downarrow} + (U' - J) \sum_{m < m', \sigma} \hat{n}_{m\sigma} \hat{n}_{m'\sigma} \quad (2.89)$$

where  $U$  is the local-on-site Coulomb repulsion,  $J$  the Hund's coupling and we choose  $U' = U - 2J$ . This expression corresponds to eq. (2.40) from Section 2.2, in which the last two terms (describing spin-flip and pair-hopping respectively) have been dropped since they need extra approximations to be treated exactly in SSMFT [66]. However, the full Hamiltonian has been studied by rotationally-invariant slave-bosons and DMFT and it has been seen that the main phenomena displayed by this multi-orbital Hubbard model in the case of SSMFT when these two terms are neglected (apart from some minor corrections). The realistic values for  $U$  and  $J$  can be obtained via ab-initio constrained random-phase approximation calculations (cRPA), like for instance in Ref. [107].



# 3

## Hund's metals

In this chapter we discuss the phenomenology of Hund's metals. We give a definition based on three main features displayed by these systems, which are strong correlations and mass enhancements, the presence of large fluctuating magnetic moments, and orbital selectivity of correlation strengths. This definition is corroborated by showing different experimental evidences in IBSC of each of these features, in particular in the 122 family of these materials. Then we give a more general insight about these phenomena by analyzing some theoretical results in models with featureless densities of states in which the physics is discussed more in detail. Finally, we present in detail a novel feature of this type of systems: the presence of a region of enhanced electronic compressibility culminating into a divergence in the doping-interaction phase diagram, and we discuss how this can have important consequences in different instabilities, in particular superconductivity.

---

Dans ce chapitre, nous discutons la phénoménologie des métaux de Hund. Nous donnons une définition basée sur trois caractéristiques principales manifestées par ces systèmes, qui sont des fortes corrélations et augmentations de masse, la présence de grands moments magnétiques fluctuants et la sélectivité orbitale des corrélations. Cette définition est corroborée en montrant différentes preuves expérimentales dans les supraconducteurs du fer de chacune de ces caractéristiques, en particulier dans la famille 122 de ces matériaux. Ensuite, nous donnons un aperçu plus général de ces phénomènes en analysant certains résultats théoriques en modèles avec densités d'états simplifiées dans lesquels la physique est discutée plus en détail. Enfin, nous présentons en détail une nouvelle caractéristique de ce type de système: la présence d'une région de compressibilité électronique augmentée culminant avec une divergence dans le diagramme de phases interaction-dopage, et nous discutons comment cela peut avoir des conséquences importantes sur différentes instabilités, en particulier la supraconductivité.

## 3.1 Introduction

The term ‘‘Hund’s metal’’ was coined for the first time in 2011 [108] in the context of the study of iron-based superconductors (IBSC). It refers to a phase in which the intra-atomic exchange interaction, known as Hund’s coupling, strongly influences the metallic properties of the material. This phase appears after a crossover in the doping-interaction phase diagram of realistic simulations of IBSC, and it responds to the behavior found in different experiments, among which, we could point out:

- Strong electronic correlations and mass enhancements.
- Large fluctuating local magnetic moments in the paramagnetic phase.
- Orbital-selective strength of the correlations.

These 3 main features, that differentiate this phase from a normal metallic phase, are enhanced with increasing interaction strength and with the proximity of the system to half-filling, where a Mott insulator favored by Hund’s coupling is realized [109, 79]. All these phenomena are not only specific of the physics of IBSC, they also appear in other compounds like ruthenates for instance [110, 111] and in simplified models with featureless densities of states.

## 3.2 Evidences in IBSC

### 3.2.1 Mass enhancement

There are many experimental evidences that show the presence of heavy electronic quasiparticles in all the different IBSC. Among them, we want first to highlight one interesting agreement between theory and experiments that will motivate the importance of the explicit treatment of many-body correlations when doing simulations of the electronic structure of these compounds. This concerns the Sommerfeld coefficient, which is the linear term of the low temperature specific heat  $C(T \rightarrow 0) = \gamma T$ . This is given by

$$\gamma = \frac{\pi^2 k_B^2}{3} D^*(\epsilon_F), \quad (3.1)$$

where  $D^*(\epsilon_F)$  is the renormalized density of states of the quasiparticles at the Fermi level. This quantity, in the one-band case, is proportional to the mass enhancement. In the multi-orbital case, to a linear combination of the different contributions from different orbitals. A correct description of the electronic density of states around the Fermi level will thus be critical to describe this quantity properly.

In Fig. 3.1 we can see the behavior of the Sommerfeld coefficient in the 122 family of IBSC. A value of around 30 mJ/mol K<sup>2</sup> for BaFe<sub>2</sub>As<sub>2</sub> (with 6 electrons in 5 orbitals) is massively enhanced to around 100 mJ/mol K<sup>2</sup> for KFe<sub>2</sub>As<sub>2</sub> (with 5.5

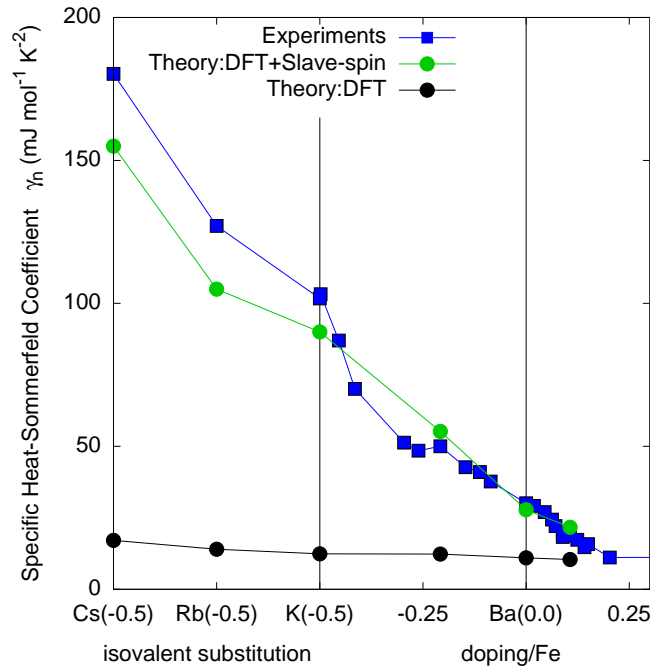


**Figure 3.1:** Sommerfeld coefficient measurements (blue squares) of the hole-doped 122 family and comparison with theoretical predictions from DFT calculations (black dots) and from a DFT+SSMFT scheme (green dots) in which the interaction parameters are fixed to  $U = 2.7$  eV and  $J/U = 0.25$  for all the compounds.  $\text{BaFe}_2\text{As}_2$  is doped with holes via the  $\text{Ba} \leftrightarrow \text{K}$  substitution until reaching a filling of 5.5 electrons in 5 orbitals. Then, isovalent substitution of  $\text{K} \leftrightarrow (\text{Rb}, \text{Cs})$  is carried out. Figure adapted from Ref. [20].

electrons in 5 orbitals). The effect of hole-doping, which brings the system closer to half-filling, is to increase the effective mass of the quasiparticles in the system due to enhanced many-body correlations. This corresponds to a narrowing of the electronic band structure of these quasiparticles, resulting in an enhanced  $D^*(\epsilon_F)$  and thus in an increase of the Sommerfeld coefficient according to eq. (3.1). Moreover, isovalent substitution  $\text{K} \leftrightarrow \text{Rb}, \text{Cs}$ , whose effect is to enlarge the Fe-Fe distance, increases  $\gamma$  even more. This is a consequence of an effective increase of the ratio between the interaction strength and kinetic energy since the electronic bands will now be less dispersive due to the larger distance between the atoms hosting the conduction electrons.

It should be pointed out here that hole doping has the biggest effect in increasing correlations among these types of chemical substitutions, while the increase of the Fe-Fe distance is secondary. This can be explained by analyzing the effect of other type of substitution,  $\text{Fe} \leftrightarrow \text{Cr}$ , that also introduces hole-doping and increases the degree of correlations [112] while barely changing the Fe-Fe distance (this will be discussed in detail in the following section).

In Fig. 3.1, a series of calculations using DFT (black points) and a scheme of DFT combined with Slave-Spin Mean-Field Theory (SSMFT, in green points) are

compared with the experimental results (blue points). Surprisingly, DFT calculations disagree strongly with the experiments while the agreement between the calculations with DFT+Slave-Spins and the experiments is quite accurate (the set of interaction parameters has been kept fixed for all these calculations). This highlights the importance of the explicit treatment of correlations in realistic simulations of IBSC. In this particular case, the mass enhancements that arise naturally from the DFT+Slave-Spins formalism and that are responsible for this enlargement of the Sommerfeld coefficient will turn out to be key when explaining many other experimental results, as we will see in the following sections.

### 3.2.2 Large fluctuating magnetic moments

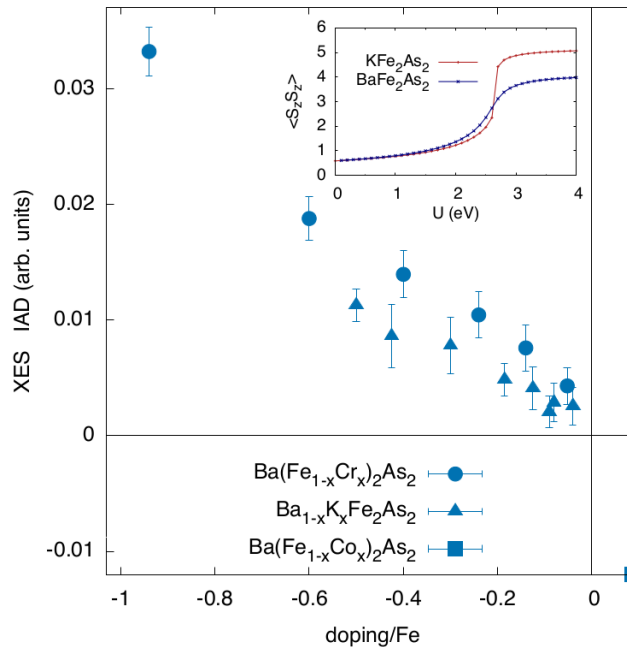


**Figure 3.2:** Local magnetic moments of different hole-doped versions of BaFe<sub>2</sub>As<sub>2</sub>, the parent compound of the 122 family, measured by X-Ray Emission Spectroscopy measurements (XES). Inset: theoretical predictions of local paramagnetic moments in BaFe<sub>2</sub>As<sub>2</sub> and KFe<sub>2</sub>As<sub>2</sub> as a function of the on-site Coulomb interaction  $U$ . Adapted from Ref. [112].

Other interesting experimental studies explore the formation of large fluctuating local magnetic moments in the paramagnetic metallic phase of IBSC in general [113] and in the 122 family in particular [112, 114], with X-Ray emission spectroscopy (XES), which is a fast-probe technique sensitive to those local moments. By shining photons to the sample at a certain energy<sup>1</sup>, an electron from a core level (typically

<sup>1</sup>The energy of these photons is usually in the hard X-Ray range and to produce an intense enough beam, synchrotron radiation (like the one produced at the ESRF in Grenoble, France) is needed.

from the  $1s$ ) is excited to a valence state leaving a core hole behind which is quickly filled by another electron from an outer shell (a  $3p$  in this case). This decaying electron can have either spin up or down and its energy will be different for these two configurations due to the presence of an open Fe- $3d$  shell in the system. The emitted line from this decay will then split with a magnitude (measured by the so-called IAD) that is proportional to that local magnetic moment.

In the case of the 122 family, the experimental results displayed in Fig. 3.2 show how the magnitude of these local magnetic moments increases with hole-doping. This is the case for the doping in the Fe plane in the compound  $\text{Ba}(\text{Fe}_{1-x}\text{Cr}_x)_2\text{As}_2$  as well as for the doping in the interlayer spacer in  $\text{Ba}_{1-x}\text{K}_x\text{Fe}_2\text{As}_2$ . The presence of these large moments can be understood in the context of Hund's metals in the following fashion: in the vicinity of a Mott insulator, the charge fluctuations required to the flow of electrons responsible for the metallic conduction to take place, tend to be suppressed and only certain local configurations prevail. In this particular case, this Mott insulator is strongly influenced by Hund's coupling, and these remaining local configurations will be of the type "high-spin", this is, with all the spins aligned trying to maximize the total local spin. Since we are in a non-magnetic phase, these high-spin configurations do not form any long-range order, but they fluctuate locally.

Theoretical predictions by realistic simulations within a DFT+Slave-Spins framework (inset in Fig. 3.2) also confirm this trend. In this case, the local spin-spin correlation function (proportional to the total local spin) shows a saturation value that is higher in the case of  $\text{KFe}_2\text{As}_2$  (that has 5.5 electrons per Fe-atom) than in the case of  $\text{BaFe}_2\text{As}_2$  (which contains 6 electrons per Fe-atom). Not only that but we can see also how there seems to be a more drastic saturation of the magnetic moments with increasing  $U$  in the case of  $\text{KFe}_2\text{As}_2$ . This will be explained more in detail in the following section, but it is related with a crossover departing from the half-filled Mott transition in the interaction/doping-plane phase diagram. This crossover is more pronounced in the proximity of the half-filled Mott insulator and it becomes smoother when moving to higher dopings.

### 3.2.3 Orbital selectivity

Another interesting experimental evidence also supported by theoretical realistic simulations has to do with the so-called orbital-selectivity, i.e. the orbitally-differentiated correlation strengths. This can be directly seen in the different quasi-particle mass renormalizations, which have been measured by different probes, among them ARPES and Quantum Oscillations, but also predicted theoretically [115, 116, 117, 118, 119, 120, 121, 122, 123, 124] and experimentally<sup>2</sup>.

In the upper panel of Fig. 3.3 several experimental measurements of the mass enhancements are presented. Measures from the specific heat and the optical con-

<sup>2</sup>For a complete list of experimental references, check section 11.4 in Ref. [125]

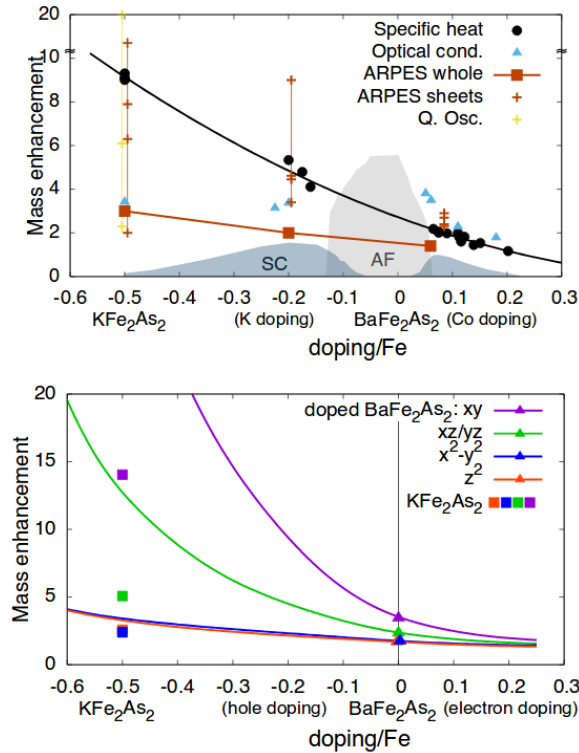


**Figure 3.3:** Upper panel: different experimental estimates of the mass enhancements in hole- and electron-doped BaFe<sub>2</sub>As<sub>2</sub>. Lower panel: theoretical prediction of the mass enhancements of the different electrons in the 122 family calculated with a DFT+SSMFT scheme. Adapted from Ref. [115].

ductivity only provide one value which is a combination of the different masses from the different orbitals, which are instead resolved by other probes like ARPES or quantum oscillations. One can see how around the stoichiometric compound BaFe<sub>2</sub>As<sub>2</sub> and moving towards the electron-doped side, all the different experiments seem to agree, whereas in the hole-doped side, different probes seem to give different results. This however can be explained by looking to how the orbital-dependent mass enhancements  $(m^*/m_b)_l$  enter in the description for the specific heat and optical conductivity in Fermi liquid theory. The Sommerfeld coefficient is proportional to the density of states at the Fermi level  $D^*(\epsilon_F)$ , that is a linear combination of the mass enhancements multiplying the orbitally-resolved bare density of states from DFT. On the other hand, in the case of the optical conductivity, this is measured through the ratio of the measured Drude peak compared to its value calculated by DFT. In this multiband case, the mass renormalization enters as a linear combination of contributions weighted by the inverse<sup>3</sup> values  $(m^*/m_b)_l^{-1}$ . This naturally

<sup>3</sup>The Drude weight calculation is analogous to a circuit with a set of different resistances coupled in parallel, where the total resistance will be dominated the smallest one. Instead in a set of resistances coupled in series, the total resistance will be dictated by the largest one, in a similar fashion as the heaviest electrons dictate the renormalization of the Sommerfeld coefficient.

explains why the less renormalized electrons tend to dominate the Drude weight while the more renormalized ones dominate the Sommerfeld coefficient.

The origin of this differentiation is a consequence of the different proximity to half filling of each of the Fe-3d orbitals. Due to the realistic band structure where orbitals hybridize with each other and even more importantly the crystal field splitting the orbital levels, the 5 orbitals will not accommodate 1.2 electrons each but there will be certain differences. In particular, the  $d_{xy}$  orbital tends to have a smaller filling (closer to 1) than the rest. When the system is doped with holes (typically by Ba  $\leftrightarrow$  K substitution), the individual filling of the  $d_{xy}$  orbital gets much closer to 1 (half-filling), thus inducing an effective quasiparticle mass for the  $d_{xy}$  electrons several times larger than in the other orbitals. This behavior can be seen in realistic simulations for doped BaFe<sub>2</sub>As<sub>2</sub> and for KFe<sub>2</sub>As<sub>2</sub> (lower panel of Fig. 3.3) and it also explains the big disagreement between the calculated electronic band structure with DFT and the measurements by ARPES. Without entering too much into details, even though the total bandwidth of an ARPES spectrum gets reduced only by a factor  $\sim 2 - 3$  compared by a DFT simulation (a number that would correspond to the least renormalized electrons), the bands around the Fermi level are much more renormalized due to the much more renormalized electrons coming from these  $d_{xy}$  orbitals.

Thus, as it can be seen from the orbital resolved probes, due to the coexistence of heavy and light electrons, it is natural that some global quantities like the specific heat, that are dominated by the heaviest electrons, are much more renormalized than others like conductivity, that are dominated by the lightest electrons, and that this difference is enhanced when approaching half-filling via hole doping. These coexistence is also qualitatively observed in the complex renormalization needed to properly describe the electronic band structure measured by ARPES.

### 3.3 General phenomenology of Hund's metals from model studies

In the previous section several supporting experimental evidences for the Hund's metal behavior found in the 122 family of IBSC were presented, and also how they are confirmed by realistic simulations (in particular within a DFT+Slave-Spins framework). In this section, we want to highlight the general character of this physics, since it is also found in simplified models with featureless densities of states and in other materials like ruthenates.

We analyze the results of a SSMFT scheme applied to a simplified multi-orbital Hubbard model with featureless densities of states. This will allow us to understand the physics in absence of the details characterizing a real material. For that we use here the Hamiltonian from eq. (2.40) where the interacting part of the Hamiltonian does not include the spin-flip and the pair hopping terms (only Ising-like density-

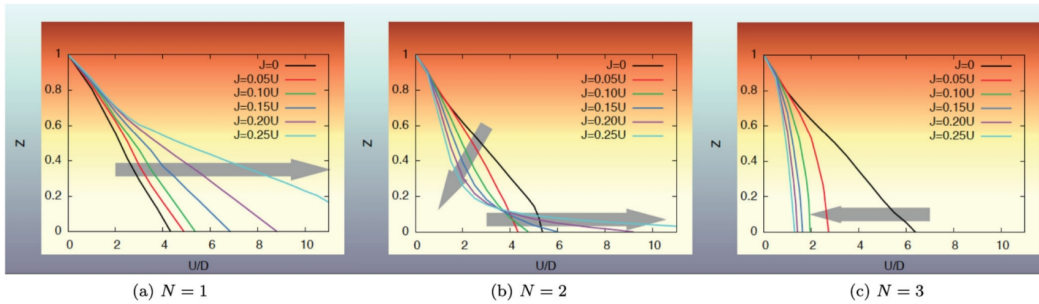


**Figure 3.4:** Quasiparticle weight  $Z$  in a 3-orbital Hubbard model with semicircular density of states as a function of the on-site Coulomb repulsion  $U$  at different values of Hund's coupling  $J/U$  and for different fillings:  $n = 1$  (left panel),  $n = 2$  (center panel) and  $n = 3$  (right panel). From Ref. [109].

density terms). In this case the hopping integrals are all equal for each band, i.e.  $t_{ij}^{ml} = \delta_{lm}t_{ij}$ , and we define the orbital energies as  $\epsilon_l = t_{ii}^l = 0$ ,  $\forall l$ , thus implying degenerate orbitals. A semicircular bare density of states is selected<sup>4</sup> with a half bandwidth<sup>5</sup> for each band given by  $D = 2t$ . The only difference among this idealized model and the realistic one is that in the later, the  $t_{ij}^{lm}$  hopping integrals come from a tight-binding parametrization of the DFT band structure, and also the orbitals are not longer fully degenerate, this is, the  $\epsilon_l$  are different from one another depending on the crystal field splitting of the system. More details of this particular method can be found in Refs. [126, 66].

In first place, we must explain in detail what do we precisely mean by a half-filled Mott insulator favored by Hund's coupling, since it will have consequences in all the phenomena occurring in these materials. By looking at Fig. 3.4, where a series of calculations in a 3-band Hubbard model at different fillings ( $n = 1, 2, 3$ ) are presented for different values of Hund's coupling  $J/U$ , we can see how  $Z$ , the quasiparticle weight<sup>6</sup> obviously diminishes with increasing local Coulomb repulsion  $U$ . However, Hund's coupling influences non-trivially the system depending on the electronic density. For all the integer fillings different from half-filling ( $n = 3$  in this case), an increasing value of Hund's coupling increases the critical value of  $U$  at which the Mott transition happens, which occurs when the quasiparticle weight vanishes ( $Z = 0$ ), thus the mass enhancement diverges<sup>7</sup>. In the case of  $n = 1$ , the effect is very straightforward, whereas in  $n = 2$  there is a more pronounced decay of

<sup>4</sup>This corresponds to the lattice geometry of a Cayley tree, also known as Bethe lattice. This lattice is not representative of any electronic system in condensed matter, but it provides a semicircular density of states with which many predictions can be made, and also it provides analytical solutions in certain problems.

<sup>5</sup>From now on, whenever we are referring to the local Coulomb interaction  $U$ , we will be actually talking about the ratio  $U/D$ , i.e. we set  $D$  (the half-bandwidth of the bare density of states) as the unit of energy.

<sup>6</sup>In this case the quasiparticle weight is the same for the 3 orbitals because they are degenerate.

<sup>7</sup>In all the methods with a local self-energy we have that  $Z = (m^*/m_b)^{-1}$ .

the quasiparticle weight with increasing  $U$ , but the Mott transition still happens at much higher values of  $U$ . In the case of half-filling instead, the effect of increasing Hund's coupling is to reduce the critical value of the on-site Coulomb repulsion  $U_c$ , and thus in this case the Mott transition is favored by the presence of Hund's coupling. This gives a first insight on how Hund's coupling has a non-trivial effect on the metallic properties of a material.

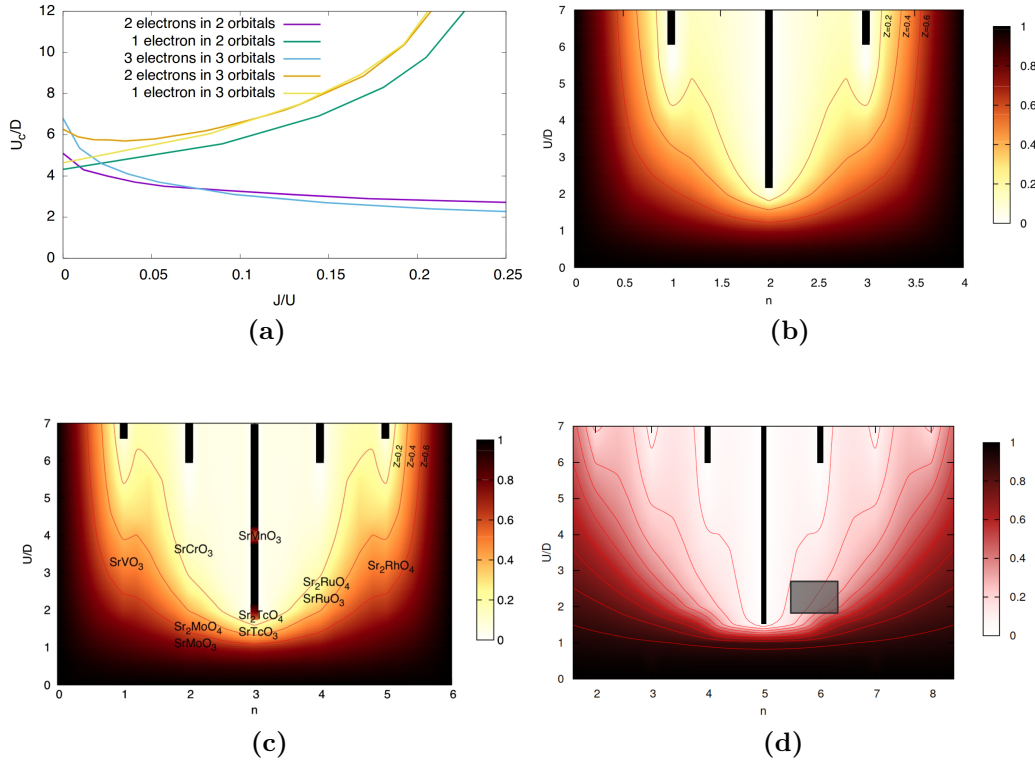


**Figure 3.5:** (a) Critical value of the on-site Coulomb interaction  $U_c$  as a function of Hund's coupling  $J/U$  at different fillings in a 2- and 3-orbital Hubbard model. (b) Color map of the quasiparticle weight  $Z$  as a function of  $U$  and the electronic density  $n$  in a 2-orbital model for  $J/U = 0.15$ . (c) The same for a 3-orbital model (some compounds are plotted around its nominal electronic density and the estimated interaction parameter). (d) The same for a 5-orbital model for  $J/U = 0.2$  (the shaded grey area corresponds to the region where the 122 family of the IBSC would be approximately located). The black lines signal the different Mott transitions. Adapted from Refs. [36, 127].

It is also worth mentioning the robustness of this behavior, which is not exclusive of a 5-orbital case like that of IBSC or the 3-orbital model explained above. Indeed, any multi-orbital system where Hund's coupling is present<sup>8</sup> displays this kind of behavior, where a half-filled Mott insulator is favored. Fig. 3.5a summarizes this for the former case of 3 orbitals and also for the case of 2 orbitals. Basically, for all the integer fillings different from the half-filled case, the Mott transition happens at

<sup>8</sup>This holds also in presence of small crystal-field splitting and/or orbital hybridization. Large crystal-field splittings or hybridizations can win over Hund's coupling and change the final behavior.

a much higher value of  $U$ . In the rest of the panels in Fig. 3.5 we compile a series of calculations of the quasiparticle weight  $Z$  as a function of the local Coulomb interaction  $U$  and the electronic density  $n$  for models with 2 (Fig. 3.5b), 3 (Fig. 3.5c) and 5 (Fig. 3.5d) orbitals at a fixed value of the Hund's coupling  $J/U$ . The Mott insulator phase is represented by the thick black lines. In all these panels it is clearly visible how the half-filled Mott insulator dominates the phase diagram and also how there is a crossover departing from that Mott transition that dominates the phase diagram specially in the 5-orbital case, not only at half filling, but also in an extended region of electronic densities. In the context of IBSC, this crossover was traced for the first time by Ishida and Liebsch [128] and it has been continuously studied [122, 129, 130].

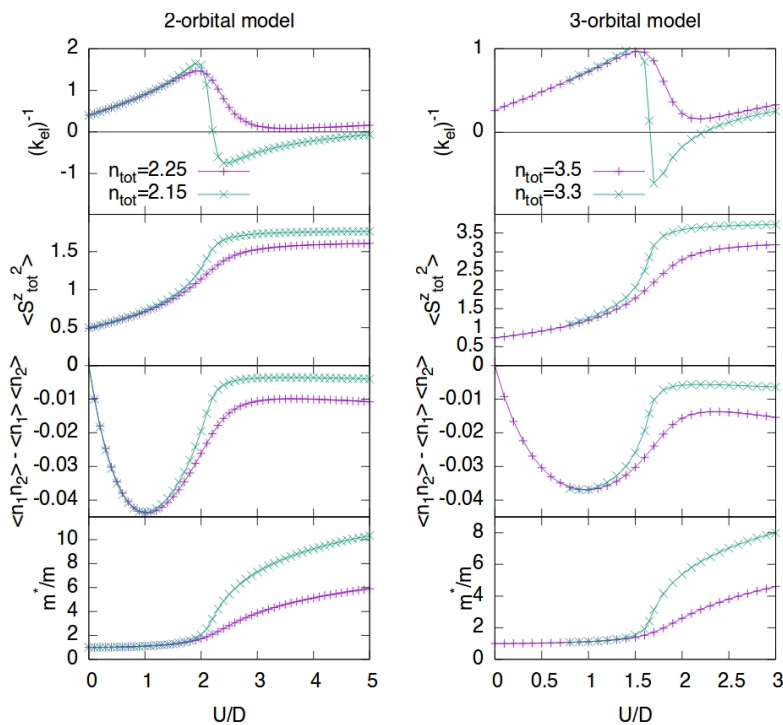


**Figure 3.6:** Quasiparticle electronic compressibility (upper panels), local spin-spin correlation function (middle-upper panels), interorbital charge fluctuations (middle-lower panels) and mass enhancement (lower panels) for 2 different doping levels in a 2-orbital Hubbard model (left column) and in a 3-orbital Hubbard model (right column) for  $J/U = 0.25$ . From Ref. [130].

In Fig. 3.6 we can see a series of relevant quantities illustrating that crossover in a 2-orbital model (left column) and in a 3-orbital model (right column): the electronic compressibility (upper panels) that will be discussed in the following section, the total local moment in the paramagnetic phase (middle-upper panels), the inter-orbital charge-fluctuation correlation function (middle-panels) and the mass enhancement (lower panels). Each panel contains the results of simulations done with SSMFT for two different fillings as a function of the interaction strength  $U$  at a fixed value of  $J/U = 0.25$ . We will analyze how all these quantities respond to

the described behavior of a Hund's metal and clearly display a crossover for  $U \gtrsim U_c$  that smoothens out with the density moving away from half filling.

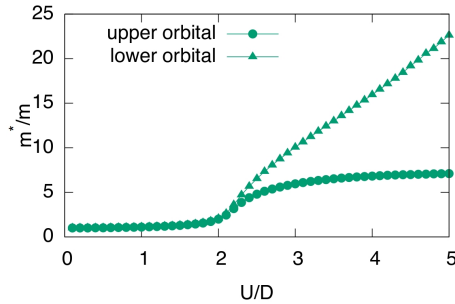


**Figure 3.7:** Mass enhancement for a 2-orbital Hubbard model with semicircular densities of states and a small splitting of the orbital energies of  $\epsilon_2 - \epsilon_1 = 0.05D$ .

In the total local magnetic moment (middle-upper panel) there is a clear build up of its magnitude until saturation, indicating the prevalence of the high-spin configurations typical of the Hund's metal phase. This saturation happens for  $U$  larger than a crossover value. Not only the magnitude of that moment is bigger, but the saturation itself is more pronounced in the case of a smaller filling, which corresponds to the behavior found in the case of the 122 family showed in Fig. 3.2, where the magnetic moments measured (and calculated) in  $\text{BaFe}_2\text{As}_2$  gradually increases with hole-doping (that brings the density closer to half-filling), and  $\text{KFe}_2\text{As}_2$  has a greater local magnetic moment than  $\text{BaFe}_2\text{As}_2$  because it is closer to half-filling.

The mass enhancement (middle-lower panel) can be understood in an analogous fashion. A clear build-up happens starting at the crossover, and is more pronounced for smaller dopings. The mass enhancement will eventually diverge at half-filling.

The orbital selectivity is a little bit more subtle to explain here. In a degenerate model like this, different mass enhancements cannot be obtained, by symmetry. However, once there is a tiny splitting of the orbital energies, this orbital-differentiated mass enhancement appears, again, after the crossover, as it can be seen in Fig. 3.7, where the same simulations for a 2-orbital model have been made, but now introducing a splitting of the orbital levels of 1/40-th of the bandwidth. For the same bandwidth, the orbital that is closer to half filling will have a larger effective mass.

Another possible way to see this is by looking at the correlation function of the inter-orbital charge fluctuations, i.e.  $\langle n_1 n_2 \rangle - \langle n_1 \rangle \langle n_2 \rangle$ , where  $n_l = \sum_{\sigma} d_{\sigma l}^{\dagger} d_{\sigma l}$  is the number operator per orbital. We can see that for  $U = 0$  this correlation function is zero (each orbital is independent from one another, as one expects in the case of completely uncorrelated electrons). Once the value of  $U$  starts to increase, charge fluctuations become correlated between orbitals. An electron cannot hop from one orbital to another that is already occupied because of the extra energy cost of a doubly occupied site due to  $U \neq 0$ , and it prefers to go for an empty one. However,

a non-trivial effect happens when approaching the crossover, which is the sudden suppression of that correlation function until it becomes almost zero again (or at least much smaller than before the crossover). This suppression is telling us that the charge fluctuations needed for the conduction of electrons become independent from orbital to orbital after a certain value of  $U$ .

This can be better understood [131] by doing an analytical study of the local physics of a 2-orbital model in the atomic limit, this is making  $t_{ij}^{ml} = 0$  and  $\epsilon_l = 0$ . If we calculate the energies of the different configurations for such a system with the chemical potential being in the particle-hole symmetric form like in eq. (B.12) and arbitrarily setting the zero of energy to the ground state energy, we will obtain the following states:

$$\left\{ \begin{array}{ll}
 |\uparrow\downarrow, \uparrow\downarrow\rangle |0, 0\rangle & E = 2U - 2J \\
 |\uparrow\downarrow, \uparrow\rangle |\uparrow\downarrow, \downarrow\rangle |0, \uparrow\rangle |0, \downarrow\rangle \\
 |\uparrow, \uparrow\downarrow\rangle |\downarrow, \uparrow\downarrow\rangle |\uparrow, 0\rangle |\downarrow, 0\rangle & E = \frac{U+J}{2} \\
 |\uparrow\downarrow, 0\rangle |0, \uparrow\downarrow\rangle & E = 3J \\
 |\uparrow, \downarrow\rangle |\downarrow, \uparrow\rangle & E = J \\
 |\uparrow, \uparrow\rangle |\downarrow, \downarrow\rangle & E = 0
 \end{array} \right. \quad (3.2)$$

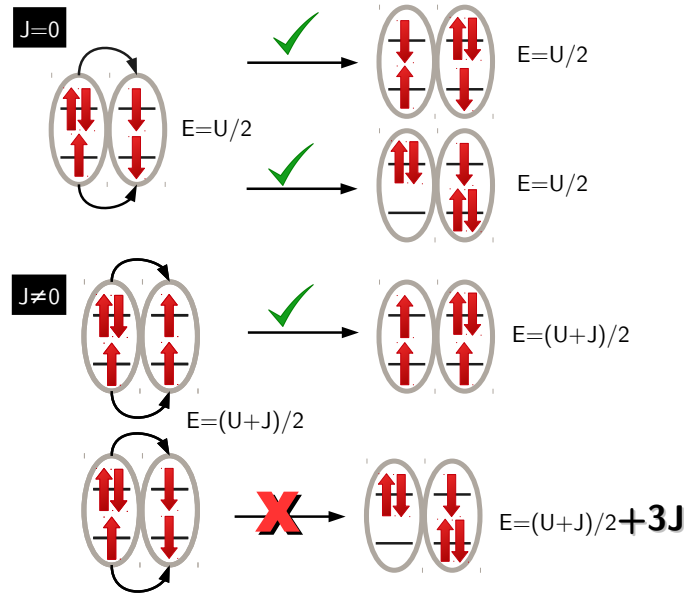


**Figure 3.8:** Schematic representation of a charge excitation propagating in a half-filled system with and without Hund's coupling. The energy of each configuration is written to the right.

It is obvious to see that in the absence of Hund's coupling ( $J = 0$ ), the local Coulomb repulsion  $U$  will split the sector with 2 particles, 3 and 1 particles and 4 and 0 particles. In particular, the ground state will be 6-fold degenerate. Now, by turning on  $J$ , the local configurations with 2 particles will split in energy according to the arrangement displayed above, and the ground state will be now 2-fold degenerate, comprising the 2 states with parallel spins, one per orbital. We now re-introduce a small but finite hopping. The ground state of such a system will be a Mott insulator, in which there will be only local high-spin configurations on each site, with one spin per orbital, aligned among themselves.

Now, if we add one more particle to the system and we look at the available channels for it to freely hop, like the case presented in Fig. 3.8, we will see immediately the consequences of having a sizable Hund's coupling in the system. If  $J = 0$ , both channels are available for hopping with the same energy cost. The charge excitation can propagate with equal probability in any of the orbitals. However, when  $J \neq 0$ , not all the hopping channels are available at the same energy cost. The charge excitations will now propagate along the same type of orbital, since now there will be an extra energy cost for leaving a doubly occupied site behind when the charge excitation happens on a different type of orbital than in that one where the extra particle has been added. This clarifies why charge fluctuations get decoupled.

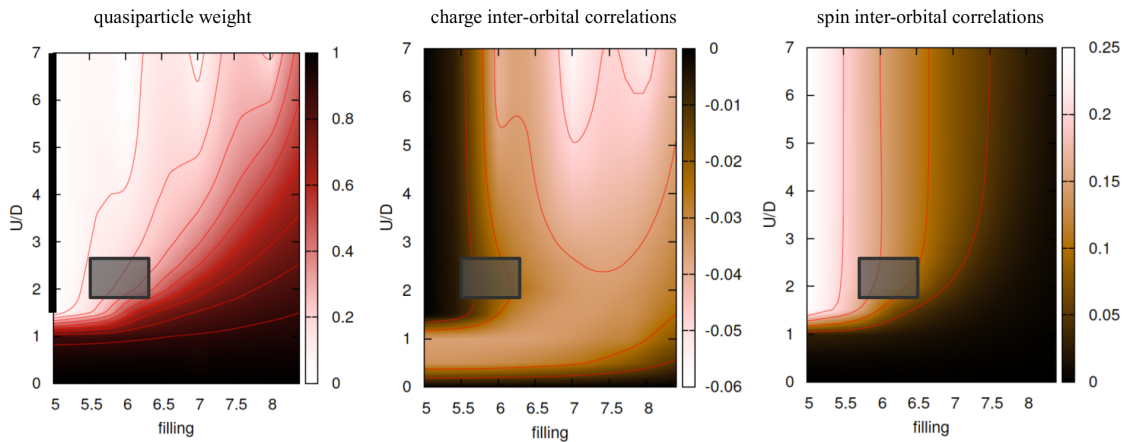


**Figure 3.9:** Color maps of the quasiparticle weight  $Z$  (left panel), charge inter-orbital correlations (center panel) and spin inter-orbital correlations (right panel) as a function of the local Coulomb repulsion  $U$  and the electronic density  $n$  in a 5-orbital Hubbard model with an idealized semicircular density of states for  $J/U = 0.25$ . The shaded grey lines correspond to the region of parameters where supposedly the 122 family of IBSC would lay. From Ref. [125].

Of course, all the different phenomena described above are also seen in the case of a 5-orbital model that is relevant for IBSC. In that particular case, the inter-orbital charge-fluctuation correlation function will exist for every pair of orbitals, and thus if a realistic density of states is added, the behavior will be different for each one of them. However, the general trends do not differ, there is a half-

filled Mott transition favored by Hund's coupling from which a crossover departs, and that strongly influences that region of the phase diagram. In Fig. 3.9 three main quantities are shown (quasiparticle weight, inter-orbital charge fluctuations and total local magnetic moment) in a color plot on the electron-doped side of the phase diagram, together with a shaded grey area that indicates the region of parameters in which the 122 family of IBSC should be encountered. That region exactly falls in the crossover between a normal- to a Hund's-metal phase. This picture also indicates how adequate these compounds are to try to characterize the Hund's metal behavior, given that by slightly doping the system or effectively modifying the local interaction (for instance by doing isovalent substitution  $K \leftrightarrow Rb$ ,  $Cs$  which has the effect of increasing the ratio  $U/D$ ) both sides of the crossover can be explored in detail. Even though the model used in this particular case is a degenerate 5-orbital model with featureless densities of states, it qualitatively describes the relevant physics for those compounds.

### 3.4 Electronic compressibility

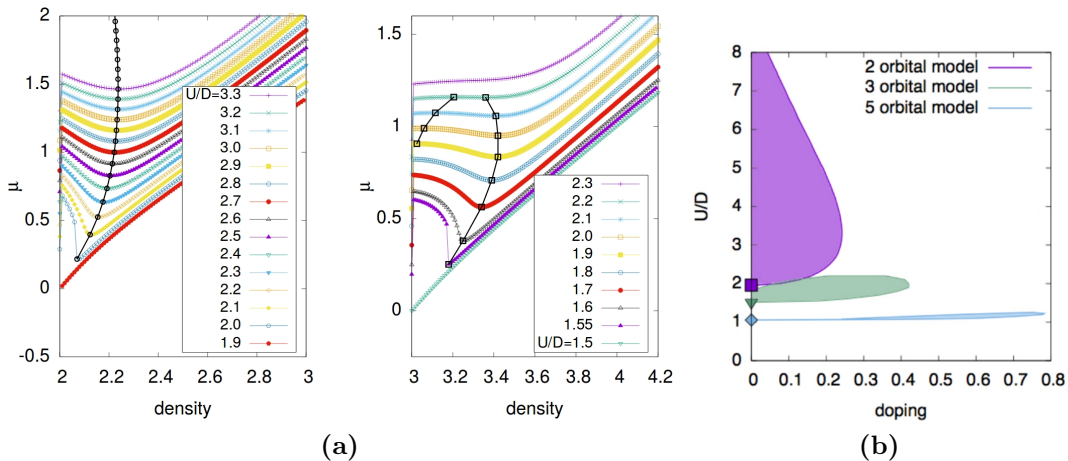


**Figure 3.10:** (a) Chemical potential  $\mu$  as a function of the electron density  $n$  in a 2-orbital model for various values of the local Coulomb interaction  $U$  with a value of Hund's coupling of  $J/U = 0.25$  and a semicircular density of states. (b) The same in a 3-orbital model. (c) Region of divergent electronic compressibility in the  $U$  vs.  $n$  plane for models with 2, 3 and 5 orbitals. From Ref. [130].

One last feature that has been recently discovered in simulations of both multi-orbital models and realistic models of IBSC, is the existence of an enhancement (culminating into a divergence) of the electronic compressibility in very close proximity to the crossover that separates the normal metal and the Hund's metal phase. The electronic compressibility of an electronic system can be defined in general like

$$\kappa_{el} \equiv \frac{dn}{d\mu}. \quad (3.3)$$

In the two panels of Fig. 3.10a we can see a series of simulations for a 2- and a 3-orbital model at different values of  $U$  for a fixed value of  $J/U$  in which the chemical potential  $\mu$  is plotted as a function of the electronic density  $n$ . The slope of these curves is the inverse of the electronic compressibility as it has been defined in eq. (3.3). One can trace the frontier of the region in which the electronic compressibility diverges (and becomes negative) which corresponds to the frontier of the region in which the system becomes unstable. In Fig. 3.10b this region is traced in the  $U$  vs.  $n$  plane for a 2-, 3-, and 5-orbital model. The common feature in all these 3 systems is that this region of instability departs from the Mott transition at half-filling, that it extends to a finite region of doping and that it coincides with the crossover mentioned above. This gives a hint to a possible connection between this instability and all the phenomena described above driven by Hund's coupling.

We will explain briefly the connection between this enhanced electronic compressibility and other instabilities from a more analytical point of view. In the case of an isotropic Fermi liquid [11], the electronic compressibility reads

$$\kappa_{el} = \frac{D^*(\mu)}{1 + F_0^s}, \quad (3.4)$$

where  $D^*(\mu)$  is the renormalized quasiparticle density of states at the Fermi level<sup>9</sup> and  $F_0^s$  is the so-called spin-symmetric Landau parameter. We can get some physical insight from a microscopical expression. Taking into account that the electronic density of a Fermi liquid is:

$$n = \int^{\mu} d\varepsilon D^*(\varepsilon), \quad (3.5)$$

we can derive now eq. (3.5) with respect to the chemical potential  $\mu$  following eq. (3.3) obtaining:

$$\begin{aligned} \kappa_{el} &= \frac{d}{d\mu} \int^{\mu} D^*(\varepsilon) d\varepsilon = D^*(\mu) + \int^{\mu} \frac{d}{d\mu} D^*(\varepsilon) d\varepsilon \\ &= D^*(\mu) + \int^{\mu} \frac{dn}{d\mu} \frac{d}{dn} D^*(\varepsilon) d\varepsilon = D^*(\mu) + \kappa_{el} \int^{\mu} \frac{dD^*}{dn}(\varepsilon) d\varepsilon. \end{aligned} \quad (3.6)$$

Finally, re-arranging eq. (3.6) we see that

$$\kappa_{el} = \frac{D^*(\mu)}{1 - \int^{\mu} d\varepsilon \frac{dD^*}{dn}(\varepsilon)}. \quad (3.7)$$

The electronic compressibility of such Fermi liquid is the value of the renormalized "rigid" band structure at the chemical potential  $D^*(\mu)$  corrected by the expression at the denominator, which is due to the change in the band structure with the filling.

---

<sup>9</sup>Although strictly speaking  $\mu$  is the chemical potential, in a fermionic system at  $T = 0$  it coincides with the Fermi level.

This last term plays the role of the Landau parameter  $F_0^s$  of an isotropic Fermi liquid. From this equation is obvious that an enhanced electronic compressibility can arise from a strong renormalization of the density of states that corresponds to a large  $D^*(\mu)$ , from a Landau parameter  $-\int^\mu d\varepsilon \frac{dD^*}{dn}(\varepsilon)$  (usually small and positive) becoming negative and approaching -1, or from a combination of both mechanisms.

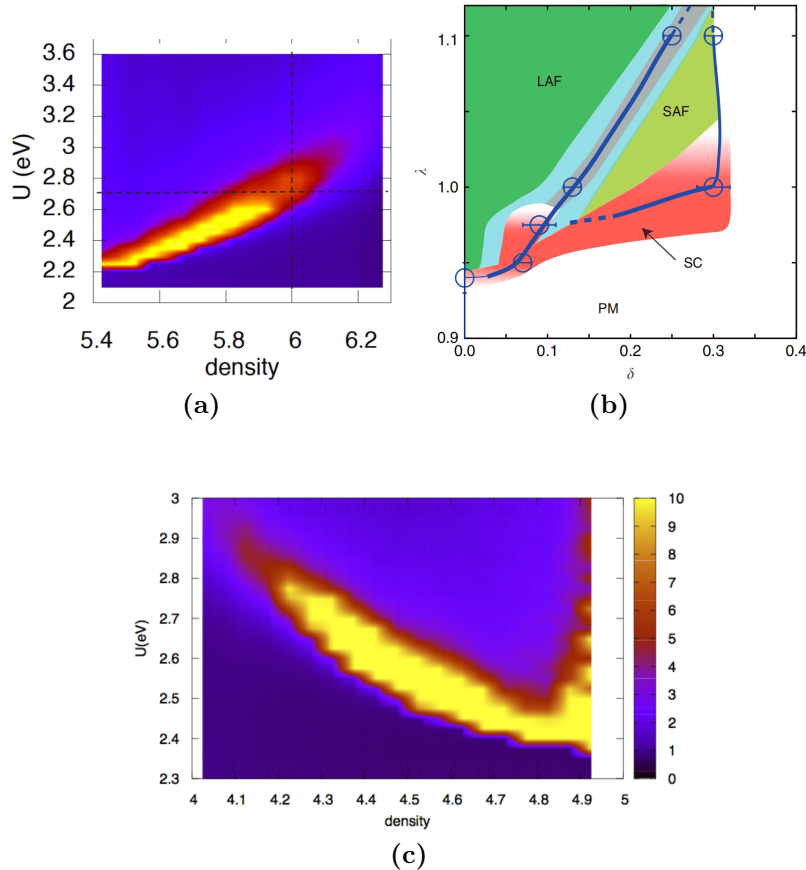


**Figure 3.11:** (a) Color map of the electronic compressibility as a function of the local Coulomb interaction  $U$  and the electronic density  $n$  for BaFe<sub>2</sub>As<sub>2</sub> (from Ref. [130]). (b) Phase diagram of LaFeAsO as a function of doping  $\delta$  and a scaled interaction parameter  $\lambda$  (from Ref. [132]). (c) The same as in (a) but for its hole-doped analogue BaCr<sub>2</sub>As<sub>2</sub> (from Ref. [133]).

Interestingly, this enhanced electronic compressibility also appears consistently in realistic simulations of IBSC using SSMFT (Refs. [130, 133]). In these cases, it also departs from the Mott transition at half filling and follows the normal-to-Hund metal crossover line. Some evidences are shown for several compounds in Fig. 3.11. It is remarkable that for the case of BaFe<sub>2</sub>As<sub>2</sub> [130] (see Fig. 3.11a) this moustache arrives at the stoichiometric density  $n = 6.0$  exactly around the value for  $U = 2.7$  eV predicted by calculations using constrained random-phase approximation (cRPA) [107]. This match allows to formulate the hypothesis that this instability, or the proximity to it, plays a role in superconductivity in these compounds, as proposed in Ref. [130].

In general the divergence of the compressibility signals an instability towards phase separation (in particular one of them could be the formation of charge-density waves). But also its enhancement signals enhanced quasiparticle interactions that can also favor instabilities. Going back to formula (3.7), we have seen that  $\kappa_{el}$  can be large (or even diverge) because of a large numerator or a small denominator. The first case simply indicates strong quasiparticle renormalization. The second, which is the case realized in this kind of instabilities [130], where the compressibility diverges while  $Z$  stays finite, indicates attractive forces in the particle-hole channel that can lead to a negative scattering amplitude in the particle-particle channel, and thus to superconductivity [134]. In addition, some electron-boson vertices can also be enhanced by electron-electron interactions, like for instance the density vertex (relevant for Holstein electron-phonon coupling). In particular the following Ward identity

$$A(q \rightarrow 0, \omega = 0) = \frac{1}{Z(1 + F_0^s)}, \quad (3.8)$$

holds for the renormalized density vertex in an isotropic Fermi liquid [135]. The renormalization of that vertex occurs in the same way<sup>10</sup> as the electronic compressibility in eq. (3.7), thus leading to an enhanced effective interaction strength which may trigger any particular mechanism mediated by this kind of interaction.

It is remarkable that within a different scheme, 2-dimensional many-variable Variational Monte Carlo (mVMC) a similar zone of phase separation is found for LaFeAsO [132] (see Fig. 3.11b). A similar behavior has been found also with a DFT+SSMFT scheme in the case of BaCr<sub>2</sub>As<sub>2</sub> [133] (see Fig. 3.11c), although in this case the zone of enhancement happens at a slightly higher value of the interaction parameter ( $U = 2.8$  eV is the estimated value for this compound). In this manuscript we will show how the same type of instability occurs in another family of IBSC, the iron-selenides (whose parent compound is FeSe).

---

<sup>10</sup>We have to remember that in the 1-band case one can write  $D^*(\epsilon) = (1/Z)D(\epsilon)$ , and so both the vertex and the electronic compressibility are enhanced exactly in the same fashion in the 1-band case for an isotropic Fermi liquid.



# 4

## d-electron heavy fermions in iron-based superconductors

In this chapter we present realistic simulations of the quasiparticle spectrum of the 122 family of IBSC within density functional theory+slave-spins mean-field theory (DFT+SSMFT) and discuss their nature as heavy-fermionic materials. We show experimental evidences in  $\text{KFe}_2\text{As}_2$  and related compounds that point in this direction. We also discuss in detail the precision of our method in capturing the main details of the electronic structure of this compound, in particular describing the positions of the Van Hove singularities seen by ARPES experiments. Conversely we study with dynamical mean-field theory (DMFT) and SSMFT how these peaks in the quasiparticle DOS can influence the transport properties in these materials. This is done in a 2-dimensional 1-band Hubbard model solved with DMFT. Finally we show how the calculated Sommerfeld coefficient of the 122 family, which can be heavily enhanced by hole-doping in our simulations, and also the computed thermoelectric response reach values that are perfectly consistent to consider these compounds as heavy-fermionic materials. We also show here preliminary results from the Karlsruhe group reporting the synthesis of hole-doped  $\text{CsFe}_2\text{As}_2$  with 2% Cr, having a Sommerfeld coefficient raised to  $\sim 250 \text{ mJ}\cdot\text{mol}^{-1}\cdot\text{K}^{-2}$  thus confirming our theoretical predictions.

---

Dans ce chapitre, nous présentons des simulations réalistes du spectre de quasiparticules de la famille 122 des IBSC dans le cadre d'un schéma DFT+SSMFT et en discutons si ces matériaux pourraient être inclus dans la catégorie des fermions lourds. Nous montrons d'abord des preuves expérimentales dans  $\text{KFe}_2\text{As}_2$  et des composés apparentés qui pointent dans cette direction. Nous discutons également en détail la précision de notre méthode pour capturer les détails principaux de la structure électronique de ce composé, en particulier décrivant les positions des singularités de Van Hove vues par les expériences ARPES. Nous étudions aussi comment les pics de quasiparticule DOS pourraient influencer les propriétés de transport dans ces matériaux. Cela se fait dans un modèle de Hubbard bidimensionnel à 1 bande, résolu avec DMFT. Enfin, nous montrons comment le coefficient de Sommerfeld calculé pour la famille 122, qui peut être fortement augmentée par le dopage de trous dans notre simulations, ainsi que la réponse thermoélectrique calculée atteignent des

valeurs parfaitement cohérentes pour pouvoir considérer ces composés comme des matériaux de type fermions lourds.

## 4.1 Signatures of heavy-fermionic behavior in the 122 family of IBSC

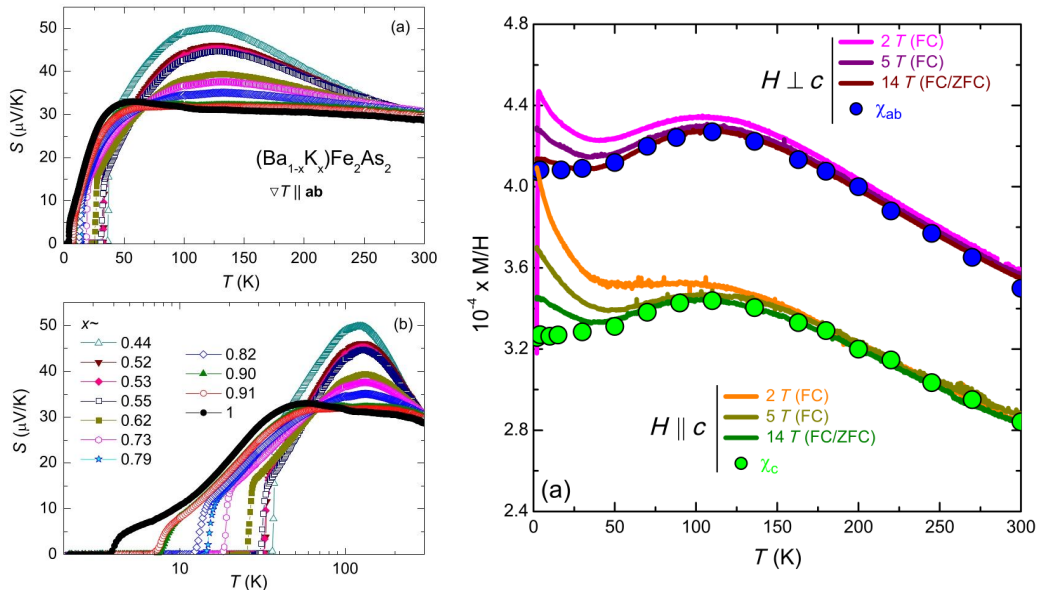


**Figure 4.1:** Left panels: experimental measurements of the Seebeck coefficient in  $(\text{Ba}_{1-x}\text{K}_x)\text{Fe}_2\text{As}_2$  as a function of temperature, from Ref. [136]. Right panel: magnetic susceptibility of  $\text{KFe}_2\text{As}_2$  for several values of the magnetic field, from Ref. [19].

Among all the different families of IBSC, the 122 turns out to be a very convenient platform to study the physics of Hund’s metals as explained in Section 3.2. One of the main features is the orbital-selectivity of orbital renormalizations, which is extremized in the hole-doped end members of that family ( $\text{KFe}_2\text{As}_2$ ,  $\text{RbFe}_2\text{As}_2$  and  $\text{Cs}_2\text{As}_2$ ), so heavy and light electrons coexist. This coexistence reminds heavy fermions, where electrons coming from localized  $f$ -shells manage to form conduction bands at the Fermi level thanks to the hybridization with more itinerant electrons coming from the more extended shells of  $s$ -,  $p$ - or  $d$ -character. Here the heavy electrons from the most renormalized  $d$ -shells mimic the role of the  $f$ -electrons in traditional heavy fermions.

Here we show that there are also clear signatures of heavy-fermionic behavior in iron-based materials. In Fig. 4.1 we show two of those for  $\text{KFe}_2\text{As}_2$ : the thermoelectric power and the magnetic susceptibility as a function of temperature. In the first case, we see a very large Seebeck coefficient that depends linearly with temperature before saturation. In the second, a constant Pauli-type magnetic susceptibility at

low temperatures before a crossover to a different Curie-Weiss-like regime. Both quantities also show a crossover at  $\sim 50$  K which can be seen as the typical coherence temperature of heavy fermions. This crossover has been already described in IBSC [19] and corresponds to a loss of coherence of the quasiparticles in the system.

This type of phenomenon can be explained due to the coexistence of heavy and light quasiparticles in IBSC, in a similar fashion as in usual heavy fermions there are light and heavy electrons coming from  $s$  and  $f$  orbitals respectively. This orbital selectivity appears as a consequence of Hund's coupling [115]. Another characteristic feature of heavy fermions is the presence of sharp spectroscopic features close to the Fermi level that can be ascribed to the presence of these heavy quasiparticles. In particular in the 122 family different Van Hove singularities (VHS) have been detected [137, 138, 139].

## 4.2 Realistic simulations of 122 stoichiometric IBSC

**Table 4.1:** Different experimental lattice parameters and relevant atomic positions of the 122 family of IBSC corresponding to the tetragonal high temperature phase. Provided in private communications by F. Hardy in Karlsruhe, Germany.

Compound	$a = b(\text{\AA})$	$c(\text{\AA})$	$z_{As}$
BaFe <sub>2</sub> As <sub>2</sub>	3.9625	13.0168	0.3545
KFe <sub>2</sub> As <sub>2</sub>	3.844	13.916	0.35249
RbFe <sub>2</sub> As <sub>2</sub>	3.873	14.459	0.34748
CsFe <sub>2</sub> As <sub>2</sub>	3.905	15.126	0.34189

The spectrum of electronic excitations is calculated within a DFT+SSMFT framework as explained in Section 2.5. The DFT calculations have been performed with the software package WIEN2K [105] using the exchange correlation functional of PBE-GGA [140], although some comparisons have been done using the local density approximation (LDA). This particular discussion can be found in Appendix F. The lattice parameters of these compounds are compiled in Table 4.1 and they correspond to the high temperature tetragonal phase, in which a Fermi liquid behavior is observed [19, 141].

We parametrize the DFT band structure with a set of maximally-localized Wannier functions [77] including only conduction bands of mainly Fe-3d character. The many-body interactions are included with a multi-orbital Hubbard-Kanamori Hamiltonian in the form of eq. (2.89). Although several scans in  $U$  are performed, for KFe<sub>2</sub>As<sub>2</sub> and RbFe<sub>2</sub>As<sub>2</sub> we choose  $U = 2.7$  eV, whereas for CsFe<sub>2</sub>As<sub>2</sub> we set  $U = 2.8$  eV<sup>1</sup>. For the Hund's coupling we fix  $J/U = 0.25$ . This value slightly differs from that obtained in cRPA-calculations [107] and that is typically used in DMFT

<sup>1</sup>The larger ionic radius of the Cs<sup>1+</sup> cation compared to Rb<sup>1+</sup> and K<sup>1+</sup> will be reflected in

( $J/U = 0.12 \div 0.15$ ) together with the full Kanamori form of the Hubbard model. In SSMFT, the same results are obtained using only the Ising-like (density-density) terms when the Hund's coupling is set to  $J/U = 0.2 \div 0.25$  [66] respectively.

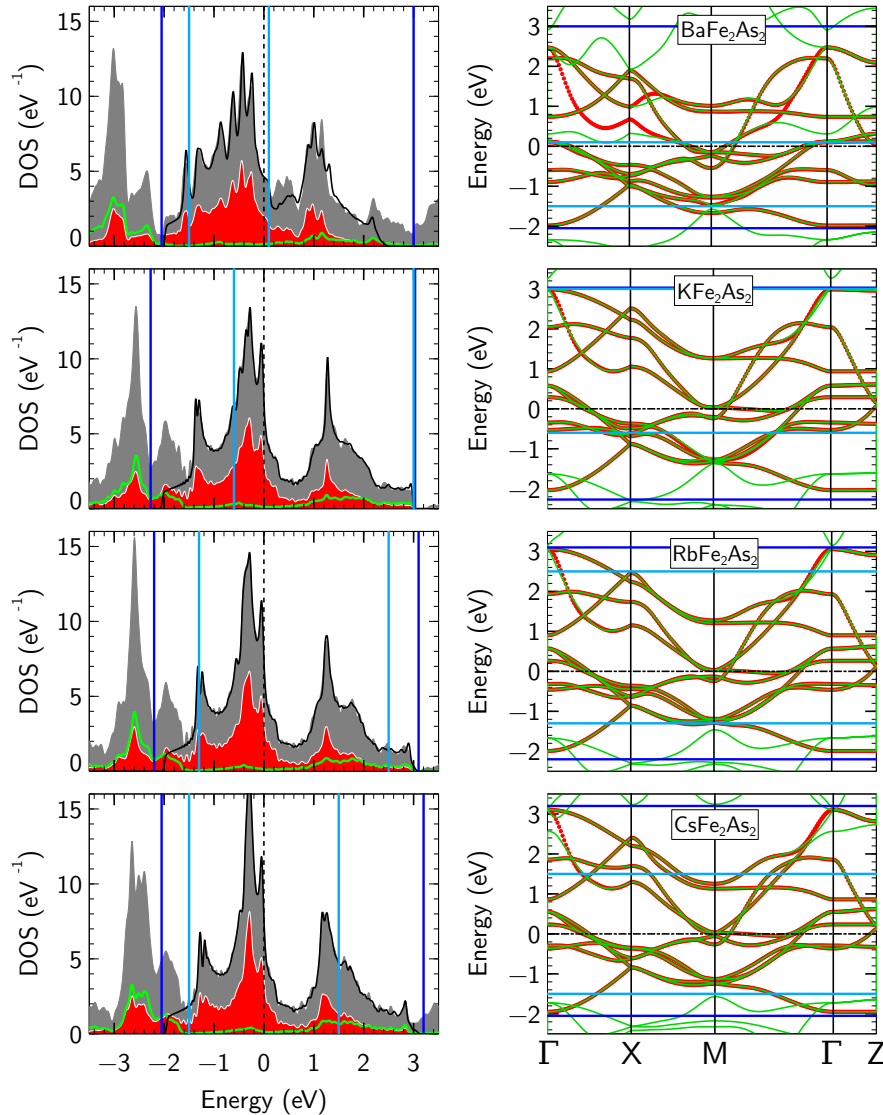


**Figure 4.2:** Left column: densities of states of the 122 family of IBSC. The shaded grey region corresponds to the total DOS of the system, the red one to the Fe DOS per atom, the green line to the DOS of the As ligands, and the black line to the total DOS of the Wannier orbitals. Right column: electronic band structure of these compounds. The green lines correspond to the DFT calculations and the red points show the dispersion relation of the tight-binding models done with WANNIER90.

a smaller value of the hopping integrals between different lattice sites (and thus in a smaller average kinetic energy). To compensate this difference we choose a slightly larger value of the local Coulomb interaction  $U$  for this compound. These values of  $U$  also correctly reproduce the value of the Sommerfeld coefficient for these compounds at the stoichiometry of  $n = 5.5$ .

### 4.3 Electronic structure of the 122 family of IBSC

The electronic band structures and densities of states (DOS) of the 122 family of IBSC from the DFT calculations and from their corresponding tight-binding parametrizations into Wannier orbitals are shown in Fig. 4.2. On the left column we show the total and orbitally-resolved DOS, from which one can immediately see the presence of a very important Fe-3*d* content around the Fermi level (red shaded zone). These Fe-3*d* bands are partially hybridized with other bands of mainly *p*-character that correspond to the As-ligand atoms (green lines), and moreover there is also some weight with *d*-character coming from the spacer atoms (Ba, K, Rb and Cs in this case) always present in the same energy range, being more important in the case of BaFe<sub>2</sub>As<sub>2</sub>. This hybridization with the *d*-symmetry orbitals of the spacer atoms is the reason of the slight mismatch of the tight-binding parametrization of BaFe<sub>2</sub>As<sub>2</sub>. However, the features around the Fermi level are almost identical to those of the DFT calculation.

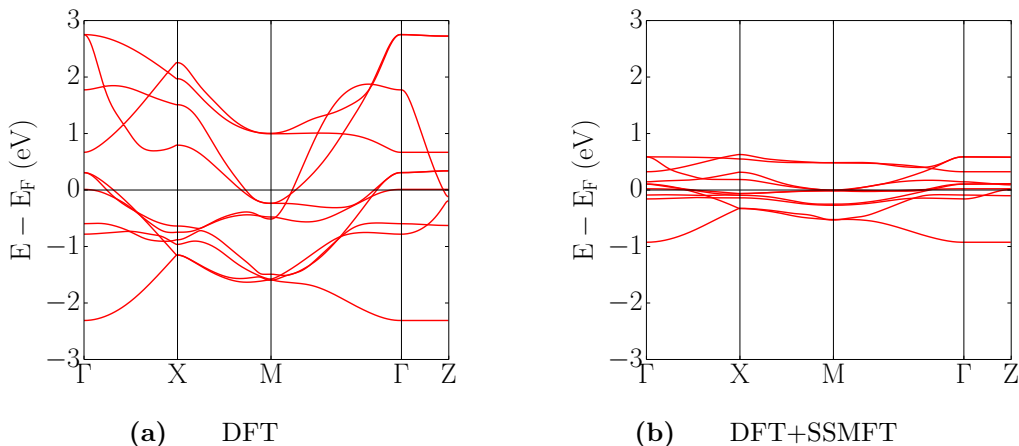


**Figure 4.3:** Comparison between the DFT band structure (a) and the renormalized band structure calculated with DFT+SSMFT (b) for KFe<sub>2</sub>As<sub>2</sub> for  $U = 2.7$  eV and  $J/U = 0.25$ .

Overall, one can see that all the electronic structures are very similar among the family, being the spectra of the compounds with K, Rb and Cs more similar among themselves since they are isovalent compounds. At first glance we see also the presence of a large Van Hove singularity in the DOS close to the Fermi level in all the compounds. However, their positions are completely off compared to experiments, as well as the large value of the DOS at the Fermi level  $D(\epsilon_F)$ , which are 4.6, 5.1, 5.5 and 6.1 eV<sup>-1</sup> for BaFe<sub>2</sub>As<sub>2</sub>, KFe<sub>2</sub>As<sub>2</sub>, RbFe<sub>2</sub>As<sub>2</sub> and CsFe<sub>2</sub>As<sub>2</sub> respectively, and are not sufficient to explain the large Sommerfeld coefficient displayed by these compounds.

The effect of including correlations can be seen in Fig. 4.3, where we show the band structure of KFe<sub>2</sub>As<sub>2</sub> calculated with DFT and within a DFT+SSMFT scheme

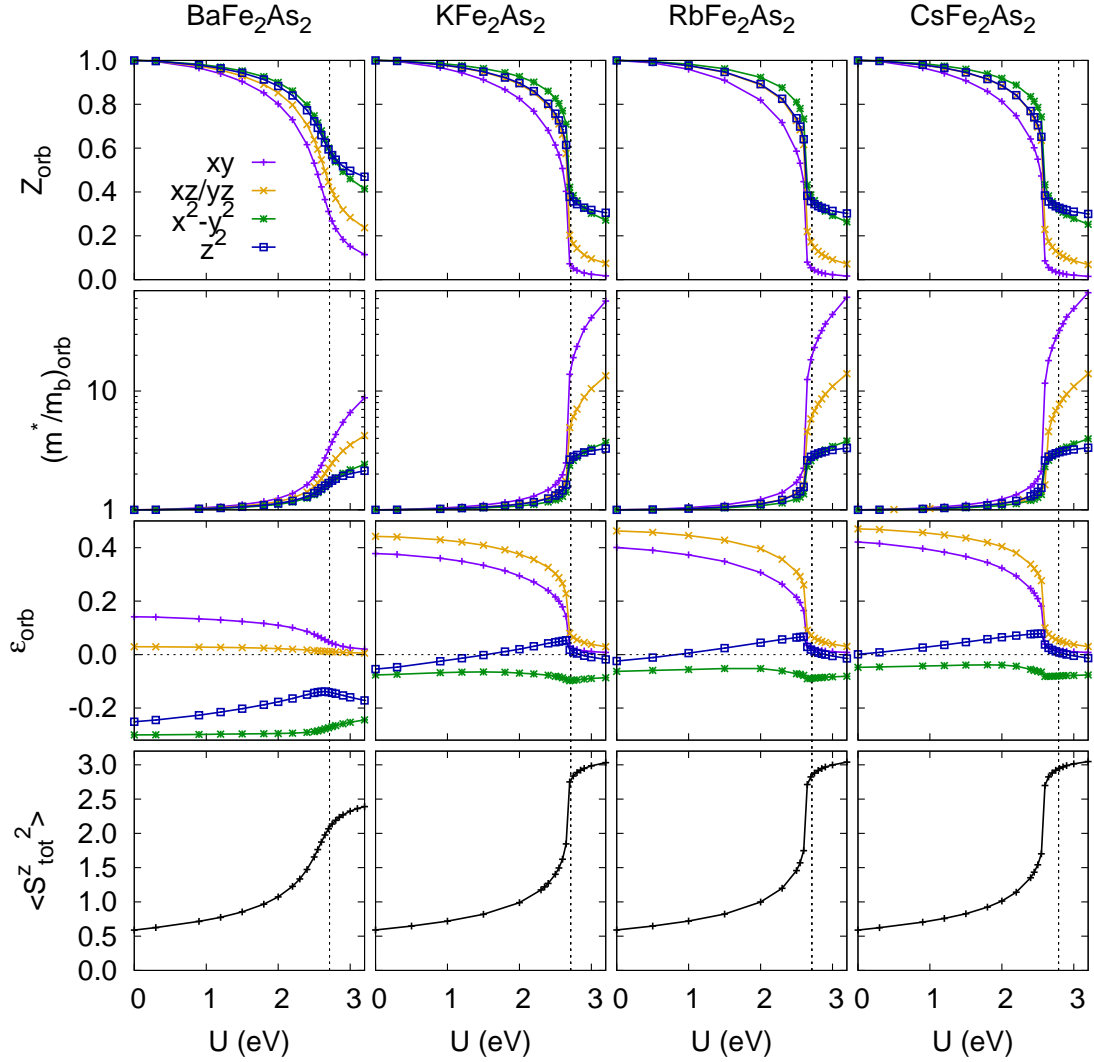


**Figure 4.4:** Orbitaly-resolved quasiparticle weights (upper panels), mass enhancements (mid-upper panels), on-site energies (mid-lower panels) and total local magnetic moment for  $\text{BaFe}_2\text{As}_2$ ,  $\text{KFe}_2\text{As}_2$ ,  $\text{RbFe}_2\text{As}_2$  and  $\text{CsFe}_2\text{As}_2$  as a function of the local Coulomb interaction  $U$  for a value of Hund's coupling of  $J/U = 0.25$ .

for an on-site Coulomb interaction of  $U = 2.7$  eV and a value of Hund's coupling of  $J/U = 0.25$ . The orbitaly-resolved quasiparticle weights  $Z_m$  obtained in this case are 0.07 for the  $d_{xy}$  orbital, 0.20 for the  $d_{xz/yz}$  orbitals and 0.42 and 0.37 for the  $e_g$  orbitals. The renormalized band structure (Fig. 4.3b) is between 2.5 and 3 times less dispersive than that calculated with DFT (Fig. 4.3a). This renormalization factor very much coincides with the phenomenological prefactor that is typically added to the DFT band structures in order to compare them with ARPES measurements. Due to this renormalization of the band structure, one would expect that the DOS of quasiparticles increases and all the features move closer to the Fermi level.

In Fig. 4.4 we show the dependence of the quasiparticle weights, mass enhance-

ments, orbital energies and total local magnetic moments for the different stoichiometric members of the 122 family of IBSC as a function of the on-site Coulomb interaction  $U$ . For the case of  $\text{KFe}_2\text{As}_2$  the renormalization of the quasiparticle spectrum described above can be easily ascribed to the large mass renormalizations present in the system at the relevant value of the Coulomb interaction  $U$ . This behavior also happens in all the other members, but is more pronounced in the case of the compounds with a filling of  $n = 5.5$  electrons per Fe-shell, which are closer to the half-filled case, this is, those containing K, Rb and Cs. In the case of  $\text{BaFe}_2\text{As}_2$ , with  $n = 6.0$ , the mass renormalizations are less pronounced, nevertheless, they are also present in the system and they help to describe properly quantities like ARPES spectra or the Sommerfeld coefficient. All these quantities go through the crossover between a normal and a Hund's metal, that happens around  $U = 2.5 \div 2.7$  eV depending on the density of the compound. This crossover is more pronounced for the case of lower densities. All the phenomena described here coincides with what has been presented in Section 3.3.

#### 4.3.1 Study of Van Hove singularities in $\text{KFe}_2\text{As}_2$

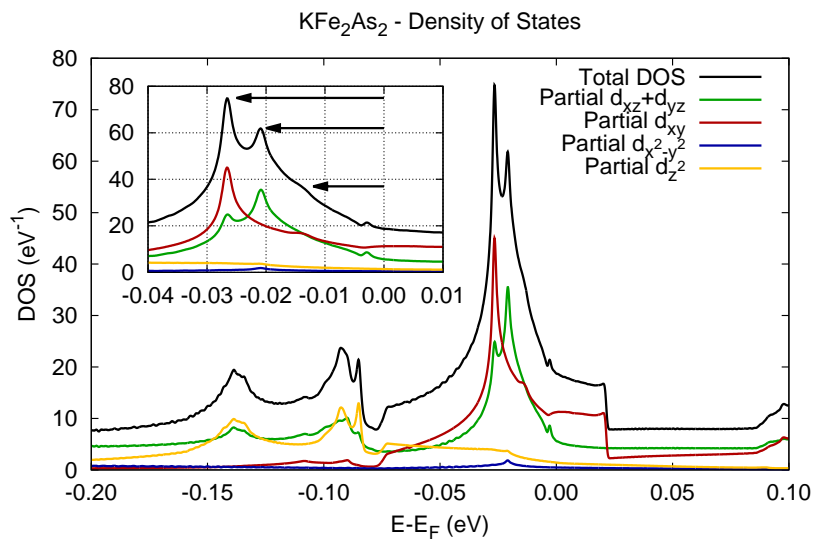


**Figure 4.5:** Total and orbitally-resolved DOS for the renormalized band structure of  $\text{KFe}_2\text{As}_2$  calculated with a DFT+SSMFT scheme around the Fermi level. The values of the interaction parameters in this case are  $U = 2.7$  eV and  $J/U = 0.25$ . The inset shows a detail of three possible Van Hove singularities.

We now compare a realistic calculation for  $\text{KFe}_2\text{As}_2$  (with values of the local interactions of  $U = 2.7$  eV and  $J/U = 0.25$ ) with some of these data from ARPES

measurements. 3 VHS are present in the ARPES maps of  $\text{KFe}_2\text{As}_2$  at 14.5 meV, 21 meV and 32 meV<sup>2</sup> and we want to show how the DFT+SSMFT scheme can be used to track the position of the VHS.

In Fig. 4.5 we plot a zoom of the quasiparticle density of states which corresponds to the renormalized band structure displayed in Fig. 4.3b, where we can observe the presence of a big enhancement in the spectrum roughly around 15-25 meV which displays a 3-peak structure, whose main contributions can be resolved orbital by orbital within this method (partial DOS are shown in colored lines in Fig. 4.5). We first test the method's sensitivity with respect to small variations of the lattice parameters. These can influence the energy splitting among the different orbitals and thus on their individual filling, which is a critical ingredient when determining the degree of correlation in Hund's metals. We test the position of these 3 peaks in the DOS against several sets of lattice parameters for  $\text{KFe}_2\text{As}_2$  available in the literature.

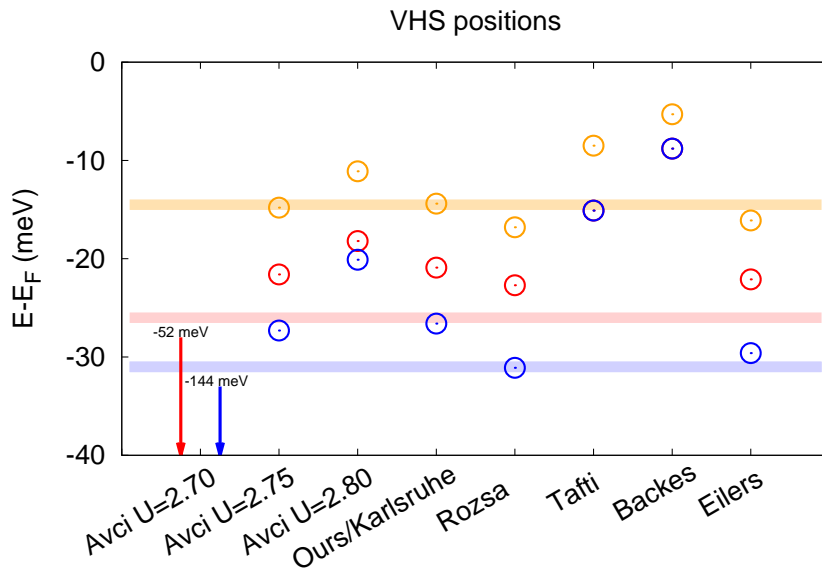


**Figure 4.6:** Positions in energy of the 3 peaks seen in the densities of states of the electronic structures obtained for each set of lattice parameters. These values have been obtained from Refs. [40, 142, 143, 144, 145] and are compiled in Table F.1. The horizontal color lines correspond to the position of the peaks in the EDC curves measured by ARPES.

In Fig. 4.6 we show a compilation of the position of these 3 peaks in the DOS for the different sets of lattice parameters compared with their experimentally reported positions at 14.5 meV, 21 meV and 32 meV (colored horizontal lines). The orbital content of these peaks can be determined with our method, and in this case the main weights correspond to:  $d_{xy}$  for the yellow peak,  $d_{xz/yz}$  for the red peak, and  $d_{xy}$

<sup>2</sup>These values have been provided in private communications with S. L. Dreschler and S. Borisenko, and the VHS at 14.5 meV has been reported in Ref. [139]

again for the blue peak. We have also checked that these peaks correspond with the presence of some flat parts in the renormalized band structure. There is a fourth small peak very close to the Fermi level (around 2~3 meV) with mixed character.

The calculations with the lattice parameters that we use along the manuscript (provided by the group in Karlsruhe) show a peak distribution which is almost identical to that obtained using the lattice structure parameters reported by Eilers et al. [145], and also to that obtained using the lattice parameters measured in Ref. [142]. Also, if we use the lattice parameters from Avci et al. [40], the results are also very close but we must use a slightly higher value of the local Coulomb repulsion of  $U = 2.75$  eV instead of the usual  $U = 2.70$  eV in order to reach the orbitally-decoupled regime in which the effective masses start to differ strongly. This can be easily explained since the lattice parameters from Ref. [40] are slightly contracted compared to those from Ref. [142] (and also to those provided by the Karlsruhe group) because they are taken at very low  $T = 1.7$  K. So with those we find slightly less correlated band structures. Calculations using the values extrapolated by us from Tafti et al. [143] and those used in Ref. [144] turn into much more correlated electronic structures. A more detailed discussion on the origin of these differences can be found in Appendix F.

The general trends found here are clear. There is large enhancement in the DOS around 15-25 meV with a 3-peak structure that is well captured in our realistic simulations of  $\text{KFe}_2\text{As}_2$  with the DFT+SSMFT method. We believe that the peak around  $\sim 14.5$  meV (with an important  $d_{xz/yz}$  character) could be compatible with the position of that VHS reported in Ref. [139].

#### 4.4 DMFT study of the influence of Van Hove singularities on correlations

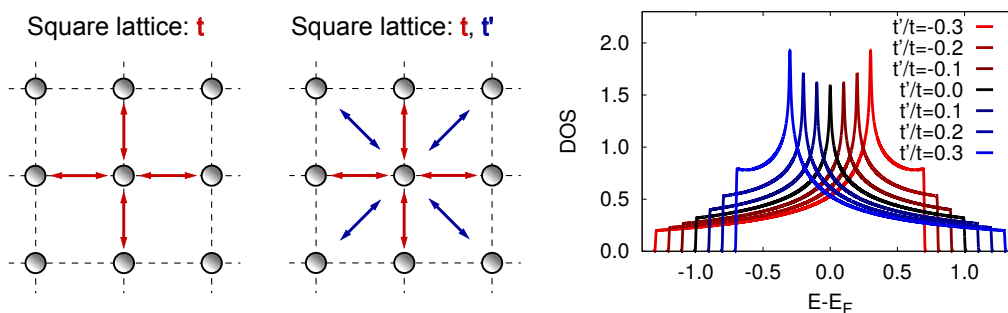


**Figure 4.7:** Scheme of a two-dimensional square lattice model with hopping parameters  $t$  between nearest-neighbor lattice sites and  $t'$  between second nearest-neighbors. The rightmost panel shows a series of non-interacting DOS for several values of the ratio  $t'/t$  at half filling (the Fermi level has been set to zero), calculated numerically.

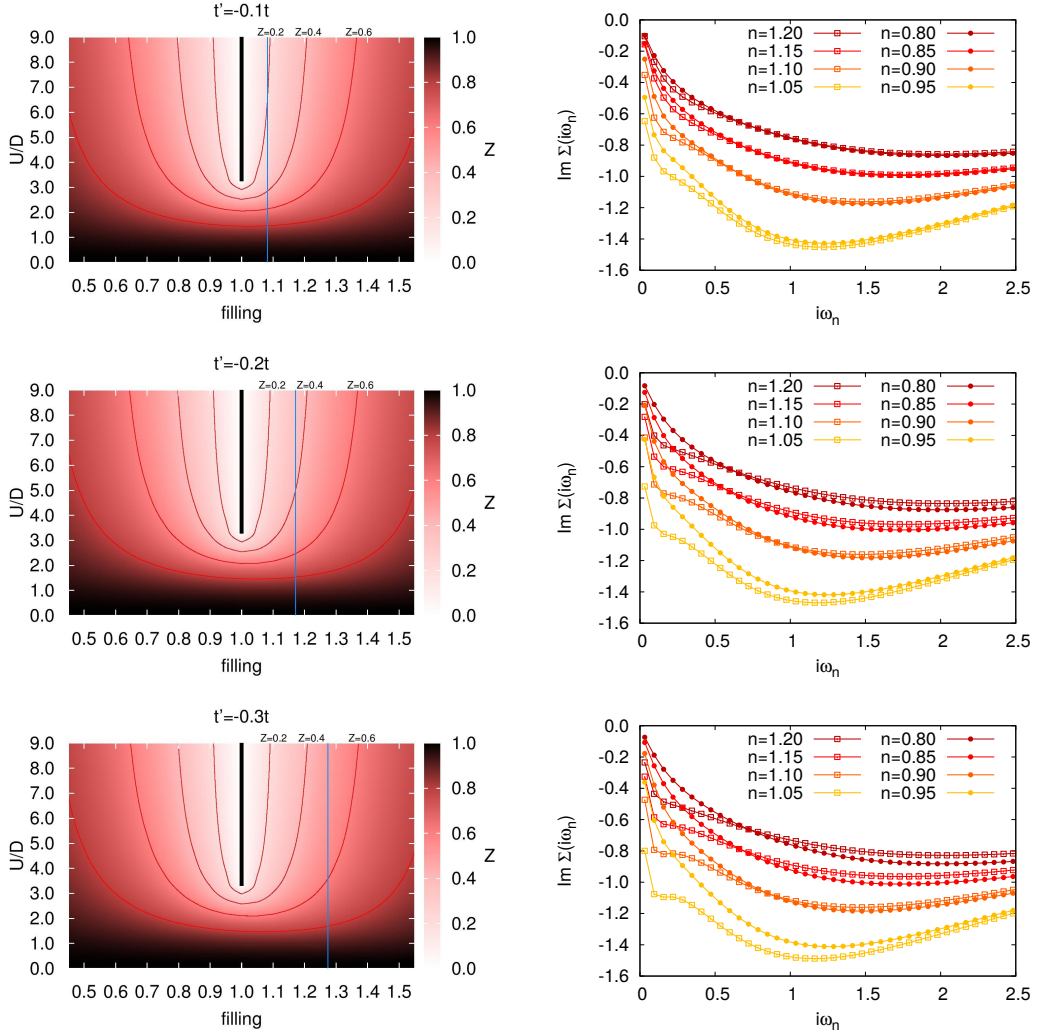


**Figure 4.8:** Left column: quasiparticle weight  $Z$  calculated with SSMFT as a function of density  $n$  and Coulomb interaction  $U$  for the square lattice for various second nearest-neighbor hoppings  $t'/t$ . The blue line represents the density at which the Van Hove singularity is located in each of the lattice models and the thick black lines signal the Mott insulating state. Right column: imaginary part of the self-energy calculated with DMFT for different densities and for the corresponding model on the left panels at  $U/D = 4.0$ .

After having investigated how correlations shift the position of VHS in a correlated system we now ask ourselves if the presence of a VHS in the bare DOS has a strong influence on the correlation strength, in particular if a VHS at the Fermi level suppresses strongly  $Z$ . For this we study a 2-dimensional square lattice with nearest- and second nearest-neighbor hoppings  $t$  and  $t'$  respectively. The bare DOS of such a system has a Van Hove singularity which is particle-hole symmetric for  $t'/t = 0$  but this symmetry is broken if one introduces second-nearest-neighbor hopping  $t'$  (Fig. 4.7 first two panels). The effect of this is to move this Van Hove singularity from its centered position, either to higher energies (negative values of

$t'/t$ ) or to lower energies (positive values of  $t'/t$ ), as it can be seen in the right panel in Fig. 4.7. The two DOS corresponding to the two possible values of  $|t'/t|$  are perfectly symmetric with respect to the particle-hole symmetric peak at  $t'/t = 0$ .

We performed DMFT calculations for this one-band model using exact diagonalization as an impurity solver with 4 states in the self-consistent bath. Green's functions have been computed along 512 Matsubara frequencies and the temperature is set by using  $\beta = 100$ . We adapt the self-consistent condition from eq. (2.84) to the following form:

$$\mathcal{G}_0^{-1}(i\omega_n) = \Sigma(i\omega_n) + \left[ \int d\epsilon \frac{D(\epsilon)}{i\omega_n + \mu - \epsilon - \Sigma(i\omega_n)} \right]^{-1}, \quad (4.1)$$

where in this case we are using a numerically calculated density of states  $D(\epsilon)$  of this 2-dimensional lattice model, one for each value of  $t, t'$ . SSMFT calculations are done using the tight-binding expression of those lattice models and using the general description presented in Section 2.3.

In Fig. 4.8 we plot different color maps of the quasiparticle weight as a function of the density  $n$  and the Coulomb interaction  $U/D$  for different values of  $t'/t$ . One can observe that there is a small asymmetry in the quasiparticle weight in these phase diagrams that increases with the asymmetry of the non-interacting DOS, this is, with the value of  $|t'/t|^3$ . However, there are no sharp features around the corresponding density in which the Van Hove singularity is located (represented by the blue lines in Figs. 4.8).

The position of the VHS for a given value of  $t'/t$  will always occur at the same density  $n$ . This can be shown by looking at how the quasiparticle DOS is renormalized in SSMFT. In a paramagnetic system we can define a general DOS like

$$D(\epsilon) = \frac{1}{V} \sum_{\vec{k}} \delta(\epsilon - \epsilon_{\vec{k}}). \quad (4.2)$$

Now, the quasiparticle DOS  $D^*(\epsilon)$  (with its own dispersion relation  $\tilde{\epsilon}_{\vec{k}}$ ) can be related to the non-interacting DOS of the system  $D(\epsilon)$  (with the dispersion relation  $\epsilon_{\vec{k}}$ ). One

---

<sup>3</sup>We have only plotted the color maps for  $t'/t$  negative, which locates the Van Hove singularity at a density larger than half filling. The corresponding maps for positive values of  $t'/t$  would be the mirror images of the plotted maps with respect to the half-filled density. Several cuts of these color maps along different densities are shown in Appendix F.2.

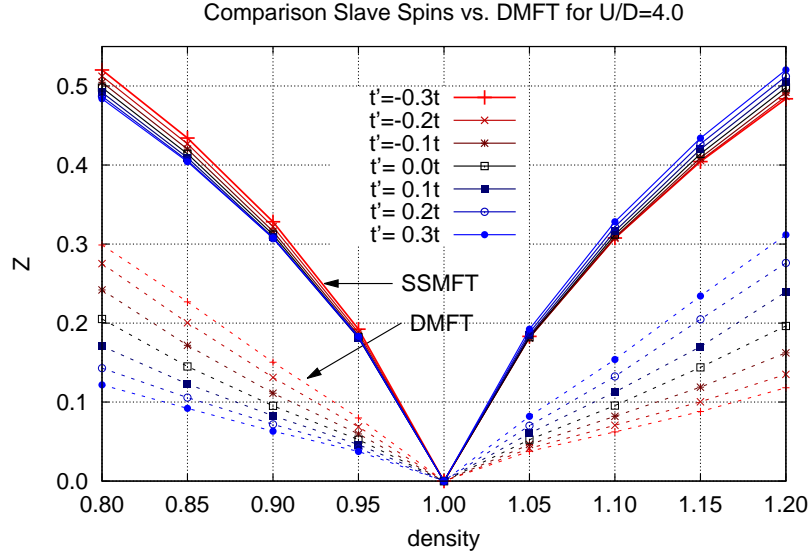


**Figure 4.9:** Quasiparticle weight  $Z$  as a function of the electron density  $n$  for a square lattice model calculated with SSMFT (solid lines) and with DMFT (dotted lines) at  $U/D = 4.0$  for different values of  $t'/t$ .

can expand<sup>4</sup>

$$\begin{aligned}
 D^*(\epsilon) &= \frac{1}{V} \sum_{\vec{k}} \delta(\epsilon - \tilde{\epsilon}_{\vec{k}}) = \frac{1}{V} \sum_{\vec{k}} \delta(\epsilon - Z\epsilon_{\vec{k}} + \lambda) \\
 &= \frac{1}{V} \sum_{\vec{k}} \frac{\delta(\epsilon_{\vec{k}} - (\epsilon + \lambda)/Z)}{|-Z|} = \frac{1}{Z} \frac{1}{V} \sum_{\vec{k}} \delta(\epsilon_{\vec{k}} - (\epsilon + \lambda)/Z) \quad (4.3) \\
 &= \frac{1}{Z} D((\epsilon + \lambda)/Z).
 \end{aligned}$$

The renormalized quasiparticle DOS is an exact copy of the bare DOS multiplied by a factor  $1/Z$  in which the energy dependence is rescaled by a factor  $1/Z$  and shifted by  $\lambda/Z$ . In this 1-band case, this means that the shape of the DOS will not be modified apart from a constant multiplicative factor and a rescale of the energies. One can also see that this implies that the position of the VHS will occur always for the same density for each value of  $t'/t$  no matter the interaction strength. Given that the number of quasiparticles in the system has to be the same than the number of particles due to Luttinger's theorem, this sum rule  $n_{QP} = \int_{-\infty}^{\mu} D^*(\epsilon) d\epsilon$  always holds and since the shape of  $D^*$  is the same as that of  $D$ , then the former integral up to the energy of the position of the VHS  $\epsilon_{VHS}$  will always yield the same density

<sup>4</sup>We have used  $\delta(f(x)) = \sum_{x_0} \frac{\delta(x)}{|f'(x_0)|}$ , where  $x_0$  are the zeros of  $f(x)$ .

$n_{VHS}$ .

In Fig. 4.9 we show cuts of the quasiparticle weights plotted in Fig. 4.8 at  $U/D = 4.0$ . The effect of the asymmetry between particles and holes is clearly seen, and also how the two values of  $|t'/t|$  are absolutely equivalent. The quasiparticle weights in this case are calculated from the self-energies displayed in the right-panels in Fig. 4.8, in which this asymmetry is also present. However, there is no signature of the presence of the VHS. This could appear like a sudden decrease of the quasiparticle weight around the density in which they are located. Despite the existence of that asymmetry in both methods, the quasiparticle weights calculated with DMFT and SSMFT are different. This is due to the fact that in the 1-band case, SSMFT is known to not reproduce perfectly the results for DMFT, in particular close to the Mott transition.

In summary, SSMFT and DMFT simulations show no signature of the presence of the Van Hove singularity in the system in the interaction-doping plane in a 1-band Hubbard model. There is only certain asymmetry in the quasiparticle weight in this interaction-doping phase diagram, which can be easily explained due to the asymmetry of the kinetic energy of holes and electrons and this asymmetry evolves among the different models depending on the value of  $t'/t$ . A similar result has been found in a multi-orbital model with finite Hund's coupling  $J/U \neq 0$  [146].

## 4.5 d-electron heavy-fermions in IBSC

In this section we show the calculated Sommerfeld coefficient and thermoelectric power (or Seebeck coefficient) of our realistic simulations of the 122 family of IBSC, and that these quantities display a behavior that is consistent with the general phenomenology of heavy fermions.

In Fig. 4.10 we show the Sommerfeld coefficient of  $\text{KFe}_2\text{As}_2$  and its isovalent analogues  $\text{RbFe}_2\text{As}_2$  and  $\text{CsFe}_2\text{As}_2$  as a function of hole doping. These values are very big, and could be considered already as typical of heavy-fermion compounds. By hole-doping this system, in principle, one can further increase the degree of correlations, thus have even larger quasiparticle weights which will translate into a larger quasiparticle DOS at the Fermi level, and thus in a larger Sommerfeld coefficient. In our SSMFT simulations, we hypothetically reach values over  $1000 \text{ mJ mol}^{-1} \text{ K}^{-2}$  for hole-doped  $\text{CsFe}_2\text{As}_2$ .

Preliminary experimental results (Hardy et al. unpublished) displayed in Fig. 4.11 show a consistent trend with our calculations. The Sommerfeld coefficient, here the linear extrapolation of the normal phase to zero temperature, for Cr-doped  $\text{CsFe}_2\text{As}_2$  (Cr introduces 2 holes per atom) is enhanced compared to the stoichiometric compound, and thus it is plausible that as long as there is no phase transition, one can reach higher values of the Sommerfeld coefficient if further hole-doping can be reached. The fabrication of these single-crystal samples turned out to

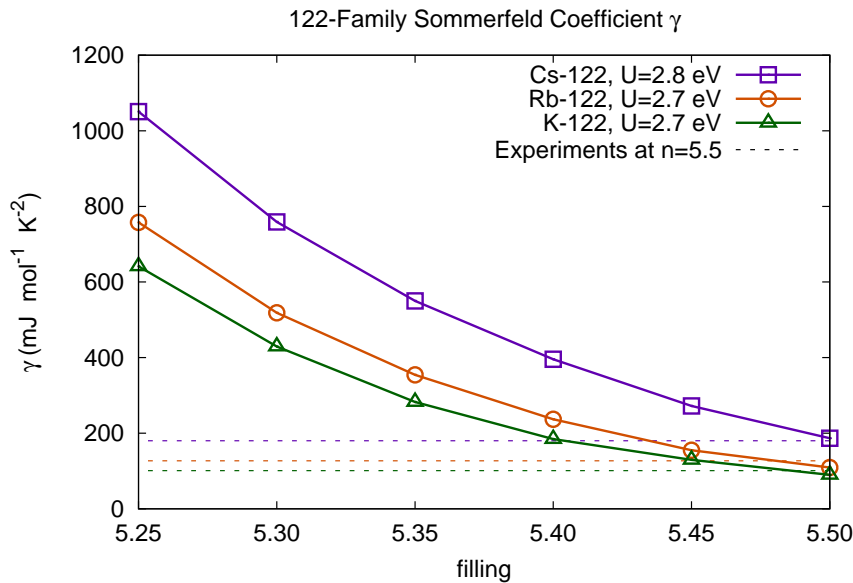


**Figure 4.10:** Calculated Sommerfeld coefficient for hole-doped  $\text{KFe}_2\text{As}_2$ ,  $\text{RbFe}_2\text{As}_2$  and  $\text{CsFe}_2\text{As}_2$  as a function of the electron density  $n$  at the optimal value of the local Coulomb interaction  $U$  and for a Hund’s coupling of  $J/U = 0.25$ . The dotted lines correspond to the experimental values for the stoichiometric compounds from Ref. [20].

be challenging from the chemistry viewpoint, and at present only 2% Cr-doping (thus 4% hole-doping) could be reached. As shown in Fig. 4.11 the Sommerfeld coefficient for these 2%-doped samples is already enhanced by 40% of its stoichiometric value of  $\gamma \sim 180 \text{ mJ mol}^{-1} \text{ K}^{-2}$ , thus reaching an impressive value of  $\gamma \sim 250 \text{ mJ mol}^{-1} \text{ K}^{-2}$ . We are waiting for further experimental confirmation of these trends.

The different correlated character of the stoichiometric compounds at  $n = 5.5$  of the 122 family can be tracked by several quantities that we show in Fig. 4.4. In particular, this can clearly be seen in Fig. 4.12, where we show the local magnetic moments in the paramagnetic phase of  $\text{BaFe}_2\text{As}_2$  ( $n = 6.0$ ) and of  $\text{KFe}_2\text{As}_2$ ,  $\text{RbFe}_2\text{As}_2$  and  $\text{CsFe}_2\text{As}_2$  ( $n = 5.5$ , and for the last case also for  $n = 5.4 - 5.3$ ) as a function of the local Coulomb interaction  $U$ . We clearly see how the crossover between a normal- to a Hund’s-metal happens first for Cs-122, then, Rb-122 and finally for K-122. Assuming that the value of  $U$  can be kept fixed for this compounds<sup>5</sup>  $\text{CsFe}_2\text{As}_2$  would be more deeply in the Hund’s metal regime, i.e. more correlated, and this would correspond to a larger mass enhancement and orbital differentiation and in principle to a larger quasiparticle DOS at the Fermi level, which in a Fermi liquid is proportional to the Sommerfeld coefficient.

This can be understood as a direct effect of the negative pressure induced by this chemical substitution. It reduces the average kinetic energy and thus the Hund’s metal phase will appear at a lower value of the interaction parameter  $U$  keeping

<sup>5</sup>Even if we had chosen a value of  $U = 2.7 \text{ eV}$  for  $\text{CsFe}_2\text{As}_2$ , the following discussion will hold.

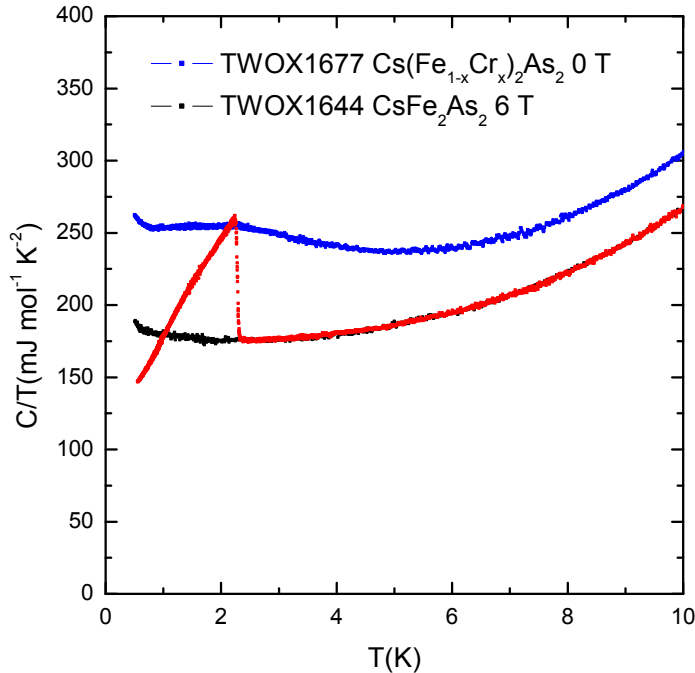


**Figure 4.11:** Experimental measurement of the specific heat for stoichiometric  $\text{CsFe}_2\text{As}_2$  (red points for zero magnetic field and black points for a magnetic field of 6 T) and for  $\text{Cs}(\text{Fe}_{1-x}\text{Cr}_x)_2\text{As}_2$  with an estimated Cr content of  $\sim 2\%$  at zero magnetic field (blue points). as a function of temperature.

$J/U$  fixed. However, this is just a minor effect and one can further increase the degree of correlation with hole doping as it can be seen in by the behavior of the total local magnetic moment in hole-doped  $\text{CsFe}_2\text{As}_2$  in Fig. 4.12. They clearly indicate an increased degree of correlation in those systems (thus implying heavier quasiparticles) which is reflected in the largely enhanced values of the Sommerfeld coefficient displayed in Fig. 4.10.

The values of the Sommerfeld coefficient for these stoichiometric compounds are in perfect correspondence with those obtained in Ref. [20], which have been obtained using a different DFT prescription as it is done in the software package QUANTUM ESPRESSO [106]<sup>6</sup>, thus proving their robustness.

In Fig. 4.13 the Seebeck coefficient in the  $ab$ -plane for  $\text{KFe}_2\text{As}_2$  is shown. Superimposed we have also calculated the thermoelectric power in this  $ab$ -plane from Boltzmann Transport theory within the relaxation-time approximation out of a DFT+SSMFT scheme. The values of the slope at low temperature are very much in the heavy-fermionic range, and after a temperature of  $\sim 50$  K, this dependence is not

<sup>6</sup>We have also made tests with this DFT software package, but we decided to stick to WIEN2K.

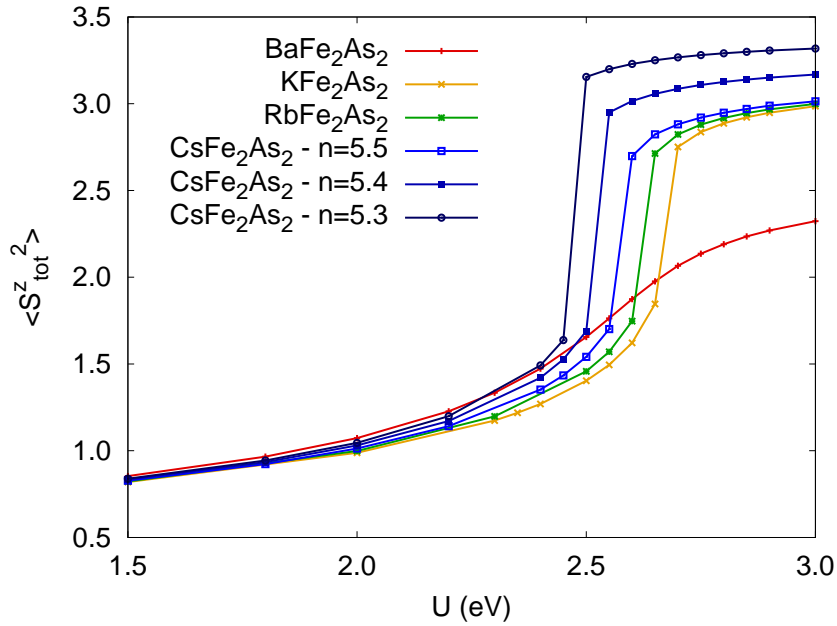


**Figure 4.12:** Total local magnetic moment  $\langle S_{tot}^z \rangle$  for  $\text{BaFe}_2\text{As}_2$ ,  $\text{KFe}_2\text{As}_2$ ,  $\text{RbFe}_2\text{As}_2$  and stoichiometric and hole-doped  $\text{CsFe}_2\text{As}_2$  as a function of the local Coulomb interaction  $U$  for a value of Hund's coupling of  $J/U = 0.25$ .

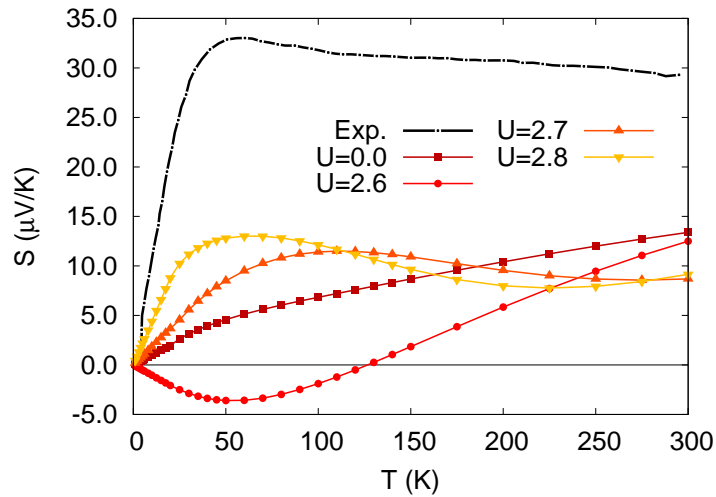


**Figure 4.13:** Experimental Seebeck coefficient in the  $ab$ -plane for  $\text{KFe}_2\text{As}_2$  from Ref. [136, 147]) as a function of temperature, and the calculated value with Boltzmann transport equation from a DFT+SSMFT scheme for several values of  $U$ .

linear anymore, being this crossover again consistent with the crossover observed in Ref. [19].

We have done calculations of the Seebeck coefficient following the Boltzmann

transport equation (BTE) within the relaxation time approximation (RTA). The transport coefficients have been calculated both in the non-interacting case ( $U = 0$ ) and as a function of the local Coulomb interaction ( $U \neq 0$ ). In the former case, we have used the software package BOLTZTRAP [148], which is interfaced with the DFT code WIEN2K, whereas in the later we have used a code implemented in FORTRAN applied to the fermionic model with renormalized hopping integrals of the form of eq. (2.64) that is obtained as a result of the SSMFT calculation. This has been tested to coincide with the WIEN2K+BOLTZTRAP calculation when  $U = 0$ . A detailed derivation of the equations used for these transport calculations can be found in Appendix C.

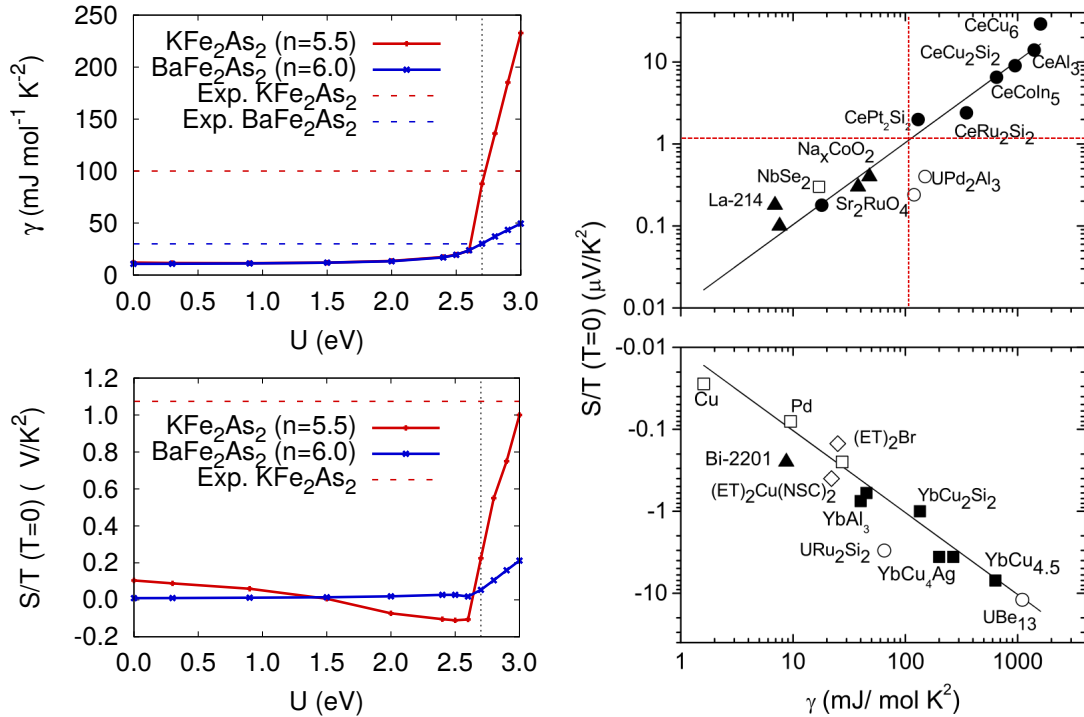


**Figure 4.14:** Sommerfeld coefficient (left-upper panel) and low-temperature slope of the Seebeck coefficient in the  $ab$ -plane (left-lower panel) of  $\text{BaFe}_2\text{As}_2$  and  $\text{KFe}_2\text{As}_2$  as a function of  $U$ , for  $J/U = 0.25$ , calculated with the Boltzmann transport equations from the renormalized band structure computed using a DFT+SSMFT scheme. The dotted lines corresponds to the experimental measurements for  $\text{KFe}_2\text{As}_2$  from Refs. [136, 20]. Behnia-Jaccard-Flouquet plot from Ref. [149] for different heavy fermionic compounds (right panels) and in red dotted lines the corresponding position of the experimental values of  $\text{KFe}_2\text{As}_2$ .

The first noticeable result is how bad is the prediction from the DFT band structure, which is only able to capture the sign of the Seebeck coefficient. However, the magnitude is around one order of magnitude smaller. We partially solved this issue including many-body correlations. In lower-left panel in Fig. 4.14 we show the slope of the Seebeck coefficient at low temperature as a function of the local Coulomb interaction  $U$  for  $\text{BaFe}_2\text{As}_2$  and  $\text{KFe}_2\text{As}_2$ . One can see how once the value

of  $U$  reaches that of the Hund's-metal crossover, the slope starts to increase suddenly, but it does it in a much faster way for the case of  $\text{KFe}_2\text{As}_2$ , which can be understood by the closer proximity of this compound to the absolute half-filled case of  $n = 5.0$ . The intermediate negative values of that slope are immediately explained by looking at the slope of the transport distribution function at the chemical potential, which in the low temperature phase is proportional to minus the slope of the Seebeck coefficient (derivation in Appendix C). We thus provide a method that allows to calculate the thermoelectric power with a higher precision than just plain DFT for these type of materials.

However, the agreement is far from being perfect. Here we explain why. In the low-temperature part, one can show that, at least for the 1 band case in our formalism one can write

$$\left. \frac{S}{T} \right|_{T \rightarrow 0} \propto -\frac{1}{Z} \frac{\Xi'(\tilde{\mu})}{\Xi(\tilde{\mu})} \quad (4.4)$$

where  $Z$  is the quasiparticle weight and  $\Xi(\tilde{\mu})$  is the transport distribution function evaluated at the chemical potential of the renormalized band structure. One would expect that in the case of a renormalized Fermi liquid, the enhancement compared to the DFT result would be proportional to the mass enhancement, however,  $\Xi$  evolves with  $U$  and for the relevant value of the interaction parameter, we find that there is a minimum in that function very close to the chemical potential and even though there is a big particle-hole asymmetry which will contribute at larger temperatures, in this particular case the compound is found around that minimum, thus the correct description of this transport distribution function is key<sup>7</sup>. Here we give a number of reasons why this function may not be perfectly reproduced in our simulations:

- It is well known that the Fermi surface is not well reproduced in the realistic simulations, in particular the size of the hole and electron pockets in experimental measurements is shrunk compared to the theoretical predictions<sup>8</sup>. This happens not only at a DFT level, but also when including correlations, and it is thought to be induced by non-local self-energy effects [150, 151]. This effect is known in the literature like “red-blue shifts”, because it looks like if the measured electron-pockets are shifted upwards in energy and hole-pockets downwards compared to the theoretical predictions [152], and can have a direct influence in all transport calculations and in general in all calculations strongly dependent on details of the fermiology.
- In our approach we assume a constant relaxation time. This approximation which works in many cases can be insufficient in this case. In particular,

---

<sup>7</sup>We have assumed an average value of the transport coefficients from the 3 crystallographic directions which can be also a big source of error. Further analysis in the right crystallographic directions show an identical shape of  $\Xi$  with a multiplicative factor in front. This, which has an influence in the conductivity, leaves untouched the value for the low-temperature slope of the Seebeck coefficient according to expression (4.4).

<sup>8</sup>See Ref. [56] and the references therein for a more detailed discussion.

depending on the scattering mechanisms in the system, there will be different dependences of this relaxation time with the energy  $\tau \propto \epsilon^r$ , where  $r$  can be  $-1/2$  if the scattering occurs with acoustic phonons or  $3/2$  if the scattering happens with ionized impurities [153]. This relaxation time can be assumed also to be equal to the lifetime of the quasiparticles in a Fermi liquid, in which case  $\tau_{QP} \propto (\epsilon^2 + \pi^2 T^2)^{-1}$  [154].

- It has been shown in DMFT calculations [155] how there are contributing terms beyond the Fermi-liquid  $\omega^2$ -dependence of the scattering rate coming from particle-hole asymmetry that have to be taken into account in the transport coefficients. In particular, in the case of ruthenates these may have some relevance [156] and may also play an important role in the case of IBSC. These terms are not considered in the semi-classical Boltzmann transport formalism that we use here.
- The effect of interactions in a Fermi liquid not only manifests itself in the renormalized quasiparticle energies but also in renormalized quasiparticle interaction vertices. In particular these vertex corrections matter in the transport quantities. For instance, the observed Drude weight reads  $D_{obs} = D_{QP}(1 + F_{1s}/d)$  [157], where  $D_{QP}$  is the calculated Drude weight with the renormalized quasiparticle velocities,  $F_{1s}$  is a Landau parameter and  $d$  the dimensionality. In a translational invariant system, given that  $D_{QP} = D_{bare}/(m^*/m)$  and  $1 + F_{1s}/d = m^*/m$ , one will have at the end that  $D_{obs} = D_{bare}$ , despite the presence of heavy renormalized quasiparticles in the system. However, it can be shown [67] that in momentum-independent self-energy approaches like DMFT or the one used here (SSMFT),  $F_{1s}$  is strictly zero, and thus this factor, which is sizeable in heavy fermionic materials [158], is missing in our case.
- There may also be a non-negligible entropy contribution to the thermopower coming from the localization of the electrons. However, we expect this contribution to happen after the coherence-incoherence crossover temperature which for this compounds is around  $\sim 50$  K [19]. This contributions have been proven to be relevant when the transport is dominated by interacting localized charge carriers [159].

In the upper-left panel of Fig. 4.14 we show the Sommerfeld coefficient as a function of the local Coulomb interaction  $U$  for  $\text{BaFe}_2\text{As}_2$  and for  $\text{KFe}_2\text{As}_2$ , which correspond to an electron density of  $n = 6.0$  and  $n = 5.5$  respectively. We also plot their corresponding experimental values (dotted lines), which are  $\gamma \sim 100 \text{ mJ mol}^{-1} \text{ K}^{-2}$  for  $\text{KFe}_2\text{As}_2$  and  $\gamma \sim 30 \text{ mJ mol}^{-1} \text{ K}^{-2}$  for  $\text{BaFe}_2\text{As}_2$ <sup>9</sup>, extracted from Ref. [20].

---

<sup>9</sup>This value corresponds to an extrapolation from the high-temperature non-magnetic phase, since  $\text{BaFe}_2\text{As}_2$  at low temperature shows anti-ferromagnetic order.

The value at  $U = 0$  eV for these two compounds (that is not plotted here) and that corresponds to the band structure calculated with DFT is far from the experimental value and is around  $\gamma \sim 12 - 14$  mJ mol<sup>-1</sup> K<sup>-2</sup> for both compounds. As we turn on the interaction we can see how the value of the Sommerfeld coefficient does not get modified significantly until we reach values around  $U = 2.5$  eV (which coincides with the entrance in the Hund's-metal phase), after which both compounds start to differ enormously. In the case of BaFe<sub>2</sub>As<sub>2</sub>, which contains on average 6 electrons per Fe-3d shell, the Sommerfeld coefficient starts to increase and at a value of  $U = 2.7$  eV (our pre-set value for this compound) one reaches the experimental value. Interestingly, for KFe<sub>2</sub>As<sub>2</sub> in which one can assume that the Coulomb interaction will not be different, the Sommerfeld coefficient starts to increase a much greater rate than for its Ba analogue. This can be easily explained by its different electron count, which in this case is of  $n = 5.5$  and thus closer to the half-filled case. The direct effect of this is a larger degree of correlations.

Given that the behavior with  $U$  of the slope of the Seebeck coefficient behaves in an analogous manner, and displays the same build-up than the mass enhancements, it is natural to think that this heavy-fermionic behavior seen in the 122 family, but more concrete here in the case of KFe<sub>2</sub>As<sub>2</sub>, can be attributed to the effect of Hund's coupling  $J$  in those systems. It generates different quasiparticle weights for the different orbitals thanks to the existing crystal-field splitting that populates differently each of them, and causes that there is some coexistence of heavy and light electrons, in a similar fashion to the usual heavy fermionic  $f$ -electron materials. All in all, with these values of the Sommerfeld coefficient and the low-temperature slope of the thermoelectric power, we can try to locate these compounds in the well known Behnia-Jaccard-Flouquet phase diagrams [149], as we have done for KFe<sub>2</sub>As<sub>2</sub> in the right panel of Fig. 4.14. We see that this compound would perfectly fit in this category of heavy-fermionic materials (and obviously follow the universal scaling of a Fermi liquid, signaled by the diagonal black line in that plot).

## 4.6 Summary and conclusions

In summary, we have modeled the 122 family of IBSC in their low-temperature tetragonal phase within a DFT+SSMFT framework. Our results show that for the case of KFe<sub>2</sub>As<sub>2</sub> the main features of the quasiparticle electronic structure are captured by this technique. The sensitivity of that scheme to subtle changes in the lattice parameters is also studied. The positions of the Van Hove singularities seen by ARPES experiments are reasonably captured as well as the value of the experimental Sommerfeld coefficient.

The proximity of this large peak in the DOS to the Fermi level and its possible influence in the quasiparticles of the system is analyzed by means of a 2-dimensional 1-band Hubbard model with nearest and second nearest-neighbor hopping solved

both with DMFT and with SSMFT. The results show no signature of the Van Hove singularity in the quasiparticle weight at any density.

Finally, the possible heavy-fermionic behavior is studied in the 122 family. The Sommerfeld coefficient is calculated for the case of  $\text{KFe}_2\text{As}_2$  and for the isovalent equivalents of  $\text{K} \longleftrightarrow \text{Rb, Cs}$ . Our simulations show a drastic enhancement of that quantity when the system is hole-doped. This behavior is precisely found by experimental measurements in hole-doped  $\text{CsFe}_2\text{As}_2$ , of which we report here preliminary results. The experimental thermoelectric power in the  $(\text{Ba/K})\text{Fe}_2\text{As}_2$  system shows similar trends. Compared to DFT, we provide an improved (although not perfect) description of this quantity using a DFT+SSMFT+BTE scheme. We conclude that,  $\text{KFe}_2\text{As}_2$  shows a behavior similar to those of “classical” heavy fermions and that it can be quite correctly described using Slave-Spins.

## 4.7 Résumé et conclusions

En résumé, nous avons modélisé la famille 122 des IBSC dans leur phase tétragonale à basse température dans un cadre DFT+SSMFT. Nos résultats montrent que dans le cas de  $\text{KFe}_2\text{As}_2$  les principales caractéristiques de la structure électronique des quasiparticules sont capturées par cette technique. La sensibilité de ce schéma à des modifications subtiles des paramètres structurales est également étudiée. Les positions des singularités de Van Hove vues par les expériences ARPES sont raisonnablement capturées, ainsi que la valeur expérimental du coefficient de Sommerfeld.

La proximité de ce grand pic dans la DOS au niveau de Fermi et son influence possible sur les quasiparticules du système sont analysées en utilisant d’un modèle Hubbard bidimensionnel à 1 bande résolu avec DMFT et SSMFT. Les résultats ne montrent aucune signature de la singularité de Van Hove dans le poids de quasiparticule à toute densité.

Enfin, le possible comportement de fermion lourd est étudié dans la famille 122. Le coefficient de Sommerfeld est calculé pour le cas de  $\text{KFe}_2\text{As}_2$  et pour ses équivalents isovalents  $\text{K} \longleftrightarrow \text{Rb, Cs}$ . Nos simulations montrent une augmentation drastique de cette quantité lorsque le système est dopé par trous. Ce comportement a été trouvé par des mesures expérimentales en  $\text{CsFe}_2\text{As}_2$  dopé par trous. Dont nous montrons ici des résultats préliminaires. Le pouvoir thermoélectrique expérimental dans le système  $(\text{Ba/K})\text{Fe}_2\text{As}_2$  montre des tendances similaires. Par rapport à la DFT, nous fournissons une description améliorée (bien que pas parfaite) de cette quantité en utilisant un schéma DFT+SSMFT+BTE. Nous concluons que  $\text{KFe}_2\text{As}_2$  présente un comportement similaire à ceux des fermions lourds “classiques” et qu’il peut être partiellement décrit de façon assez correcte en utilisant Slave-Spins.



# 5

## Electronic compressibility in FeSe

In this chapter we study the compressibility of the conduction electrons in both bulk orthorhombic FeSe and mono-layer FeSe on SrTiO<sub>3</sub> substrate within a DFT+SSMFT scheme. The results show that there is a zone of enhancement of the electronic compressibility present in the interaction-doping phase diagram of these compounds that departs from a Mott insulator at half filling. This is in accord with previous simulations on IBSC, in particular BaFe<sub>2</sub>As<sub>2</sub> [130] and in general with the phenomenology of Hund's metals, whose main features are also present in the case of FeSe. We find that at ambient pressure FeSe is found slightly away from the zone with enhanced compressibility but increasing hydrostatic pressure moves it into it. In the case of mono-layer FeSe the stronger enhancement region is realized on the electron-doped side. These findings correlate positively with the enhancement of superconductivity seen in experiments, and support the possibility that many-body correlations induced by Hund's coupling may boost superconductive pairing when the system is at the frontier of the normal- to Hund's-metal crossover. The main results of this chapter are published in Ref. [160].

---

Dans ce chapitre, nous étudions la compressibilité des électrons de conduction en FeSe orthorhombique et FeSe monocouche sur un substrat de SrTiO<sub>3</sub> avec un schéma DFT+SSMFT. Les résultats montrent qu'il existe une zone d'augmentation de la compressibilité électronique présente dans le diagramme des phases interaction-dopage de ces composés, qui part d'un isolant Mott à demi-remplissage. Ceci est en accord avec des simulations précédentes sur IBSC, en particulier BaFe<sub>2</sub>As<sub>2</sub> [130] et en général avec la phénoménologie des métaux de Hund, dont les caractéristiques principales sont également présentes dans le cas du FeSe. Nous trouvons que, à la pression ambiante, FeSe se trouve légèrement à l'écart de la zone à compressibilité augmentée mais la pression hydrostatique le déplace à son intérieur. Dans le cas de FeSe monocouche la région d'augmentation plus forte est réalisée du côté dopé en électrons. Ces résultats sont en corrélation positive avec l'augmentation de la supraconductivité vue dans les expériences et soutiennent la possibilité de que les corrélations multi-corps induites par le couplage de Hund peuvent renforcer l'appariement supraconducteur lorsque le système est à la frontière entre un métal normal et un métal de Hund. Les principaux résultats de ce chapitre sont publiés dans la Réf. [160].

## 5.1 The special case of FeSe

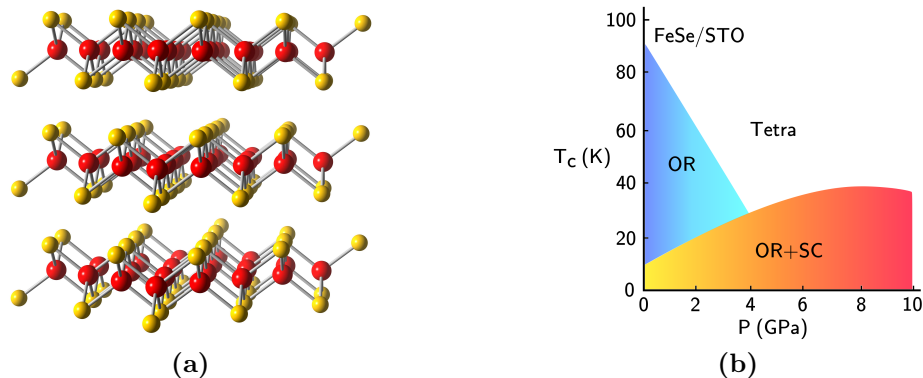


**Figure 5.1:** (a) One layer of FeSe. In red Fe atoms and in yellow the Se ligands. (b) A simplified phase diagram of FeSe. The superconducting critical temperature  $T_c$  is plotted as a function of hydrostatic pressure. The blue region corresponds to the so-called nematic phase, the orange region to the superconducting phase and in the high-temperature regime the compound is in a paramagnetic phase with a tetragonal crystal structure.

As we have discussed already, the origin of superconductivity in IBSC is not clear yet. One very much accepted scenario is motivated by the presence of long-range magnetic order (typically stripe anti-ferromagnetic order) in the parent compounds of many families of IBSC that is suppressed in favor of a superconducting phase when the compound is doped or put under pressure [35, 36, 37]. This suggests that the pairing mechanism could be mediated by spin fluctuations, or at least that they could play an important role [161]. However there exist notable exceptions to this phenomenology that pose serious questions about its general validity. The case of FeSe is one of the most striking ones since there is no long-range magnetic order in the parent compound at any temperature, only nematic order below 90 K [52]. Moreover, these spin fluctuations potentially responsible for the high- $T_c$  superconductivity arise quite naturally out of nesting between roughly equally-sized hole and electron Fermi pockets. These pockets are typically found in most of the band structures of IBSC calculated by DFT simulations, however FeSe/STO, which has the highest  $T_c$  of all IBSC appears to be electron doped [162], since ARPES measurements show only electron pockets but not hole pockets, making impossible this nesting and thus questioning the spin-fluctuation scenario in this material.

Correlations, which are neglected on DFT calculations are also a fundamental contribution to the physics of IBSC and need to be included in ab-initio realistic simulations [116, 120, 121, 122, 163, 164] to fit most experimental results. In particular Hund’s coupling, i.e. the intra-atomic exchange interaction, plays a fundamental role, so much that IBSC are considered a paradigm for “Hund’s metals” [79, 116], as described in Chapter 3. FeSe, as we will see, is not an exception, as it has been

discussed theoretically by DMFT studies [116, 120] and also due to some more recent spectroscopic evidences also supported theoretically [165, 166].

Recently [130] it was shown that an enhanced electronic compressibility (culminating in a divergence) ubiquitously accompanies the crossover between the Hund's metal and the normal metal in multi-orbital Hubbard models in presence of Hund's coupling. This crossover departs from the Mott transition that is found at half-filling at rather low interaction strength [115, 118, 122, 129] and extends to finite doping and larger interaction strengths. In a realistic simulation [130] of the "122" family of IBSC (BaFe<sub>2</sub>As<sub>2</sub> and similar compounds) the tip of this region of enhanced compressibility was shown to extend into the region where high-T<sub>c</sub> superconductivity and the other instabilities happen experimentally, and it was advanced that the enhanced quasiparticle interactions causing the enhanced electronic compressibility might also be the cause of enhancement of all the other instabilities, including superconductivity (in line with [132] and in the general framework of Refs. [134, 167, 168]). Here we show that the enhancement of the electronic compressibility is also found in a realistic simulation of FeSe under pressure and of electron-doped FeSe mono-layer on STO, which are the cases of maximum T<sub>c</sub> in chalcogenides, thus corroborating this suggestion.

## 5.2 Calculations of electronic compressibility

Like many other IBSC, FeSe has 5 bands of mainly Fe-3*d* character cross the Fermi level, with a total bandwidth around 4 eV. With this information and also given the importance of treating explicitly correlations, as it has been already mentioned, we model the conduction electrons in FeSe following a DFT+SSMFT scheme described in Section 2.5 with a 5-orbital Hubbard-Kanamori Hamiltonian. DFT calculations have been done using the software package WIEN2K [105], which in this case is used with the GGA-PBE exchange-correlation functional [140]. The parametrization of this band structure into a local basis is computed using the WANNIER90 code [78]. For the DFT calculations, the lattice parameters and atomic positions for the bulk in the orthorhombic phase (which is the one realized at low temperature in the range of pressures of interest here [51, 53, 169]) are taken from Ref. [53], and for the mono-layer we fix the *a* and *b* lattice parameters to those of STO (*a* = *b* = 3.905 Å) and *z*<sub>Se</sub> (the height of the ligand) is taken from Ref. [170]. These are summarized in Table 5.1.

For the second part of the model Hamiltonian that includes the many-body interaction term we choose *U* = 4.2 eV for FeSe (although several scans in *U* are performed) and we fix *J/U* = 0.2. These values are obtained by ab-initio constrained random-phase approximation (cRPA) calculations from Ref. [107].

As explained in Section 2.3, SSMFT allows to describe this low-temperature paramagnetic Fermi-liquid metallic phase of such a model with an effective quasi-

**Table 5.1:** Table of the different lattice parameters and relevant atomic positions of bulk FeSe at different pressures and for the mono-layer of FeSe on top of an STO substrate that have been used in our calculations. The space group is  $Cmma$  (67).

Compound	Ref.	$a(\text{\AA})$	$b(\text{\AA})$	$c(\text{\AA})$	$h_{Se}(\text{\AA})$
FeSe @ 0.0 GPa	[53]	5.3051	5.3294	5.4827	1.4518
FeSe @ 6.6 GPa	[53]	5.1122	5.1568	5.0824	1.4226
FeSe @ 9.0 GPa	[53]	5.0835	5.1126	5.0304	1.4281
FeSe/STO	[170]	$3.905 \times \sqrt{2}$	$3.905 \times \sqrt{2}$	-	1.241

particle Hamiltonian [66] of the form

$$\hat{\mathcal{H}}_{QP} = \sum_{i \neq j, m, m', \sigma} \sqrt{Z_m Z_{m'}} t_{ij}^{mm'} f_{im\sigma}^\dagger f_{jm'\sigma} + \sum_{i, m, \sigma} (\varepsilon_m - \lambda_m) \hat{n}_{im\sigma}^f, \quad (5.1)$$

where

$$f_{im\sigma}^\dagger = \sum_k e^{ik \cdot r_i} f_{km\sigma}^\dagger / \sqrt{\mathcal{N}_{sites}}, \quad (5.2)$$

and  $f_{km\sigma}^\dagger$  creates a quasiparticle with corresponding quantum numbers. The number of quasiparticles equals the number of particles owing to the Luttinger theorem and thus we can write

$$n_f \equiv \sum_{km\sigma} \langle f_{km\sigma}^\dagger f_{km\sigma} \rangle = \int^\mu d\varepsilon D^*(\varepsilon) = n, \quad (5.3)$$

where  $n$  is the average electron density.  $D^*(\varepsilon)$  is the renormalized (quasiparticle) density of states (DOS), and this renormalization due to the interaction term in eq. (2.89) in SSMFT is brought in by the factors  $Z_m$  (that act as inverse mass enhancements factors) and  $\lambda_m$  (that shift the on-site energy) that appear in eq. 5.1. These renormalization factors are calculated in a set of self-consistent mean-field equations that involve the auxiliary slave-spin variables [66], as described in Section 2.3, and they depend on all the physical parameters of the problem in a non-trivial way. This means that, for a given set of interaction parameters  $U$  and  $J$ , the quasiparticle model is not just a "rigid" renormalized band structure by respect to i.e. filling or temperature, but a structure that evolves when these parameters change. Basically, one obtains a different set of  $Z_m$  and  $\lambda_m$  for each value of  $U$ ,  $J$  and  $n$ .

From this model we can finally calculate the electronic compressibility, which is defined like

$$\kappa_{el} = \frac{dn}{d\mu}. \quad (5.4)$$

This is done in the following fashion: for a fixed value of  $n$  we do a scan in  $U$ , obtaining for each of these values its corresponding chemical potential  $\mu$  (and also all the renormalization parameters). Once all the scans have been done, we calculate

the numerical derivative and we thus obtain a map of the electronic compressibility as a function of doping  $n$  and on-site Coulomb interaction  $U$ .

### 5.3 FeSe under pressure

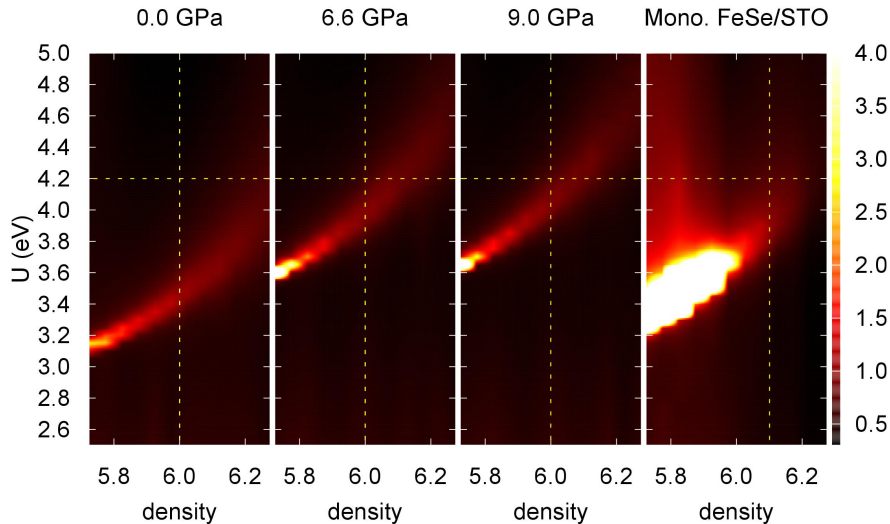


**Figure 5.2:** Color map of the electronic compressibility  $\kappa_{el} = dn/d\mu$  (in color scale) of FeSe as a function of the electron density per Fe atom  $n$ , and the on-site Coulomb interaction  $U$ . The brighter the color, the larger the electronic compressibility, until reaching the white color, which denotes a divergence in the electronic compressibility. The stair structure that can be observed is unphysical and corresponds to the discretization of the numerical derivative. From left to right: electronic compressibility for 0, 6.6 and 9.0 GPa cases and for a mono-layer of FeSe over a substrate of STO. The vertical yellow dashed lines represent the stoichiometric filling ( $n = 6.0$ ) and the horizontal ones our estimated value of  $U = 4.2$  eV for this system. The crossing point locates the stoichiometric compound in this  $U$ -filling plane.

The main result is shown in Fig. 5.2, where the calculated electronic compressibility is plotted in a color map as a function of the Coulomb repulsion  $U$  and the electronic density in a range of dopings in the vicinity of stoichiometric value of FeSe ( $n = 6.0$ ). The value of Hund’s coupling has been kept fixed to  $J/U = 0.20$  in all the calculations. Each of these sets of calculations was performed for FeSe at three different values of the hydrostatic pressure of 0.0, 6.0 and 9.0 GPa, and also for a mono-layer of FeSe on top of a substrate of STO. In this model, these four systems correspond to a different  $\hat{\mathcal{H}}_0$  coming from a different DFT calculation, to which then interactions are added through  $\hat{\mathcal{H}}_{int}$ .

We focus first on the results of FeSe under pressure (first three panels in Fig. 5.2), which clearly show that the enhancement in the electronic compressibility with a “moustache” shape is present in this doping-interaction plane. This region, which corresponds to the brighter zones in the color maps, happens in FeSe analogously to the case of  $\text{BaFe}_2\text{As}_2$  [130], but unlike the latter compound, which is exactly on top of

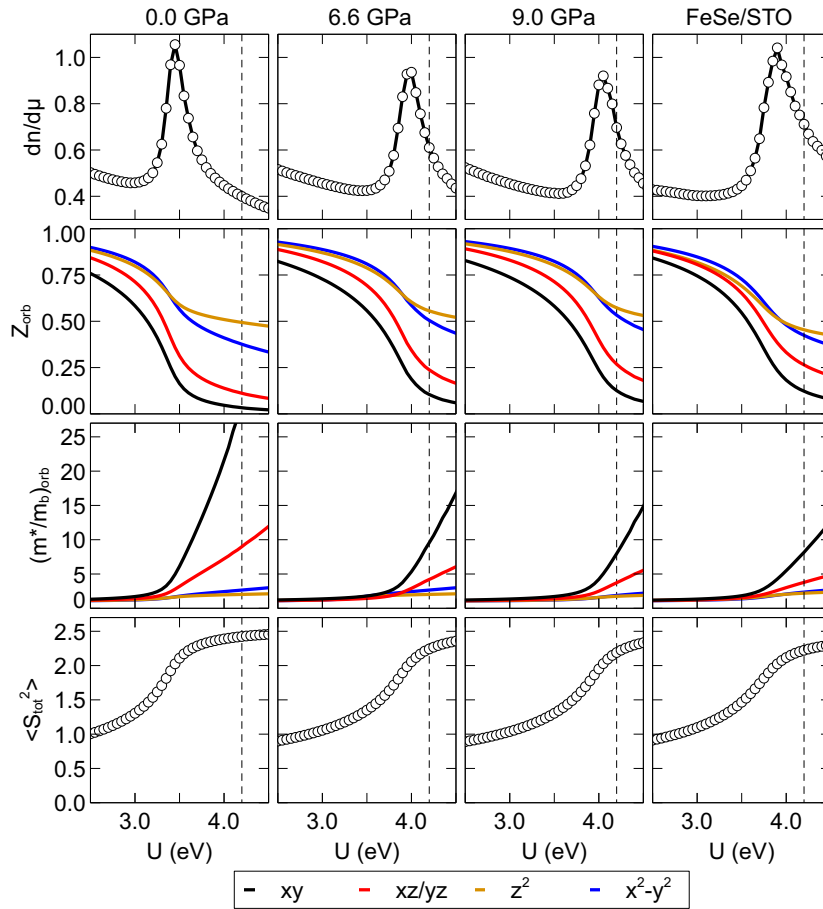


**Figure 5.3:** Results for bulk FeSe for three different values of applied hydrostatic pressure and for mono-layer FeSe/STO. Upper panels: electronic compressibility as a function of the on-site Coulomb interaction  $U$ . Middle-upper panels: quasiparticle weights of the different orbitals as a function of  $U$ . Middle-lower panels: mass enhancement of the different orbitals ( $1/Z_m$ ) as a function of  $U$ . Lower panels: total local spin-spin correlation function as a function of  $U$ . All calculations are performed for a filling of  $n = 6.0$  and  $J/U=0.2$ .

the region of enhancement, the realistic values of the parameters for stoichiometric bulk FeSe (dotted lines) are located at some distance from the zone of enhanced compressibility, in the region after the crossover.

The first interesting result here is how increasing pressure moves this enhancement region closer to the physical values (corresponding to  $U = 4.2$  eV and  $n = 6.0$ ), which can be seen in Fig. 5.2 by the orange moustache approaching to the cross between the dotted lines as pressure increases. This is further illustrated by the upper panel of Fig. 5.3, where we plot cuts along  $n = 6.0$  for the color maps in Fig. 5.2, showing the electronic compressibility as a function of the on-site Coulomb interaction  $U$ . Realistically assuming that the interaction strength is not sensibly modified by the applied pressure<sup>1</sup>, one sees that for 6-9 GPa the enhancement region has basi-

<sup>1</sup>Effectively, pressure may change the on-site Coulomb interaction. However, the kinetic energy

cally reached (although not completely) the physical parameters. This is remarkable in that the same trend is observed in the experimental  $T_c$ , which tops in the same range of pressures, before crystallographic changes intervene [51, 54].

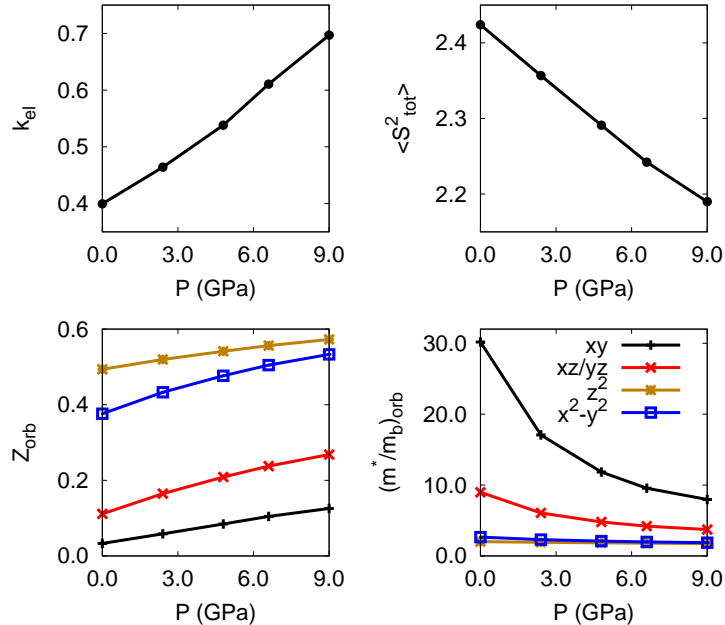


**Figure 5.4:** Electronic compressibility (upper-left panel), local magnetic moment (upper-right panel), orbitally-resolved quasiparticle weights (lower-left panel) and orbitally-resolved mass enhancements (lower-right panel) as a function of hydrostatic pressure. All calculations are done at  $n = 6.0$  filling,  $U = 4.2$  eV and  $J/U=0.2$ .

It is worth signaling that even though the DFT description of the bare band structure in IBSC may not be quantitatively accurate, the main role here will be played by many-body physics, that is dominated by the local energetics determined by  $\hat{\mathcal{H}}_{int}$ . Although the influence of the bare electronic structure through  $\hat{\mathcal{H}}_0$  is still strong, this happens mainly through local quantities, like the crystal-field splitting of orbital energies, or the (total and orbital-resolved) kinetic energy, all quantities that are more or less well captured by DFT. We thus expect the results to be robust to subtle changes and eventual improvements in  $\hat{\mathcal{H}}_0$ .

Apart from this enhanced electronic compressibility, IBSC as the prototype of Hund's metals (as introduced in chapter 3) present also other phenomenology. We have also seen that all these characteristic features start to be visible after the crossover between a normal- to a Hund's-metal phase. FeSe is believed to be more correlated than  $\text{BaFe}_2\text{As}_2$  [116] and thus it is plausible that if the latter lies on top of the crossover (as found in Ref. [130]), the former might be well inside the Hund's metal region. This fact is clearly confirmed in our results (plotted in Fig. 5.3) by FeSe at ambient pressure showing the hallmarks of the Hund's metals: *i)* large fluc-

is expected to grow much more than the interaction, making this assumption more realistic.

tuating total local magnetic moment  $\langle S_z \rangle$  (lower panels), *ii*) orbitally differentiated mass enhancements (middle-lower panels), *iii*) strong correlations and low Fermi-liquid coherence scales (due to the low quasiparticle weights - middle-upper panels - corresponding to the large values of the mass enhancement for the conduction electrons, of main orbital character  $xy, xz, yz$ ). The crossover in these quantities towards their typical behavior in a more conventional metal is clearly visible at lower  $U$  than the "realistic" value 4.2 eV. As expected the compressibility enhancement (upper panels) is also shown to track this crossover.

This general tendency is further confirmed in Fig. 5.4, where the same quantities calculated previously are now plotted in the case of an electronic density of  $n = 6.0$ , a local Coulomb interaction of  $U = 4.2$  eV and at a value of Hund's coupling of  $J/U = 0.2$ , as a function of pressure (two more points have been added for the sake of clarity, at 2.4 GPa and 4.8 GPa). The behavior with pressure becomes very clear here. In the case of the electronic compressibility (upper-left panel), its value increases as a function of pressure, in a similar fashion as the superconducting  $T_c$  as we previously signaled. The total local magnetic moment (upper-right panel) decreases with increasing pressure, since the crossover (and thus the increase towards a saturation value) is moved to a higher value of  $U$ . The quasiparticle weights increase (lower-left panel) since the bandwidth of the system gets enlarged with increasing pressure while  $U$  is kept fixed. This is reflected in the mass enhancements (lower-right panel), which are not only reduced but also the differentiation between orbitals (i.e. the orbital selectivity) is less pronounced, because the system moves closer to the crossover and is not lying anymore deeply in the Hund's metal regime.

In our calculations basically at the pressure 6-9 GPa the compound is predicted (within all the previously outlined caveats) almost on top of the Hund's-to-normal metal crossover. We see from Figs. 5.3 and 5.4 that at the crossover  $\langle S_z \rangle$  is expected to reduce rapidly and that the enhancement of the masses should go back to moderate and with small differentiation among the different orbitals. Consequently the Fermi-liquid coherence scale is expected to grow much larger. Some experimental support of our findings with theoretical simulations can be found in the literature for the case of FeSe:

- The estimate of the local paramagnetic moment by X-ray Emission Spectroscopy (XES) is seen to drop monotonously in the range of pressures 0-9 GPa [171] (before the system undergoes a change of structure producing an even higher value for the moment [172]).
- Orbital selective correlations have been directly reported from ARPES or Quantum Oscillations in all Fe-chalcogenides [173] and in FeSe in particular [174], in the normal phase. Remarkably, it was shown lately by quasiparticle interference on STM measures that the superconducting gap shape cannot be explained without including heavily orbitally-differentiated quasiparticle weights [62, 63]. It is quite safe to conclude that FeSe lies in a regime

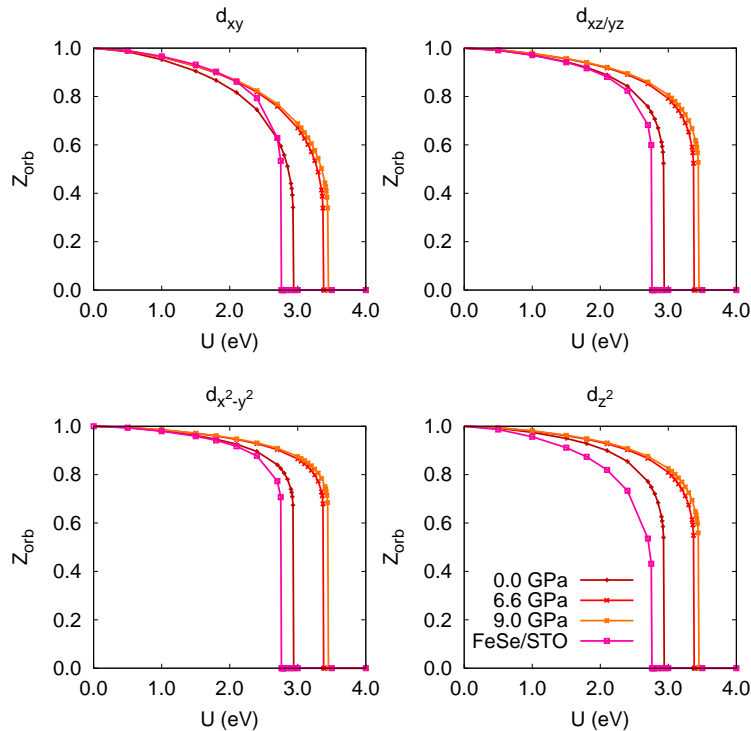


**Figure 5.5:** Quasiparticle weights of the different orbitals  $Z_m$  at half-filling density  $n = 5.0$  for FeSe bulk in the orthorhombic phase at different pressures (0, 6.6 and 9.0 GPa) and for FeSe/STO, as a function of the local Coulomb interaction  $U$ . The value of Hund’s coupling is fixed to  $J/U = 0.20$ .

of strong orbital differentiation of the correlation strength as predicted theoretically [116, 175] and in agreement with the general mechanism outlined in Ref. [176].

- A remarkable crossover is found in the resistivity around 350K [177]. While at low temperature the behavior is metallic, after a shoulder located around 350K it starts decreasing with temperature, signaling a crossover towards bad-metallic/semiconducting behavior. This fact is readily interpreted as a low coherence scale of the metallic carriers.

We can thus conclude that the calculations at the estimated values for the interactions seem to reproduce correctly the Hund’s metal behavior of FeSe found in experiments, and the prediction of the zone of enhanced compressibility at 6-9 GPa can be deemed robust.

## 5.4 Results in FeSe/STO

Let’s now turn to the case of FeSe/STO. As visible in the rightmost panel in Fig. 5.2 in our calculations, the enhancement region is much larger and the enhancement

itself is more intense overall. This can be correlated positively with the enhanced experimental  $T_c$  of the mono-layer, in the same spirit as the case of FeSe under pressure. A peculiar shape is also noticeable in the enhancement region, that seems to "bifurcate" for  $U \gtrsim 3.8\text{eV}$  in a branch that extends to electron doping (density values of  $n$  from 6.1 to 6.2) and another to hole doping ( $n$  from 5.7 to 5.9). By analyzing the renormalized DOS at the Fermi level  $D^*(\mu)$  one can show that the hole-doping branch is due to an enhanced structure in  $D^*(\mu)$ , while the one at electron doping is not, and there  $\kappa_{el}$  is thus enhanced by the denominator in formula (3.7). This means that the enhancement branch at electron doping is the genuine continuation of the "moustache" structure, carrying over all the physical considerations done so far about it (indeed the behavior of all the quantities analyzed in Fig. 5.3 for FeSe/STO parallels the corresponding ones in FeSe). This again correlates positively with experiments in that FeSe/STO with the enhanced  $T_c$  is electron-doped [162]. It might also be worth to stress here that the STO substrate has a very high dielectric constant which might contribute to the screening of the electronic interactions in FeSe, so that the actual value of  $U$  for the Fe-3d electrons in this system could eventually become a bit lower.

The Mott transition for the case of FeSe/STO occurs at a lower value of the on-site Coulomb interaction  $U$  (see Fig. 5.5), which is the point from which the instability region departs. This can be due to the reduced dimensionality of the FeSe/STO system, which is completely 2-dimensional, and thus the overall bandwidth of the bare band structure disperses a bit less which translates into a smaller average kinetic energy, thus the Mott transition will happen at a smaller value of the local Coulomb interaction  $U$ . This explains why the instability region and the crossover to a Hund's metal occur at lower values of  $U$  in the interaction-doping plane. The fact that this zone is larger (a brighter region in the rightmost color map in Fig. 5.2) is not fully understood yet, but we think it can be related with the 1st order character of the Mott transition seen in the quasiparticle weights for the different orbitals in Fig. 5.5 although this is just pure speculation at this point.

A missed ingredient that might contribute substantially to the superconductive pairing in this case or in general in other IBSC is phonons. In the beginning they were very early ruled out as the main source of pairing in the iron pnictides by DFT simulations [178, 179], which showed that the phonon coupling was around one order of magnitude smaller than expected and thus negligible to induce phonon-mediated superconductivity. However, with the appearance of the FeSe/STO system they have been called into the game again. In particular phonons of the substrate are thought to be more effective in enhancing the superconductivity of the mono-layer than those of FeSe itself [180, 181], but recent theoretical calculations claimed [182] that this electron-phonon coupling is substantially screened by the same electrons of FeSe. However, these calculations neglect vertex corrections, which can be effectively enhanced by the instabilities found in this work, according to the already

mentioned Ward identity (eq. 3.8 introduced already in Section 3.4). If the present scenario is realized then, one might reconsider the suppression of electron-phonon coupling due to the screening of FeSe conduction electrons estimated in Ref. [182]. Electron-phonon coupling might actually be boosted in the rather narrow region corresponding to the enhanced compressibility, as also calculated in Ref. [183] for bulk FeSe, and thus contribute substantially to the high-temperature superconductivity, not only in FeSe bulk, but more importantly in the case of the FeSe/STO system.

## 5.5 Summary and conclusions

In summary, we have modeled FeSe bulk at different pressures and a mono-layer of FeSe within the SSMFT framework, and studied the electronic compressibility  $\kappa_{el} = dn/d\mu$  in each of these systems. A moustache-shaped zone of compressibility enhancement is found (see Fig. 5.2), as it happens in other multi-orbital systems with a sizable Hund's coupling. It departs from the Mott transition point at half filling (see Fig. 5.5) and extends at finite dopings. This region parallels the universal crossover [126] between a normal (at low- $U$  and large doping) and a Hund's metal (at large  $U$  and small doping), as it is shown in Fig. 5.3.

At ambient pressure, an enhancement of  $\kappa_{el}$  is found in the doping-interaction plane but is slightly off from the realistic value of the on-site Coulomb repulsion  $U$  for this compound at the stoichiometric filling of  $n = 6.0$ . This enhancement region (which at lower electron densities - i.e. strong hole doping and lower interaction strengths - turns into a divergence, signaling an instability region towards phase separation there) is moved closer to the realistic parameters for FeSe when pressure is increased, showing an enhancement similar to that of the experimental critical temperature ( $T_c$ ) of FeSe. The largest electronic compressibility is finally achieved in the range of pressures in which FeSe presents the highest  $T_c$  (around 9 GPa). These trends are consistent in the case of a mono-layer of FeSe, where the instability region is larger and culminates at electron doping.

## 5.6 Résumé et conclusions

En résumé, nous avons modélisé FeSe à différentes pressions et une monocouche de FeSe avec SSMFT, et étudié la compressibilité électronique  $\kappa_{el} = dn/d\mu$  dans chacun de ces systèmes. On trouve une augmentation de la compressibilité en forme de moustache (voir Fig. 5.2), du façon analogue à d'autres systèmes multi-orbitaux avec un couplage de Hund important. Cette zone part du point de transition de Mott à mi-remplissage (voir Fig. 5.5) et se prolonge à dopages finis. Cette région est parallèle au crossover universel [126] entre un métal normal (à  $U$  faible et grand

dopage) et un métal de Hund ( $U$  grand et petit dopage), comme il est montré dans la Fig. 5.3.

À la pression ambiante, on trouve une augmentation de  $\kappa_{el}$  dans le plan interaction-dopage pour FeSe, mais elle est légèrement éloigné par rapport à la valeur réaliste de la répulsion de Coulomb  $U$  pour ce composé au remplissage stochiométrique de  $n = 6.0$ . Cette région d'augmentation (qui à des densités électroniques plus faibles - c'est-à-dire un fort dopage de trous - se transforme en une divergence, signalant une région d'instabilité vers la séparation de phase) se rapproche des paramètres réalistes pour FeSe lorsque la pression est augmentée, montrant une augmentation analogue à celle de la température critique ( $T_c$ ) expérimentale de FeSe. Le maximum de la compressibilité électronique est finalement obtenu dans la région de pressions dans laquelle FeSe présente la  $T_c$  maximale (environ 9 GPa). Ces tendances sont analogues dans le cas d'une monocouche de FeSe, où la région d'instabilité est plus grande et culmine dans la region dopée en electrons.

# 6

## Study of magnetism in $\text{YFe}_2\text{Ge}_2$ and related compounds

In this chapter we study the mechanisms with which ferromagnetic tendencies detrimental for superconductivity are induced in the 122 family of IBSC when the As ligand is replaced with Ge and how they are instead limited by substitutions of the ions in the spacer layers ( $\text{Ca} \rightarrow \text{Y}$ ). Intermediate compounds isolating only one of these two kinds of substitutions are studied within DFT, among them the ferromagnet  $\text{CaFe}_2\text{Ge}_2$ , which has been synthesized for the first time recently. We thus single out the control of spacer ions as a way to preserve superconductivity, and we also suggest that superconductivity in  $\text{YFe}_2\text{Ge}_2$  might be enhanced under pressure, which is also found to suppress ferromagnetic tendencies in our simulations. The outcome of this chapter can be found in Ref. [184].

---

Dans ce chapitre, nous étudions les mécanismes avec lesquels les tendances ferromagnétiques préjudiciables à la supraconductivité sont induits dans le supraconducteurs de fer 122 lorsque le ligand As est remplacé avec Ge et comment ils sont plutôt limités par des substitutions des ions dans les couches d'espacement ( $\text{Ca} \rightarrow \text{Y}$ ). Composés intermédiaires isolant un des ces deux types de substitutions sont étudiés au sein de DFT, et l'un d'eux, le ferromagnétique  $\text{CaFe}_2\text{Ge}_2$  a été synthétisé pour la première fois. Nous choisissons donc le contrôle d'espacement comme un moyen de préserver la supraconductivité, et nous suggérons également que la supraconductivité dans  $\text{YFe}_2\text{Ge}_2$  pourrait être augmenté sous la pression, qui est également trouvé pour supprimer les tendances ferromagnétiques dans nos simulations. Les résultats de ce chapitre peuvent être trouvés dans la Réf. [184].

## 6.1 The $\text{YFe}_2\text{Ge}_2$ system and related compounds

In most of the iron-based superconductors (IBSC), the Fe atom is typically associated with a pnictogen (As, P) or a chalcogen (Se, Te, S) and in practice, the highest superconducting critical temperatures ( $T_c$ ) are always obtained with either As or Se [185], the reason for this still being a matter of discussion. One interesting proposal for the origin of this “chemical” limitation is the emergence of ferromagnetic tendencies, which are detrimental for superconductivity, as one moves from As/Se to the left in the periodic table [186]. However, there are two notable exceptions to this rule. Namely, the novel silicide hydride  $\text{LaFeSiH}$  displaying superconductivity with onset 11 K, i.e. the highest among the 1111 parent compounds [187], and the germanide  $\text{YFe}_2\text{Ge}_2$  with  $T_c \lesssim 1.8$  K [48]. In this chapter, we examine  $\text{YFe}_2\text{Ge}_2$  and other related compounds, and study how these systems run away from ferromagnetism so that superconductivity can eventually emerge in these intriguing Fe-based variants.

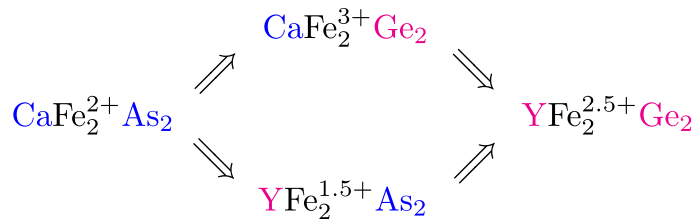


**Figure 6.1:** Schematic representation of the two possible intercalating compounds between  $\text{CaFe}_2\text{As}_2$  and  $\text{YFe}_2\text{Ge}_2$  with the nominal charge per Fe atom.

$\text{YFe}_2\text{Ge}_2$  shares the same crystal structure of the 122 family of iron pnictides, but it is in the collapsed phase, i.e. the  $c$  crystallographic axis is smaller compared to the usual 122 family. Its electronic structure can be seen as a electron-doped version of that of  $\text{CaFe}_2\text{As}_2$  in this collapsed tetragonal phase [48]. In order to understand the effects of the chemical substitution, we propose two novel intermediate compounds that interpolate the two previously reported superconductors, as shown schematically in Fig. 6.1.

The first of them,  $\text{CaFe}_2\text{Ge}_2$ , is expected to be a hole-doped version of both aforementioned IBSC, with a nominal valence in the iron atom of  $\text{Fe}^{3+}$ . This means that, in principle, one should see a more or less upwards rigid shift in energy of the electronic structure when moving from  $\text{CaFe}_2\text{As}_2$  to  $\text{CaFe}_2\text{Ge}_2$  that then will be slightly shifted downwards by having introduced Y and thus modifying the valence of Fe when going from  $\text{CaFe}_2\text{Ge}_2$  to  $\text{YFe}_2\text{Ge}_2$ . This new compound  $\text{CaFe}_2\text{Ge}_2$  has been synthesized very recently for the first time [184]. Its crystal structure at room temperature has been characterized by X-Ray diffraction. It exhibits a

tetragonal structure (space group  $I4/mmm$ ) and the measured lattice parameters are  $a = 3.9922(6)\text{\AA}$  and  $c = 10.702(2)\text{\AA}$  with the internal coordinate of Ge being  $z_{\text{Ge}} = 0.3774(6)$ . These lattice parameters are very similar to those reported in  $\text{YFe}_2\text{Ge}_2$  [44] and in the collapsed tetragonal phase of  $\text{CaFe}_2\text{As}_2$  [43], which is highly desirable when comparing the effects of chemical substitution between different compounds.

Since we want to study the effect of the  $\text{As} \leftrightarrow \text{Ge}$  substitution, we have also considered another alternative interpolation via the imaginary compound  $\text{YFe}_2\text{As}_2$ . This intermediate compound can be seen as an electron-doped version of the germanide since the nominal oxidation of the iron is reduced from  $\text{Fe}^{2.5+}$  to  $\text{Fe}^{1.5+}$ . Again, moving from left to right in the series of compounds proposed here, one should see now a shift of the electronic structure downwards after the first substitution, and then a shift upwards in the second substitution. We also point out that as far as we know, this compound has not been yet synthesized.

The strategy here is to study the electronic structure and magnetism in realistic simulations of these two novel compounds ( $\text{CaFe}_2\text{Ge}_2$  and  $\text{YFe}_2\text{As}_2$ ) and compare it with that of two already-existing materials ( $\text{CaFe}_2\text{As}_2$  and  $\text{YFe}_2\text{Ge}_2$ ). In particular we are interested in studying the effect of the presence of Ge or As ligands in these systems and whether this is favorable or detrimental for superconductivity. Another complementary study we have done is the effect of hydrostatic pressure in the magnetism in  $\text{YFe}_2\text{Ge}_2$ . Pressure is known to be very effective tool for enhancing superconductivity [188], and in particular in some IBSC [35, 36, 37].

## 6.2 DFT calculations

**Table 6.1:** Lattice parameters and relevant atomic positions of the different compounds taken from the literature that we have used in our calculations. The energies are per formula unit, and the magnetic moments per Fe atom.

Compound	Ref.	$a(\text{\AA})$	$c(\text{\AA})$	$z_{\text{As/Ge}}$
$\text{CaFe}_2\text{As}_2$	[43]	3.9792	10.6073	0.3663
$\text{CaFe}_2\text{Ge}_2$	Pierre Toulemonde	3.9922	10.702	0.3774
$\text{YFe}_2\text{Ge}_2$	[44]	3.9617	10.421	0.3789
$\text{YFe}_2\text{As}_2$	-	3.9617	10.421	0.3789

The electronic structure simulations in all the compounds listed above have been done within density functional theory (DFT). We have used the generalized gradient approximation (GGA) of Perdew, Burke and Ernzerhof [140] as implemented in the WIEN2K software package [105]. Even though DFT has some limitations in its predictive power in IBSC, this method has been previously used in studies of magnetism in similar compounds [189, 190]. We use here a similar approach.

For  $\text{CaFe}_2\text{As}_2$  we use the same lattice parameters and atomic positions from Ref. [43], which correspond to its collapsed phase, and for  $\text{YFe}_2\text{Ge}_2$  and the imaginary compound  $\text{YFe}_2\text{As}_2$  we use the experimental parameters of the first taken from Ref. [44]. In the case of  $\text{CaFe}_2\text{Ge}_2$  we use the lattice parameters and atomic positions that we have measured experimentally. All these are summarized in Table 6.1. We have selected muffin-tin radii of  $R_{mt}^{\text{Y,Ca}} = 2.50$  a.u. and  $R_{mt}^{\text{Fe,Ge,As}} = 2.20$  a.u., and all our calculations have been done with the same number of plane waves, which in WIEN2K is set by the cutoff  $R_{mt} \cdot K_{max} = 9.0$ . For the study of  $\text{YFe}_2\text{Ge}_2$  under pressure all the lattice parameters and atomic positions have been optimized for each of the values of pressure<sup>1</sup>. The densities of states (DOS), band structures and Fermi surfaces displayed along this chapter have been calculated in the paramagnetic phase. For the DOS we have chosen a k-mesh of  $40 \times 40 \times 40$ .

For the magnetic simulations we have imposed the following magnetic orders among the Fe atoms: ferromagnetic, A-, C-, and G-type anti-ferromagnetic, and single- and double-stripe anti-ferromagnetic orders<sup>2</sup>. We have used 3 different magnetic super-cells in order to accommodate all the possible magnetic structures and we have converged a k-mesh for each of them. However, this introduces an error when comparing the energies of the different magnetic orders due to the finiteness of this k-mesh. This error has been estimated to be 6 meV.

## 6.3 Results

We first analyze the electronic structure of  $\text{CaFe}_2\text{Ge}_2$  in the paramagnetic phase, whose main features are summarized in Fig. 6.2. Like many other IBSC, it has several bands of mainly Fe-3d character crossing the Fermi level. These Fe bands extend in a range of energies between -3 eV and 2 eV around the Fermi level. An analysis of the orbital content shows that these Fe-3d bands are hybridized with a Ca band of mainly d character (apart from the obvious hybridization with the Ge-ligands). The DOS of this paramagnetic phase at the Fermi level is  $10.2 \text{ eV}^{-1}$ .

In order to understand better the electronic structure of this new compound, we compare it to that of  $\text{CaFe}_2\text{As}_2$  and  $\text{YFe}_2\text{Ge}_2$  (all in Fig. 6.2), that we have also calculated. We want to note that  $\text{YFe}_2\text{Ge}_2$  has also a Y band of mainly d character hybridized with the Fe-3d bands that cross the Fermi level, what seems to be a common feature in all the IBSC in this collapsed tetragonal phase. Comparing the electronic band structure, the DOS and the Fermi surface of  $\text{CaFe}_2\text{Ge}_2$  with those of  $\text{CaFe}_2\text{As}_2$  and  $\text{YFe}_2\text{Ge}_2$ , we see that the new compound displays very similar features near the Fermi level with several bands of mainly Fe-3d character crossing the Fermi level and a large value of the DOS. However, there is a shift upwards of these features so that there is effective hole-doping in the system. This could have

---

<sup>1</sup>This structural optimizations have been carried out by Prof. Fabio Bernardini.

<sup>2</sup>Nevertheless, we were not able to converge all these proposed magnetic orders in all compounds.

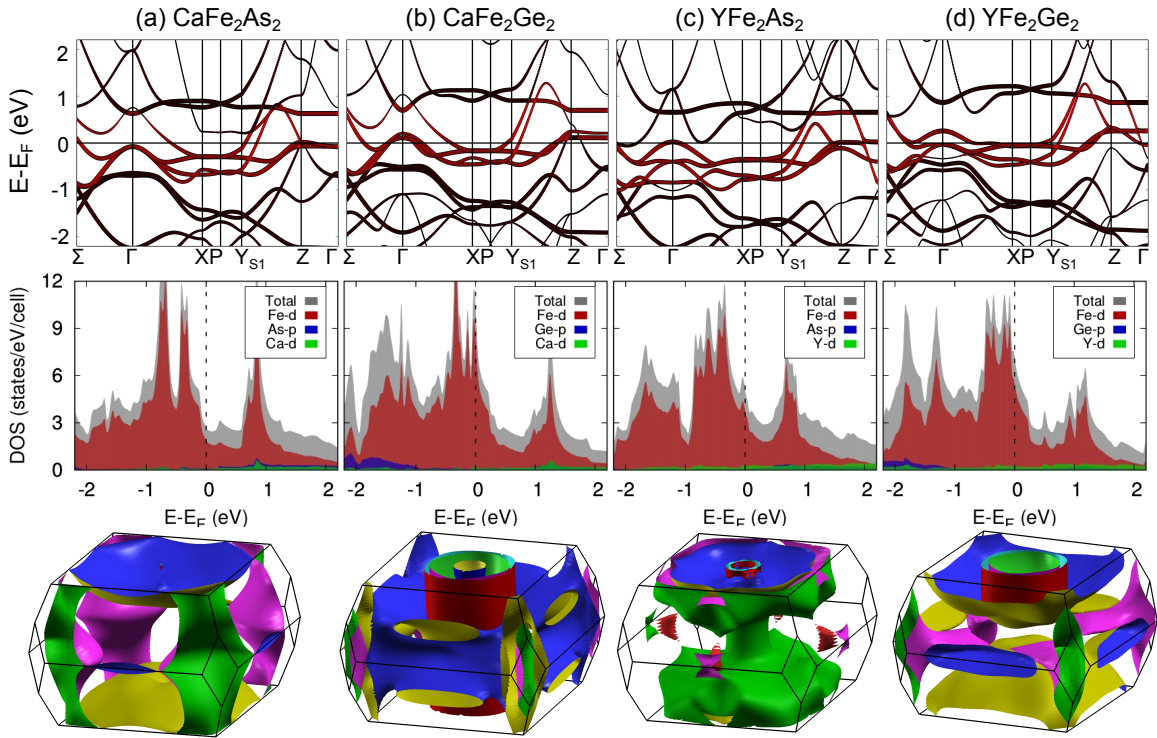


**Figure 6.2:** Electronic band structure (upper panels), total and partial DOS (middle panels) and Fermi surfaces (lower panels) of the non-magnetic phases of  $\text{CaFe}_2\text{As}_2$  (a),  $\text{CaFe}_2\text{Ge}_2$  (b),  $\text{YFe}_2\text{As}_2$  (c) and  $\text{YFe}_2\text{Ge}_2$  (d).

**Table 6.2:** Energy difference with respect to the non-spin-polarized calculation and corresponding value of the Fe magnetic moment (in units of  $\mu_B$ ) for different magnetic orders in the four studied compounds.

Order	$\text{CaFe}_2\text{As}_2$		$\text{CaFe}_2\text{Ge}_2$		$\text{YFe}_2\text{As}_2$		$\text{YFe}_2\text{Ge}_2$	
	E(meV)	M.M.	E(meV)	M.M.	E(meV)	M.M.	E(meV)	M.M.
A-type	-260	2.35	-233	1.33	268	1.64	<b>-118</b>	1.00
C-type	-251	1.89	-	-	-	-	-	-
G-type	-216	1.85	-198	1.78	-	-	-	-
Ferro.	-320	2.36	<b>-265</b>	1.33	213	1.64	-103	0.98
SS-type	<b>-321</b>	2.07	-225	1.61	-	-	-111	1.27
DS-type	-269	2.00	-255	1.74	-	-	-74	1.34

been anticipated, as we mentioned, from the fact that the nominal oxidation of the iron becomes  $\text{Fe}^{3+}$  in the new system. Despite this increase, the resulting Fermi surface remains essentially similar.

This extra doping in  $\text{CaFe}_2\text{Ge}_2$  yields a substantial increase in the DOS at the Fermi level: from  $\sim 7.2 \text{ eV}^{-1}$  in  $\text{YFe}_2\text{Ge}_2$  to  $\sim 10.2 \text{ eV}^{-1}$  in  $\text{CaFe}_2\text{Ge}_2$ . These values are summarized in Table 6.3.  $\text{YFe}_2\text{Ge}_2$  has been argued to display incipient ferro-

**Table 6.3:** DOS at the Fermi level for the different compounds that we have studied.

Compound	DOS( $E_F$ ) ( $\text{eV}^{-1}$ )
$\text{CaFe}_2\text{As}_2$	2.68
$\text{CaFe}_2\text{Ge}_2$	10.21
$\text{YFe}_2\text{As}_2$	5.07
$\text{YFe}_2\text{Ge}_2$	7.18

magnetism due to a Stoner instability<sup>3</sup> [186, 189, 190]. In the case of  $\text{CaFe}_2\text{Ge}_2$ , since the DOS at the Fermi level is even larger, this can lead to an enhanced ferromagnetic instability which, by analogy, can again be understood as a Stoner instability. We have performed spin-polarized calculations in different magnetic configurations. The results, which are shown in Table 6.2, support this view. As we can see, the new system displays different magnetic instabilities among which we do find a ferromagnetic one. These calculations are confirmed by the magnetic response of  $\text{CaFe}_2\text{Ge}_2$  measured experimentally. We want to point out that in the case of  $\text{YFe}_2\text{Ge}_2$  we have found the same magnetic ground state than other previously reported calculations [189, 190], in particular we find a very similar value for the ground state energy compared to the paramagnetic solution, magnetic moments and paramagnetic DOS at the Fermi level to those reported in Ref. [189], where an identical exchange-correlation potential and very similar lattice parameters and atomic positions were used.

The other route we propose between  $\text{CaFe}_2\text{As}_2$  and  $\text{YFe}_2\text{Ge}_2$  is via an intermediate imaginary compound:  $\text{YFe}_2\text{As}_2$ . As we mentioned above, it is expected to be a electron-doped version of these two compounds. This is confirmed in the electronic band structure and the DOS, whose main features near the Fermi level are now shifted downwards compared to the previous systems (see Fig. 6.2). This shift reduces the DOS at the Fermi level and hence can be expected to weaken the ferromagnetic instability. In fact, the spin-polarized solutions either disappear or become energetically unfavorable, among them the ferromagnetic one (see Table 6.2).

This exercise confirms that the ferromagnetic tendencies in this family are inherently associated to the  $\text{As} \leftrightarrow \text{Ge}$  substitution in the 122 compounds, as already suggested in Ref. [186], and not necessarily to the other elements. Indeed our results also show that the  $\text{Ca} \leftrightarrow \text{Y}$  substitution gets rid of these ferromagnetic tendencies, and could be used as a tool to restore superconductivity in these compounds.

---

<sup>3</sup>A Stoner instability is in an instability of the Fermi surface of a metal. When the amount of states at the Fermi level is very high the electrostatic repulsion in the cloud of electrons may be such that it is energetically more favorable for the system to split its Fermi surface into an up-spin and a down-spin Fermi surface, leading to an imbalance of up- and down-spin electrons in the system, which becomes ferromagnetic.

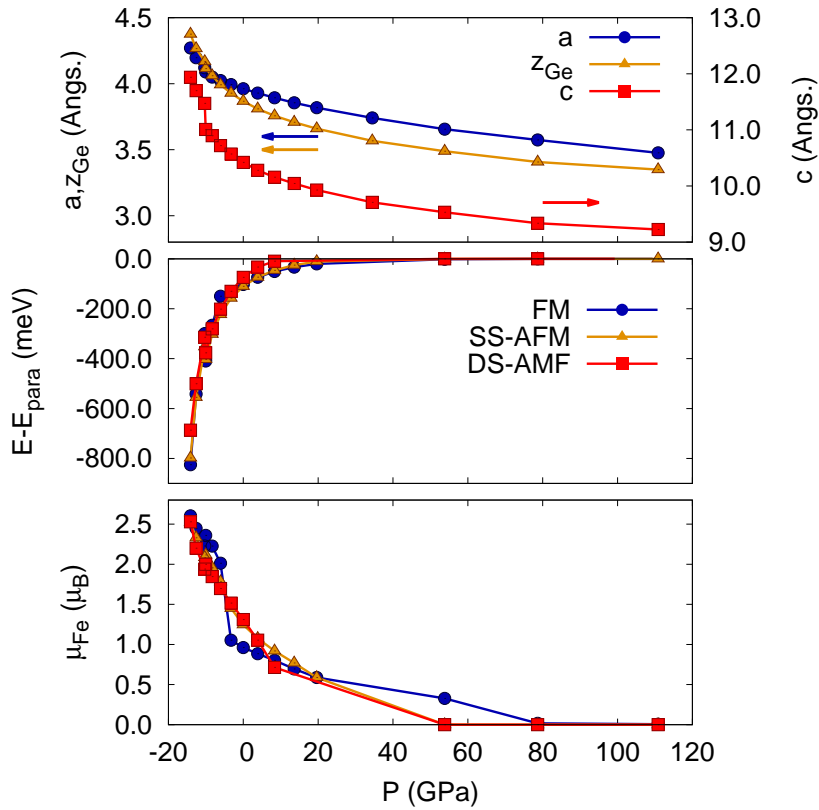


**Figure 6.3:** Optimized lattice parameters  $a$  and  $c$  and  $z$ -coordinate of the Ge atom (upper panel), energy difference per formula unit of the different magnetic orders with respect to the paramagnetic solution (mid panel) and magnetic moment per Fe atom for the different magnetic configurations (lower panel) as a function of hydrostatic pressure.

### 6.3.1 $\text{YFe}_2\text{Ge}_2$ under pressure

We have also performed a series of calculations in  $\text{YFe}_2\text{Ge}_2$  under hydrostatic pressure (positive and negative). The main results are summarized in Fig. 6.3. We point out first that with negative pressure the ground state of the system calculated by DFT has a single-stripe anti-ferromagnetic order. With increasing positive pressure, the ground state tends to be a ferromagnet, but in very close proximity to the single-stripe anti-ferromagnet, thus signaling a tendency towards a magnetic instability in a wide range of pressures. In summary, we observe how increasing hydrostatic pressure unfavors magnetism in this case, which can be seen in the two lower panels of Fig. 6.3 as a reduction of the magnetic moment per Fe atom and as a reduction in the energy difference between the magnetic and paramagnetic configurations as pressure increases. This general suppression of magnetism can in principle favor superconductivity.

## 6.4 Summary and conclusions

In summary, we have studied the effect that the  $\text{As} \leftrightarrow \text{Ge}$  substitution has in the magnetism of the 122 family of iron-germanides. For that we have studied two novel compounds,  $\text{CaFe}_2\text{Ge}_2$  and  $\text{YFe}_2\text{As}_2$ , that interpolate between  $\text{CaFe}_2\text{As}_2$  in its collapsed tetragonal phase, and  $\text{YFe}_2\text{Ge}_2$ . Simulations of the electronic structure have been done for the four compounds both in the paramagnetic phase to understand the direct effect of chemical substitution, and also in several magnetic configurations to see whether these compounds display any magnetic instability. A strong ferromagnetic instability is found in the case of  $\text{CaFe}_2\text{Ge}_2$  that even becomes the magnetic ground state, in contrast to  $\text{YFe}_2\text{As}_2$ , which is paramagnetic.

From the point of view of the emergence of itinerant magnetism, we observe that  $\text{CaFe}_2\text{Ge}_2$  has a much larger (almost twice) paramagnetic DOS at the Fermi level than its cousins  $\text{YFe}_2\text{Ge}_2$  and  $\text{CaFe}_2\text{As}_2$ , meaning that the substitution of  $\text{As} \leftrightarrow \text{Ge}$  is favorable for inducing ferromagnetic instabilities in a Stoner-like picture, whereas the inclusion of the cation  $\text{Y}^{3+}$  instead of  $\text{Ca}^{2+}$  is clearly detrimental in this particular case. The other intermediate compound we propose,  $\text{YFe}_2\text{As}_2$ , which shows no signature of magnetism in our simulations, has a much lower DOS at the Fermi level, again pointing in the same direction of our reasoning.

Also, we have studied how hydrostatic pressure affects the magnetism of  $\text{YFe}_2\text{Ge}_2$ . Our calculations show that increasing pressure decreases the magnetic instabilities (and thus possibly stabilizes superconductivity).

## 6.5 Résumé et conclusions

En résumé, nous avons étudié l'effet que la substitution  $\text{As} \leftrightarrow \text{Ge}$  a sur le magnétisme de la famille des 122 germanides de fer. Pour cela, nous avons étudié deux nouveaux composés,  $\text{CaFe}_2\text{Ge}_2$  et  $\text{YFe}_2\text{As}_2$ , qui interpolent entre  $\text{CaFe}_2\text{As}_2$  dans sa phase tétragonale collapsée et  $\text{YFe}_2\text{Ge}_2$ . Des simulations de la structure électronique ont été effectuées pour les quatre composés, à la fois en phase paramagnétique, afin de comprendre l'effet direct de la substitution chimique, ainsi que dans plusieurs configurations magnétiques, afin de déterminer si ces composés présentent une instabilité magnétique. On trouve une forte instabilité ferromagnétique dans le cas de  $\text{CaFe}_2\text{Ge}_2$  qui devient même l'état fondamental magnétique, contrairement à le cas de  $\text{YFe}_2\text{As}_2$ , qui est paramagnétique.

Du point de vue de l'émergence du magnétisme itinérant, on observe  $\text{CaFe}_2\text{Ge}_2$  a un densité des états paramagnétique au niveau de Fermi beaucoup plus grand (presque deux fois) par rapport à  $\text{YFe}_2\text{Ge}_2$  et  $\text{CaFe}_2\text{As}_2$ . Ce qui signifie que la substitution de  $\text{As} \leftrightarrow \text{Ge}$  est favorable pour instabilités ferromagnétiques dans une image à la Stoner, alors que l'inclusion du cation  $\text{Y}^{3+}$  au lieu de  $\text{Ca}^{2+}$  est clairement préjudiciable dans ce cas particulier. L'autre composé intermédiaire que nous

proposons,  $\text{YFe}_2\text{As}_2$ , qui ne montre aucune signature de magnétisme dans nos simulations, a une DOS beaucoup plus basse au niveau de Fermi, encore une fois pointant dans la même direction de notre raisonnement.

Nous avons également étudié l'incidence de la pression hydrostatique sur le magnétisme de  $\text{YFe}_2\text{Ge}_2$ . Nos calculs montrent que l'augmentation de la pression diminue les instabilités magnétiques (et donc éventuellement stabilise la supraconductivité).



## A.1 Exchange-Correlation functionals

The DFT derivation is exact, but the main inconvenient is that there is no information about the analytic expression of  $E_{xc}[n(\mathbf{r})]$  or of its functional derivative  $V_{xc}[n(\mathbf{r})]$ . A first order approximation can be done if we assume that, for those systems in which the electronic density  $n(\mathbf{r})$  varies smoothly in relation to the scale of the Fermi wavelength, the exchange-correlation functional is only a function of the local electron density. In general, we have

$$E_{xc}^{LDA}[n(\mathbf{r})] = \int f[n(\mathbf{r})]d\mathbf{r}, \quad (\text{A.1})$$

which can also be written as

$$E_{xc}^{LDA}[n(\mathbf{r})] = \int n(\mathbf{r})\varepsilon_{xc}[n(\mathbf{r})]d\mathbf{r}, \quad (\text{A.2})$$

in which  $\varepsilon_{xc}[n(\mathbf{r})]$  is the exchange-correlation functional for one electron. This is the so-called *local density approximation* (LDA) and it produces very good results in many cases. The functional  $f[n(\mathbf{r})]$  can be determined from complementary models, like the homogeneous electron gas.

In other cases, it is common to consider higher order approximations for the exchange-correlation functional, taking into account spatial inhomogeneities which can be present in the real electron density via the gradient  $\nabla n(\mathbf{r})$ . Thus, we can write the general expression for any exchange-correlation functional as

$$E_{xc}^{GGA}[n(\mathbf{r})] = \int f[n(\mathbf{r}), \nabla n(\mathbf{r})]d\mathbf{r}. \quad (\text{A.3})$$

This is the so-called *generalized gradient approximation* (GGA). The expression for spin-polarized cases is simply

$$E_{xc}^{GGA}[n_{\uparrow}(\mathbf{r}), n_{\downarrow}(\mathbf{r})] = \int f[n_{\uparrow}(\mathbf{r}), n_{\downarrow}(\mathbf{r}), \nabla n_{\uparrow}(\mathbf{r}), \nabla n_{\downarrow}(\mathbf{r})]d\mathbf{r}. \quad (\text{A.4})$$

The main advantage of GGA over LDA is the wide variety of different functionals which can be put forward. In the case of LDA, though various parametrizations exist

for  $\varepsilon_{xc}[n(\mathbf{r})]$  in (A.2), if we restrict ourselves to the homogeneous case, these are nothing more than different ways of writing the same approximation. Nonetheless, from GGA, one can write as many approximations as can be imagined, as the functional dependence with  $\nabla n(\mathbf{r})$  is only an initial approximation. In principle, an infinite number of different proposals can be put forward.

We have to emphasize that, in addition to the total energy of the system, many other properties of the system can be calculated with DFT, once we have the ground-state density. Even though the total energy can be very similar comparing two different exchange-correlation functionals, there are other properties which depend on spatial variations of the electron density that could be much different. In general, each functional works for a more or less limited number of electronic systems, and it is something one has to live with. As time goes by, new and more complex systems are studied. This makes new functionals arise continuously, many of them being updates of the classical ones. In any case, the choice of the correct exchange-correlation functional is a matter of experience. More details about exchange-correlation functionals can be found in Refs. [140, 191, 192, 193].

## A.2 The APW+lo method

Electronic structures are calculated within the DFT framework using the all-electron, full potential code WIEN2K [105]. This code uses the augmented plane waves plus local orbitals (APW+lo) method [194]. The APW method [195] basically consists in dividing the space in two regions: non-overlapping muffin-tin (MT)<sup>1</sup> spheres, which are centered at the atomic positions and where a typical radial Schrödinger equation is solved, and an interstitial region where a plane-wave expansion treatment is carried out because the potential is assumed to be constant there. Plane-waves are augmented with radial solutions inside the muffin-tin spheres, and linked through the appropriate boundary conditions. The main problem of this method is that the basis set of spherical waves which expands the crystal wave function is energy-dependent, which causes the secular problem to be non-linear in energy and, as a consequence, makes the computational problem much more complicated and time-consuming. An important improvement of this method was carried out when the secular problem was linearized (the LAPW method [196]) but with an extra price to pay: a larger number of non energy-dependent basis functions are required to solve the problem. The APW+lo method includes both the advantages of APW and LAPW methods, just by introducing an alternative functional basis set of local orbitals which are completely confined inside the muffin-tin spheres. Within this framework, plane-wave expansions are obviously not infinite, so we must introduce a cut-off which ensures the Brillouin zone is well mapped.

<sup>1</sup>The word “muffin-tin” is due to the shape of the potential, which is spherically symmetric inside the sphere, and constant elsewhere.

This cut-off is controlled by the dimensionless quantity  $R_{mt} \cdot K_{max}$ , where  $R_{mt}$  is the smallest muffin-tin sphere radius and  $K_{max}$  is the largest reciprocal vector used in the plane-wave expansion.



# B

## Hubbard model in the particle-hole symmetric form

### B.1 1 band Hubbard model

Applying the following particle-hole transformation

$$d_{i\sigma}^\dagger \longrightarrow d_{i\bar{\sigma}} \quad ; \quad d_{i\sigma} \longrightarrow d_{i\bar{\sigma}}^\dagger \quad (\text{B.1})$$

to the Hamiltonian in eq. (2.36) and adding a term with a chemical potential  $\mu$ , the result will be

$$\hat{\mathcal{H}}_e - \mu\hat{N} = - \sum_{ij\sigma} t_{ij} d_{i\sigma}^\dagger d_{j\sigma} + U \sum_i n_{i\uparrow} n_{i\downarrow} + (\mu - U) \sum_{i\sigma} n_{i\sigma} + U - 2\mu. \quad (\text{B.2})$$

This Hamiltonian can be thought to act in two sub-lattices  $A$  and  $B$  that form the original lattice and with electrons hopping from sub-lattice  $A$  to  $B$ . Now, if we apply a gauge transformation only to one of those sub-lattices

$$d_{i\sigma}^\dagger \longrightarrow -d_{i\sigma} \quad ; \quad d_{i\sigma} \longrightarrow -d_{i\sigma}^\dagger \quad i \in \text{sublattice } A \quad (\text{B.3})$$

we end up having

$$\hat{\mathcal{H}}_e - \mu\hat{N} = \sum_{ij\sigma} t_{ij} d_{i\sigma}^\dagger d_{j\sigma} + U \sum_i n_{i\uparrow} n_{i\downarrow} + (\mu - U) \sum_{i\sigma} n_{i\sigma} + U - 2\mu, \quad (\text{B.4})$$

which is identical to  $\hat{\mathcal{H}}_e - \mu\hat{N}$  using  $\hat{\mathcal{H}}_e$  in eq. (2.36) if the chemical potential has the value  $\mu = U/2$ .

We have shown that  $\mu = U/2$  enforces particle-hole symmetry. In this case, one can rewrite the interaction part in eq. (B.2) in an completely equivalent way like:

$$U \sum_i (n_{i\uparrow} - \frac{1}{2})(n_{i\downarrow} - \frac{1}{2}) = U \sum_i n_{i\uparrow} n_{i\downarrow} - \frac{U}{2} \sum_{i\sigma} n_{i\sigma} + \frac{U}{4}, \quad (\text{B.5})$$

where we have just rescaled the chemical potential.

Another possible form is:

$$\begin{aligned}
 \frac{U}{2} \sum_i (n_{i\uparrow} + n_{i\downarrow} - 1)^2 &= \frac{U}{2} \sum_i (n_{i\uparrow} + n_{i\downarrow})^2 - U \sum_i (n_{i\uparrow} + n_{i\downarrow}) + \frac{U}{2} \\
 &= \frac{U}{2} \sum_i (n_{i\uparrow}^2 + n_{i\downarrow}^2 + 2n_{i\uparrow}n_{i\downarrow}) - U \sum_i (n_{i\uparrow} + n_{i\downarrow}) + \frac{U}{2} \\
 &= \frac{U}{2} \sum_i (n_{i\uparrow} + n_{i\downarrow} + 2n_{i\uparrow}n_{i\downarrow}) - U \sum_i (n_{i\uparrow} + n_{i\downarrow}) + \frac{U}{2} \\
 &= U \sum_i n_{i\uparrow}n_{i\downarrow} - \frac{U}{2} \sum_i (n_{i\uparrow} + n_{i\downarrow}) + \frac{U}{2},
 \end{aligned} \tag{B.6}$$

again yielding the same result up to a rescaling constant. This last form has also the advantage that it can be written in a much more convenient way for our interest:

$$\frac{U}{2} \sum_i (n_{i\uparrow} + n_{i\downarrow} - 1)^2 = \sum_i \left( \sum_{\sigma} (n_{i\sigma} - \frac{1}{2}) \right)^2. \tag{B.7}$$

## B.2 Multi-orbital Hubbard model

Let's consider the Hubbard-Kanamori form:

$$\begin{aligned}
 \hat{\mathcal{H}}_e &= \sum_{ijmm'\sigma} t_{ij}^{mm'} d_{im\sigma}^\dagger d_{jm'\sigma} \\
 &+ U \sum_{im} n_{im\uparrow} n_{im\downarrow} + U' \sum_{im \neq m'} n_{im\uparrow} n_{im'\downarrow} + (U' - J) \sum_{im < m'\sigma} n_{im\sigma} n_{im'\sigma} \\
 &- J \sum_{im \neq m'} d_{im\uparrow}^\dagger d_{im\downarrow} d_{im'\downarrow}^\dagger d_{im'\uparrow} + J \sum_{im \neq m'} d_{im\uparrow}^\dagger d_{im\downarrow}^\dagger d_{im'\downarrow} d_{im'\uparrow}.
 \end{aligned} \tag{B.8}$$

For our case of interest we take only into account the density-density terms and drop the spin-flip and pair-hopping terms. This is, considering only one site  $i$ :

$$\hat{\mathcal{H}}_{int} = U \sum_m n_{m\uparrow} n_{m\downarrow} + U' \sum_{m \neq m'} n_{m\uparrow} n_{m'\downarrow} + (U' - J) \sum_{m < m'\sigma} n_{m\sigma} n_{m'\sigma}. \tag{B.9}$$

Introducing these new number operators:

$$\tilde{n}_{m\sigma} \equiv n_{m\sigma} - \frac{1}{2}, \tag{B.10}$$

which are basically the usual number operators plus a shift, the interaction term can be written like:

$$\hat{\mathcal{H}}_{int} = U \sum_m \tilde{n}_{m\uparrow} \tilde{n}_{m\downarrow} + U' \sum_{m \neq m'} \tilde{n}_{m\uparrow} \tilde{n}_{m'\downarrow} + (U' - J) \sum_{m < m'\sigma} \tilde{n}_{m\sigma} \tilde{n}_{m'\sigma}. \tag{B.11}$$

Developing the expression (B.11) in the same manner as for the 1-band case and making it equal to  $\hat{\mathcal{H}}_{int} - \mu \sum_{m\sigma} n_{m\sigma}$  with  $\hat{\mathcal{H}}_{int}$  from eq. (B.9) one finds that:

$$\mu_{\frac{1}{2}\text{-filling}} = \frac{U(2N - 1) - 5J(N - 1)}{2}. \quad (\text{B.12})$$



# C

## Derivation of transport equations

### C.1 Boltzmann Transport formalism

Several kinds of currents can be present inside a solid. An electric current appears as a consequence of an electric field acting on charged particles. A heat current happens when a temperature gradient is present across the material influencing all the particles. A particle diffusion current appears when there exist gradients in the concentration. These currents can be expressed in a simple way as

$$\mathbf{j}_e = \sigma \mathbf{E} = -\sigma \nabla \varphi \quad ; \quad \mathbf{j}_Q = -\kappa \nabla T \quad ; \quad \mathbf{j}_n = -D \nabla n. \quad (\text{C.1})$$

In the previous expressions we have the following tensorial quantities: the electrical conductivity  $\sigma$ , the thermal conductivity  $\kappa$  and the diffusion coefficient  $D$ . In general these currents can be characterized by what is being transported through the solid. We have particle currents  $\mathbf{j}_n$ , electric currents  $\mathbf{j}_e$ , heat currents  $\mathbf{j}_Q$ , entropy currents  $\mathbf{j}_s$ , energy currents  $\mathbf{j}_E$ , and many others, but let's focus only in these ones at the moment. Some relations can be established among them:

$$\mathbf{j}_Q = T \mathbf{j}_s \quad ; \quad \mathbf{j}_e = -e \mathbf{j}_n. \quad (\text{C.2})$$

The last equation yields if the carriers are electrons. From thermodynamics we know that for a solid in which the volume variations are negligible ( $dV = 0$ , which is a reasonable approximation in many cases) we have

$$T dS = dU - \mu dN. \quad (\text{C.3})$$

When considering currents, a similar relation can be written

$$T \mathbf{j}_s = \mathbf{j}_E - \mu \mathbf{j}_n. \quad (\text{C.4})$$

In the case of the time rate of change of entropy, internal energy and number of particles, we have that

$$T \frac{\partial S}{\partial t} = \frac{\partial U}{\partial t} - \mu \frac{\partial N}{\partial t}, \quad (\text{C.5})$$

or referring to these quantities per unit volume this is

$$T \frac{\partial s}{\partial t} = \frac{\partial u}{\partial t} - \mu \frac{\partial n}{\partial t}. \quad (\text{C.6})$$

On the other side we can also write three continuity equations for the number of particles, energy in the system and entropy, namely

$$\frac{\partial n}{\partial t} + \nabla \cdot \mathbf{j}_n = 0 \quad ; \quad \frac{\partial u}{\partial t} + \nabla \cdot \mathbf{j}_E = \mathbf{E} \cdot \mathbf{j}_e \quad ; \quad \frac{\partial s}{\partial t} + \nabla \cdot \mathbf{j}_s = \dot{s}, \quad (\text{C.7})$$

where the generation of Joule heat and the local entropy production rate have been included in the second and third equations respectively. Now making use of these definitions together with eqs. (C.6), (C.2) and (C.4) we can write that

$$\begin{aligned} \dot{s} &= \frac{1}{T} \left( \frac{\partial u}{\partial t} - \mu \frac{\partial n}{\partial t} \right) + \nabla \cdot \left( \frac{\mathbf{j}_Q}{T} \right) \\ &= \frac{1}{T} \left( \mathbf{E} \cdot \mathbf{j}_e - \nabla \cdot \mathbf{j}_E + \mu \nabla \cdot \mathbf{j}_n + \nabla \cdot \mathbf{j}_Q - \mathbf{j}_Q \frac{\nabla T}{T} \right) \\ &= \frac{1}{T} \left( \mathbf{E} \cdot \mathbf{j}_e - \mathbf{j}_n \nabla \mu - \mathbf{j}_Q \frac{\nabla T}{T} \right) \\ &= \frac{1}{T} \left[ \left( \mathbf{E} + \frac{\nabla \mu}{e} \right) \mathbf{j}_e - \frac{\nabla T}{T} \mathbf{j}_Q \right]. \end{aligned} \quad (\text{C.8})$$

We now rewrite the last term like

$$\dot{s} = \frac{1}{T} (\mathbf{X}_e \cdot \mathbf{j}_e + \mathbf{X}_Q \cdot \mathbf{j}_Q) \quad \text{where} \quad \mathbf{X}_e = \mathbf{E} + \frac{\nabla \mu}{e} = -\nabla \left( \varphi - \frac{\mu}{e} \right) \quad ; \quad \mathbf{X}_Q = -\frac{\nabla T}{T}. \quad (\text{C.9})$$

In general one may write that the local entropy production rate is

$$\dot{s} = \frac{1}{T} \sum_i \mathbf{X}_i \cdot \mathbf{j}_i, \quad (\text{C.10})$$

where  $\mathbf{X}_i$  are the driving forces which produce the currents  $\mathbf{j}_i$ . If one assumes that the currents are proportional to the driving forces, i.e. a linear response regime, one can write a general expression for these currents like

$$\mathbf{j}_i = \sum_j \mathsf{L}_{ij} \mathbf{X}_j, \quad (\text{C.11})$$

where the tensorial quantities  $\mathsf{L}_{ij}$  are known as the transport coefficients. According to irreversible thermodynamics and to Onsager's theorem, these coefficients fulfill the following properties

$$\mathsf{L}_{ij}^{\alpha\beta} = \mathsf{L}_{ji}^{\beta\alpha} \quad \text{and} \quad \mathsf{L}_{ij}^{\alpha\beta}(\mathbf{B}) = -\mathsf{L}_{ji}^{\beta\alpha}(\mathbf{B}). \quad (\text{C.12})$$

If in the system there is only present an electric field plus a temperature gradient, then an electric current and a heat current will appear. These two currents can be expressed taking into account eqs. (C.9) and (C.11) like

$$\mathbf{j}_e = L_{11} \left( \mathbf{E} + \frac{\nabla\mu}{e} \right) + L_{12} \left( -\frac{\nabla T}{T} \right), \quad (\text{C.13})$$

$$\mathbf{j}_Q = L_{21} \left( \mathbf{E} + \frac{\nabla\mu}{e} \right) + L_{22} \left( -\frac{\nabla T}{T} \right). \quad (\text{C.14})$$

Our goal will be determine these coefficients  $L_{ij}$ , for what we must now introduce the Boltzmann equation and the relaxation time approximation.

The occupation of electronic states in a system in thermal equilibrium is characterized by the Fermi-Dirac distribution function, which is expressed by

$$f_0(\mathbf{k}) = \frac{1}{e^{\frac{\epsilon_{\mathbf{k}} - \mu}{k_B T}} + 1}, \quad (\text{C.15})$$

or if the temperature distribution and the chemical potential are not uniform, by

$$f_0(\mathbf{r}, \mathbf{k}) = \frac{1}{e^{\frac{\epsilon_{\mathbf{k}} - \mu(\mathbf{r})}{k_B T(\mathbf{r})}} + 1}. \quad (\text{C.16})$$

In the semi-classical approximation, which will be used in this case, the non-equilibrium state can be specified also by a non-equilibrium distribution function that can be derived through semi-classical arguments. To define this non-equilibrium transport distribution function we consider a point in the phase space of coordinates  $\mathbf{r}, \mathbf{k}$ , to which an infinitesimal volume  $d\mathbf{r}d\mathbf{k}$  is associated. If we now define the number of particles inside this volume element at a time  $t$  as  $dN(\mathbf{r}, \mathbf{k}, t)$ , the non-equilibrium distribution function  $f(\mathbf{r}, \mathbf{k}, t)$  is then defined by

$$dN(\mathbf{r}, \mathbf{k}, t) = f(\mathbf{r}, \mathbf{k}, t) \frac{d\mathbf{r}d\mathbf{k}}{4\pi^3}. \quad (\text{C.17})$$

This equation already includes the factor 2 which takes into account both spin species. To determine the non-equilibrium distribution function, we must study the motion of the particles inside the volume  $d\mathbf{r}d\mathbf{k}$  in the phase space. If there are no collisions in the system, the position  $\mathbf{r}$  and the momentum  $\mathbf{k}$  after a time  $dt$  will be related by  $\mathbf{r}' = \mathbf{r} + \dot{\mathbf{r}}dt$  and  $\mathbf{k}' = \mathbf{k} + \dot{\mathbf{k}}dt$ , while the time evolves like  $t' = t + dt$ . Since the number of particles is conserved, we have

$$f(\mathbf{r}, \mathbf{k}, t)d\mathbf{r}d\mathbf{k} = f(\mathbf{r} + \dot{\mathbf{r}}dt, \mathbf{k} + \dot{\mathbf{k}}dt, t + dt)d\mathbf{r}'d\mathbf{k}', \quad (\text{C.18})$$

and since Liouville's theorem states that the volume of the phase space is constant

( $d\mathbf{r}d\mathbf{k} = d\mathbf{r}'d\mathbf{k}'$ ) then we end having

$$f(\mathbf{r}, \mathbf{k}, t) = f(\mathbf{r} + \dot{\mathbf{r}}dt, \mathbf{k} + \dot{\mathbf{k}}dt, t + dt). \quad (\text{C.19})$$

Now, expanding the first term in the linear order for small time differences we obtain

$$\frac{df(\mathbf{r}, \mathbf{k}, t)}{dt} = \frac{\partial f}{\partial t} + \dot{\mathbf{r}} \cdot \frac{\partial f}{\partial \mathbf{r}} + \dot{\mathbf{k}} \cdot \frac{\partial f}{\partial \mathbf{k}} = 0, \quad (\text{C.20})$$

also known as the equation of continuity in the phase space. On the other hand, when scattering is present, we can write

$$f(\mathbf{r} + \dot{\mathbf{r}}dt, \mathbf{k} + \dot{\mathbf{k}}dt, t + dt) = f(\mathbf{r}, \mathbf{k}, t) + \left( \frac{\partial f(\mathbf{r}, \mathbf{k}, t)}{\partial t} \right)_{coll} dt, \quad (\text{C.21})$$

and expanding in linear order in  $dt$  like we did in the previous case we end up with

$$\frac{\partial f}{\partial t} + \dot{\mathbf{r}} \cdot \frac{\partial f}{\partial \mathbf{r}} + \dot{\mathbf{k}} \cdot \frac{\partial f}{\partial \mathbf{k}} = \left( \frac{\partial f}{\partial t} \right)_{coll}, \quad (\text{C.22})$$

which is known as the Boltzmann equation or Boltzmann transport equation. In the semi-classical approximation we have  $\dot{\mathbf{r}} = \mathbf{v}_{\mathbf{k}} = (1/\hbar)(\partial\epsilon_{\mathbf{k}}/\partial\mathbf{k})$  and  $\hbar\dot{\mathbf{k}} = -e(\mathbf{E} + \mathbf{v}_{\mathbf{k}} \times \mathbf{B})$  so the Boltzmann equation can be written like

$$\cancel{\frac{\partial f}{\partial t}} + \mathbf{v}_{\mathbf{k}} \cdot \frac{\partial f}{\partial \mathbf{r}} - \frac{e}{\hbar}(\mathbf{E} + \mathbf{v}_{\mathbf{k}} \times \mathbf{B}) \cdot \frac{\partial f}{\partial \mathbf{k}} = \left( \frac{\partial f}{\partial t} \right)_{coll}, \quad (\text{C.23})$$

where the first term cancels out due to the fact that calculating transport properties demands starting from the steady-state condition.

Now it is the time to make a new approximation, which consists in assuming that the distribution function  $f$  will be just slightly different from the thermal-equilibrium function  $f_0$ . Using the notation  $f = f_0 + f_1$  where  $f_1$  is that slightly different part, the Boltzmann equation can be transformed into an equation for  $f_1$ , the deviation from the thermal-equilibrium distribution. We have that

$$\mathbf{v}_{\mathbf{k}} \cdot \frac{\partial f_0}{\partial \mathbf{r}} - \frac{e}{\hbar}(\mathbf{E} + \mathbf{v}_{\mathbf{k}} \times \mathbf{B}) \cdot \frac{\partial f_0}{\partial \mathbf{k}} = \left( \frac{\partial f}{\partial t} \right)_{coll} - \mathbf{v}_{\mathbf{k}} \cdot \frac{\partial f_1}{\partial \mathbf{r}} + \frac{e}{\hbar}(\mathbf{E} + \mathbf{v}_{\mathbf{k}} \times \mathbf{B}) \cdot \frac{\partial f_1}{\partial \mathbf{k}}. \quad (\text{C.24})$$

Considering that the thermal-equilibrium distribution function is in its more general form, this means,  $f_0 = f_0(\mathbf{r}, \mathbf{k})$ , using the expression (C.16) in the last eq. (C.24) leads us, after some manipulations, to

$$\frac{\partial f_0}{\partial \epsilon_{\mathbf{k}}} \mathbf{v}_{\mathbf{k}} \cdot \left[ -e \left( \mathbf{E} + \frac{\nabla \mu}{e} \right) - (\epsilon_{\mathbf{k}} - \mu) \frac{\nabla T}{T} \right] = \left( \frac{\partial f}{\partial t} \right)_{coll} - \mathbf{v}_{\mathbf{k}} \cdot \frac{\partial f_1}{\partial \mathbf{r}} + \frac{e}{\hbar}(\mathbf{v}_{\mathbf{k}} \times \mathbf{B}) \cdot \frac{\partial f_1}{\partial \mathbf{k}}. \quad (\text{C.25})$$

Note that the term with  $\mathbf{B}$  disappears since we have a product of the form  $\mathbf{v}_{\mathbf{k}} \cdot (\mathbf{v}_{\mathbf{k}} \times$

$\mathbf{B}$ ), which is 0 by definition. Also  $\mathbf{E}$  has disappeared on the right since  $f_1$  itself is proportional to the electric field, which would lead to a higher order correction. A lot of considerations can be made over the different terms on the right-hand side of this equation, like studying the main dependences of the scattering processes as well as making some assumptions on the shape of  $f_1$  in order to simplify the calculations to be done. At this point is where the relaxation time approximation turns to be very helpful.

### C.1.1 Relaxation time approximation

The relaxation time approximation is the simplest approximation which can be made to determine the distribution function by direct integration of the Boltzmann equation. For it to be carried out, there must be only collisions in the system that fulfill the following conditions:

1. The collisions should not modify the distribution function in the thermal equilibrium.
2. After each collision, the distribution function should be independent of the state before the collision, this means that the system should have no “memory” of which was its previous state before the collision.

In that case, if there were only collisions in the system, then it would relax towards the equilibrium state with a characteristic time  $\tau(\mathbf{r}, \mathbf{k})$  called relaxation time.

In our case, when  $\mathbf{B} = 0$  and the driving forces are uniform we could assume the relaxation time approximation. That way, we can neglect all the terms in the right-hand side of (C.25) involving  $f_1$  (which will be spatially uniform due to the fact of having a zero magnetic field), and write the collision term in a very simplified way, ending with

$$\frac{\partial f_0}{\partial \epsilon_{\mathbf{k}}} \mathbf{v}_{\mathbf{k}} \left[ -e \left( \mathbf{E} + \frac{\nabla \mu}{e} \right) - (\epsilon_{\mathbf{k}} - \mu) \frac{\nabla T}{T} \right] = -\frac{f(\mathbf{k}) - f_0(\mathbf{k})}{\tau_{\mathbf{k}}}. \quad (\text{C.26})$$

which can be easily solved obtaining

$$f(\mathbf{k}) = f_0(\mathbf{k}) + \left( -\frac{\partial f_0}{\partial \epsilon_{\mathbf{k}}} \right) \tau_{\mathbf{k}} \mathbf{v}_{\mathbf{k}} \left[ -e \left( \mathbf{E} + \frac{\nabla \mu}{e} \right) - (\epsilon_{\mathbf{k}} - \mu) \frac{\nabla T}{T} \right]. \quad (\text{C.27})$$

This means that the non-equilibrium distribution function under the relaxation time approximation is directly the distribution function in thermal equilibrium plus some corrections which are linear in the temperature gradient, chemical potential gradient and electric field (electric potential gradient). This deviation from the equilibrium turns out to determine the distribution of the particles which are responsible for the transport phenomena. If we try now to determine the electric current or the heat

current in a system in which driving forces are present, with the help of eqs. (C.2) and (C.4) we will have for the electric current

$$\mathbf{j}_e = -e \int \frac{d\mathbf{k}}{4\pi^3} \mathbf{v}_\mathbf{k} [f(\mathbf{k}) - f_0(\mathbf{k})], \quad (\text{C.28})$$

and for the heat current

$$\mathbf{j}_Q = \int \frac{d\mathbf{k}}{4\pi^3} (\epsilon_\mathbf{k} - \mu) \mathbf{v}_\mathbf{k} [f(\mathbf{k}) - f_0(\mathbf{k})]. \quad (\text{C.29})$$

Now, if we rewrite eqs. (C.13) and (C.14)

$$\begin{aligned} \mathbf{j}_e &= \mathsf{L}_{11} \left( \mathbf{E} + \frac{\nabla\mu}{e} \right) + \mathsf{L}_{12} \left( -\frac{\nabla T}{T} \right) \\ \mathbf{j}_Q &= \mathsf{L}_{21} \left( \mathbf{E} + \frac{\nabla\mu}{e} \right) + \mathsf{L}_{22} \left( -\frac{\nabla T}{T} \right), \end{aligned}$$

taking into account Ohm's law ( $\mathbf{j}_e = \sigma \mathbf{E}$ ), Fourier's law of thermal conduction ( $\mathbf{j}_Q = -\kappa \nabla T$ ) and the Seebeck effect ( $S = \nabla\varphi / \nabla T$ ) under their strict definition, this means, only with the correct driving forces present in the system, it is very straightforward to obtain the expression for the tensorial quantities in the relaxation time approximation

$$\sigma = \mathsf{L}_{11} = e^2 \int \frac{d\mathbf{k}}{4\pi^3} \left( -\frac{\partial f_0}{\partial \epsilon_\mathbf{k}} \right) \tau_\mathbf{k} \mathbf{v}_\mathbf{k} \otimes \mathbf{v}_\mathbf{k} \quad (\text{C.30})$$

$$S = \frac{\mathsf{L}_{12}}{T \mathsf{L}_{11}} = \frac{-e}{T \sigma} \int \frac{d\mathbf{k}}{4\pi^3} \left( -\frac{\partial f_0}{\partial \epsilon_\mathbf{k}} \right) \tau_\mathbf{k} \mathbf{v}_\mathbf{k} \otimes \mathbf{v}_\mathbf{k} (\epsilon_\mathbf{k} - \mu), \quad (\text{C.31})$$

having introduced the dyadic product of the velocities  $\mathbf{v}_\mathbf{k} \otimes \mathbf{v}_\mathbf{k}$  in order to obtain the tensorial quantities. If we want to obtain each component, we will have

$$\sigma_{ij} = e^2 \int \frac{d\mathbf{k}}{4\pi^3} \left( -\frac{\partial f_0}{\partial \epsilon_\mathbf{k}} \right) \tau_\mathbf{k} v_{i,\mathbf{k}} v_{j,\mathbf{k}}, \quad (\text{C.32})$$

$$S_{ij} = \frac{-e}{T \sigma_{ij}} \int \frac{d\mathbf{k}}{4\pi^3} \left( -\frac{\partial f_0}{\partial \epsilon_\mathbf{k}} \right) \tau_\mathbf{k} v_{i,\mathbf{k}} v_{j,\mathbf{k}} (\epsilon_\mathbf{k} - \mu). \quad (\text{C.33})$$

We now introduce a mathematical relation which will make easy to treat this expressions. This relation comes directly from the definition of the density of states and is obtained using the properties of the Dirac delta function. We use

$$d\mathbf{k} = d\mathcal{S} dk_\perp = \frac{d\mathcal{S} d\epsilon}{|\nabla_\mathbf{k} \epsilon|} \quad (\text{C.34})$$

to rewrite the differentials of the integrals, and then we use

$$g(\epsilon) = 2 \sum_{\mathbf{k}} \delta(\epsilon_{\mathbf{k}} - \epsilon) = \frac{1}{4\pi^3} \int_{\epsilon_{\mathbf{k}}=\epsilon} \frac{d\mathbf{S}}{|\nabla_{\mathbf{k}}\epsilon|}, \quad (\text{C.35})$$

in which a factor of 2 has been included to take both spin orientations into account. With that we can easily rewrite for the electrical conductivity

$$\begin{aligned} \sigma_{ij} &= e^2 \int d\epsilon \left( -\frac{\partial f_0}{\partial \epsilon} \right) \frac{1}{4\pi^3} \int_{\epsilon_{\mathbf{k}}=\epsilon} \frac{d\mathbf{S}}{|\nabla_{\mathbf{k}}\epsilon|} \tau_{\mathbf{k}} v_{i,\mathbf{k}} v_{j,\mathbf{k}} \\ &= e^2 \int d\epsilon \left( -\frac{\partial f_0}{\partial \epsilon} \right) 2 \sum_{\mathbf{k}} \tau_{\mathbf{k}} v_{i,\mathbf{k}} v_{j,\mathbf{k}} \delta(\epsilon_{\mathbf{k}} - \epsilon) \\ &= e^2 \int d\epsilon \left( -\frac{\partial f_0}{\partial \epsilon} \right) \Xi_{ij}(\epsilon), \end{aligned} \quad (\text{C.36})$$

whereas for the Seebeck coefficient

$$\begin{aligned} S_{ij} &= \frac{-e}{T\sigma_{ij}} \int d\epsilon \left( -\frac{\partial f_0}{\partial \epsilon} \right) (\epsilon - \mu) \frac{1}{4\pi^3} \int_{\epsilon_{\mathbf{k}}=\epsilon} \frac{d\mathbf{S}}{|\nabla_{\mathbf{k}}\epsilon|} \tau_{\mathbf{k}} v_{i,\mathbf{k}} v_{j,\mathbf{k}} \\ &= \frac{-e}{T\sigma_{ij}} \int d\epsilon \left( -\frac{\partial f_0}{\partial \epsilon} \right) (\epsilon - \mu) 2 \sum_{\mathbf{k}} \tau_{\mathbf{k}} v_{i,\mathbf{k}} v_{j,\mathbf{k}} \delta(\epsilon_{\mathbf{k}} - \epsilon) \\ &= \frac{-e}{T\sigma_{ij}} \int d\epsilon \left( -\frac{\partial f_0}{\partial \epsilon} \right) \Xi_{ij}(\epsilon) (\epsilon - \mu). \end{aligned} \quad (\text{C.37})$$

In the former derivations we have separated the derivative of the Fermi function since it depends only on the energy and not on the wave vector  $\mathbf{k}$ . We have also defined the transport distribution function  $\Xi_{ij}(\epsilon)$  like

$$\Xi_{ij}(\epsilon) = 2 \sum_{\mathbf{k},m} \tau_{\mathbf{k},m} v_{i,\mathbf{k},m} v_{j,\mathbf{k},m} \delta(\epsilon - \epsilon_{\mathbf{k},m}), \quad (\text{C.38})$$

where the index  $\mathbf{k}$  runs along the different k-points in the First Brillouin Zone and the index  $m$  is used to label the different orbitals (bands) which contribute to the thermoelectric coefficients (in this case the Fe- $d$  orbitals). The factor 2 is to account for spin degeneracy. The velocities  $\mathbf{v}_{\mathbf{k},m}$  are calculated as the group velocities of the dispersion relation of the energy bands

$$\mathbf{v}_{\mathbf{k},m} = \frac{1}{\hbar} \frac{\partial \epsilon_{\mathbf{k},m}}{\partial \mathbf{k}}. \quad (\text{C.39})$$

## C.2 Sommerfeld expansion for the transport coefficients

The Sommerfeld expansion is a very useful tool to calculate integrals which involve the Fermi-Dirac distribution function. In this particular case, we will derive the analytic expressions for the equations obtained solving the Boltzmann Transport equation in the relaxation time approximation. In these last two equations we have that the carrier distribution function in the steady state will be proportional to the energy derivative of the Fermi function. One typically uses the Sommerfeld expansion when facing integrals of the type

$$I = \int_{-\infty}^{+\infty} d\epsilon H(\epsilon) f_0(\epsilon). \quad (\text{C.40})$$

We can define the function

$$K(\epsilon) = \int_{-\infty}^{\epsilon} dx H(x), \quad (\text{C.41})$$

which satisfies the condition

$$H(\epsilon) = \frac{dK(\epsilon)}{d\epsilon}. \quad (\text{C.42})$$

Integrating by parts in eq. (C.40) we have

$$I = \int_{-\infty}^{+\infty} d\epsilon H(\epsilon) f_0(\epsilon) = \cancel{K(\epsilon) f_0(\epsilon) \Big|_{-\infty}^{+\infty}} - \int_{-\infty}^{+\infty} d\epsilon \left( \frac{\partial f_0}{\partial \epsilon} \right) K(\epsilon) \quad (\text{C.43})$$

in which the first term cancels out because in the limits the product of the Fermi function times  $K(\epsilon)$  goes to zero. One has that

$$I = \int_{-\infty}^{+\infty} d\epsilon \left( -\frac{\partial f_0}{\partial \epsilon} \right) K(\epsilon) \quad (\text{C.44})$$

which is equivalent to eq. (C.40) but in terms of the derivative of the Fermi function. The next step now is to write the Taylor expansion of  $K(\epsilon)$  around  $\epsilon = \mu$

$$K(\epsilon) \approx K(\mu) + \sum_{n=1}^{\infty} \left[ \frac{(\epsilon - \mu)^n}{n!} \right] \frac{d^n K(\epsilon)}{d\epsilon^n} \Big|_{\epsilon=\mu} \quad (\text{C.45})$$

If we now insert eq. (C.45) in eq. (C.44) we will have

$$\int_{-\infty}^{+\infty} d\epsilon \left( -\frac{\partial f_0}{\partial \epsilon} \right) K(\epsilon) \approx K(\mu) \int_{-\infty}^{\infty} d\epsilon \left( -\frac{\partial f_0}{\partial \epsilon} \right) + \sum_{n=1}^{\infty} \frac{K^{(n)}(\mu)}{n!} \int_{-\infty}^{\infty} d\epsilon \left( -\frac{\partial f_0}{\partial \epsilon} \right) (\epsilon - \mu)^n. \quad (\text{C.46})$$

In the last equation, the integral in the first term on the right hand side is equal (by definition) to 1 and on the second term of that right hand side, the odd powers of  $n$  cancel out due to the fact that the integrand will be odd since the energy of the Fermi function is an even function centered at the chemical potential. This allow us to rewrite

$$\begin{aligned}
 \int_{-\infty}^{+\infty} d\epsilon \left( -\frac{\partial f_0}{\partial \epsilon} \right) K(\epsilon) &\approx K(\mu) + \sum_{n=1}^{\infty} \frac{K^{(2n)}(\mu)(k_B T)^{2n}}{2n!} \int_{-\infty}^{\infty} d\epsilon \left( -\frac{\partial f_0}{\partial \epsilon} \right) \left( \frac{\epsilon - \mu}{k_B T} \right)^{2n} \\
 &= K(\mu) + \sum_{n=1}^{\infty} K^{(2n)}(\mu)(k_B T)^{2n} \int_{-\infty}^{\infty} dx \frac{x^{2n}}{(2n)!} \left[ -\frac{d}{dx} \left( \frac{1}{e^x + 1} \right) \right] \\
 &= K(\mu) + \sum_{n=1}^{\infty} K^{(2n)}(\mu)(k_B T)^{2n} a_n,
 \end{aligned} \tag{C.47}$$

where we have made the change of variable  $x = (\epsilon - \mu)/k_B T$  and we identify  $a_n$  with the integrals on the second term of the right hand side of the second row with a minus sign. These integrals can be solved exactly with the help of the Riemann zeta function as

$$a_n = \int_{-\infty}^{\infty} dx \frac{x^{2n}}{(2n)!} \left[ -\frac{d}{dx} \left( \frac{1}{e^x + 1} \right) \right] = \dots = \left( 2 - \frac{1}{2^{2(n-1)}} \right) \zeta(2n). \tag{C.48}$$

We now write the expansion up to  $n = 1$  (for which  $\zeta(2) = \pi^2/6$ ), which will lead us to the final result we will use to perform our integrals of the form of eq. (C.44)

$$\int_{-\infty}^{+\infty} d\epsilon \left( -\frac{\partial f_0}{\partial \epsilon} \right) K(\epsilon) = K(\mu) + \frac{\pi^2}{6} (k_B T)^2 K''(\mu). \tag{C.49}$$

If we apply this equation to the integrals (C.36) and (C.37) we will obtain for the electrical conductivity tensor

$$\sigma_{ij} = e^2 \int_{-\infty}^{+\infty} d\epsilon \left( -\frac{\partial f_0}{\partial \epsilon} \right) \Xi_{ij}(\epsilon) = e^2 \left[ \Xi_{ij}(\mu) + \frac{\pi^2}{6} (k_B T)^2 \Xi_{ij}''(\mu) \right], \tag{C.50}$$

and for the thermoelectric tensor

$$\begin{aligned}
 S_{ij} &= \frac{-e}{T\sigma_{ij}} \int_{-\infty}^{+\infty} d\epsilon \left( -\frac{\partial f_0}{\partial \epsilon} \right) \Xi_{ij}(\epsilon)(\epsilon - \mu) \\
 &= \frac{-e}{T\sigma_{ij}} \left[ \Xi_{ij}(\epsilon)(\epsilon - \mu) + \frac{\pi^2}{6} (k_B T)^2 \frac{d^2}{d\epsilon^2} (\Xi_{ij}(\epsilon)(\epsilon - \mu)) \right]_{\epsilon=\mu} \\
 &= -\frac{e\pi^2 k_B^2 T}{3\sigma_{i,j}} \Xi_{ij}' \approx -\frac{\pi^2 k_B^2 T}{3e} \frac{\Xi_{ij}'(\mu)}{\Xi_{ij}(\mu)},
 \end{aligned} \tag{C.51}$$

where we have made an extra approximation in order to remain with a linear term in temperature.

### C.3 Sommerfeld coefficient

We are now going to determine the Sommerfeld coefficient for the specific heat of the free-electron gas with the help of the Sommerfeld expansion, that we write now explicitly for  $H(\epsilon) = K'(\epsilon)$  to first order  $n = 1$  (second order in temperature) following eqs. (C.43) and (C.49) like

$$\int_{-\infty}^{\infty} d\epsilon f(\epsilon)H(\epsilon) \approx \int_{-\infty}^{\mu} d\epsilon H(\epsilon) + \frac{\pi^2}{6}(k_B T)^2 H'(\mu) + \mathcal{O}(T^4). \quad (\text{C.52})$$

The specific heat is defined like

$$c_V = \frac{\partial u}{\partial T}, \quad (\text{C.53})$$

where  $u$  is the total energy of the electron gas which can be easily calculated through the equation

$$u = \int_{-\infty}^{\infty} d\epsilon f(\epsilon)D(\epsilon)\epsilon, \quad (\text{C.54})$$

where  $D(\epsilon)$  is the density of states of the system. If we now make use of eq. (C.52) we can rewrite the last expression as

$$u \approx \int_{-\infty}^{\mu} d\epsilon D(\epsilon)\epsilon + \frac{\pi^2}{6}(k_B T)^2 (D'(\mu)\mu + D(\mu)). \quad (\text{C.55})$$

We introduce the Sommerfeld expansion for the number of particles in the system like

$$n = \int_{-\infty}^{\infty} d\epsilon f(\epsilon)D(\epsilon) \approx \int_{-\infty}^{\mu} d\epsilon D(\epsilon) + \frac{\pi^2}{6}(k_B T)^2 D'(\mu). \quad (\text{C.56})$$

It is known that for low temperatures, the chemical potential  $\mu$  barely differs from the Fermi energy  $\epsilon_F$ , so it is possible to expand the upper limit of the previous integral about  $\epsilon_F$  and rewrite the expression as

$$n = \int_{-\infty}^{\epsilon_F} d\epsilon D(\epsilon) + (\mu - \epsilon_F)D(\epsilon_F) + \frac{\pi^2}{6}(k_B T)^2 D'(\epsilon_F). \quad (\text{C.57})$$

Since we are in a system with constant density of particles, the term on the left hand side and the integral on the right cancel each other, and we obtain

$$0 = (\mu - \epsilon_F)D(\epsilon_F) + \frac{\pi^2}{6}(k_B T)^2 D'(\epsilon_F). \quad (\text{C.58})$$

If now we follow the same procedure of expanding the upper limit of the integral in eq. (C.55) we will have

$$u \approx \int_{-\infty}^{\epsilon_F} d\epsilon D(\epsilon)\epsilon + (\mu - \epsilon_F)D(\epsilon_F)\epsilon_F + \frac{\pi^2}{6}(k_B T)^2(D'(\epsilon_F)\epsilon_F + D(\epsilon_F)). \quad (\text{C.59})$$

Rewriting it and taking into account eq. (C.58) we have that

$$\begin{aligned} u &\approx \int_{-\infty}^{\epsilon_F} d\epsilon D(\epsilon)\epsilon + \epsilon_F \left[ (\mu - \epsilon_F)D(\epsilon_F) + \frac{\pi^2}{6}(k_B T)^2 D'(\epsilon_F) \right] + \frac{\pi^2}{6}(k_B T)^2 D(\epsilon_F) \\ &= u_0 + \frac{\pi^2}{6}(k_B T)^2 D(\epsilon_F). \end{aligned} \quad (\text{C.60})$$

Finally the specific heat will be

$$c = \frac{\pi^2}{3} D(\epsilon_F) k_B^2 T. \quad (\text{C.61})$$

The Sommerfeld coefficient  $\gamma$  is the slope of the curve of the specific heat with the temperature  $c = \gamma T$ , then

$$\gamma = \frac{\pi^2}{3} D(\epsilon_F) k_B^2. \quad (\text{C.62})$$



# D Green's functions formalism

Here we present a basic collection of formulas and derivations that may be particularly useful to understand Section 2.4 where DMFT is presented.

## D.1 Quick reminder about statistical mechanics

Let's consider a system with a Hamiltonian  $\hat{\mathcal{H}}$  from which we know its eigenvalues  $E_n$  and eigenvectors  $|n\rangle$ . The probability to find the system in a state  $|n\rangle$  with an energy  $E_n$  at a temperature  $T$  is given by

$$p_n = \frac{e^{-\beta E_n}}{\mathcal{Z}}, \quad \text{where} \quad \beta = \frac{1}{k_B T}, \quad (\text{D.1})$$

where we introduce the partition function  $\mathcal{Z}$  of such a system in three equivalent ways.

$$\mathcal{Z} = \sum_n e^{-\beta E_n} = \sum_n \langle n | e^{-\beta \hat{\mathcal{H}}} | n \rangle = \text{Tr} \left( e^{-\beta \hat{\mathcal{H}}} \right). \quad (\text{D.2})$$

With this we can write the thermal expectation value of an operator  $A$  of the system like

$$\langle A \rangle = \frac{\text{Tr}(A e^{-\beta \hat{\mathcal{H}}})}{\mathcal{Z}} = \sum_n \frac{\langle n | A e^{-\beta \hat{\mathcal{H}}} | n \rangle}{\mathcal{Z}} = \sum_n p_n \langle n | A | n \rangle. \quad (\text{D.3})$$

## D.2 Green's function

A system can be characterized by its responses and a very particular type of response is that of a system whenever we add a particle to it. This is fully described by the so-called retarded Green's function, that can be defined like:

$$G_{ab}(t - t') = -i\Theta(t - t') \left\langle \{c_a(t), c_b^\dagger(t')\} \right\rangle, \quad (\text{D.4})$$

where the operators  $c, c^\dagger$  act on the one-particle states  $a, b$  of the Hamiltonian  $\hat{\mathcal{H}}$ . In the Heisenberg picture, these creation and annihilation operators are written like:

$$c(t) = e^{i\hat{\mathcal{H}}t} c e^{-i\hat{\mathcal{H}}t} \quad \text{and} \quad c^\dagger(t) = e^{i\hat{\mathcal{H}}t} c^\dagger e^{-i\hat{\mathcal{H}}t}. \quad (\text{D.5})$$

Now, we can expand expression (D.4) according to eq. (D.3) and plug these operators in. We will obtain:

$$\begin{aligned}
 G_{ab}(t-t') &= -i\Theta(t-t') \left\langle \left[ c_a(t)c_b^\dagger(t') + c_b^\dagger(t')c_a(t) \right] \right\rangle \\
 &= -i\Theta(t-t') \sum_n p_n \langle n | \left[ c_a(t)c_b^\dagger(t') + c_b^\dagger(t')c_a(t) \right] | n \rangle \\
 &= -i\Theta(t-t') \sum_{n,m} p_n \langle n | \left[ c_a(t) | m \rangle \langle m | c_b^\dagger(t') + c_b^\dagger(t') | m \rangle \langle m | c_a(t) \right] | n \rangle \\
 &= -i\Theta(t-t') \sum_{n,m} p_n \left( \langle n | c_a(t) | m \rangle \langle m | c_b^\dagger(t') | n \rangle \right. \\
 &\quad \left. + \langle n | c_b^\dagger(t') | m \rangle \langle m | c_a(t) | n \rangle \right) \\
 &= -i\Theta(t-t') \sum_{n,m} p_n \left( \langle n | e^{i\hat{H}t} c_a e^{-i\hat{H}t} | m \rangle \langle m | e^{i\hat{H}t'} c_b^\dagger e^{-i\hat{H}t'} | n \rangle \right. \\
 &\quad \left. + \langle n | e^{i\hat{H}t'} c_b^\dagger e^{-i\hat{H}t'} | m \rangle \langle m | e^{i\hat{H}t} c_a e^{-i\hat{H}t} | n \rangle \right) \\
 &= -i\Theta(t-t') \sum_{n,m} p_n \left( \langle n | c_a | m \rangle \langle m | c_b^\dagger | n \rangle e^{i(E_n - E_m)(t-t')} \right. \\
 &\quad \left. + \langle n | c_b^\dagger | m \rangle \langle m | c_a | n \rangle e^{-i(E_n - E_m)(t-t')} \right) \\
 &= -i\Theta(t-t') \sum_{n,m} (p_n + p_m) \langle n | c_a | m \rangle \langle m | c_b^\dagger | n \rangle e^{-i(\omega_{mn})(t-t')},
 \end{aligned} \tag{D.6}$$

where in the last step we have flipped the indices  $n \leftrightarrow m$  in the second term inside the summation, which introduces the  $p_m$  term in the pre-factor, and we have also defined  $\omega_{mn} = E_m - E_n$ . Now, if we Fourier transform that quantity to go in the frequency domain (simplifying the pre-factor including the summation in  $m$  and  $n$  of the thermal probabilities  $p_m$  and  $p_m$  times the matrix elements by calling it  $\mathcal{A}$ ) we will obtain:

$$\begin{aligned}
 G_{ab}(\omega) &= \mathcal{A} \int_{-\infty}^{\infty} e^{i\omega(t-t')} G_{ab}(t-t') \\
 &= \mathcal{A} \int_{-\infty}^{\infty} d(t-t') -i\Theta(t-t') e^{i\omega(t-t')} e^{-i\omega_{mn}(t-t')} \\
 &= -i\mathcal{A} \int_0^{\infty} d(t-t') e^{i(\omega - \omega_{mn})(t-t')} \\
 &= -i\mathcal{A} \frac{i}{\omega^+ - \omega_{mn}} \\
 &= \sum_{m,n} (p_n + p_m) \frac{\langle n | c_a | m \rangle \langle m | c_b^\dagger | n \rangle}{\omega - \omega_{nm}},
 \end{aligned} \tag{D.7}$$

where we have made use of the Fourier transform of the  $\Theta$  function<sup>1</sup>.

### D.3 Finite temperature formalism

Since thermal averages usually involve a density matrix, with a thermal distribution given by  $e^{-\beta\hat{H}}$ , it is useful to represent time propagation in a similar manner. A usual trick is to express thermal averages as “equivalent” to a propagation in imaginary time  $\tau$  up to “time”  $\beta$ . That way, we can define correlation functions (like Green's functions) such that the time propagators are replaced by analogous operators using an imaginary time  $\tau$ . The Schrödinger evolution operation in this imaginary time can be defined like

$$\mathcal{U}_s(\tau) = e^{-\tau\hat{H}} \quad , \quad \text{and also} \quad \frac{\partial \mathcal{U}_s}{\partial \tau} = -\hat{H} \mathcal{U}_s. \quad (\text{D.8})$$

The Heisenberg picture of the operators in imaginary time can be written like

$$A(\tau) = e^{\tau\hat{H}} A e^{-\tau\hat{H}}. \quad (\text{D.9})$$

Now, we can write a general response function in imaginary time involving operators  $A$  and  $B$ . This will be

$$\chi_{AB}(\tau - \tau') = -\langle \mathcal{T}_\tau A(\tau) B(\tau') \rangle \quad \text{with} \quad \tau, \tau' \in (0, \beta) \quad (\text{D.10})$$

where  $\mathcal{T}_\tau$  is the time-ordering operator<sup>2</sup> in imaginary time, whose action on the operators  $A$  and  $B$  is the following:

$$\mathcal{T}_\tau A(\tau) B(\tau') = \begin{cases} A(\tau) B(\tau') & \text{if } \tau > \tau' \\ \pm B(\tau') A(\tau) & \text{if } \tau' > \tau \end{cases}, \quad (\text{D.11})$$

where the “+” sign is for bosonic operators and the “−” sign is for fermionic operators. Now, in eq. (D.10) we can define a new imaginary time  $\tau$  belonging now to the interval  $(-\beta, \beta)$  and thus rewrite

$$\chi_{AB}(\tau) = -\langle \mathcal{T}_\tau A(\tau) B(0) \rangle \quad (\text{D.12})$$

---

<sup>1</sup>The Fourier transform of the step function is defined like:  $\Theta(\omega^+) = \int_0^\infty e^{i\omega^+ t} dt = \frac{i}{\omega^+}$ , where  $\omega^+ = \omega + i\eta$ , and  $\eta$  is an infinitesimal positive real positive quantity that is sent to zero after having done all the calculations.

<sup>2</sup>This is actually not an operator in the quantum mechanical sense of the word, but a time-ordering rule. However, it is the convention in the field to call it like a time-ordering operator.

Let's study some properties of this response function in imaginary time. For instance, a very interesting property is that if  $\tau > 0$  we can write:

$$\chi_{AB}(\tau - \beta) = \pm \chi_{AB}(\tau), \quad (\text{D.13})$$

where again + is for bosons and - for fermions. It can be easily proved by applying the definition of the Heisenberg operators in eq. (D.9) and then using the cyclic invariance of the trace:

$$\begin{aligned} \chi_{AB}(\tau - \beta) &= - \langle \mathcal{T}_\tau A(\tau - \beta) B(0) \rangle = \mp \langle B(0) A(\tau - \beta) \rangle \\ &= \mp \text{Tr} \left( e^{-\beta \hat{H}} B e^{(\tau - \beta) \hat{H}} A e^{-(\tau - \beta) \hat{H}} \right) \\ &= \mp \text{Tr} \left( e^{-(\tau - \beta) \hat{H}} e^{-\beta \hat{H}} B e^{(\tau - \beta) \hat{H}} A \right) \\ &= \mp \text{Tr} \left( A e^{-(\tau - \beta) \hat{H}} e^{-\beta \hat{H}} B e^{(\tau - \beta) \hat{H}} \right) \\ &= \mp \text{Tr} \left( e^{(\tau - \beta) \hat{H}} A e^{-(\tau - \beta) \hat{H}} e^{-\beta \hat{H}} B \right) \\ &= \mp \text{Tr} \left( e^{-\beta \hat{H}} e^{\tau \hat{H}} A e^{-\tau \hat{H}} B \right) \\ &= \mp \langle A(\tau) B(0) \rangle = \pm \chi_{AB}(\tau). \end{aligned} \quad (\text{D.14})$$

Now, since we are dealing with a function that is defined in an interval  $[-\beta, \beta]$  we can always define its Fourier transform. In this case we will have:

$$\chi_{AB}(\tau) = \sum_n e^{-i\omega_n \tau} \chi_{AB}(i\omega_n), \quad \text{where } \omega_n = \frac{2\pi n}{2\beta} \quad (\text{D.15})$$

Now, if we substitute  $\tau \rightarrow \tau - \beta$  we will have:

$$\chi_{AB}(\tau - \beta) = \sum_n e^{-i\omega_n(\tau - \beta)} \chi_{AB}(i\omega_n) = \pm \chi_{AB}(\tau), \quad (\text{D.16})$$

where we have used the property in eq. (D.13). From this, we immediately see that these frequencies  $\omega_n$  have to fulfill the following condition:

$$e^{i\omega_n \beta} = \pm 1 \rightarrow \begin{cases} \omega_n = \frac{2n\pi}{\beta} & \text{for bosonic operators} \\ \omega_n = \frac{(2n+1)\pi}{\beta} & \text{for fermionic operators} \end{cases}. \quad (\text{D.17})$$

These frequencies are the so-called bosonic or fermionic Matsubara frequencies.

## E.1 Different limits for DMFT

The dynamical mean-field approximation is exact in two limits: the non-interacting limit and the atomic limit. It also provides the connection between them, which is the key aspect that allows to treat the intermediate coupling regime. The infinite coordination limit is another interesting case.

### E.1.1 The non-interacting limit

In this limit ( $U=0$ ), one has that  $G(i\omega_n) = \mathcal{G}_0$ , and that  $\Sigma_{imp} = 0$ . That way, the on-site Green's function  $G(i\omega_n)$  turns out to be the bare on-site Green's function,  $G(i\omega_n) = \sum_{\mathbf{k}} [i\omega_n + \mu - \varepsilon_0 - \varepsilon_{\mathbf{k}}]^{-1}$ . Obviously, DMFT is exact in this limit since the condition of having a local self-energy is automatically fulfilled since it vanishes.

### E.1.2 The atomic limit

This limit can be achieved if we make the hopping integrals to be zero ( $t_{ij} = 0$ ). In this case, one ends up having a set of independent atoms on each lattice site and thus there is no dispersion relation ( $\varepsilon_{\mathbf{k}}$ ). In this case, by applying (2.82) we realize that  $\Delta(i\omega_n) = 0$ , which is basically telling us that since all the atoms are independent, the mean field vanishes. In this case, the self energy will only have a local component, and thus DMFT is again exact in this limit.

### E.1.3 Infinite coordination limit

DMFT becomes also exact in the limit in which the connectivity  $z$  of the lattice is taken to infinity, which is also the case for the mean-field approximation in classical statistical mechanics. In that particular case, the exchange coupling between nearest-neighbor sites has to scale as  $J_{ij} = J/z$ , so that the Weiss mean field  $h_i^{eff} \approx h + zJm$  remains of order one. This condition also ensures that the entropy and the internal energy per site remains finite and hence the competition between these quantities which is essential for having some magnetic ordering is preserved.

In the case of quantum systems that DMFT has to deal with, an appropriate scaling has to be made in order to keep the same competition between delocalization due to kinetic energy and localization due to Coulomb repulsion. In this particular case, the nearest-neighbor hopping integrals must be scaled as  $t_{ij} = t/\sqrt{z}$ . That way, the non-interacting DOS  $D(\varepsilon)$  has a non trivial limit as  $z \rightarrow \infty$ . In practice, two lattices are considered in the  $z = \infty$  limit:

- The  $d$ -dimensional cubic lattice with  $z = 2d \rightarrow \infty$  and  $\varepsilon_{\mathbf{k}} = -2t \sum_{p=1}^d \cos(k_p)/\sqrt{z}$ . In this case the non-interacting DOS becomes a Gaussian.
- The Bethe lattice (Cayley tree) with coordination number  $z \rightarrow \infty$  and nearest-neighbor hopping  $t_{ij} = t/\sqrt{z}$ . In this case one has a semicircular DOS and the self-consistency condition can be inverted explicitly so one can relate the dynamical mean-field to the local Green's function as  $\Delta(i\omega_n) = t^2 G(i\omega_n)$ .

## E.2 Some remarks about the calculations

- $\Im G(i\omega_n^+ \rightarrow 0)$  has to be negative because the spectral function  $A(\omega) = -\frac{1}{\pi} \Im G(\omega)$  has to be equal or greater than zero.
- If  $\Im G(\omega = 0) = 0$  then the system is an insulator (there is no spectral weight at zero energy/frequency). If it is different from zero, the system is a metal.
- To determine the mass enhancement in DMFT one has to write the lattice Green's function in the Matsubara axis and expand the self-energy to the linear term in  $i\omega$ . There will be 3 terms then:  $\Re \Sigma$  that will renormalize the chemical potential,  $\Im \Sigma$  which is a damping term and a coefficient with  $i\omega$ . Since the expansion is in the Matsubara axis (purely complex frequency) the term that will determine the mass enhancement comes from the imaginary part of the self energy.
- If we are working on the real-frequency axis, then it is the real part of the self energy which determines the mass enhancement, but in the imaginary frequency axis one has to use the imaginary part of the self-energy (this is due to the Cauchy-Riemann equations).

# F

## Heavy-fermionic behavior of the 122 family of IBSC

### F.1 Van Hove singularities in the 122 family of IBSC

**Table F.1:** Lattice parameters and relevant atomic positions of  $\text{KFe}_2\text{As}_2$  taken from different references.

Convention	$a = b(\text{\AA})$	$c(\text{\AA})$	$z_{\text{As}}$	Comments
Avci	3.8251	13.7846	0.35314	[40]. Powder at low T.
Ours/Karlsruhe	3.844	13.916	0.35249	
Rosza	3.842	13.861	0.3525	[142].
Tafti	3.8502	13.853	0.35565	[143]. Extrapolated from high-P in powder
Backes	3.8488	13.883	0.359337	[144], but extrapolated from [143].
Eilers	3.844	13.87	0.35241	[145]. At room T, 0.5 – 1% of impurities.

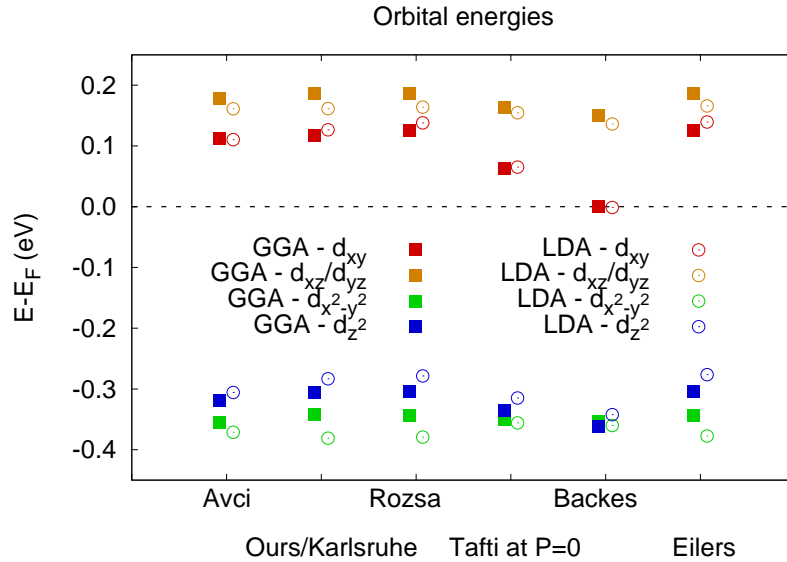


**Figure F.1:** Orbital energies of the bare electronic structure extracted from the tight-binding parametrizations of the DFT band structures having used the different lattice parameters from the references compiled in Table F.1.

In Table F.1 we present different sets of lattice parameters for  $\text{KFe}_2\text{As}_2$  that have been compiled from the literature. Although they all look very similar, there are certain differences in the resulting electronic structures simulated with those lattice parameters and internal atomic positions, as we have started discussing already in Section 4.3.1. The causes of these differences in the lattice parameters can be several: different sources of uncertainty from the experimental techniques, slightly different Rietveld refinements on each of the X-Ray diffraction measurements, different qualities of the samples, powder samples versus single crystals, or measurements at different temperatures, to name a few. One thing we should note is that our extrapolation from the high-pressure data of Tafti et al. [143] and the extrapolation performed in Ref. [144] (called “Tafti” and “Backes” respectively in our convention) slightly differ from one another but they are overall similar compared with the other values. However, these sets of parameters give different results than all the others as long as orbital energies and quasiparticle weights are concerned.

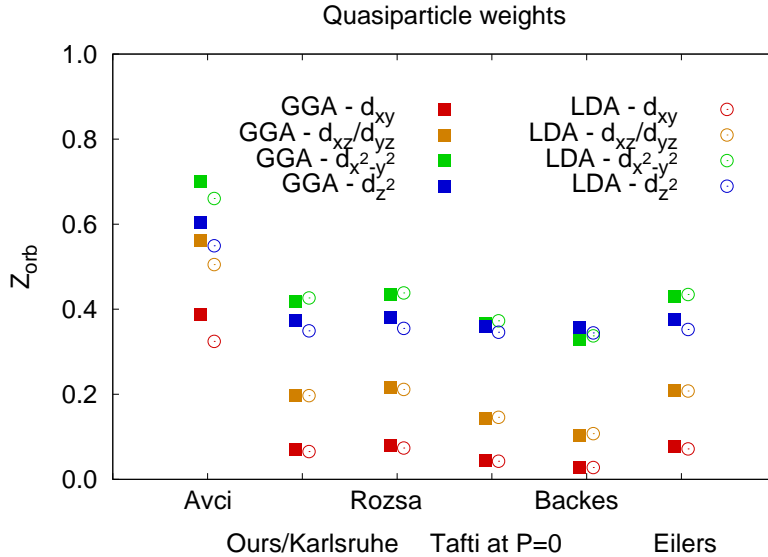


**Figure F.2:** Orbitally-resolved quasiparticle weights  $Z_m$  of  $\text{KFe}_2\text{As}_2$  calculated with a DFT+SSMFT scheme at  $U = 2.7$  eV and  $J/U = 0.25$ . The different sets of points correspond to the different sets of experimental lattice parameters enumerated in Table F.1.

In Fig. F.1 we show the orbital energies ( $\epsilon_m = t_{00}^{mm}$  in our formalism) for the different sets of lattice parameters, that is the main outcome of our DFT calculations. These values are obtained directly from the bare Hamiltonians resulting from the tight-binding parametrization of the DFT band structures and from them we can obtain the crystal-field splitting in  $\text{KFe}_2\text{As}_2$ . As we can see, in the cases corresponding to the lattice parameters from the high-pressure extrapolations (in our convention “Tafti” and “Backes”), the orbital energies differ much more from the other cases. The degeneracy in the  $e_g$  orbitals ( $d_{z^2}$  and  $d_{x^2-y^2}$ ) is almost suppressed compared to all the other cases. On the contrary, the energy difference among the  $t_{2g}$  orbitals

seems to be much larger than for the  $e_g$ , and this splitting is even further increased in the case of the lattice parameters coming from Ref. [143]. We attribute this difference to the extrapolation itself. In our case we assumed a linear dependence of the values of the lattice parameters for low values of pressure, but this may not be that case. In addition, high-pressure measurements are very invasive and the lattice parameters at low pressure may also correspond to samples that have been damaged if the measurements were started at high pressures. This result illustrates the importance of choosing a correct set of lattice parameters (and/or atomic positions) when doing simulations of a material. A more general tendency that is also seen for every case is that the splitting among the  $t_{2g}$  orbitals tends to be larger when using the exchange-correlation functional GGA-PBE [140] and on the contrary the splitting among the  $e_g$  orbitals is smaller. This whole tendency is inverted when one uses LDA instead. However, as we can see clearly, the main source of the different crystal-field splittings are the differences in the experimental lattice parameters, and not the choice of GGA-PBE versus LDA as an exchange-correlation functional.

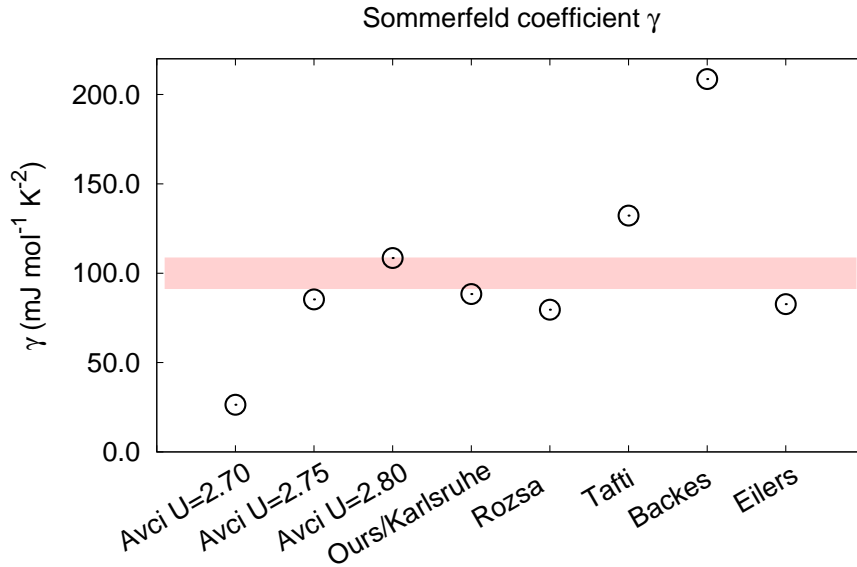


**Figure F.3:** Calculated Sommerfeld coefficient for  $\text{KFe}_2\text{As}_2$  with a local Coulomb interaction  $U = 2.7$  eV and a Hund’s coupling of  $J/U = 0.25$ . The different points correspond to a series of DFT calculations done using different values of the lattice parameters found in the literature.

Once correlations have been included with SSMFT, we can compare the differences in the orbitally-resolved quasiparticle weights obtained for  $\text{KFe}_2\text{As}_2$  at  $U = 2.7$  eV and  $J/U = 0.25$  which are the values that we conventionally choose for this compound. In general, we find an overall agreement among most of the cases, which is consistent with having found very similar bare electronic structures with DFT (very similar crystal-field splittings and DOS). However, interestingly we find that the results obtained in the case of lattice parameters from Avci et al. [40] point

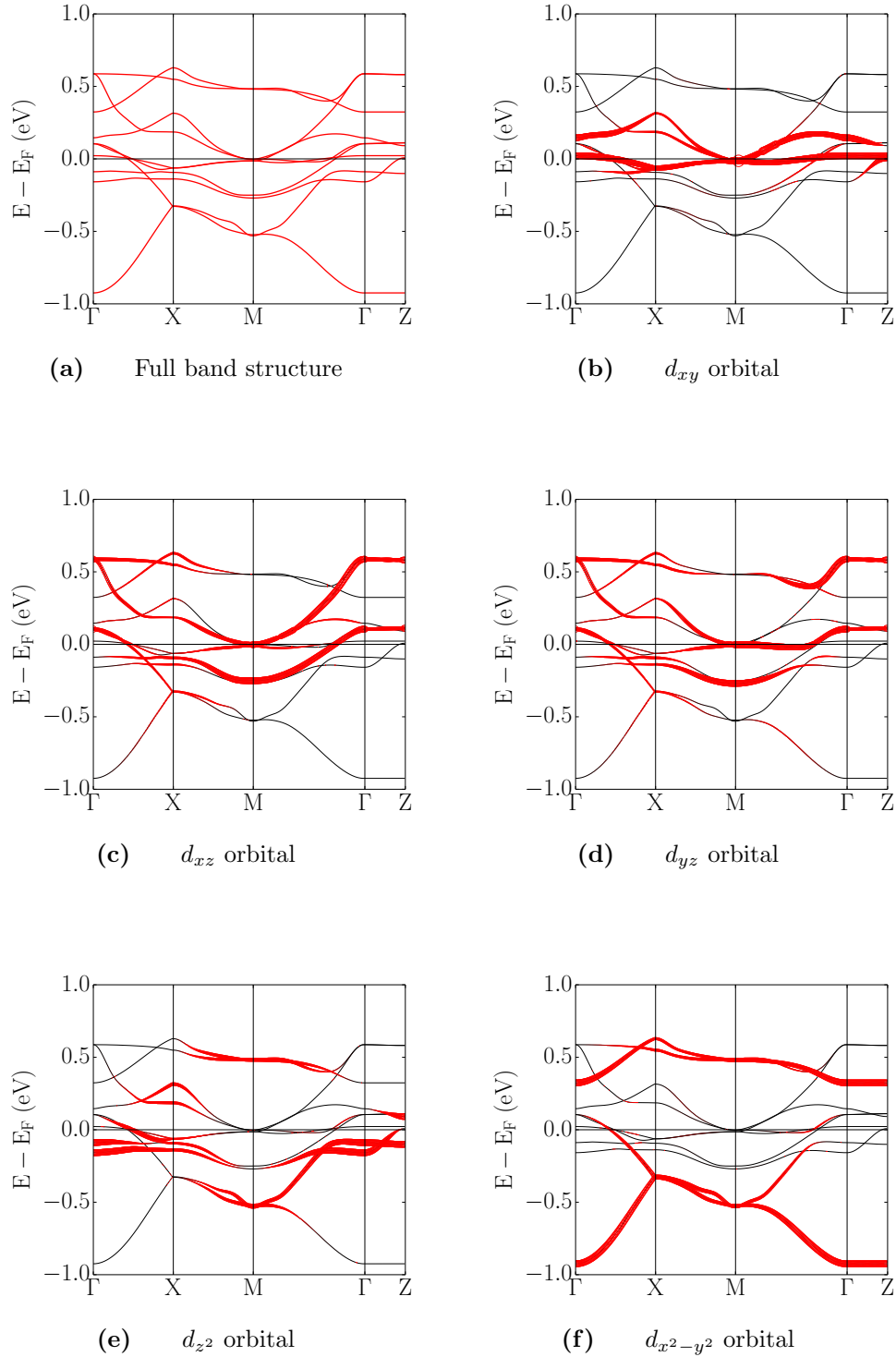


**Figure F.4:** Orbitaly-resolved weight of the renormalized band structure of  $\text{KFe}_2\text{As}_2$  calculated with SSMFT.

to a much less correlated compound at first sight. What is really happening is that in  $\text{KFe}_2\text{As}_2$ , the transition between a normal and a Hund's metal is very abrupt,

and in the case corresponding to these lattice parameters, that transition happens very close to  $U = 2.7$  eV. By slightly increasing the value of  $U$  to 2.75 eV the Hund's metal regime is achieved and then the results are essentially similar to all the rest, and at  $U = 2.80$  eV, the Hund's metal regime is completely achieved.

The calculated Sommerfeld coefficient is another quantity that is very sensitive to the correct description of electronic spectra around the Fermi level. We see that for all the cases in which the orbital energies and the quasiparticle weights are similar, the calculated Sommerfeld coefficient is in very good agreement with the experimental value  $100 \text{ mJ}\cdot\text{mol}^{-1}\text{K}^{-2}$ , as it can be seen in Fig. F.3. In general we can see that there are some differences, however they are small. We roughly find almost identical results using  $U = 2.7$  eV with the lattice parameters from the Karlsruhe group and  $U = 2.75$  eV with the lattice parameters from Ref. [40]. This is largely within the precision that we can ask to our semi-quantitative Slave-Spin approach, and even largely inside the error bars of present-day ab-initio estimates for the screened interactions, which for  $\text{KFe}_2\text{As}_2$  are  $U = 2.7$  eV and  $J/U = 0.25$  (the latter differs from ab-initio estimates and it is customarily adjusted for Slave-Spins).

Finally, in Fig. F.4 we show the so-called "fat bands" of the renormalized band structure of  $\text{KFe}_2\text{As}_2$  calculated with DFT+SSMFT. These show the orbital content of each of the bands. In particular we show here the results corresponding to the lattice parameters provided by the Karlsruhe group although the general trends found in other renormalized band structures corresponding to the rest of the sets of lattice parameters (not shown here) are the same except for those lattice parameters coming from the extrapolation at high pressures, for which we find a more correlated electronic band structure.

## F.2 Van Hove singularities in a 1-band model

In Fig. F.5 we plot for 6 different values of the second nearest-neighbor hopping  $t'/t$  the quasiparticle weight  $Z$  as a function of the local Coulomb interaction  $U/D$  at different fillings  $n$ . The first thing we can notice is that there is an asymmetry between the electron- and the hole-doped regimes, and that this difference is bigger when the value of  $|t'/t|$  increases. This is a direct consequence of the lack of particle-hole symmetry induced by the presence of this second-nearest hopping. The second and most obvious result is the symmetry between the 2 values of  $|t'/t|$ . We show this result here to illustrate the complete equivalence between a hole-doped case with a positive value of  $t'/t$  and an electron-doped case with a negative value of  $t'/t$  and vice-versa.

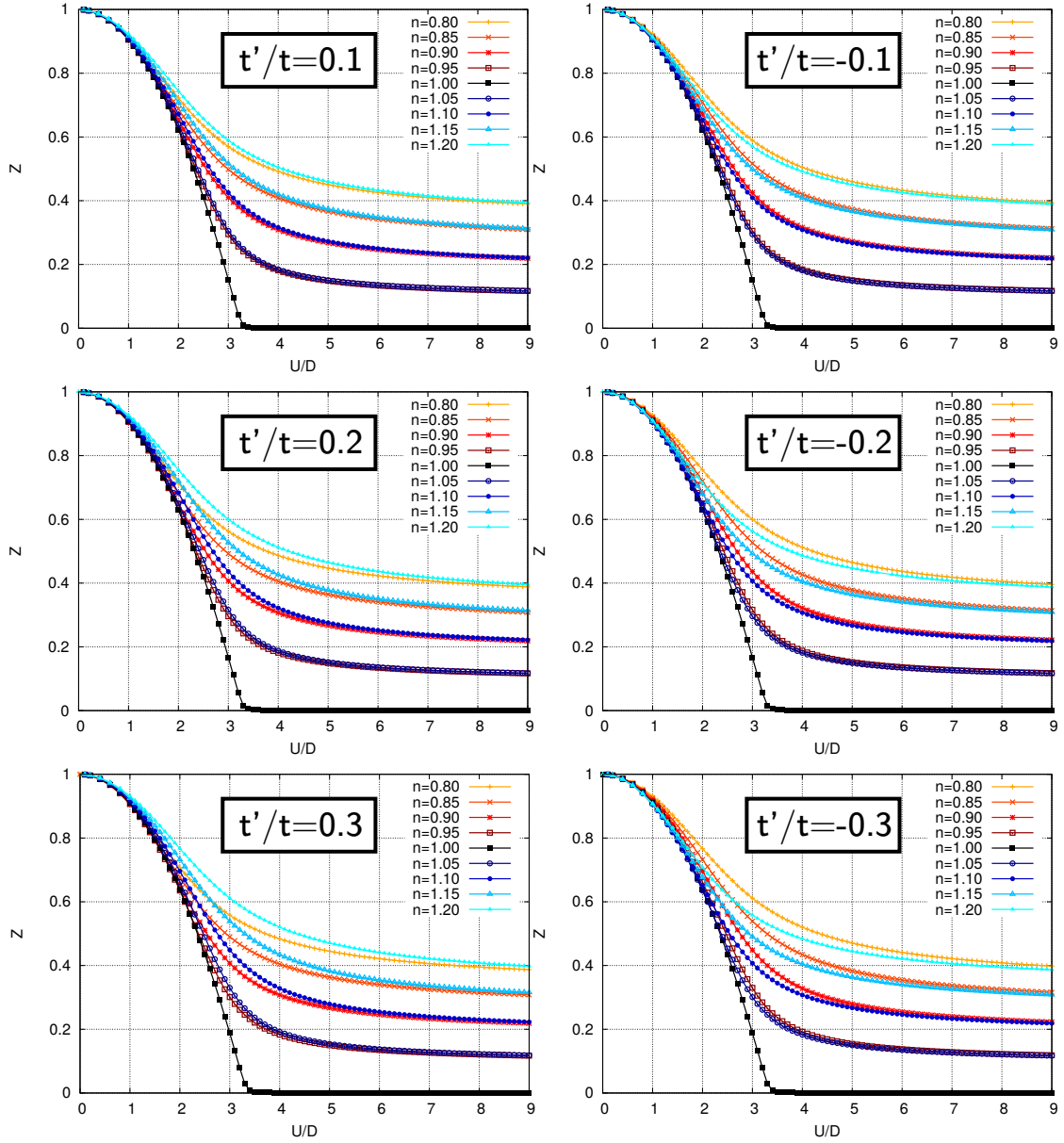


**Figure F.5:** Quasiparticle weight  $Z$  calculated with SSMFT as a function of the Coulomb interaction  $U/D$  for the square lattice with different second nearest-neighbor hoppings  $t'/t$  and for different particle densities  $n$ .

# Bibliography

- [1] N. F. Mott, “The Basis of the Electron Theory of Metals, with Special Reference to the Transition Metals,” *Proceedings of the Physical Society. Section A*, vol. 62, no. 7, p. 416, 1949.
- [2] M. Imada, A. Fujimori, and Y. Tokura, “Metal-insulator transitions,” *Rev. Mod. Phys.*, vol. 70, pp. 1039–1263, Oct 1998.
- [3] D. B. McWhan and J. P. Remeika, “Metal-Insulator Transition in  $(V_{1-x}Cr_x)_2O_3$ ,” *Phys. Rev. B*, vol. 2, pp. 3734–3750, 1970.
- [4] D. B. McWhan, J. P. Remeika, T. M. Rice, W. F. Brinkman, J. P. Maita, and A. Menth, “Electronic Specific Heat of Metallic Ti-Doped  $V_2O_3$ ,” *Phys. Rev. Lett.*, vol. 27, pp. 941–943, 1971.
- [5] A. Hebard, M. Rosseinsky, R. Haddon, D. Murphy, S. Glarum, T. Palstra, A. Ramirez, and A. Karton, “Potassium-doped  $C_{60}$ ,” *Nature*, vol. 350, pp. 600–601, 1991.
- [6] M. Capone, M. Fabrizio, C. Castellani, and E. Tosatti, “Strongly Correlated Superconductivity,” *Science*, vol. 296, no. 5577, pp. 2364–2366, 2002.
- [7] J. Coey, M. Viret, and S. Von Molnar, “Mixed-valence manganites,” *Advances in physics*, vol. 48, no. 2, pp. 167–293, 1999.
- [8] J. G. Bednorz and K. A. Müller, “Perovskite-type oxides—The new approach to high- $T_c$  superconductivity,” *Rev. Mod. Phys.*, vol. 60, pp. 585–600, 1988.
- [9] W. E. Pickett, “Electronic structure of the high-temperature oxide superconductors,” *Rev. Mod. Phys.*, vol. 61, pp. 433–512, 1989.
- [10] E. Dagotto, “Correlated electrons in high-temperature superconductors,” *Rev. Mod. Phys.*, vol. 66, pp. 763–840, 1994.

- 
- [11] P. Nozières, *Theory of Interacting Fermi systems*. Westview Press, 1997.
- [12] J. Kondo, “Resistance Minimum in Dilute Magnetic Alloys,” *Progress of Theoretical Physics*, vol. 32, no. 1, pp. 37–49, 1964.
- [13] P. W. Anderson, “Localized Magnetic States in Metals,” *Phys. Rev.*, vol. 124, pp. 41–53, 1961.
- [14] N. Grewe and F. Steglich, “Heavy fermions,” *Handbook on the Physics and Chemistry of Rare Earths*, vol. 14, pp. 343–474, 1991.
- [15] P. Coleman, “Heavy fermions: Electrons at the edge of magnetism,” *arXiv preprint cond-mat/0612006*, 2006.
- [16] G. R. Stewart, “Heavy-fermion systems,” *Rev. Mod. Phys.*, vol. 56, pp. 755–787, Oct 1984.
- [17] A. C. Hewson, *The Kondo problem to heavy fermions*, vol. 2. Cambridge university press, 1997.
- [18] S. Kondo, D. C. Johnston, C. A. Swenson, F. Borsa, A. V. Mahajan, L. L. Miller, T. Gu, A. I. Goldman, M. B. Maple, D. A. Gajewski, E. J. Freeman, N. R. Dilley, R. P. Dickey, J. Merrin, K. Kojima, G. M. Luke, Y. J. Uemura, O. Chmaissem, and J. D. Jorgensen, “ $\text{LiV}_2\text{O}_4$ : A Heavy Fermion Transition Metal Oxide,” *Phys. Rev. Lett.*, vol. 78, pp. 3729–3732, 1997.
- [19] F. Hardy, A. E. Böhmer, D. Aoki, P. Burger, T. Wolf, P. Schweiss, R. Heid, P. Adelman, Y. X. Yao, G. Kotliar, J. Schmalian, and C. Meingast, “Evidence of Strong Correlations and Coherence-Incoherence Crossover in the Iron Pnictide Superconductor  $\text{KFe}_2\text{As}_2$ ,” *Phys. Rev. Lett.*, vol. 111, p. 027002, 2013.
- [20] F. Hardy, A. E. Böhmer, L. de’ Medici, M. Capone, G. Giovannetti, R. Eder, L. Wang, M. He, T. Wolf, P. Schweiss, R. Heid, A. Herbig, P. Adelman, R. A. Fisher, and C. Meingast, “Strong correlations, strong coupling, and s-wave superconductivity in hole-doped  $\text{BaFe}_2\text{As}_2$  single crystals,” *Phys. Rev. B*, vol. 94, p. 205113, 2016.
- [21] J. Bardeen, L. N. Cooper, and J. R. Schrieffer, “Microscopic theory of superconductivity,” *Phys. Rev.*, vol. 106, pp. 162–164, 1957.
- [22] J. Bardeen, L. N. Cooper, and J. R. Schrieffer, “Theory of superconductivity,” *Phys. Rev.*, vol. 108, pp. 1175–1204, 1957.
- [23] A. Migdal, “Interaction between electrons and lattice vibrations in a normal metal,” *Sov. Phys. JETP*, vol. 7, no. 6, pp. 996–1001, 1958.

- 
- [24] G. Eliashberg, “Interactions between electrons and lattice vibrations in a superconductor,” *Sov. Phys. JETP*, vol. 11, no. 3, pp. 696–702, 1960.
- [25] J. P. Carbotte, “Properties of boson-exchange superconductors,” *Rev. Mod. Phys.*, vol. 62, pp. 1027–1157, 1990.
- [26] J. Nagamatsu, N. Nakagawa, T. Muranaka, Y. Zenitani, and J. Akimitsu, “Superconductivity at 39 K in magnesium diboride,” *nature*, vol. 410, no. 6824, p. 63, 2001.
- [27] J. Kortus, I. I. Mazin, K. D. Belashchenko, V. P. Antropov, and L. L. Boyer, “Superconductivity of Metallic Boron in  $\text{MgB}_2$ ,” *Phys. Rev. Lett.*, vol. 86, pp. 4656–4659, May 2001.
- [28] A. Y. Liu, I. I. Mazin, and J. Kortus, “Beyond Eliashberg Superconductivity in  $\text{MgB}_2$ : Anharmonicity, Two-Phonon Scattering, and Multiple Gaps,” *Phys. Rev. Lett.*, vol. 87, p. 087005, 2001.
- [29] N. W. Ashcroft, “Metallic Hydrogen: A High-Temperature Superconductor?,” *Phys. Rev. Lett.*, vol. 21, pp. 1748–1749, 1968.
- [30] A. Drozdov, M. Eremets, I. Troyan, V. Ksenofontov, and S. Shylin, “Conventional superconductivity at 203 kelvin at high pressures in the sulfur hydride system,” *Nature*, vol. 525, no. 7567, p. 73, 2015.
- [31] M. Somayazulu, M. Ahart, A. K. Mishra, Z. M. Geballe, M. Baldini, Y. Meng, V. V. Struzhkin, and R. J. Hemley, “Evidence for superconductivity above 260 k in lanthanum superhydride at megabar pressures,” *arXiv preprint arXiv:1808.07695*, 2018.
- [32] J. G. Bednorz and K. A. Müller, “Possible high $T_c$  superconductivity in the Ba–La–Cu–O system,” *Zeitschrift für Physik B Condensed Matter*, vol. 64, no. 2, pp. 189–193, 1986.
- [33] Y. Kamihara, T. Watanabe, M. Hirano, and H. Hosono, “Iron-Based Layered Superconductor  $\text{La}[\text{O}_{1-x}\text{F}_x]\text{FeAs}$  ( $x=0.05\text{--}0.12$ ) with  $T_c=26$  K,” *Journal of the American Chemical Society*, vol. 130, no. 11, pp. 3296–3297, 2008.
- [34] H. Hosono, A. Yamamoto, H. Hiramatsu, and Y. Ma, “Recent advances in iron-based superconductors toward applications,” *Materials Today*, vol. 21, no. 3, pp. 278 – 302, 2018.
- [35] J. Paglione and R. L. Greene, “High-temperature superconductivity in iron-based materials,” *Nature Physics*, vol. 6, no. 9, pp. 645–658, 2010.
- [36] P. D. Johnson, G. Xu, and W.-G. Yin, *Iron-based superconductivity*, vol. 211. Springer, 2015.

- [37] A. Martinelli, F. Bernardini, and S. Massidda, “The phase diagrams of iron-based superconductors: theory and experiments,” *Comptes Rendus Physique*, vol. 17, no. 1, pp. 5–35, 2016.
- [38] G. R. Stewart, “Superconductivity in iron compounds,” *Rev. Mod. Phys.*, vol. 83, pp. 1589–1652, 2011.
- [39] E. Dagotto, “Colloquium: The unexpected properties of alkali metal iron selenide superconductors,” *Rev. Mod. Phys.*, vol. 85, pp. 849–867, 2013.
- [40] S. Avci, O. Chmaissem, D. Y. Chung, S. Rosenkranz, E. A. Goremychkin, J. P. Castellán, I. S. Todorov, J. A. Schlueter, H. Claus, A. Daoud-Aladine, D. D. Khalyavin, M. G. Kanatzidis, and R. Osborn, “Phase diagram of  $\text{Ba}_{1-x}\text{K}_x\text{Fe}_2\text{As}_2$ ,” *Phys. Rev. B*, vol. 85, p. 184507, 2012.
- [41] T. Yildirim, “Strong Coupling of the Fe-Spin State and the As-As Hybridization in Iron-Pnictide Superconductors from First-Principle Calculations,” *Phys. Rev. Lett.*, vol. 102, p. 037003, 2009.
- [42] M. S. Torikachvili, S. L. Bud’ko, N. Ni, and P. C. Canfield, “Pressure Induced Superconductivity in  $\text{CaFe}_2\text{As}_2$ ,” *Phys. Rev. Lett.*, vol. 101, p. 057006, 2008.
- [43] A. Kreyssig, M. A. Green, Y. Lee, G. D. Samolyuk, P. Zajdel, J. W. Lynn, S. L. Bud’ko, M. S. Torikachvili, N. Ni, S. Nandi, J. B. Leão, S. J. Poulton, D. N. Argyriou, B. N. Harmon, R. J. McQueeney, P. C. Canfield, and A. I. Goldman, “Pressure-induced volume-collapsed tetragonal phase of  $\text{CaFe}_2\text{As}_2$  as seen via neutron scattering,” *Phys. Rev. B*, vol. 78, p. 184517, 2008.
- [44] G. Venturini and B. Malaman, “X-ray single crystal refinements on some  $\text{RT}_2\text{Ge}_2$  compounds ( $\text{R} = \text{Ca}, \text{Y}, \text{La}, \text{Nd}, \text{U}$ ;  $\text{T} = \text{Mn-Cu}, \text{Ru-Pd}$ ): evolution of the chemical bonds,” *Journal of Alloys and Compounds*, vol. 235, no. 2, pp. 201 – 209, 1996.
- [45] M. Avila, S. Bud’ko, and P. Canfield, “Anisotropic magnetization, specific heat and resistivity of  $\text{RFe}_2\text{Ge}_2$  single crystals,” *Journal of Magnetism and Magnetic Materials*, vol. 270, no. 1, pp. 51 – 76, 2004.
- [46] Y. Zou, Z. Feng, P. W. Logg, J. Chen, G. Lampronti, and F. M. Grosche, “Fermi liquid breakdown and evidence for superconductivity in  $\text{YFe}_2\text{Ge}_2$ ,” *Physica Status Solidi (RRL) – Rapid Research Letters*, vol. 8, no. 11, pp. 928–930.
- [47] H. Kim, S. Ran, E. Mun, H. Hodovanets, M. Tanatar, R. Prozorov, S. Bud’ko, and P. Canfield, “Crystal growth and annealing study of fragile, non-bulk superconductivity in  $\text{YFe}_2\text{Ge}_2$ ,” *Philosophical Magazine*, vol. 95, no. 7, pp. 804–818, 2015.

- [48] J. Chen, K. Semeniuk, Z. Feng, P. Reiss, P. Brown, Y. Zou, P. W. Logg, G. I. Lampronti, and F. M. Grosche, “Unconventional Superconductivity in the Layered Iron Germanide  $\text{YFe}_2\text{Ge}_2$ ,” *Phys. Rev. Lett.*, vol. 116, p. 127001, Mar 2016.
- [49] J. Ferstl, H. Rosner, and C. Geibel, “Evidence for fluctuating Fe-moments in  $\text{RFe}_2\text{Ge}_2$  (R=Lu,Yb),” *Physica B: Condensed Matter*, vol. 378-380, pp. 744 – 745, 2006. Proceedings of the International Conference on Strongly Correlated Electron Systems.
- [50] N. Sirica, F. Bondino, S. Nappini, I. Píš, L. Poudel, A. D. Christianson, D. Mandrus, D. J. Singh, and N. Mannella, “Spectroscopic evidence for strong quantum spin fluctuations with itinerant character in  $\text{YFe}_2\text{Ge}_2$ ,” *Phys. Rev. B*, vol. 91, p. 121102, 2015.
- [51] S. Medvedev, T. M. McQueen, I. A. Troyan, T. Palasyuk, M. I. Eremets, R. J. Cava, S. Naghavi, F. Casper, V. Ksenofontov, G. Wortmann, *et al.*, “Electronic and magnetic phase diagram of  $\beta\text{-Fe}_{1.01}\text{Se}$  with superconductivity at 36.7 K under pressure,” *Nature Materials*, vol. 8, no. 8, pp. 630–633, 2009.
- [52] A. E. Böhmer, T. Arai, F. Hardy, T. Hattori, T. Iye, T. Wolf, H. v. Löhneysen, K. Ishida, and C. Meingast, “Origin of the Tetragonal-to-Orthorhombic Phase Transition in FeSe: A Combined Thermodynamic and NMR Study of Nematicity,” *Phys. Rev. Lett.*, vol. 114, p. 027001, 2015.
- [53] S. Margadonna, Y. Takabayashi, Y. Ohishi, Y. Mizuguchi, Y. Takano, T. Kagayama, T. Nakagawa, M. Takata, and K. Prassides, “Pressure evolution of the low-temperature crystal structure and bonding of the superconductor FeSe ( $T_c = 37$  K),” *Phys. Rev. B*, vol. 80, p. 064506, 2009.
- [54] V. Svitlyk, M. Raba, V. Dmitriev, P. Rodière, P. Toulemonde, D. Chernyshov, and M. Mezouar, “Complex biphase nature of the superconducting dome of the FeSe phase diagram,” *Phys. Rev. B*, vol. 96, p. 014520, 2017.
- [55] J.-F. Ge, Z.-L. Liu, C. Liu, C.-L. Gao, D. Qian, Q.-K. Xue, Y. Liu, and J.-F. Jia, “Superconductivity above 100 K in single-layer FeSe films on doped  $\text{SrTiO}_3$ ,” *Nature Materials*, vol. 14, no. 3, pp. 285–289, 2015.
- [56] A. I. Coldea and M. D. Watson, “The Key Ingredients of the Electronic Structure of FeSe,” *Annual Review of Condensed Matter Physics*, vol. 9, no. 1, pp. 125–146, 2018.
- [57] D. V. Evtushinsky, M. Aichhorn, Y. Sassa, Z.-H. Liu, J. Maletz, T. Wolf, A. N. Yaresko, S. Biermann, S. V. Borisenko, and B. Buchner, “Direct observation of dispersive lower Hubbard band in iron-based superconductor FeSe,” *arXiv preprint arXiv:1612.02313*, 2016.

- 
- [58] M. D. Watson, S. Backes, A. A. Haghighirad, M. Hoesch, T. K. Kim, A. I. Coldea, and R. Valentí, “Formation of Hubbard-like bands as a fingerprint of strong electron-electron interactions in FeSe,” *Phys. Rev. B*, vol. 95, p. 081106, 2017.
- [59] Y. Kushnirenko, A. A. Kordyuk, A. Fedorov, E. Haubold, T. Wolf, B. Büchner, and S. V. Borisenko, “Anomalous temperature evolution of the electronic structure of FeSe,” *arXiv preprint arXiv:1702.02088*, 2017.
- [60] L. C. Rhodes, M. D. Watson, A. A. Haghighirad, M. Eschrig, and T. K. Kim, “Strongly enhanced temperature dependence of the chemical potential in FeSe,” *arXiv preprint arXiv:1702.06321*, 2017.
- [61] V. Brouet, P.-H. Lin, Y. Texier, J. Bobroff, A. Taleb-Ibrahimi, P. Le Fèvre, F. Bertran, M. Casula, P. Werner, S. Biermann, F. Rullier-Albenque, A. Forget, and D. Colson, “Large Temperature Dependence of the Number of Carriers in Co-Doped BaFe<sub>2</sub>As<sub>2</sub>,” *Phys. Rev. Lett.*, vol. 110, p. 167002, 2013.
- [62] P. O. Sprau, A. Kostin, A. Kreisel, A. E. Böhmer, V. Taufour, P. C. Canfield, S. Mukherjee, P. J. Hirschfeld, B. M. Andersen, and J. C. S. Davis, “Discovery of orbital-selective Cooper pairing in FeSe,” *Science*, vol. 357, no. 6346, pp. 75–80, 2017.
- [63] A. Kostin, P. O. Sprau, A. Kreisel, Y. Xue Chong, A. E. Böhmer, P. C. Canfield, P. J. Hirschfeld, B. M. Andersen, and J. C. Séamus Davis, “Visualizing Orbital-selective Quasiparticle Interference in the Hund’s Metal State of FeSe,” *ArXiv e-prints*, 2018.
- [64] J. Solyom, *Fundamentals of the Physics of Solids, vol. III: Normal, Broken-Symmetry, and Correlated Systems*. Springer, 2010.
- [65] D. J. Singh and L. Nordstrom, *Planewaves, Pseudopotentials, and the LAPW method*. Springer Science & Business Media, 2006.
- [66] L. de’ Medici and M. Capone, *Modeling Many-Body Physics with Slave-Spin Mean-Field: Mott and Hund’s Physics in Fe-Superconductors*, pp. 115–185. Cham: Springer International Publishing, 2017.
- [67] A. Georges, G. Kotliar, W. Krauth, and M. J. Rozenberg, “Dynamical mean-field theory of strongly correlated fermion systems and the limit of infinite dimensions,” *Rev. Mod. Phys.*, vol. 68, pp. 13–125, 1996.
- [68] A. Georges, “Strongly Correlated Electron Materials: Dynamical Mean-Field Theory and Electronic Structure,” *AIP Conference Proceedings*, vol. 715, no. 1, pp. 3–74, 2004.

- 
- [69] R. O. Jones, “Density functional theory: Its origins, rise to prominence, and future,” *Rev. Mod. Phys.*, vol. 87, pp. 897–923, Aug 2015.
- [70] M. Born and R. Oppenheimer, “Zur Quantentheorie der Molekeln,” *Annalen der Physik*, vol. 389, pp. 457–484, 1927.
- [71] P. Hohenberg and W. Kohn, “Inhomogeneous Electron Gas,” *Physical Review*, vol. 136, pp. B864–B871, Nov 1964.
- [72] W. Kohn and L. J. Sham, “Self-Consistent Equations Including Exchange and Correlation Effects,” *Physical Review*, vol. 140, pp. A1133–A1138, Nov 1965.
- [73] M. C. Gutzwiller, “Effect of Correlation on the Ferromagnetism of Transition Metals,” *Phys. Rev. Lett.*, vol. 10, pp. 159–162, 1963.
- [74] J. Kanamori, “Electron Correlation and Ferromagnetism of Transition Metals,” *Progress of Theoretical Physics*, vol. 30, no. 3, pp. 275–289, 1963.
- [75] J. Hubbard, “Electron correlations in narrow energy bands,” *Proceedings of the Royal Society of London A: Mathematical, Physical and Engineering Sciences*, vol. 276, no. 1365, pp. 238–257, 1963.
- [76] G. H. Wannier, “The Structure of Electronic Excitation Levels in Insulating Crystals,” *Phys. Rev.*, vol. 52, pp. 191–197, Aug 1937.
- [77] N. Marzari, A. A. Mostofi, J. R. Yates, I. Souza, and D. Vanderbilt, “Maximally localized Wannier functions: Theory and applications,” *Rev. Mod. Phys.*, vol. 84, pp. 1419–1475, 2012.
- [78] A. A. Mostofi, J. R. Yates, Y.-S. Lee, I. Souza, D. Vanderbilt, and N. Marzari, “Wannier90: A tool for obtaining maximally-localised Wannier functions,” *Computer Physics Communications*, vol. 178, no. 9, pp. 685–699, 2008.
- [79] A. Georges, L. de’ Medici, and J. Mravlje, “Strong Correlations from Hund’s Coupling,” *Annual Review of Condensed Matter Physics*, vol. 4, no. 1, pp. 137–178, 2013.
- [80] G. Kotliar and A. E. Ruckenstein, “New Functional Integral Approach to Strongly Correlated Fermi Systems: The Gutzwiller Approximation as a Saddle Point,” *Phys. Rev. Lett.*, vol. 57, pp. 1362–1365, 1986.
- [81] L. de’ Medici, A. Georges, and S. Biermann, “Orbital-selective Mott transition in multiband systems: Slave-spin representation and dynamical mean-field theory,” *Phys. Rev. B*, vol. 72, p. 205124, 2005.

- 
- [82] S. R. Hassan and L. de' Medici, "Slave spins away from half filling: Cluster mean-field theory of the Hubbard and extended Hubbard models," *Phys. Rev. B*, vol. 81, p. 035106, 2010.
- [83] S. Florens and A. Georges, "Quantum impurity solvers using a slave rotor representation," *Phys. Rev. B*, vol. 66, p. 165111, 2002.
- [84] S. Florens and A. Georges, "Slave-rotor mean-field theories of strongly correlated systems and the Mott transition in finite dimensions," *Phys. Rev. B*, vol. 70, p. 035114, 2004.
- [85] A. Rüegg, S. D. Huber, and M. Sigrist, " $Z_2$ -slave-spin theory for strongly correlated fermions," *Phys. Rev. B*, vol. 81, p. 155118, Apr 2010.
- [86] M. Schiró and M. Fabrizio, "Quantum quenches in the Hubbard model: Time-dependent mean-field theory and the role of quantum fluctuations," *Phys. Rev. B*, vol. 83, p. 165105, Apr 2011.
- [87] M. Mardani, M.-S. Vaezi, and A. Vaezi, "Slave-spin approach to the strongly correlated systems," *arXiv preprint arXiv:1111.5980*, 2011.
- [88] A. B. Georgescu and S. Ismail-Beigi, "Symmetry breaking in occupation number based slave-particle methods," *Phys. Rev. B*, vol. 96, p. 165135, 2017.
- [89] A. B. Georgescu and S. Ismail-Beigi, "Generalized slave-particle method for extended Hubbard models," *Phys. Rev. B*, vol. 92, p. 235117, Dec 2015.
- [90] R. Yu and Q. Si, " $U(1)$  slave-spin theory and its application to Mott transition in a multiorbital model for iron pnictides," *Phys. Rev. B*, vol. 86, p. 085104, 2012.
- [91] A. Georges and G. Kotliar, "Hubbard model in infinite dimensions," *Phys. Rev. B*, vol. 45, pp. 6479–6483, 1992.
- [92] W. Metzner and D. Vollhardt, "Correlated Lattice Fermions in  $d = \infty$  Dimensions," *Phys. Rev. Lett.*, vol. 62, pp. 324–327, 1989.
- [93] M. Jarrell, "Hubbard model in infinite dimensions: A quantum Monte Carlo study," *Phys. Rev. Lett.*, vol. 69, pp. 168–171, 1992.
- [94] M. J. Rozenberg, X. Y. Zhang, and G. Kotliar, "Mott-Hubbard transition in infinite dimensions," *Phys. Rev. Lett.*, vol. 69, pp. 1236–1239, 1992.
- [95] A. Georges and W. Krauth, "Numerical solution of the  $d=\infty$  hubbard model: Evidence for a mott transition," *Phys. Rev. Lett.*, vol. 69, pp. 1240–1243, Aug 1992.

- 
- [96] E. Gull, A. J. Millis, A. I. Lichtenstein, A. N. Rubtsov, M. Troyer, and P. Werner, “Continuous-time Monte Carlo methods for quantum impurity models,” *Rev. Mod. Phys.*, vol. 83, pp. 349–404, 2011.
- [97] N. Dasari, W. R. Mondal, P. Zhang, J. Moreno, M. Jarrell, and N. S. Vidhyadhiraja, “A multi-orbital iterated perturbation theory for model Hamiltonians and real material-specific calculations of correlated systems,” *The European Physical Journal B*, vol. 89, no. 9, p. 202, 2016.
- [98] R. Bulla, “Zero Temperature Metal-Insulator Transition in the Infinite-Dimensional Hubbard Model,” *Phys. Rev. Lett.*, vol. 83, pp. 136–139, 1999.
- [99] R. Bulla, T. A. Costi, and T. Pruschke, “Numerical renormalization group method for quantum impurity systems,” *Rev. Mod. Phys.*, vol. 80, pp. 395–450, 2008.
- [100] D. J. García, K. Hallberg, and M. J. Rozenberg, “Dynamical Mean Field Theory with the Density Matrix Renormalization Group,” *Phys. Rev. Lett.*, vol. 93, p. 246403, 2004.
- [101] D. Bauernfeind, M. Zingl, R. Triebl, M. Aichhorn, and H. G. Evertz, “Fork Tensor-Product States: Efficient Multiorbital Real-Time DMFT Solver,” *Phys. Rev. X*, vol. 7, p. 031013, 2017.
- [102] M. Caffarel and W. Krauth, “Exact diagonalization approach to correlated fermions in infinite dimensions: Mott transition and superconductivity,” *Phys. Rev. Lett.*, vol. 72, pp. 1545–1548, 1994.
- [103] Q. Si, M. J. Rozenberg, G. Kotliar, and A. E. Ruckenstein, “Correlation induced insulator to metal transitions,” *Phys. Rev. Lett.*, vol. 72, pp. 2761–2764, 1994.
- [104] M. J. Rozenberg, G. Moeller, and G. Kotliar, “The Metal-Insulator Transition in the Hubbard Model at zero temperature II,” *Modern Physics Letters B*, vol. 08, no. 08n09, pp. 535–543, 1994.
- [105] K. Schwarz and P. Blaha, “Solid state calculations using WIEN2k,” *Comp. Mater. Sci.*, vol. 28, pp. 259–273, 2003.
- [106] P. Giannozzi, S. Baroni, N. Bonini, M. Calandra, R. Car, C. Cavazzoni, D. Ceresoli, G. L. Chiarotti, M. Cococcioni, I. Dabo, A. D. Corso, S. de Gironcoli, S. Fabris, G. Fratesi, R. Gebauer, U. Gerstmann, C. Gougoussis, A. Kokalj, M. Lazzeri, L. Martin-Samos, N. Marzari, F. Mauri, R. Mazzarello, S. Paolini, A. Pasquarello, L. Paulatto, C. Sbraccia, S. Scandolo, G. Sclauzero, A. P. Seitsonen, A. Smogunov, P. Umari, and R. M. Wentzcovitch, “QUANTUM ESPRESSO: a modular and open-source software project for quantum

- simulations of materials,” *Journal of Physics: Condensed Matter*, vol. 21, no. 39, p. 395502, 2009.
- [107] T. Miyake, K. Nakamura, R. Arita, and M. Imada, “Comparison of ab initio low-energy models for LaFePO, LaFeAsO, BaFe<sub>2</sub>As<sub>2</sub>, LiFeAs, FeSe, and FeTe: electron correlation and covalency,” *Journal of the Physical Society of Japan*, vol. 79, no. 4, p. 044705, 2010.
- [108] Z. Yin, K. Haule, and G. Kotliar, “Kinetic frustration and the nature of the magnetic and paramagnetic states in iron pnictides and iron chalcogenides,” *Nature materials*, vol. 10, no. 12, p. 932, 2011.
- [109] L. de’ Medici, J. Mravlje, and A. Georges, “Janus-Faced Influence of Hund’s Rule Coupling in Strongly Correlated Materials,” *Phys. Rev. Lett.*, vol. 107, p. 256401, 2011.
- [110] J. Mravlje, M. Aichhorn, T. Miyake, K. Haule, G. Kotliar, and A. Georges, “Coherence-Incoherence Crossover and the Mass-Renormalization Puzzles in Sr<sub>2</sub>RuO<sub>4</sub>,” *Phys. Rev. Lett.*, vol. 106, p. 096401, 2011.
- [111] T. Kondo, M. Ochi, M. Nakayama, H. Taniguchi, S. Akebi, K. Kuroda, M. Arita, S. Sakai, H. Namatame, M. Taniguchi, Y. Maeno, R. Arita, and S. Shin, “Orbital-Dependent Band Narrowing Revealed in an Extremely Correlated Hund’s Metal Emerging on the Topmost Layer of Sr<sub>2</sub>RuO<sub>4</sub>,” *Phys. Rev. Lett.*, vol. 117, p. 247001, Dec 2016.
- [112] S. Lafuerza, H. Gretarsson, F. Hardy, T. Wolf, C. Meingast, G. Giovannetti, M. Capone, A. S. Sefat, Y.-J. Kim, P. Glatzel, and L. de’ Medici, “Evidence of Mott physics in iron pnictides from x-ray spectroscopy,” *Phys. Rev. B*, vol. 96, p. 045133, 2017.
- [113] H. Gretarsson, A. Lupascu, J. Kim, D. Casa, T. Gog, W. Wu, S. R. Julian, Z. J. Xu, J. S. Wen, G. D. Gu, R. H. Yuan, Z. G. Chen, N.-L. Wang, S. Khim, K. H. Kim, M. Ishikado, I. Jarrige, S. Shamoto, J.-H. Chu, I. R. Fisher, and Y.-J. Kim, “Revealing the dual nature of magnetism in iron pnictides and iron chalcogenides using x-ray emission spectroscopy,” *Phys. Rev. B*, vol. 84, p. 100509, 2011.
- [114] J. Pellicciari, Y. Huang, K. Ishii, C. Zhang, P. Dai, G. F. Chen, L. Xing, X. Wang, C. Jin, H. Ding, *et al.*, “Magnetic moment evolution and spin freezing in doped BaFe<sub>2</sub>As<sub>2</sub>,” *Scientific reports*, vol. 7, no. 1, p. 8003, 2017.
- [115] L. de’ Medici, G. Giovannetti, and M. Capone, “Selective Mott Physics as a Key to Iron Superconductors,” *Phys. Rev. Lett.*, vol. 112, p. 177001, 2014.

- 
- [116] Z. P. Yin, K. Haule, and G. Kotliar, “Kinetic frustration and the nature of the magnetic and paramagnetic states in iron pnictides and iron chalcogenides,” *Nature Materials*, vol. 10, no. 12, pp. 932–935, 2011.
- [117] S. Backes, H. O. Jeschke, and R. Valentí, “Microscopic nature of correlations in multiorbital  $A\text{Fe}_2\text{As}_2$  ( $A = \text{K}, \text{Rb}, \text{Cs}$ ): Hund’s coupling versus Coulomb repulsion,” *Phys. Rev. B*, vol. 92, p. 195128, Nov 2015.
- [118] H. Ishida and A. Liebsch, “Fermi-liquid, non-Fermi-liquid, and Mott phases in iron pnictides and cuprates,” *Phys. Rev. B*, vol. 81, p. 054513, 2010.
- [119] A. O. Shorikov, M. A. Korotin, S. V. Streltsov, S. L. Skornyakov, D. M. Korotin, and V. I. Anisimov, “Coulomb correlation effects in  $\text{LaFeAsO}$ : An LDA + DMFT(QMC) study,” *Journal of Experimental and Theoretical Physics*, vol. 108, no. 1, pp. 121–125, 2009.
- [120] M. Aichhorn, S. Biermann, T. Miyake, A. Georges, and M. Imada, “Theoretical evidence for strong correlations and incoherent metallic state in  $\text{FeSe}$ ,” *Phys. Rev. B*, vol. 82, p. 064504, 2010.
- [121] P. Werner, M. Casula, T. Miyake, F. Aryasetiawan, A. J. Millis, and S. Biermann, “Satellites and large doping and temperature dependence of electronic properties in hole-doped  $\text{BaFe}_2\text{As}_2$ ,” *Nature Physics*, vol. 8, no. 4, pp. 331–337, 2012.
- [122] T. Misawa, K. Nakamura, and M. Imada, “*Ab Initio* Evidence for Strong Correlation Associated with Mott Proximity in Iron-Based Superconductors,” *Phys. Rev. Lett.*, vol. 108, p. 177007, 2012.
- [123] E. Bascones, B. Valenzuela, and M. J. Calderón, “Magnetic interactions in iron superconductors: A review,” *Comptes Rendus Physique*, vol. 17, no. 1, pp. 36 – 59, 2016. Iron-based superconductors / Supraconducteurs à base de fer.
- [124] Q. Si, R. Yu, and E. Abrahams, “High-temperature superconductivity in iron pnictides and chalcogenides,” *Nature Reviews Materials*, vol. 1, no. 4, p. 16017, 2016.
- [125] L. de’ Medici, “Weak and Strong Correlations in Fe Superconductors,” in *Iron-Based Superconductivity*, pp. 409–441, Springer, 2015.
- [126] L. de’ Medici, *Hund’s metals explained*. E. Pavarini, E. Koch, R. Scalettar, and R. Martin (eds.) The Physics of Correlated Insulators, Metals, and Superconductors Modeling and Simulation Vol. 7 Forschungszentrum Juelich, ISBN 978-3-95806-224-5, 2017.

- 
- [127] L. de' Medici, "Hund's coupling and its key role in tuning multi-orbital correlations," *Phys. Rev. B*, vol. 83, p. 205112, 2011.
- [128] H. Ishida and A. Liebsch, "Fermi-liquid, non-Fermi-liquid, and Mott phases in iron pnictides and cuprates," *Phys. Rev. B*, vol. 81, p. 054513, 2010.
- [129] L. Fanfarillo and E. Bascones, "Electronic correlations in Hund metals," *Phys. Rev. B*, vol. 92, p. 075136, 2015.
- [130] L. de' Medici, "Hund's Induced Fermi-Liquid Instabilities and Enhanced Quasiparticle Interactions," *Phys. Rev. Lett.*, vol. 118, p. 167003, 2017.
- [131] A. Koga, N. Kawakami, T. M. Rice, and M. Sgrist, "Orbital-Selective Mott Transitions in the Degenerate Hubbard Model," *Phys. Rev. Lett.*, vol. 92, p. 216402, 2004.
- [132] T. Misawa and M. Imada, "Superconductivity and its mechanism in an ab initio model for electron-doped LaFeAsO," *Nat Commun*, vol. 5, p. 5738, 2014.
- [133] M. Edelmann, G. Sangiovanni, M. Capone, and L. de' Medici, "Chromium analogs of iron-based superconductors," *Phys. Rev. B*, vol. 95, p. 205118, 2017.
- [134] M. Grilli, R. Raimondi, C. Castellani, C. Di Castro, and G. Kotliar, "Phase separation and superconductivity in the  $U=\infty$  limit of the extended multiband Hubbard model," *International Journal of Modern Physics B*, vol. 05, pp. 309–321, 1991.
- [135] M. Grilli and C. Castellani, "Electron-phonon interactions in the presence of strong correlations," *Phys. Rev. B*, vol. 50, pp. 16880–16898, 1994.
- [136] H. Hodovanets, Y. Liu, A. Jesche, S. Ran, E. D. Mun, T. A. Lograsso, S. L. Bud'ko, and P. C. Canfield, "Fermi surface reconstruction in  $(\text{Ba}_{1-x}\text{K}_x)\text{Fe}_2\text{As}_2$  ( $0.44 \leq x \leq 1$ ) probed by thermoelectric power measurements," *Phys. Rev. B*, vol. 89, p. 224517, 2014.
- [137] P. Richard, A. van Roekeghem, X. Shi, P. Seth, T. Kim, X.-H. Chen, S. Biermann, and H. Ding, "Chemical pressure tuning of the van Hove singularity in  $\text{KFe}_2\text{As}_2$  and  $\text{CsFe}_2\text{As}_2$  revealed by angle-resolved photoemission spectroscopy," *arXiv preprint arXiv:1807.00193*, 2018.
- [138] S.-L. Drechsler, S. Johnston, V. Grinenko, J. M. Tomczak, and H. Rosner, "Constraints on the total coupling strength to bosons in the iron based superconductors," *physica status solidi (b)*, vol. 254, no. 10, p. 1700006, 2017.
- [139] S.-L. Drechsler, H. Rosner, V. Grinenko, S. Aswartham, I. Morozov, M. Liu, A. Boltalin, K. Kihou, C. H. Lee, T. Kim, D. Evtushinsky, J. M. Tomczak, S. Johnston, and S. Borisenko, "Mass Enhancements and Band Shifts in

- Strongly Hole-Overdoped Fe-Based Pnictide Superconductors:  $\text{KFe}_2\text{As}_2$  and  $\text{CsFe}_2\text{As}_2$ ,” *Journal of Superconductivity and Novel Magnetism*, vol. 31, no. 3, pp. 777–783, 2018.
- [140] J. P. Perdew, K. Burke, and M. Ernzerhof, “Generalized Gradient Approximation Made Simple,” *Physical Review Letters*, vol. 77, pp. 3865–3868, Oct 1996.
- [141] F. Rullier-Albenque, “Influence of the electronic structure on the transport properties of some iron pnictides,” *Comptes Rendus Physique*, vol. 17, no. 1–2, pp. 164 – 187, 2016.
- [142] S. Rózsa and H.-U. Schuster, “Crystal Structure of  $\text{KFe}_2\text{As}_2$ ,  $\text{KCo}_2\text{As}_2$ ,  $\text{KRh}_2\text{As}_2$  and  $\text{KRh}_2\text{P}_2$ ,” *Zeitschrift für Naturforschung B*, vol. 36, no. 12, pp. 1668–1670, 1981.
- [143] F. F. Tafti, J. P. Clancy, M. Lapointe-Major, C. Collignon, S. Faucher, J. A. Sears, A. Juneau-Fecteau, N. Doiron-Leyraud, A. F. Wang, X.-G. Luo, X. H. Chen, S. Desgreniers, Y.-J. Kim, and L. Taillefer, “Sudden reversal in the pressure dependence of  $T_c$  in the iron-based superconductor  $\text{CsFe}_2\text{As}_2$ : A possible link between inelastic scattering and pairing symmetry,” *Phys. Rev. B*, vol. 89, p. 134502, 2014.
- [144] S. Backes, D. Guterding, H. O. Jeschke, and R. Valentí, “Electronic structure and de Haas–van Alphen frequencies in  $\text{KFe}_2\text{As}_2$  within LDA+DMFT,” *New Journal of Physics*, vol. 16, no. 8, p. 083025, 2014.
- [145] F. Eilers, K. Grube, D. A. Zocco, T. Wolf, M. Merz, P. Schweiss, R. Heid, R. Eder, R. Yu, J.-X. Zhu, Q. Si, T. Shibauchi, and H. v. Löhneysen, “Strain-Driven Approach to Quantum Criticality in  $A\text{Fe}_2\text{As}_2$  with  $A = \text{K}, \text{Rb},$  and  $\text{Cs}$ ,” *Phys. Rev. Lett.*, vol. 116, p. 237003, Jun 2016.
- [146] A. S. Belozеров, A. A. Katanin, and V. I. Anisimov, “Effect of density of states peculiarities on Hund’s metal behavior,” *Phys. Rev. B*, vol. 97, p. 115141, 2018.
- [147] I. Pallecchi, F. Caglieris, and M. Putti, “Thermoelectric properties of iron-based superconductors and parent compounds,” *Superconductor Science and Technology*, vol. 29, no. 7, p. 073002, 2016.
- [148] G. K. H. Madsen and D. J. Singh, “BoltzTraP. A code for calculating band-structure dependent quantities.” *Computer Physics Communications*, vol. 175, no. 1, pp. 67–71, 2006.
- [149] K. Behnia, D. Jaccard, and J. Flouquet, “On the thermoelectricity of correlated electrons in the zero-temperature limit,” *Journal of Physics: Condensed Matter*, vol. 16, no. 28, p. 5187, 2004.

- 
- [150] L. Ortenzi, E. Cappelluti, L. Benfatto, and L. Pietronero, “Fermi-Surface Shrinking and Interband Coupling in Iron-Based Pnictides,” *Phys. Rev. Lett.*, vol. 103, p. 046404, 2009.
- [151] L. Benfatto and E. Cappelluti, “Effects of the Fermi-surface shrinking on the optical sum rule in pnictides,” *Phys. Rev. B*, vol. 83, p. 104516, 2011.
- [152] S. V. Borisenko, D. V. Evtushinsky, Z.-H. Liu, I. Morozov, R. Kappenberger, S. Wurmehl, B. Büchner, A. N. Yaresko, T. K. Kim, M. Hoesch, *et al.*, “Direct observation of spin-orbit coupling in iron-based superconductors,” *Nature Physics*, vol. 12, no. 4, pp. 311–317, 2016.
- [153] H. J. Goldsmid, *Thermoelectric Properties of Metals and Semiconductors*, pp. 25–44. Berlin, Heidelberg: Springer Berlin Heidelberg, 2016.
- [154] P. Coleman, *Introduction to Many-Body Physics*. Cambridge University Press, 2015.
- [155] K. Haule and G. Kotliar, “Thermoelectrics near the mott localization—delocalization transition,” in *Properties and Applications of Thermoelectric Materials* (V. Zlatić and A. C. Hewson, eds.), (Dordrecht), pp. 119–131, Springer Netherlands, 2009.
- [156] J. Mravlje and A. Georges, “Thermopower and Entropy: Lessons from  $\text{Sr}_2\text{RuO}_4$ ,” *Phys. Rev. Lett.*, vol. 117, p. 036401, Jul 2016.
- [157] A. J. Millis, *Optical conductivity and correlated electron physics*, pp. 195–235. Dordrecht: Springer Netherlands, 2004.
- [158] F. Gross, B. S. Chandrasekhar, D. Einzel, K. Andres, P. J. Hirschfeld, H. R. Ott, J. Beuers, Z. Fisk, and J. L. Smith, “Anomalous temperature dependence of the magnetic field penetration depth in superconducting  $\text{UBe}_{13}$ ,” *Zeitschrift für Physik B Condensed Matter*, vol. 64, no. 2, pp. 175–188, 1986.
- [159] P. M. Chaikin and G. Beni, “Thermopower in the correlated hopping regime,” *Phys. Rev. B*, vol. 13, pp. 647–651, 1976.
- [160] P. Villar Arribi and L. de’ Medici, “Hund-Enhanced Electronic Compressibility in FeSe and its Correlation with  $T_c$ ,” *Phys. Rev. Lett.*, vol. 121, p. 197001, 2018.
- [161] R. M. Fernandes, A. V. Chubukov, and J. Schmalian, “What drives nematic order in iron-based superconductors?,” *Nature Physics*, vol. 10, no. 2, pp. 97–104, 2014.
- [162] S. Tan, Y. Zhang, M. Xia, Z. Ye, F. Chen, X. Xie, R. Peng, D. Xu, Q. Fan, H. Xu, *et al.*, “Interface-induced superconductivity and strain-dependent spin

- density waves in FeSe/SrTiO<sub>3</sub> thin films,” *Nature Materials*, vol. 12, no. 7, p. 634, 2013.
- [163] A. O. Shorikov, M. A. Korotin, S. V. Streltsov, S. L. Skornyakov, D. M. Korotin, and V. I. Anisimov, “Coulomb correlation effects in LaFeAsO: An LDA + DMFT(QMC) study,” *Journal of Experimental and Theoretical Physics*, vol. 108, no. 1, pp. 121–125, 2009.
- [164] Q. Si, R. Yu, and E. Abrahams, “High-temperature superconductivity in iron pnictides and chalcogenides,” *Nature Reviews Materials*, vol. 1, p. 16017, 2016.
- [165] M. D. Watson, S. Backes, A. A. Haghighirad, M. Hoesch, T. K. Kim, A. I. Coldea, and R. Valentí, “Formation of Hubbard-like bands as a fingerprint of strong electron-electron interactions in FeSe,” *Phys. Rev. B*, vol. 95, p. 081106, 2017.
- [166] D. V. Evtushinsky, M. Aichhorn, Y. Sassa, Z.-H. Liu, J. Maletz, T. Wolf, A. N. Yaresko, S. Biermann, S. V. Borisenko, and B. Buchner, “Direct observation of dispersive lower Hubbard band in iron-based superconductor FeSe,” *ArXiv e-prints*, 2016.
- [167] V. Emery and S. Kivelson, “Frustrated electronic phase separation and high-temperature superconductors,” *Physica C: Superconductivity*, vol. 209, no. 4, pp. 597 – 621, 1993.
- [168] C. Castellani, C. Di Castro, and M. Grilli, “Singular Quasiparticle Scattering in the Proximity of Charge Instabilities,” *Phys. Rev. Lett.*, vol. 75, pp. 4650–4653, 1995.
- [169] R. S. Kumar, Y. Zhang, S. Sinogeikin, Y. Xiao, S. Kumar, P. Chow, A. L. Cornelius, and C. Chen, “Crystal and electronic structure of FeSe at high pressure and low temperature,” *The Journal of Physical Chemistry B*, vol. 114, no. 39, pp. 12597–12606, 2010.
- [170] S. Mandal, P. Zhang, S. Ismail-Beigi, and K. Haule, “How Correlated is the FeSe/SrTiO<sub>3</sub> System?,” *Phys. Rev. Lett.*, vol. 119, p. 067004, 2017.
- [171] R. S. Kumar, Y. Zhang, Y. Xiao, J. Baker, A. Cornelius, S. Veeramalai, P. Chow, C. Chen, and Y. Zhao, “Pressure induced high spin-low spin transition in FeSe superconductor studied by x-ray emission spectroscopy and ab initio calculations,” *Applied Physics Letters*, vol. 99, no. 6, p. 061913, 2011.
- [172] B. W. Lebert, V. Balédent, P. Toulemonde, J. M. Ablett, and J.-P. Rueff, “Emergent high-spin state above 7 GPa in superconducting FeSe,” *ArXiv e-prints*, 2017.

- 
- [173] M. Yi, Z.-K. Liu, Y. Zhang, R. Yu, J. X. Zhu, J. J. Lee, R. G. Moore, F. T. Schmitt, W. Li, S. C. Riggs, J. H. Chu, B. Lv, J. Hu, M. Hashimoto, S. K. Mo, Z. Hussain, Z. Q. Mao, C. W. Chu, I. R. Fisher, Q. Si, Z. X. Shen, and D. H. Lu, “Observation of universal strong orbital-dependent correlation effects in iron chalcogenides,” *Nat Commun*, vol. 6, p. 7777, 2015.
- [174] M. D. Watson, T. K. Kim, A. A. Haghighirad, N. R. Davies, A. McCollam, A. Narayanan, S. F. Blake, Y. L. Chen, S. Ghannadzadeh, A. J. Schofield, M. Hoesch, C. Meingast, T. Wolf, and A. I. Coldea, “Emergence of the nematic electronic state in FeSe,” *Phys. Rev. B*, vol. 91, p. 155106, 2015.
- [175] N. Lanatà, H. U. R. Strand, G. Giovannetti, B. Hellsing, L. de’ Medici, and M. Capone, “Orbital selectivity in Hund’s metals: The iron chalcogenides,” *Phys. Rev. B*, vol. 87, p. 045122, 2013.
- [176] L. de’ Medici, S. R. Hassan, M. Capone, and X. Dai, “Orbital-Selective Mott Transition out of Band Degeneracy Lifting,” *Phys. Rev. Lett.*, vol. 102, p. 126401, 2009.
- [177] S. Karlsson, P. Strobel, A. Sulpice, C. Marcenat, M. Legendre, F. Gay, S. Pairis, O. Leynaud, and P. Toulemonde, “Study of high-quality superconducting FeSe single crystals: crossover in electronic transport from a metallic to an activated regime above 350 K,” *Superconductor Science and Technology*, vol. 28, no. 10, p. 105009, 2015.
- [178] L. Boeri, O. V. Dolgov, and A. A. Golubov, “Is LaFeAsO<sub>1-x</sub>F<sub>x</sub> an Electron-Phonon Superconductor?,” *Phys. Rev. Lett.*, vol. 101, p. 026403, 2008.
- [179] K. Haule, J. H. Shim, and G. Kotliar, “Correlated Electronic Structure of LaO<sub>1-x</sub>F<sub>x</sub>FeAs,” *Phys. Rev. Lett.*, vol. 100, p. 226402, 2008.
- [180] D.-H. Lee, “What makes the T<sub>c</sub> of FeSe/SrTiO<sub>3</sub> so high?,” *Chinese Phys. B*, vol. 24, p. 117405, 2015.
- [181] L. Rademaker, Y. Wang, T. Berlijn, and S. Johnston, “Enhanced superconductivity due to forward scattering in FeSe thin films on SrTiO<sub>3</sub> substrates,” *New Journal of Physics*, vol. 18, no. 2, p. 022001, 2016.
- [182] Y. Zhou and A. J. Millis, “Dipolar phonons and electronic screening in monolayer FeSe on SrTiO<sub>3</sub>,” *Phys. Rev. B*, vol. 96, p. 054516, 2017.
- [183] S. Mandal, R. E. Cohen, and K. Haule, “Strong pressure-dependent electron-phonon coupling in FeSe,” *Phys. Rev. B*, vol. 89, p. 220502, 2014.
- [184] P. Villar Arribi, F. Bernardini, L. de’ Medici, P. Toulemonde, S. Tencé, and A. Cano, “Magnetic competition in iron-based germanide and silicide superconductors,” *arXiv preprint arXiv:1810.10306*, 2018.

- 
- [185] H. Hosono and K. Kuroki, “Iron-based superconductors: Current status of materials and pairing mechanism,” *Physica C: Superconductivity and its Applications*, vol. 514, pp. 399 – 422, 2015.
- [186] D. Guterding, H. O. Jeschke, I. I. Mazin, J. K. Glasbrenner, E. Bascones, and R. Valentí, “Nontrivial Role of Interlayer Cation States in Iron-Based Superconductors,” *Phys. Rev. Lett.*, vol. 118, p. 017204, Jan 2017.
- [187] F. Bernardini, G. Garbarino, A. Sulpice, M. Núñez Regueiro, E. Gaudin, B. Chevalier, M.-A. Méasson, A. Cano, and S. Tencé, “Iron-based superconductivity extended to the novel silicide LaFeSiH,” *Phys. Rev. B*, vol. 97, p. 100504, Mar 2018.
- [188] A. Drozdov, M. Eremets, I. Troyan, V. Ksenofontov, and S. Shylin, “Conventional superconductivity at 203 kelvin at high pressures in the sulfur hydride system,” *Nature*, vol. 525, no. 7567, p. 73, 2015.
- [189] D. J. Singh, “Superconductivity and magnetism in YFe<sub>2</sub>Ge<sub>2</sub>,” *Phys. Rev. B*, vol. 89, p. 024505, Jan 2014.
- [190] A. Subedi, “Unconventional sign-changing superconductivity near quantum criticality in YFe<sub>2</sub>Ge<sub>2</sub>,” *Phys. Rev. B*, vol. 89, p. 024504, Jan 2014.
- [191] K. Capelle, “A bird’s-eye view of density-functional theory,” *Brazilian Journal of Physics*, vol. 36, no. 4A, pp. 1318–1343, 2006.
- [192] K. Burke and L. O. Wagner, “DFT in a nutshell,” *International Journal of Quantum Chemistry*, vol. 113, no. 2, pp. 96–101, 2013.
- [193] N. M. Harrison, “An introduction to density functional theory,” *NATO SCIENCE SERIES SUB SERIES III COMPUTER AND SYSTEMS SCIENCES*, vol. 187, pp. 45–70, 2003.
- [194] E. Sjöstedt, L. Nordström, and D. J. Singh, “An alternative way of linearizing the augmented plane-wave method,” *Solid state communications*, vol. 114, no. 1, pp. 15–20, 2000.
- [195] J. C. P. Slater, “Wave functions in a periodic potential,” *Physical Review*, vol. 51, no. 10, p. 846, 1937.
- [196] O. K. Andersen, “Linear methods in band theory,” *Physical Review B*, vol. 12, no. 8, p. 3060, 1975.